Meta-liquid-based metasurfaces and applications

Qinghua Song

UNIVERSITÉ PARIS-EST

Ecole Doctorale

Mathématiques, Sciences de l'Information et de la Communication (MSTIC)

THÈSE

pour obtenir le grade de

Docteur de l'Université Paris-Est

Spécialité : Electronique, Optronique et Systèmes

présentée et soutenue publiquement par

Qinghua SONG

le 02 Juin 2017

Meta-Liquid Based Metasurfaces and Applications

Jury

Habiba OUSLIMANI, Professeur, Université Paris Nanterre, IUT-GEII (Rapporteur)
Catherine SCHWOB, Professeur, Université Pierre & Marie Curie, INSP(Rapporteur)
Yamin LEPRINCE-WANG, Professeur, Université Paris-Est, UPEM-ESYCOM (Directrice de thèse)
Tarik BOUROUINA, Professeur, Université Paris-Est, ESIEE Paris-ESYCOM (Directeur de thèse)
Ai-Qun LIU, Professor, Nanyang Technological University, Singapore (Co-Directeur de thèse)
Elodie RICHALOT, Professeur, Université Paris-Est, UPEM-ESYCOM (Examinateur - Présidente)
Elyes NEFZAOUI, Professeur Assistant, Université Paris-Est, ESIEE Paris-ESYCOM (Membre invité)

ACKNOWLEDGMENTS

First and foremost, I would like to express my sincere gratitude and deepest appreciation to my supervisors: Professor Yamin Leprince-Wang, Professor Tarik Bourouina, Professor Ai-Qun Liu, for their continuous support of my PhD study and related research throughout these years. This PhD project could not have been possible without their invaluable guidance, encouragement and insightful suggestions.

Next, I would also like to express my deep appreciation to my co-supervisor Professor Zhong Xiang Shen and Professor Peter Han Joo Chong, School of EEE, Nanyang Technological University, for there constant supervision and advices in the field of RF/Antennas. They have also provided me with technical supports for the setup of microwave experiments. I would like to express my deep gratitude to my seniors Dr. Zhu Weiming, Dr. Wu Pin Chieh and Dr. Zhang Wu, for their patient guidance of this project in the past years and their great contribution in the development of this project. In addition, I would also like to express my sincere appreciation to my senior Dr Patricia Liu Yang, for her tremendous help and valuable comments that greatly improved this thesis.

I would also like to thank all other group members, past and present: Dr. Zhang Jing Bo, Dr. Chin Lip Ket, Dr. Lei Lei, Dr. Dong Bin, Dr. Xiong Sha, Dr. Chen Yanyu, Mr Zhao Haitao, Mr Shi Yuzhi, Mr Huang Jianguo and Mr Yan Libin for their strong support and enlightening discussions.

Besides, I would like to acknowledge Professor Federico Capasso from Harvard University and Professor Din Ping Tsai from National Taiwan University

for their useful discussions and valuable suggestions. I would also like to thank Dr. Teng Jinghua and Dr. Steve Wu from the Institute of Materials Research and Engineering (IMRE), A*STAR, for their support in the terahertz measurement.

I would like to express my sincere gratitude to UPEM, Université Paris-Est and VALENS Center, School of EEE, Nanyang Technological University for supporting this PhD project and providing me with excellent platforms and working environments.

Finally, I would like to express my sincerest appreciation to my parents for their unconditional love, my sisters for their constant support and care all these years.

Song Qinghua

CONTENTS

NOMENCLATURE

EM	Electromagnetic
UV	Ultraviolet
PDMS	Polydimethylsiloxane
LHM	Left-handed material
NIM	Negative-index material
SRR	Split ring resonator
PMA	Perfect metasurface absorber
TE	Transverse electric
TM	Transverse magnetic
EIT	Electromagnetically induced transparency
FSS	Frequency selective surface
GHz	Gigahertz
THz	Terahertz
IR	Infrared
TiO_2	Titanium dioxide
NA	Numerical aperture
MEMS	Microelectromechanical system
PCB	Printed circuit board
EGaIn	Eutectic gallium-indium

MF-SRR	Microfluidic split ring resonator
HCl	Hydrochloric
RARM	Random access reconfigurable metasurface
LCP	Left circular polarized
RCP	Right circular polarized
CST	Computer simulation technology
FDTD	Finite difference time domain
IPA	Isopropanol solution
VNA	Vector network analyzer
FP	Fabry-Pérot
DRIE	Deep Reactive Ion Etching

CHAPTER 1

INTRODUCTION

1.1 Motivations

This PhD research topic is motivated by the potential significance of effective control and manipulation of the electromagnetic (EM) wave using meta-liquid-based metasurfaces based on photolithography fabrication processes. The development of the meta-liquid-based metasurface offers great opportunity to dynamically tailor the EM wave for real life applications, which allows the optical properties to go beyond the possibility of conventional materials. Specifically, metasurfaces have a great potential in manipulating EM wave by enhancing, absorbing, rotating, bending, redirecting waves, etc.

The metasurface refers to the class of technology with the ability to obtain its properties from both the geometric structure and the chemical composition. Although the term of metasurface is relatively new in the scientific world, the manipulation of light can be traced back to the dawn of civilization. For example, the usage of a burning-glass in ancient world to start fires is caused by accumulating different optical phase to concentrate the sunlight. The Lycurgus Cup shows a different color depending on the direction of the incident light due to the dichroic effect induced by the inclusions of gold and silver nanoparticles in the glass

material [1]. Advancements in the understanding of light as an EM wave composed

of synchronized oscillations of electric and magnetic fields marked a new chapter in light research.

Optical devices are developed to control EM wave by altering its phase, amplitude and polarization in a desired manner. Conventional optical components are usually based on refraction, reflection or diffraction of EM wave. The phase, amplitude and polarization changes of the EM wave are accumulated through propagation in the medium of given refractive index. This propagation effect is also used in transformation optics to control the light trajectory [2]. The metamaterial, which is artificially designed with subwavelength structures and has spatially varying refractive index from positive to negative, is developed to control the EM wave more effectively [3]. Recently, the metasurface, a two-dimensional planar metamaterial, breaks the propagation effect by introducing abrupt changes of optical properties in optically thin films [4]. Such new technology opens the door for a new generations of flat optics.

Similar with natural materials which respond to the incident EM wave through large amount of atoms or molecules, the metasurface interacts with EM wave by an array of artificially repetitive unit cells with their spatial resolution much smaller than the wavelength. These subwavelength inclusions respond resonantly to the two fundamental components of the EM wave, *i.e.*, electric field and magnetic field. In this way the effective permittivity ε and permeability μ of the metasurface change abruptly at the resonant frequency, even to a negative value [5]. The advancement of metasurfaces compared to natural materials is that one can easily obtain the desired permittivity and permeability by simply designing

the geometric architecture of structures, even if the component materials of the metasurfaces are the same.

Although a proper design of geometric architecture is essential for metasurface, the component materials also play an important role. Early metasurfaces are usually based on metallic structures which induce plasmonic resonances to introduce dispersion for the abrupt changes of optical properties. However, the high lossy of metal inevitably causes significant energy dissipation and reduces device efficiency, which impedes many practical applications. As an alternative, all-dielectric metasurfaces are developed for low-loss electromagnetic responses by using completely transparent and high-refractive-index dielectric building blocks. They basically rely on the Mie-type electric and magnetic resonances. Similar to the metal-based-metasurfaces, the dielectric metasurfaces can also realize all four quadrants of electromagnetic responses: $\varepsilon > 0$, $\mu > 0$; $\varepsilon < 0$, $\mu > 0$; $\varepsilon < 0$, $\mu < 0$; and $\varepsilon > 0$, $\mu < 0$ [6].

Due to the resonance nature of the sub-wavelength structures, many metasurfaces are hampered by the lack of tuning capabilities and limited working bandwidth. Therefore, a tunable metasurface that can control the resonant properties is developed [7]. Studies on tunable metasurfaces show vast approaches via external excitations. In general, tunable metasurfaces are categorized into two groups: one uses the nonlinear effect of the consisting materials, the other one reconfigures the structure of the metamolecules or the lattice arrangement. Recently, tunable metasurfaces incorporating liquid materials are developed. Liquid crystal, which is a kind of nonlinear material, is used to control the

refractive index due to its voltage dependent birefringence [8]. The development of microfluidic technology enables creating microfluidic channels for both liquid-based structure injection and its reconfiguration [9]. Based on this platform, liquid metal and liquid dielectric are widely demonstrated for the realization of tunable metasurfaces [10, 11].

The realization of metasurfaces benefits from various fabrication technologies. The basic fabrication technology employed to develop metasurfaces is based on the scale of the resonant structures ranging from millimeter to nanometer, promising the operating frequency from microwave to optical range. Additionally, the structure of the meta-atom and the geometric architecture also require different fabrication methods. For metasurfaces operating in microwave range, the size of the meta-atom is in millimeter, which can be fabricated using the print circuit board (PCB) printing method [12]. When the size scales down to micrometer, more precise fabrication method is required, such as optical lithography [13]. However, its resolution is restricted by the optical diffraction limitation, which is about hundreds of nanometers using UV light exposure. When the frequency goes to optical range, electron-beam lithography is widely used [14]. Compared to the photolithography, e-beam lithography uses a focused beam of electrons to draw the patterns, which has high resolution up to sub-10 nm, but low throughput. It is recommended to employ nanoimprint lithography for high throughput fabrication with low-cost and sub-10 nm high resolution [15].

In summary, metasurfaces not only miniaturize optical devices into optically thin, but also provide novel properties in the realization of diverse

functionalities to expand the application of optical devices. The studies of the tunable metasurfaces enable the real time control of EM wave and broadens the working bandwidth for practical applications. Overall, the development of metasurface for EM wave control has been a goal actively pursued by both academia and industry. Hence the study of meta-liquid-based metasurface is chosen as the topic of this thesis.

1.2 Objectives

The main objective of this research is to develop meta-liquid-based metasurfaces for microwave and terahertz wave applications. These meta-liquid-based metasurfaces are based on soft material, polydimethylsiloxane (PDMS), and use microfluidic technology to control the shape of the structures to realize different functions. Three kinds of meta-liquid-based metasurfaces using different materials are investigated. They are (1) water-resonator-based metasurface in microwave using liquid water and water-ethanol solution; (2) liquid-metal-based metasurface in terahertz by using mercury; (3) tunable chiral metasurface in microwave by patterning solid metal on PDMS. The primary target is to develop microfluidic systems which can provide functionalities of EM wave manipulation by microfluidic design. The research investigations include theoretical analysis, structural designs, fabrication processes and experimental studies. The theoretical analysis for the three different metasurfaces guide the designs of the corresponding microfluidic system, including structure designs and control system. Different

fabrication processes are developed in this PhD research, including photolithography and e-beam evaporation. The experimental studies are carried out on the developed metasurfaces for characterizations and EM wave measurements.

The water-resonator-based metasurface consists of a water-resonator array embedded in the PDMS, which realizes the impedance-matching to free space needed to suppress the reflection in microwave range. Together with a metallic ground to block all of the transmission, a near-unity absorption is realized. The size of the water-resonator is controlled by applying different water pressure through the microfluidic channels. The photolithography fabrication process is developed. The experiment results are discussed and compared with the theoretical analysis.

The liquid-metal-based metasurface consists of a liquid-metal-pillar array formed in a triple layer structure, PDMS/silicon/PDMS. High absorption of terahertz wave is obtained by magnetic resonance of the liquid-metal-pillars. The vertical tuning of the liquid structure provides a large tunability of the absorption frequency and enables wide-angle absorption in broad bandwidth. The fabrication process for the PDMS channel and penetrated silicon cavity is developed. The frequency agile and wide-angle absorption are experimentally characterized and discussed.

The tunable chiral metasurface consists of a PDMS layer sandwiched between two metallic spiral structures. The tunable chiral metasurface can be controlled from achiral to chiral by using microfluidic technology, whereby the transmission can be controlled from symmetric transmission to asymmetric transmission. Furthermore, the asymmetric transmission parameter and its

bandwidth can be tuned by controlling the height of the spiral structures. The fabrication processes for tunable chiral metasurface combining photolithography and e-beam evaporation are developed. The experimental results of the characterization of tunable chiral metasurface are discussed.

1.3 Major Contributions

The major contributions of this PhD thesis lie in various aspects of the theoretical analysis, structural designs, fabrications, and experiments of the three different meta-liquid-based metasurfaces for EM wave manipulation. The details are listed below:

(a) A new approach for EM wave manipulation is proposed by using meta-liquid-based metasurfaces based on soft substrate of PDMS. Optical responses of the metasurfaces are effectively controlled through the microfluidic technology. The proposed meta-liquid-based metasurfaces provide a new paradigm for dynamical control on both microwave and terahertz wave.

(b) Fabrication processes of the PDMS channels, silicon structures and metallic patterns are developed for both the metasurface resonant structure and the control system. The tunability is substantially demonstrated on different optical responses.

(c) A near-unity and ultra-broadband absorption is realized across the entire Ku, K and Ka bands by using water-resonator-based metasurface. The

theoretical model of the impedance matching is developed and forms the foundation in designing the water structure. The water or water-ethanol solutions confined in the PDMS channels acts as a resonator which induces magnetic resonance for impedance matching and microwave absorption (See Chapter 3).

(d) An omnidirectional absorption on curved surface is developed. Specifically, the experimental setup for the far-field characterization of omnidirectional absorption is developed (See Chapter 3).

(e) A frequency-agile and wide-angle absorption in terahertz by using liquid-metal-based metasurface is designed, fabricated and experimentally characterized. The tuning range of the central frequency reached 51.1% with higher than 90% absorption. The tuning range maintains at high level with a wide angular tolerance up to 60° (See Chapter 4).

(f) A tunable chiral metasurface is developed together with the design model. The bi-layer structures provide the opportunity for the metasurface tuned from achiral to chiral. Particularly, the propagating wave tuned from symmetric transmission to asymmetric transmission is studied (See Chapter 5).

(g) The asymmetric transmission is enhanced to > 50° in the optimized designed bi-layer structures. It can be reduced to 0 continuously by applying different air pressure to reconfigure the structures (See Chapter 5).

1.4 Organization of Thesis

The thesis is organized into six chapters. The introduction of the thesis covers the motivation, objective, and major contributions as presented in this chapter. The motivation section explains why and how the PhD research is carried out. The objective states the main focus of this thesis, and the contribution section lists the innovations and important findings in both the theoretical and technological aspects.

In Chapter 2, literatures on the developments of metasurfaces are reviewed. This chapter reviews the fundamental concepts of the metasurfaces and some related novel optical properties. Different applications of metasurfaces are briefly summarized. The research background of the dielectric metasurfaces, meta-liquid-based metasurfaces and the chiral metasurfaces are discussed. All such important background work provides the guidance and impetus for the research, and also determines the technological foundations on which the work of this thesis is built.

In Chapter 3, the design, fabrication and experiments of water-resonator-based metasurface in microwave are presented. The mechanism on the combination of magnetic resonance and diffraction grating effect inducing near-unity absorption in the metasurface is investigated. The geometric size dependence of the magnetic resonance is discussed. The ultra-broadband absorption is realized by controlling the absorption peak frequencies of magnetic resonance and diffraction grating effect. The omnidirectional absorption on curved surface is

presented. And a broadband intensity modulator by injecting different concentration of water-ethanol solutions is realized.

In Chapter 4, the design, fabrication and experiments of liquid-metal-based metasurface in terahertz are elaborated. The design of the terahertz liquid-metal-based metasurface is focused on the vertical design of the liquid-metal-pillars and the triple-layer supported substrate for liquid-metal reservation, liquid-metal-pillar formation and reconfiguration. The theoretical analysis on the size dependence of magnetic resonance is discussed. The fabrication processes for the penetrated silicon cavity is developed. The large tunability of absorption frequency and wide-angle absorption are studied and discussed.

In Chapter 5, the design, fabrication and experiments of tunable chiral metasurface are presented. The theory of the asymmetric transmission is provided. The mechanism on the transition from achiral to chiral is studied to guide the design of metasurface and realize the control of propagating wave from symmetric transmission and asymmetric transmission. The theoretical analysis by using plasmon hybridization is studied. The enhancement of the asymmetric transmission is realized through structure modification. The large tunability on the asymmetric transmission are experimentally presented and discussed.

Chapter 6 concludes the major contributions of this thesis, and follows by the recommendations for future work.

CHAPTER 2

LITERATURE SURVEY

This chapter is divided into four parts. The first part of the chapter presents an overview on the metasurface fundamental concepts, optical properties and applications. The second part of the chapter briefly introduce the development of the dielectric metasurface. The electric and magnetic resonances induced by the all-dielectric material instead of traditional metallic structure have wide research interest to be explored. The third part of the chapter is focused on the study of liquid based metasurfaces. Large tunability by using different kinds of liquid materials, including liquid crystal, liquid metal and liquid dielectric is reviewed. The fourth part of the chapter discusses the chiral metasurface, which has the properties of optical activity, circular dichroism and asymmetric transmission. All these works lay the foundation for the contributions of this thesis in the research field of meta-liquid-based metasurface and its applications.

2.1 Metasurfaces

2.1.1 Fundamental Concepts

The manipulation of light can be traced back to thousands of years by using lenses, prisms and mirrors in ancient society. Natural materials interact with light obeying right-handed rule. In 1968, the concept of left-handed materials (LHMs) was theoretically proposed by Victor Veselago [16], in which the right-hand rule was failed. Such LHMs showed a phase velocity anti-parallel to the direction of Poynting vector, which were also known as negative-index materials (NIMs). However, LHMs did not attract too much attention until John Pendry first proposed a practical way to make a double negative medium in 1999 [17]. In 2000, David R. Smith experimentally demonstrated a negative-index material in microwave range by using wire elements to produce negative electric permittivity and split ring resonators (SRRs) to produce negative magnetic permeability in an overlapping frequency region [18]. Such artificial materials consist of periodic or non-periodic structures whose functionality is derived by not only their chemical composition, but also the cellular architecture, which is called metamaterial (from the Greek word meta, meaning “beyond”). The structure of the metamaterial is much smaller than the wavelength of interest, which is called “meta-atom” like the “atom” in natural materials. An average effect is encountered in large amount of meta-atoms due to the fact that light does not see the small deviations of meta-atom much smaller than wavelength, such that the metamaterial can be accurately described by the effective refractive index. Since then, considerable interests in metamaterials

have been sparked. To date, in addition to the negative refractive index, various optical properties have been explored by using the concepts of metamaterials.

The term of metasurface refers to the class of 2D planar metamaterial, due to the fact that it provides similar phenomena as metamaterial, except that the thickness of the metasurface is sub-wavelength thin. Compare to the bulky metamaterial, metasurface is much easier to fabricate and void of the complicated assembling of 3D structures.

2.1.2 Optical Properties

The electric permittivity and magnetic permeability are two fundamental quantities that are used to determine the propagation of electromagnetic waves in matters. A metasurface with electric permittivity $\varepsilon = \varepsilon_r \varepsilon_0$ and magnetic permeability $\mu = \mu_r \mu_0$ (where ε_0 and μ_0 are the permittivity and permeability in the free space, ε_r and μ_r are the relative permittivity and permeability of the metasurface) interacts with the electromagnetic wave, which can be described by Maxwell's equations as

$$\begin{cases} \nabla \cdot \boldsymbol{D} = \rho_v \\ \nabla \cdot \boldsymbol{B} = 0 \\ \nabla \times \boldsymbol{E} = -\dfrac{\partial \boldsymbol{B}}{\partial t} \\ \nabla \times \boldsymbol{H} = \dfrac{\partial \boldsymbol{D}}{\partial t} + \boldsymbol{J} \end{cases} \tag{2.1}$$

where $\boldsymbol{E}$ and $\boldsymbol{H}$ are the electric and magnetic field, $\boldsymbol{D}$ and $\boldsymbol{B}$ are the electric and magnetic flux density, ρ_v is the charge density and $\boldsymbol{J}$ is the current density. The relationship of $\boldsymbol{E}$, $\boldsymbol{H}$, $\boldsymbol{B}$ and $\boldsymbol{D}$ can be described by the constitutive relations as

$$\begin{cases} \boldsymbol{B} = \mu \boldsymbol{H} \\ \boldsymbol{D} = \varepsilon \boldsymbol{E} \end{cases} \tag{2.2}$$

The permittivity and permeability of the metasurface can be controlled to realize various properties by rationally designing the geometric and the composition of the structures.

Negative Refractive Index

One of the most exciting properties of the metasurface is negative refractive index, which has been widely explored. The materials can be divided into four categories according to the sign of the permittivity ε and permeability μ as shown in Fig. 2.1. The first quadrant ($\varepsilon > 0$ and $\mu > 0$) represents a right-handed medium, in which the electric field, magnetic field and wave vector follow the right-hand rule. The second quadrant ($\varepsilon < 0$ and $\mu > 0$) represents the electric plasma, which occurs in most metals in nature. The third quadrant ($\varepsilon < 0$ and $\mu < 0$) denotes a LHM, in which the electric field, magnetic field and wave vector follow the left-handed rule. The LHM does not exist in nature, which can only be designed artificially. The fourth quadrant ($\varepsilon > 0$ and $\mu < 0$) denotes the magnetic plasma, which occurs in some ferrite materials in microwave frequencies.

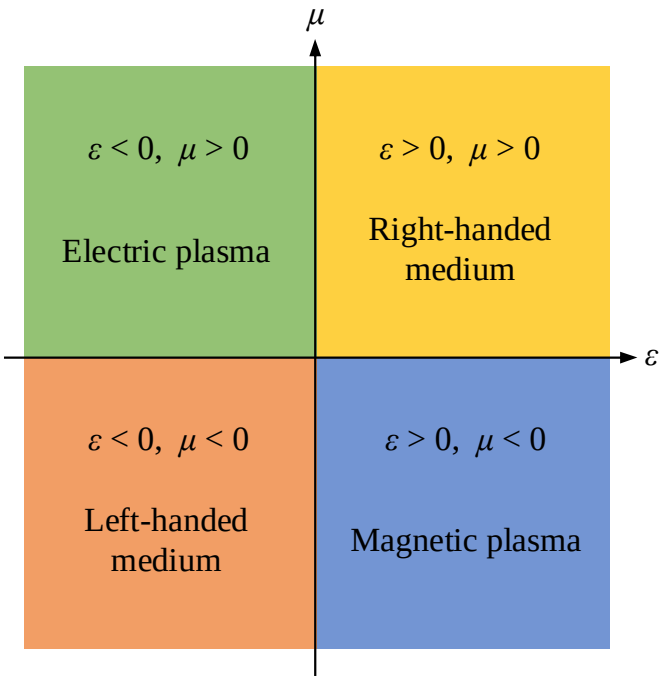

Figure 2.1 Category of isotropic materials according to the permittivity and permeability.

The LHM is responsible for the negative refractive index by simplifying Maxwell's equations (Eq 2.1) and constitutive equations (Eq 2.2), which can be explained as

$$\begin{cases} \boldsymbol{k} \times \boldsymbol{E} = \mu \omega \boldsymbol{H} \\ \boldsymbol{k} \times \boldsymbol{H} = -\varepsilon \omega \boldsymbol{E} \end{cases} \tag{2.3}$$

where $\boldsymbol{k}$ is the wave vector, ω is the frequency. If $\varepsilon < 0$ and $\mu < 0$, the Poynting vector, defined as $\boldsymbol{S} = \boldsymbol{E} \times \boldsymbol{H}$, is antiparallel to $\boldsymbol{k}$. The phase refractive index, defined as $n = \pm\sqrt{|\varepsilon_r||\mu_r|}$ must take a negative sign, so that the causality is still

conserved [6]. By overlapping the negative permittivity and negative permeability in the same frequency, a negative-index material is expected to be realized. Therefore, a LHM also refers to negative-index material (NIM).

Inspired by this concept, much effort has been made in the realization of negative permittivity and negative permeability simultaneously across the entire electromagnetic magnetic spectrum, including the microwave range [5, 19], terahertz [20, 21], infrared [22-24], and the visible region [25-27]. Various structures have been used to achieve the electric and magnetic resonances. A typical design to realize a negative permeability is called split ring resonator (SRR), which induces strong magnetic resonance [17]. By incorporating with a metallic wire that can obtain a negative permittivity through the electric resonance, a negative refractive index was realized [18]. However, the size of the SRR is very difficult to be scaled down to the visible range. A fishnet structure is designed to solve this problem by using two crossed paired stripes separated by a dielectric layer [23]. The negative permittivity and permeability are realized through the paired stripes which are parallel to the electric field and magnetic field, respectively. A pair of metallic rods is also demonstrated as NIM [22]. The electric field is oriented parallel to the rods, which induces electric resonance. The magnetic field is oriented perpendicular to the rods, which induces strong magnetic resonance due to the antiparallel current mode in the paired rods.

Perfect Absorption

The metasurface also attracts much attention in the absorber due to its capability to obtain perfect absorption by designing the structures of the metasurface, which is called perfect metasurface absorber (PMA). In order to realize a perfect absorption, two main issues should be considered. One is to suppress the reflection through the impedance matching to the free space; the other is to reduce the transmission, such that no EM wave is allowed to be radiated out from the object. The block of the transmission is relatively easy, which has been known for thousands of years by simply using a metallic mirror. Metasurface is a good candidate to suppress the reflection through the impedance matching to the free space due to the fact that the metasurface can tailor both the permittivity and permeability by properly designing the structures, so that the impedance of the metasurface $Z = \sqrt{\mu / \varepsilon}$ can be matched to the free space Z_0.

Based on this idea, the triple layer design is usually exploited to realize the perfect absorption, which consists of a dielectric layer sandwiched between two metallic layers. The top layer is a patterned metallic structures which is designed to match the impedance to the free space to reduce the reflection of the metasurface. The bottom layer is usually a continuous metallic film that can block all of the transmissions. In additional, the electric current induced in these two metallic layers will couple with each other and induce a magnetic resonance, which will enhance the confinement of the EM wave. A dielectric layer is sandwiched between these two metallic layers, in which the EM wave is confined and

absorbed. The first demonstration of the PMA is working in microwave range [28]. In this paper, the bottom metallic layer is a cut wire, which has similar function as the metallic film. It also proves that the absorption is mainly attributed to the central dielectric layer. The dielectric loss is an order of magnitude greater than Ohmic losses in the microwave range [29]. Besides the demonstrations in the microwave range [30, 31], many reports have also been done in terahertz [32, 33], infrared [34, 35], and visible region [36, 37].

The PMAs can be categorized into two classes: narrow band absorbers and broadband absorbers. As the name suggests, the narrow band absorbers only have perfect absorption in a narrow bandwidth, while the broadband absorbers have perfect absorption that is frequency independent and therefore can absorb EM wave in a broad bandwidth. The PMAs based on the metallic structures usually have narrow band absorption due to the plasmonic resonance of the metallic structure [38, 39]. In order to realize a broadband absorber, complicated structures are used to generate multi-resonances, which will merge with each other and become a broadband absorption [40-42]. Such complicated structures are usually hard to fabricate and the number of resonance is limited.

Besides bandwidth control, the versatility of PMA also enables absorption with desired polarization. In general, PMAs are polarization dependent due to the asymmetric pattern structure. In order to realize a polarization independent absorption, the structures are designed with symmetric four fold rotational symmetry [43, 44]. A racemic mixtures of unit cells is also used to eliminate the bi-anisotropy [45, 46].

The PMAs also support perfect absorption in a wide incident angle demonstrated in many studies [47-50]. Most of the designs have a decrease of the absorption with TE mode incidence when the incident angle is larger than 45°. While for TM mode incidence, the perfect absorption can be maintained at nearly 80°. This is because for TE mode incidence, the parallel magnetic field component reaches near zero. Antiparallel currents induced between the top and bottom metallic layers is weakened when the incident angle is increasing, hence resulting in a decrease of the magnetic flux. However, for most of the proposed PMAs with wide incident angle, the absorption frequency position usually varies as a function of the incident angle.

Optical Phase Jumps

Conventional optical components like lenses, wave plates and holograms rely on the gradual phase shifts accumulated during light propagation along the propagation optical path to shape the light beams, which is inevitably bulky compared to the operating wavelength. Metasurface produces abrupt phase changes under the scale of free space wavelength through the resonance of the patterned structure. As a result, the metasurface is able to adjust the optical wavefront into arbitrary shape by introducing spatial variations of light scatters according to Huygens' Principle. Assuming a constant gradient of phase jump on an optical interface, the conventional Snell's law of refraction is amended to the generalized form, which can be expressed as [4]

$$\begin{cases} n_t \sin(\theta_t) - n_i \sin(\theta_i) = \dfrac{1}{k_0}\dfrac{d\Phi}{dx} \\ \cos(\theta_t)\sin(\varphi_t) = \dfrac{1}{n_t k_0}\dfrac{d\Phi}{dy} \end{cases} \tag{2.4}$$

and the generalized law of reflection is derived as

$$\begin{cases} \sin(\theta_r) - \sin(\theta_i) = \dfrac{1}{n_i k_0}\dfrac{d\Phi}{dx} \\ \cos(\theta_r)\sin(\varphi_r) = \dfrac{1}{n_r k_0}\dfrac{d\Phi}{dy} \end{cases} \tag{2.5}$$

where the definition of angles is shown in Fig. 2.2, k_0 is the wave vector in the free

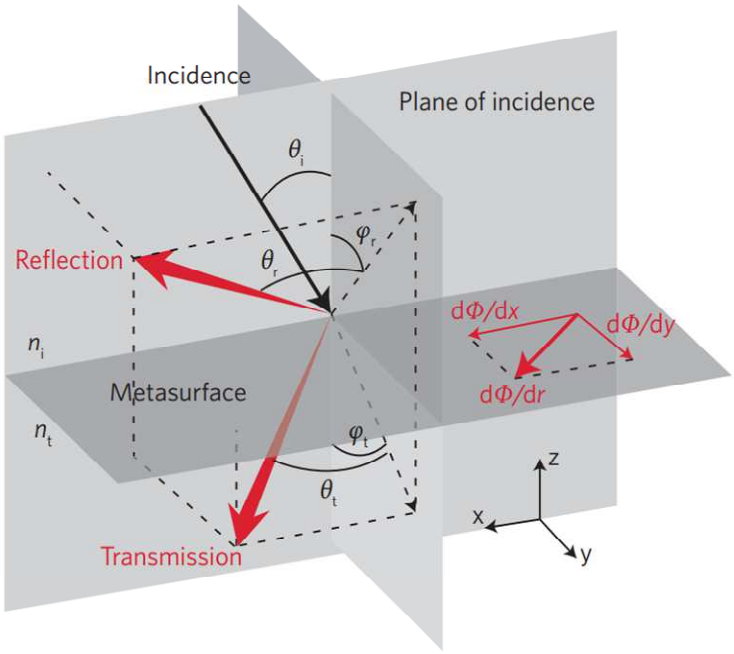

Figure 2.2 Generalized laws of refraction and reflection. A gradient of phase jump dΦ/dx introduced along the x direction reflect and transmit light to arbitrary direction of θ_r and θ_t. The phase jump dΦ/dy introduced along the y direction leads to out-of-plane refraction and reflection with the angle of φ_r and φ_t.

space, n_i and n_t are the refractive indices of the medium on the incident and transmitted side of the metasurface, $d\Phi/dx$ and $d\Phi/dy$ are the gradient of the phase jump along the x and y direction. The overall effect of the phase gradient along the x and y directions allows the reflected and transmitted light beams to bend into arbitrary directions in their respective half space.

In order to realize full control of the wavefront, the phase shift needs to be covered from 0 to 2π. The first demonstration of the generalized laws is using V-shaped resonators, which can provide double-resonance properties to achieve a 2π phase coverage of the cross-polarized light [51]. Besides the V-shaped resonators [52-55], the SRRs and other structure designs have also been demonstrated in many studies for the abnormal transmission of the cross-polarized wave [56-58]. The generalized law of reflection has also been demonstrated by using reflect-arrays [59-61]. The essence of the reflect-arrays is to use the top metallic structures coupled with their dipolar images in the back metallic film to achieve a phase coverage of 2π. Such reflect-array design not only realize a co-polarization modulation, but also improve the scattering efficiency because the transmission is blocked by the metallic film. It is also shown that abrupt phase changes can be produced without introducing of dispersion of the structure resonance. By using the Pancharatnam-Berry phase, abrupt phase changes can be simply linked with orientation of the structure [62-65]. The phase shift of the metasurface would cover the entire 0-2π range by rotating the structures from 0 to 180°. The mechanism of phase change by using Pancharatnam-Berry phase is only applicable to the circular polarized wave.

Other Properties

The metasurface shows its versatility in many other areas. The electromagnetically induced transparency (EIT) is presented with extraordinarily narrow-band transmission by introducing a subradiant (dark mode) element coupled with a superradiant (bright mode) element [66, 67]. The Fano resonance is shown through the interference between a spectrally overlapping broad resonance or continuum and a narrow discrete resonance [68, 69]. The nonlinearity is demonstrated by using nonlinear insertions in resonance meta-atoms [70, 71], nonlinear host medium [72, 73], local field enhancement [74, 75], and nonlinear transmission line [76, 77], etc..

2.1.3 Applications

A number of intriguing properties of the metasurface enable tremendous applications in many fields, which will be presented in this section.

Invisible Cloak

One of the most exciting applications of the metasurface is invisible cloak. Naturally, the invisible cloak is impossible due to the fact that light usually scatters and changes its trajectory when it encounters an object and makes the object visible or detectable. Metamaterial can redistribute the spatial refractive index arbitrarily and guide the ray trajectories purposely according to the transformation optics, such that light would propagate along the original direction as if there is no

object ahead and a cloaked region is realized [2, 78]. Plasmonic cloaking is also applied based on the scattering cancellation features of low-permittivity metamaterials [79, 80]. Such metamaterial-based optical cloaks are bulky. The surface cloaking is first demonstrated using a single patterned frequency selective surface (FSS) with an ideal limit of thickness to zero [81]. A carpet cloak is demonstrated by using a quasi-conformal mapping technology that conceals an object by restoring the wavefront as if it was reflected from a flat surface [82-84]. However, the carpet cloak introduces an additional phase in the reflected light and become detectable by phase-sensitive detector. Such phase change can be compensated by introducing the resonant structures, which is called metasurface skin cloak [85].

Sensing

Metasurface can be used as sensors due to its high dependence on the geometric size, shape and surrounding dielectric environment. Especially in the field of the bio-sensing, many studies have been demonstrated using a microwave sensor [86, 87], terahertz sensor [88, 89] and plasmonic sensor [90, 91]. The ability of strong localization and enhancement of EM wave using metasurface improves the sensor sensitivity and enables the detection of small amounts of substance. The local confinement is strongly dependent on the effective refractive index of the surrounding dielectric environment. A small fluctuation of the refractive index caused by the small amounts of analytes affects the transmission or reflection spectra of the metasurface [92, 93]. Such refractive index sensing is widely

demonstrated in biosensing which is label-free and low cost [94, 95]. Besides, the metasurface has also been used as a wireless strain sensor with high *Q*-factors because the external load changes the shape of the metasurface structure, resulting in the operating resonance frequency shift [96-98]. Other sensing applications based on metasurfaces are also demonstrated, including a highly sensitive terahertz surface wave sensor [99], a gas sensor to wirelessly measure the gas pressure, gas density, temperature, etc. [100], and a chemical sensing in the visible-IR regime [101].

Wavefront Shaping

Metasurface can reshape the wavefront arbitrarily by introducing phase jump using resonant scatters, which has applications in the wavefront shaping such as imaging and radar tracking system. The first and most exciting components among these wavefront shaping devices is flat lens. To date, tremendous works have been studied for the realization of metasurface based flat lens in microwave [59], terahertz [58, 102], infrared [103] and visible range [104, 105]. Some works are shown that the metasurface can correct the aberration of the lens. An aberration-free ultrathin flat lens based on plasmonic metasurfaces is performed at telecom wavelengths by using V-shaped nano-antennas [54]. A chromatic aberration flat lens is also accomplished using aperiodic gratings in the near-infrared region [106]. In addition, a flat lens with tunable phase gradient by using random access reconfigurable metasurface is presented in microwave [107]. Other wavefront

shaping are also investigated by using metasurface, such as beam steering [108-111], and holograms [60, 61, 65, 112-114], etc.

Other Applications

Metasurface can also find its applications in many other areas. The plasmon ruler, which can determine nanoscale distances within chemical or biological species, is an exciting application in the fields of biology and soft materials science [115, 116]. The plasmonic coupling of the metasurface lead to light-scattering spectra that are sensitive to a complete set of three dimensional motions, such that the spatial configuration of complex macromolecular can be retrieved [117]. The metasurface is also widely designed for the realization of polarizers, which can manipulate the polarization state of the EM wave due to the chirality or anisotropy effects of the metasurface [118-122].

2.2 Dielectric Metasurfaces

2.2.1 Fundamental Concepts

Metal based metasurface obtains its properties from the plasmonic resonance of the metallic structures. As an alternative, dielectric material can also be used to create a resonator in the design of metasurface, which is called dielectric metasurface. Compared with metal based metasurface, dielectric metasurface induces Mie

resonance instead of plasmonic resonance. Mie resonance induced in the dielectric particles results in electric and magnetic resonance based on displacement currents.

Light scattering by dielectric spherical particles (relative to the incident light wavelength) is well studied, and is based upon the exact Mie solution of the diffraction problem [123]. The scattered field of a single isolated dielectric sphere with radius r_0 and relative refractive index n can be decomposed into a multipole series with the 2^m-pole term of the scattered electric field proportional to

$$a_m = \frac{n\psi_m(nx)\psi_m'(x) - \psi_m(x)\psi_m'(nx)}{n\psi_m(nx)\xi_m'(x) - \xi_m(x)\psi_m'(nx)} \tag{2.6}$$

whereas the 2^m-pole term of the scattered magnetic field is proportional to

$$b_m = \frac{\psi_m(nx)\psi_m'(x) - n\psi_m(x)\psi_m'(nx)}{\psi_m(nx)\xi_m'(x) - n\xi_m(x)\psi_m'(nx)} \tag{2.7}$$

where $x = k_0 r_0$, k_0 is the wave number in vaccum, $\psi_m(x)$ and $\xi_m(x)$ are the Riccati-Bessel functions. The primes indicate derivation with respect to the arguments. a_m and b_m are the scattering coefficient related to the electric and magnetic responses of the dielectric sphere, respectively. The electric and magnetic dipole coefficients, a_1 and b_1, can be calculated from the Eqs 2.6 and 2.7.

The dielectric spheres that can induce electric and magnetic dipole resonances can be assembled together to become a material with arbitrary values of effective permittivity and permeability. The optical response of an array of dielectric spheres with a permittivity and permeability of ε_2 and μ_2 embedded in a

host medium with a permittivity and permeability of ε_1 and μ_1 has been studied by Lewin back in 1946 [124].

By applying the Mie scattering theory and combining it with Clausius-Mossotti effective medium theory, the effective permittivity and permeability can be expressed as

$$\varepsilon_{eff} = \varepsilon_1 \left(1 + \frac{3v_f}{\frac{F(\theta)+2b_e}{F(\theta)-b_e} - v_f} \right) \tag{2.8}$$

$$\mu_{eff} = \mu_1 \left(1 + \frac{3v_f}{\frac{F(\theta)+2b_m}{F(\theta)-b_m} - v_f} \right) \tag{2.9}$$

where $F(\theta)$ is a resonant function, b_e and b_m are the effective permittivity and permeability which are described as

$$F(\theta) = \frac{2(\sin\theta - \theta\cos\theta)}{(\theta^2 - 1)\sin\theta + \theta\cos\theta} \tag{2.10}$$

$$b_e = \frac{\varepsilon_1}{\varepsilon_2}, b_m = \frac{\mu_1}{\mu_2} \tag{2.11}$$

where the filling fraction of the spherical dielectric particles $\nu_f = \frac{4}{3}\pi(\frac{r_0}{s})^3$, $\theta = k_0 r_0 \sqrt{\varepsilon_2 \mu_2}$, r_0 is the radius of the dielectric sphere and s is the lattice constant as shown in Fig 2.3. It should be noted that the constitutive parameters retrieved from Lewin's model were formulated only considering the dielectric particles resonating either in the first or second resonance modes of the Mie series.

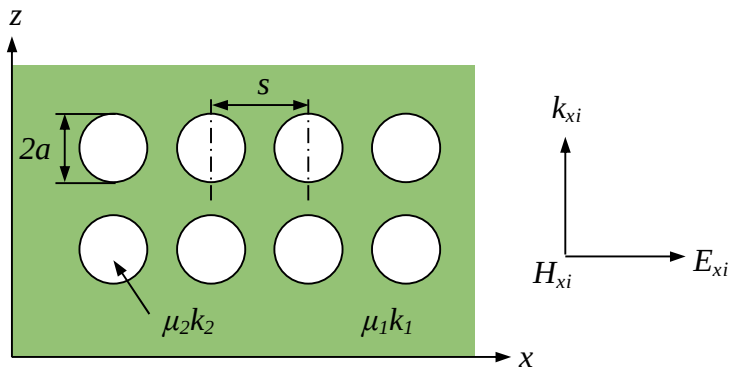

Figure 2.3 Schematic of a dielectric sphere array (ε_2 and μ_2) embedded in a host medium (ε_1 and μ_1).

From Eqs 2.8 and 2.9, it can be seen that both the permittivity ε_{eff} and permeability μ_{eff} of the material can be tailored by controlling the size and refractive index of the dielectric inclusions, which can be used to design the metasurfaces. The firstdemonstration of the dielectric metamaterial is demonstrated in 2003 to realize a negative index materials [125]. Since then, tremendous works has been studied by using dielectric metasurface.

2.2.2 Optical Properties

The dielectric metasurfaces share the same properties with the metal based metasurfaces by manipulating the Mie-type electric and magnetic resonances. Mie resonances occur in any dielectric particle and their ordering and resonant frequency are related to the size and shape of the dielectric particle. The first property is negative index. From Eqs. 2.8 and 2.9, it can be seen that a negative permittivity

$\varepsilon_{eff} < 0$ and negative permeability $\mu_{eff} < 0$ can be obtained when the following conditions are satisfied as

$$\frac{3\nu_f}{\frac{F(\theta)+2b_e}{F(\theta)-b_e}-\nu_f} < -1 \tag{2.12}$$

$$\frac{3\nu_f}{\frac{F(\theta)+2b_m}{F(\theta)-b_m}-\nu_f} < -1 \tag{2.13}$$

In the case of sphere or cubes, the lowest resonance frequency corresponds to a magnetic dipole and the second resonance corresponds to an electric dipole, which can be used to realize the negative permittivity and permeability [126]. Various works have studied the negative index by using different size or materials of dielectric structures to excite the permittivity and permeability in the same frequency band [126-128]. Recently, L. Peng experimentally presents a left-handed

behavior in a two-dimensional array of standard dielectric resonators, where the second resonant mode was considered [129].

Compare to the metal based metasurface, dielectric metasurface is capable to provide high transmission efficiencies for the creation of arbitrary optical wavefronts by using low loss dielectric materials. At near-infrared range, various functional dielectric metasurfaces have been demonstrated based on silicon structure, including blazed gratings [130], and achromatic beam deflectors and lenses [106]. The transmission efficiency even reaches near-unity by using the concept of the all-dielectric Huygens's metasurfaces. The reflection can be suppressed due to the matching of the electric and magnetic polarizabilities of the dielectric particles. Such dielectric particles behave as electromagnetically dual-symmetric scatterers [131, 132], which simultaneously excite the electric and magnetic dipole resonances. These two resonances are controlled to occur at the same frequency by controlling the size and shape of the dielectric particles for a given period [133, 134]. The strength of the resonances can be adjusted by controlling the refractive index of the dielectric particles and the surrounding medium [135]. The localized electric and magnetic Mie-type resonances using low-loss dielectric particles enable a phase coverage from 0 to 2π and a transmittance efficiency of near-unity [135, 136]. However, when the operating frequency goes up to the visible range (400 to 700 nm), the silicon becomes lossy and prevents the realization of highly efficient metasurfaces. Other materials such as gallium phosphide (GaP), silicon mononitride (SiN) and titanium dioxide (TiO_2) that have a transparency window in the visible range become good candidates to

overcome the loss problems. However, due to the limitation of fabrication, only TiO_2 has been shown in the visible range for the full control over the phase of light [137]. The high-aspect-ratio TiO_2 metasurfaces has a high numerical aperture (NA) of 0.8 with efficiencies as high as 86%. Such metalens is also capable of focusing light into diffraction-limited spots.

The dielectric metasurfaces also exhibit high-quality factor (*Q*-factor) of electromagnetically induced transparency (EIT) [138]. A silicon bar resonator serves as an electric dipole antenna, which couples with the incident electric field and induces a “bright” mode resonance. A silicon ring resonator supports a magnetic dipole, which couples with the bar resonator instead of the incident field and induces a “dark” mode resonance. Due to the low loss property of the silicon resonator in the operating frequency, the dielectric metasurface possess a sharp EIT-like resonance with an ultra-high *Q*-factor.

However, for perfect absorption, the losses are highly desired and are considered as the key factors to reach optimum performance. Therefore, high lossy dielectric materials are usually preferred to achieve near-unity absorption. For example, an ultra-thin and highly absorptive dielectric film coated on metal surface has been demonstrated to selectively absorb various frequency ranges of the incident EM wave in optical frequency based on interference effects [139]. Although TiO_2 is transparent in visible range, it becomes lossy when the frequency decreases to the terahertz region. By using an array of quasi-monodisperse dielectric particles of TiO_2, a dual band absorbing material is achieved [140]. The low loss dielectric materials can be also used to realize high absorption by

introducing free carriers. A broadband absorption is demonstrated in the terahertz range by using a doping semiconductor to capture the terahertz wave in the free carriers and then be absorbed [141].

Other properties are also demonstrated by using dielectric metasurface, such as bianisotropy [142-144], Fano resonance [145-147], polarization conversion [148, 149], and spin hall effect [150, 151], etc.

2.3 Meta-Liquid-Based Metasurfaces

2.3.1 Fundamental Concepts

The meta-liquid-based metasurfaces are defined as the metasurfaces that are partially made of liquid materials, either the surrounding medium, or the resonant structures. They belong to the class of tunable metasurfaces, which are capable of controlling the properties of the metasurfaces in real time through external excitations.

Traditional tunable metasurfaces without the assistance of liquid materials have been widely studied. Various tuning methods have been developed in the realization of real time control. The nonlinear tunable metasurfaces are using nonlinear materials whose optical properties are changed under an external excitation, such as EM wave pumping, thermal effect, electric field and magnetic field, etc. The ferrite materials, such as yttrium iron garnet (YIG), have different permeability depending on the intensity of magnetic field in microwave regime, which can be used to control the effective permeability of the metasurface [152,

153]. Such ferrite materials lose the tunability when the operating frequency goes up to the optical range due to a constant permeability of the ferrite materials occurring in optical frequency. At high frequency range, the superconductor is exploited, whose conductivity can be controlled by temperature [154-158]. The resonant frequency and *Q*-factor of the metasurface are related to the temperature-dependent resistivity of the superconductor, which are widely used to control the EIT effect [159]. Other nonlinear metasurfaces using semiconductors such as diode based metasurfaces are also developed [160-162]. Besides, the reconfigurable tunable metasurfaces are also used to control the properties of the metasurface, which are based on the reconfiguration of the shape of meta-atoms. A micromachined tunable method based on the technology of micro-electromechanical systems (MEMS) is developed. The shape of the structures is reconfigured by using micromachined actuators [163-165]. Two separated structures are designed, in which one is anchored on the substrate and the other is connected to the micromachined actuators. When one of them is moved by the actuator, the coupling between these two structures will be changed, such that the properties of the metasurface can be controlled [166-168]. Another approach is using thermal actuators, which can reconfigure the structures based on the applied temperature. Such thermal actuators usually consist of two materials with different thermal expansion coefficients, such as a stacked cantilever using SiN_x and Au [169]. The cantilever that initially lie in the plane of the substrate will bend out of plane by changing the temperature. Such micromachined actuators or thermal actuators based tunable metasurface are widely demonstrated in terahertz regime

[170, 171]. For nanometer sized actuation in optical frequency tuning, the optical force and Casimir force are utilized which have much precise control on the nanometer sized structures [172-175].

Previously proposed metasurfaces are usually based on rigid substrates, such as silicon, PCB board or glass, for the supporting of structures. A new class of metasurface is developed by using soft or elastic materials, such as PDMS [176], polyimide [177], silk [178] or papers [179], which is called flexible metasurface. The advantage of the flexible metasurfaces is that the tuning method is relatively simple by reshaping the substrates, which have been demonstrated in different spectra from microwave to visible range [180-183]. A PDMS based flexible metasurface by stretching the substrate is demonstrated, which not only changes the geometric size of the structure, but also changes the lattice constant of the metasurface [176]. Other bendable metasurfaces are also demonstrated, which can be applied to the circumstance of curved surface, such as negative index materials [184], perfect absorbers [185], and filters [182], etc.

Liquid Crystal Based Metasurfaces

Recently, a novel platform to design the tunable metasurfaces by using liquid materials is developed. The pioneer work on the meta-liquid-based metasurface is using liquid crystal [186-189]. Liquid crystal belongs to the class of nonlinear materials, which has the property of voltage dependent birefringence. In an aligned nematic liquid crystal, the permittivity ε_{LC} under an extraordinary wave incidence with linearly polarization is given by

$$\varepsilon_{LC} = \frac{\varepsilon_{\parallel}\varepsilon_{\perp}}{\varepsilon_{\parallel}\cos^2\theta + \varepsilon_{\perp}\sin^2\theta} \tag{2.14}$$

where $\varepsilon_{\parallel}$ and $\varepsilon_{\perp}$ are the permittivities for EM wave polarized parallel and perpendicular to the director axis, respectively. θ is the orientation angle between the director axis and the optical wave vector. Such nematic liquid crystal has permittivity in two orthogonal polarizations of $\varepsilon_{\parallel}$ = 2 and $\varepsilon_{\perp}$ = 4, respectively, resulting in a tuning range for the refractive index of 0.6. Various works of the liquid crystal based metasurface have been studied by changing the refractive index of the liquid crystal [8, 190-195].

Liquid Metal Based Metasurfaces

Liquid metals at room temperature, such as mercury and gallium-indium alloy (eutectic gallium-indium (EGaIn) or gallium-indium-tin (Galinstan)), can be used to design the metasurface as the resonant structures due to their fair electric conductivity compared to other solid metals and low reactivity compared to sodium-potassium alloy (NaK). The liquid metal based metasurfaces are usually using microfluidic technology to create microfluidic channels for liquid metal injection and reconfiguration. The first demonstration on the liquid metal based metasurface is demonstrated in 2009 by using mercury as the resonant structures [10]. The microfluidic split-ring resonator (MF-SRR) is created in the PDMS by employing rapid prototyping. Two polymer fibers are placed to define in and out channels. The proposed metasurface shows large tunability when the MF-SRR

array is changed from non-filling state to mercury full-filling state. However, mercury is a toxic material, which restrict its usage in the development of liquid metal based metasurface. Another liquid metal, gallium-indium alloy, is a good candidate due to its nontoxic properties. An EGaIn based metasurface is demonstrated in terahertz by using microfluidic technology [196]. It should be noted that the gallium-indium alloy is easily oxidized when it is exposed to the air. In this work, they use hydrochloric (HCl) vapor to selectively dissolve the oxide layer. Complete reconfigurability of the metasurface structure is accomplished by refilling the liquid metal into the unfilled microchannels to recover the initial structure. Thus the transmission spectrum of the metasurface is significantly changed by changing the EGaIn structures from erasure to refilling.

Liquid Dielectric Based Metasurfaces

As discussed, the liquid metals at room temperature have many restrictions. For example, the mercury is toxic; gallium-indium alloy is easily oxidized in the air and wetting the glass, silicon or PDMS surface; sodium-potassium alloy is highly reactive and flammable. Liquid dielectric materials is subsequently developed, such as water and sodium chloride solution, which are abundant, low-cost, and bio-compatible materials on Earth. Recently, a theoretical analysis on the water-based metasurface is demonstrated, which shows different tuning mechanism on the periodically positioned water-filled reservoirs by thermal tuning, mechanical tuning and gravitational tuning of the magnetic and electric resonances [197]. Heating not only causes the shift of the resonance, but also changes the loss

of water. Thus, the resonator *Q*-factor is modified, which can be provided by various options, such as chemical reactions, microwave, radioactivity, etc. Mechanical motion allows the liquid water to redistribute into different shapes, which can be provided by active pumps to reshape water in the containers, introducing air bubbles in water, using ultrasound to vibrate water structures, etc. Gravitation is naturally distributing on the Earth surface, which allows water to reshape in partially filled containers on a rotating plate. Water is also demonstrated as a phase transition between photonic crystals and dielectric metamaterial based on the physics of Mie and Bragg resonances [198]. It shows that a metamaterial is achieved when the wavelength of the Mie mode higher than the Bragg wavelength. Conversely, a photonic crystal is achieved when the Bragg wavelength is larger than the wavelength of the Mie mode. Recently, water droplet array are designed to suppress the reflection for high absorption [199]. However, the in-depth physics understanding of water droplet is limited to its high absorption properties. In the view of material functions, the lack of real-time controllability and suffering from the gravity effect by simply arranging water droplets on the substrate restrict its functionality in practical applications. Such water based metasurfaces are usually demonstrated in microwave because the refractive index is relatively high in microwave and it drops significantly when the frequency is increasing. Recently, sodium chloride solution is used as the resonant structure in terahertz region [11]. Two layers of “S” shaped microfluidic channels separated by a PDMS layer are created for the injection of sodium chloride solution. The symmetry is broken by

pumping the top and bottom layers with different concentration of sodium chloride solution, such that a tunable polarization rotation angle can be achieved.

2.3.2 Properties

Compared to the solid materials, liquid materials provide excellent opportunities to either change the refractive index of the liquid structures, or reshape the liquid structures from non-filling state to full-filling state continuously, which have large tunability for the developing of tunable metasurfaces. Such meta-liquid-based metasurfaces have the properties of uniform tuning and random access tuning for individual unit cell.

Uniform Tuning

The meta-liquid-based metasurface enables a uniform tuning for all of the structures, such that each unit cell responds with EM wave indistinguishably. For most of the liquid crystal based metasurfaces, the refractive index of the liquid crystal is uniformly tuned as a function of applied electric field. A tunable metasurface absorber is demonstrated in the terahertz regime by incorporation of active liquid crystal into strategic locations within the unit cell [200]. The random alignment of liquid crystal in the unbiased case will be realigned to the same direction with applied bias. Thus a 30% tuning on the absorption and a 4% tuning on the frequency are realized at terahertz. Other properties such as tunable negative index [187, 201-205], intensity and phase modulation [192], and electro-optical

switching [191, 206] are also demonstrated by using liquid crystal. Besides, liquid metals are also widely used in uniform tuning of the metasurfaces. In the first mercury based metasurface, a switchable permeability from positive to negative is realized from non-filling to full-filling state is demonstrated. In addition, the gallium-indium alloy based metasurfaces are also demonstrated in the uniform tuning. An array of L-shape micro-cavity is fabricated in the PDMS, which can be injected into galinstan. Each arm of the L-shape resonator is connected to the HCl outlet [207]. The injection of HCl vapor will expel away the galinstan. The pressures between the input and output of the microfluidic channel can be controlled by syringe pumps, such that different arm length of the L-shape resonator can be achieved. In this way, a real time control of reflective multifunctional polarization converter with broadband and large angular tolerance of incidence is realized. Such polarization converter can convert the reflected microwave to three different polarization states, including linear polarization, circular polarization and elliptic polarization states. Another gallium-indium alloy, EGaIn, is demonstrated in terahertz regime [208]. A C-shape microfluidic channel is connected with two horizontal channels. When all of the channels are injected with EGaIn, the resonator is an irregular closed ring. By applying different injection pressure, two other geometries of liquid resonators can be obtained, which is split ring resonator and closed ring resonator. Thus the transmission spectrum of the metasurface will be changed and a pressure memory is realized.

Random Access Tuning

The property of random access tuning for the metasurface is essential for the realization of a tunable flat lens, in which each unit cell should be controlled individually to gain different phase jumps for wavefront shaping. A flat lens with tunable phase gradient via random access reconfigurable metasurface (RARM) is demonstrated by using mercury in microwave [107]. Two layers of PDMS channels are created for the structure layer and control layer, respectively. The control layer behaves as an array of micro valve aligned to the bottom structure layer as shown in Fig. 2.4 [9, 209].

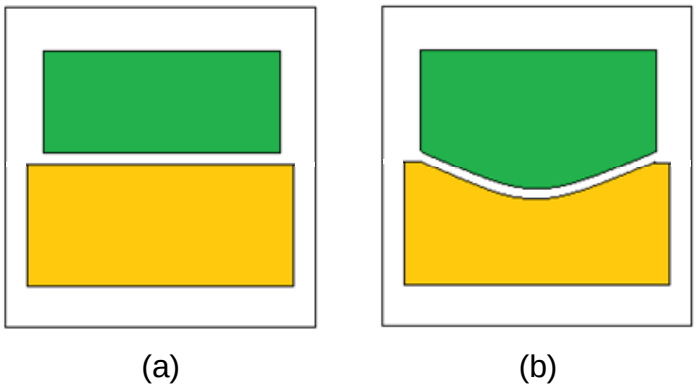

Figure 2.4 Schematic illustration of working principle of the micro valve (a) on state and (b) off state.

The air in both control channels and structure channels are indicated as green and yellow color, respectively, which are separated with a PDMS membrane. The original state of the PDMS membrane is planar due to the equal air pressure in both channels. When the air pressure in the top control channel is increased by an air pump, the unbalanced air pressure results in a downward force applied to the

PDMS membrane. Since the PDMS membrane is soft, the downward force will cause the deformation of the membrane and thus the space of the bottom channels will be squeezed. When the bottom air channel is connected to the mercury-filled SRR, the squeezed space of the channel forces the air to be injected into the SRR, resulting in the reconfiguration of the shape of SRR.

The random access control is realized by using a ternary valve multiplexer addressing the unit cells individually at will [210]. A simplified ternary coded control system is shown in Fig. 2.5, which is used to address one of the nine channels individually. Each bit is controlled by three channels. The control channels are pumped with air to block the channels 0 to 8. Only one channel is left unblocked for each ternary code. The number of the controlled channels increased exponentially when the Bits increased, which enables large-scale of unit cells control of the metasurface by using limited control channels. In this report [107], the gap arc of the SRR is individually controlled from 10° to 120°, such that a full control over the phase shift is realized. Such RARM based flat lens has a focal length tuning from 5λ to 15λ.

Apart from the uniform tuning and random access tuning for the periodic structure, others tuning such as partial tuning for aperiodic structure is also demonstrated in the meta-liquid-based metasurfaces [196, 211]. It is also shows that by incorporating with the PDMS, the meta-liquid-based metasurfaces can be either bent [212], or stretched [213] to realize different functionalities.

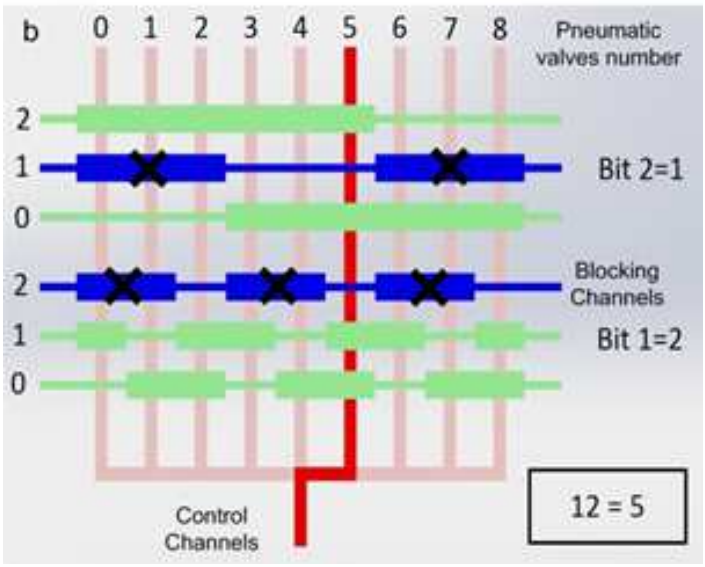

Figure 2.5 Schematic illustration of a simplified ternary coded control system.

2.4 Chiral Metasurfaces

2.4.1 Fundamental Concepts

A chiral medium is composed of structures that are not superimposable on their mirror images. The chiral structure and its mirror image are called enantiomers. The word “chirality” originates from the Greek word, which means “hand” because the left and right hands are mirror images of each other which cannot superimpose on each other. A chiral structure has a cross-coupling between the electric field and magnetic field when EM wave propagates through a chiral medium. Such cross-coupling effect is described by a dimensionless chirality parameter κ. The chirality has been long studied since the early 19th century when Biot and others observe an optical rotation of polarized light going through the quartz crystals. However, the term “chirality” is first used in 1873 by Lord Kelvin to describe the handedness of the chiral medium [214]. In fact, in chemistry,

pharmaceuticals and biology, many biologically active molecules are chiral, such as sugar, tartaric acid and turpentine.

From the electromagnetic point of view, the constitutive relations of chiral medium are expressed as

$$\begin{cases} \boldsymbol{D} = \varepsilon_0 \varepsilon_r \boldsymbol{E} + i\kappa\sqrt{\varepsilon_0 \mu_0}\,\boldsymbol{H} \\ \boldsymbol{B} = \mu_0 \mu_r \boldsymbol{H} - i\kappa\sqrt{\varepsilon_0 \mu_0}\,\boldsymbol{E} \end{cases} \tag{2.15}$$

where κ is the dimensionless chirality parameter of the chiral material with a non-zero value. It is shown that the constitutive relations for chiral medium is different from that for the isotropic materials in Eq 2.2. The electrical (or magnetic) flux depends on both the electric and magnetic field of the EM wave, because the cross-coupling between the electric and magnetic field in the chiral medium. When a left or right circular polarized light propagate in a chiral medium, the refractive index can be derived as

$$n_{L/R} = \sqrt{\varepsilon_r \mu_r} \pm \kappa \tag{2.16}$$

where the refractive index n_L corresponds to the eigenvector of the left circular polarized (LCP) wave and n_R corresponds to the eigenvector of the right circular polarized (RCP) wave.

The chiral metasurface are a metasurface consisting of chiral structured meta-atoms. It attracts many research attentions because they exhibit many novel optical properties, especially for the realization of polarization dependent devices which are discussed in the following section.

2.4.2 Optical Properties

Negative Refractive Index

Apparently, from Eq. 2.16, it shows that if the chirality parameter κ is larger than $\sqrt{\varepsilon_r \mu_r}$, one refractive index of the circular polarization will become negative. This concept was first proposed by Tretyakov [215] and Pendry [216] independently. In the report [216], Pendry theoretically demonstrated that the negative refraction can be realized by introducing the resonant dipoles into a chiral medium. Chirality splits the degenerate transverse modes and creates a range of frequencies where the group velocity has the opposite sign to the phase velocity for one circular polarization. In contrast with the double negative approach discussed in previous section 2.1.2, the chiral route does not require simultaneously negative permittivity and permeability in the same frequency range. This report proposed a practical realization of a resonant chiral structure by using a Swiss roll structure wound in a helix manner. The resonance results from the inductance in the coiled helix and capacitance between the inner and outer layers of the helix. A parallel direction of the induced magnetic polarization and electric polarization is achieved when the current flows along the helix. This feature that electric polarization and magnetic polarization are parallel is consistent with what Eq 2.15 implies for chiral materials.

There is much research interest in using the chiral metasurface to achieve negative refractive index. A terahertz chiral negative index metasurface is

demonstrated based on vertical metallic chiral resonator, in which the chirality is introduced by tilting the loop of the resonator out of the plane with its gap [217]. Such a vertical resonator allows the oscillating current flowing through the metal loop to be excited by either an electric field across the gap of a magnetic field perpendicular to the loop, so that an electric dipole and a magnetic dipole oriented with a small angle is generated in the same frequency. Strong chirality is induced, leading to negative refraction for circular polarized waves. Other chiral metasurface induced negative refractive index are also demonstrated by using bilayer structures of twisted rosettes [218], twisted crosswires [219], gammadion [220] and four U split ring resonators [221].

Optical Activity and Circular Dichroism

Optical activity is the rotation of the plane of polarization of linearly polarized light when it propagates through a material. This polarization effect characterized by the polarization azimuth rotation angle θ can be expressed as

$$\theta = \frac{\pi d}{\lambda_0}\left(n_L^{'} - n_R^{'}\right) = \frac{1}{2}\left[\arg\left(T_R\right) - \arg\left(T_L\right)\right] \qquad (2.17)$$

where d is the thickness of the medium, λ_0 is wavelength in the free space, T_L and T_R are the transmission of the LCP and RCP wave, respectively. In fact, the transmitted wave is still linearly polarized after propagating through the medium when the material absorption is ignored and only the real part of the refractive

index is considered. If the absorption of the material is considered, the absorptivity of a chiral medium will be different for the LCP and RCP wave, which is called circular dichroism. Since the impedance of chiral medium is equal for LCP and RCP wave, the reflections of these two polarization are the same. Therefore, the transmission of the two polarizations is different, resulting in an elliptically polarized wave. The circular dichroism characterized by the ellipticity of the elliptically polarized wave can be described as

$$\eta = \frac{1}{2}\arctan\left(\frac{|T_L|^2 - |T_R|^2}{|T_L|^2 + |T_R|^2}\right) \tag{2.18}$$

The optical activity and circular dichroism have been demonstrated in many works by using chiral metasurfaces. A two-dimensional gammadion array patterned on the substrate having a 30° of polarization azimuth rotation is demomstrated due to the symmetric breaking effect by the substrate [222]. The optical activity can also be realized by 3D structures [223]. Besides, even an achiral metasurface can exhibit optical activity and circular dichroism under oblique incidence, which is called extrinsically chiral system [224]. In such a system an achiral structure together with the incident wave forms a geometrical arrangement that cannot be superimposed with its mirror image and thus the whole arrangement is chiral.

Asymmetric Transmission

Non-reciprocal material, usually refers to a ferrite that is biased by a static magnetic field, transmitting microwave signal from one direction, while absorbing energy in opposite directions. Recently, it was found that metasurfaces with strong symmetric breaking can also exhibit propagation direction-dependent transmission effect without violating Lorentz' reciprocity theorem, known as asymmetric transmission [225-228]. The asymmetric transmission for circular polarized wave is demonstrated by using planar chiral structure, which requires simultaneous presence of planar chirality and anisotropy in the structure [229]. However, the magnitude of the asymmetric transmission is very small. A giant asymmetric transmission is demonstrated by using bi-layered structures, which increase the asymmetric transmission to 0.6 [230]. Apart from the circular polarization, the asymmetric transmission is also demonstrated in the linear polarized wave by using bi-layered chiral metasurface [231-237]. Furthermore, a twisted SRR pattern on both sides of a dielectric slab is demonstrated in the asymmetric transmission for linearly polarized wave only, but none for circular polarized wave [238].

In conclusion, the chiral metasurface can exhibit the properties of negative refractive index, optical activity, circular dichroism and asymmetric transmission, which has huge potential applications in optical communication, signal processing, etc.

2.5 Summary

Based on the literature survey presented, metasurfaces are artificially designed materials at subwavelength scale, which exhibit novel optical properties from microwave frequency to optical regime. Although the properties of the metasurfaces mainly rely on the geometric architecture of the meta-atoms, the base materials also play an important role. The metal based metasurfaces and dielectric metasurfaces, which are based on the plasmonic resonance and Mie resonance, respectively, have their different advantages and disadvantages. Particularly, a meta-liquid-based metasurface is presented, which consists of liquid materials including liquid crystal, liquid metals and liquid dielectrics, not only providing exotic optical properties, but also enabling a large tunability of the metasurface. Such meta-liquid-based metasurfaces can flexibly control and manipulate the EM wave, including the propagation direction, amplitude, phase, and polarization states. Meanwhile, microfluidic technology based on soft material PDMS to control the liquid materials is presented. Finally, the development of the chiral metasurfaces and the strong chiral behaviors are reviewed. Metasurface is a new and exciting research area, and this thesis seeks to show the significance of EM wave manipulation by using meta-liquid-based metasurface.

CHAPTER 3

WATER-RESONATOR-BASED METASURFACE

This chapter presents the design, fabrication and experiment of the water-resonator-based metasurface for ultra-broadband and near-unity absorption across the entire Ku, K and Ka bands. The structure designs of the water-resonator-based metasurface are presented. It is using a water-resonator array embedded in the PDMS by using microfluidic technology. Subsequently, theoretical analysis on the impedance-matching at water-air interface and the combination of the magnetic resonance and diffraction effect to achieve ultra-broadband absorption are discussed. Then, the fabrication processes for the water-resonator-based metasurface are illustrated. Finally, the experimental results are presented and discussed. The results include a tunable absorption by tuning the heights of the water-resonators, a broadband absorption with large angular tolerance, an omnidirectional absorption on curved surfaces and a broadband intensity modulation by injecting different concentration of water-ethanol solution into the liquid reservoir.

3.1 Design and Theoretical Analysis

The metasurface can be characterized by a complex electric permittivity $\varepsilon(\omega) = \varepsilon' + \varepsilon''$ and magnetic permeability $\mu(\omega) = \mu' + \mu''$. It is essential to adjust the $\varepsilon(\omega)$ and $\mu(\omega)$ of the metasurface to achieve the impedance-matching to free space to suppress the reflection, together with the metallic film to block all transmissions, a near-unity absorption can be realized. As discussed in Section 2, in microwave range, the absorption of electromagnetic wave by PMAs is mainly attributed to the dielectric (volume) loss in comparison to the Ohmic (surface) loss of metal structure. Therefore, high lossy dielectric metasurface, in which the EM wave is well confined, is a good candidate for perfect absorption. As a proof of principle, an array of water droplet embedded in PDMS is demonstrated to realize a broadband and near-unity absorption by using microfluidic technology.

3.1.1 Design of Water-Resonator-Based Metasurface

Water is highly absorptive with large value of imaginary part of permittivity ε" in microwave range due to hydrogen bonded network among water molecules, which make it suitable for perfect EM wave absorption in this regime. The two Debye processes deal with complex permittivity of water, which can be expressed as [239]

$$\varepsilon(\omega) = \frac{\varepsilon_0 - \varepsilon_1}{1 - i\omega\tau_1} + \frac{\varepsilon_1 - \varepsilon_\infty}{1 - i\omega\tau_2} + \varepsilon_\infty \tag{3.1}$$

where ω is the radiation frequency (in gigahertz), ε_0 is the relative permittivity at low frequencies (static region), ε_1 is the intermediate relative permittivity, ε_∞ is the relative permittivity at infinite frequency, τ_1 and τ_2 are the relaxation times. In this paper, all temperature conditions are under room temperature. The complex permittivity of water is shown in Fig. 3.1.

Although large imaginary part of permittivity is essential to high absorption, the large contrast of permittivity between water and air causes the impedance mismatch to free space of the water film, creating a huge reflection of microwave at the water-air interface and deteriorating the absorption function as shown in Fig. 3.2.

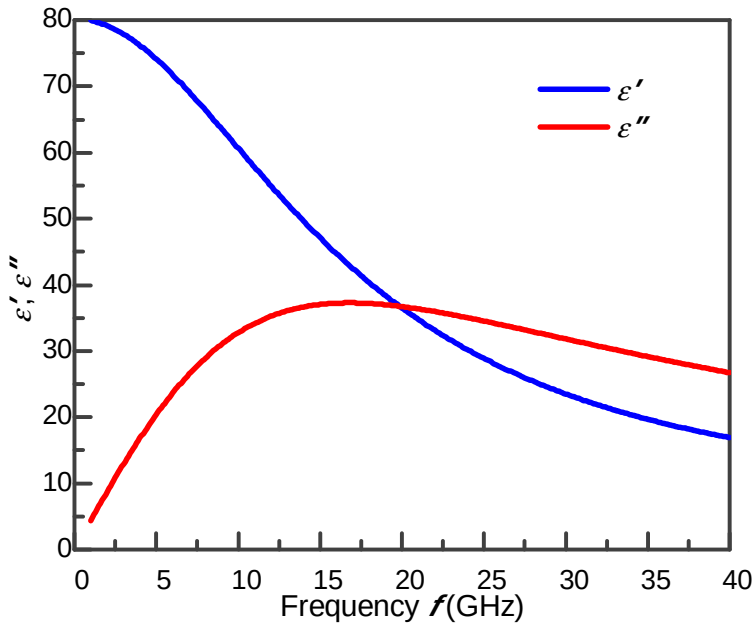

Figure 3.1 Complex permittivity of water. The blue line indicates the real part of permittivity; the red line indicates the imaginary part of permittivity.

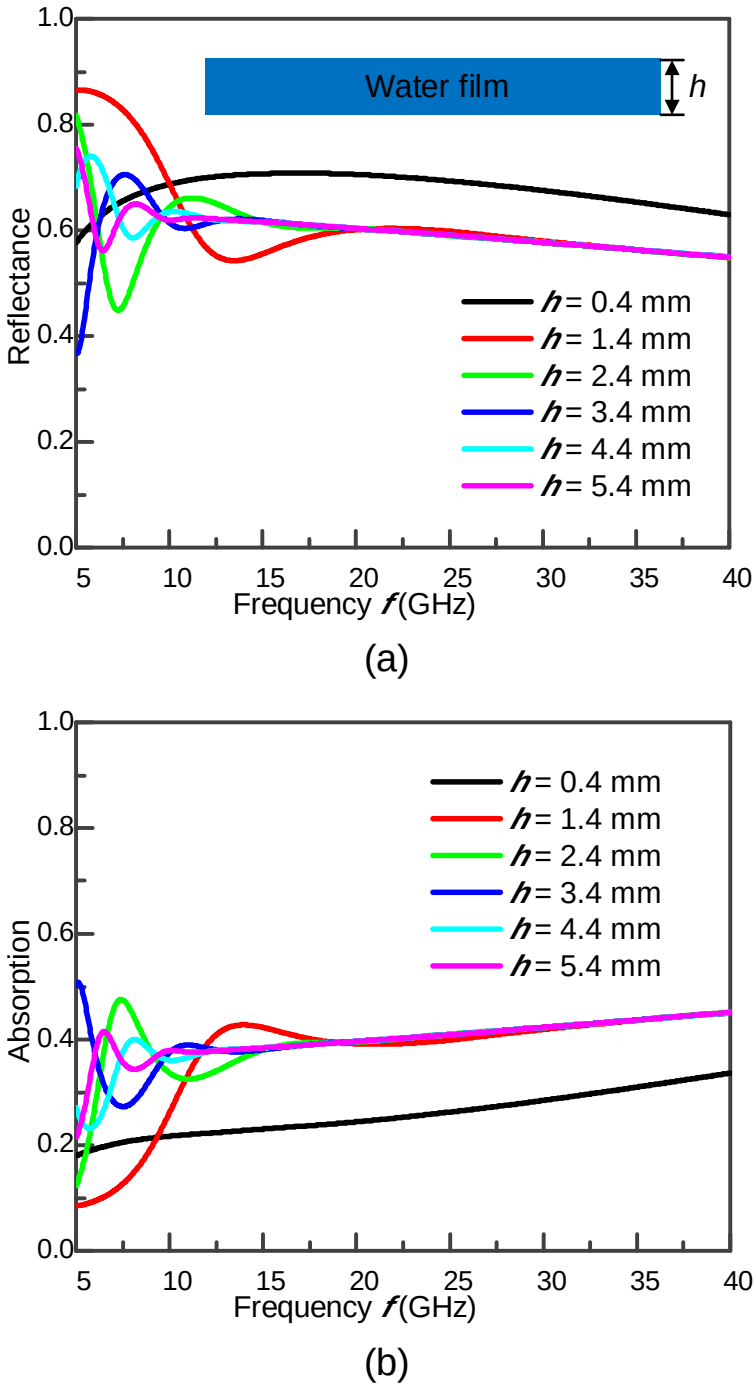

Figure 3.2 Reflectance and absorption spectra of a continuous water film with the height from 0.4 mm to 5.4 mm.

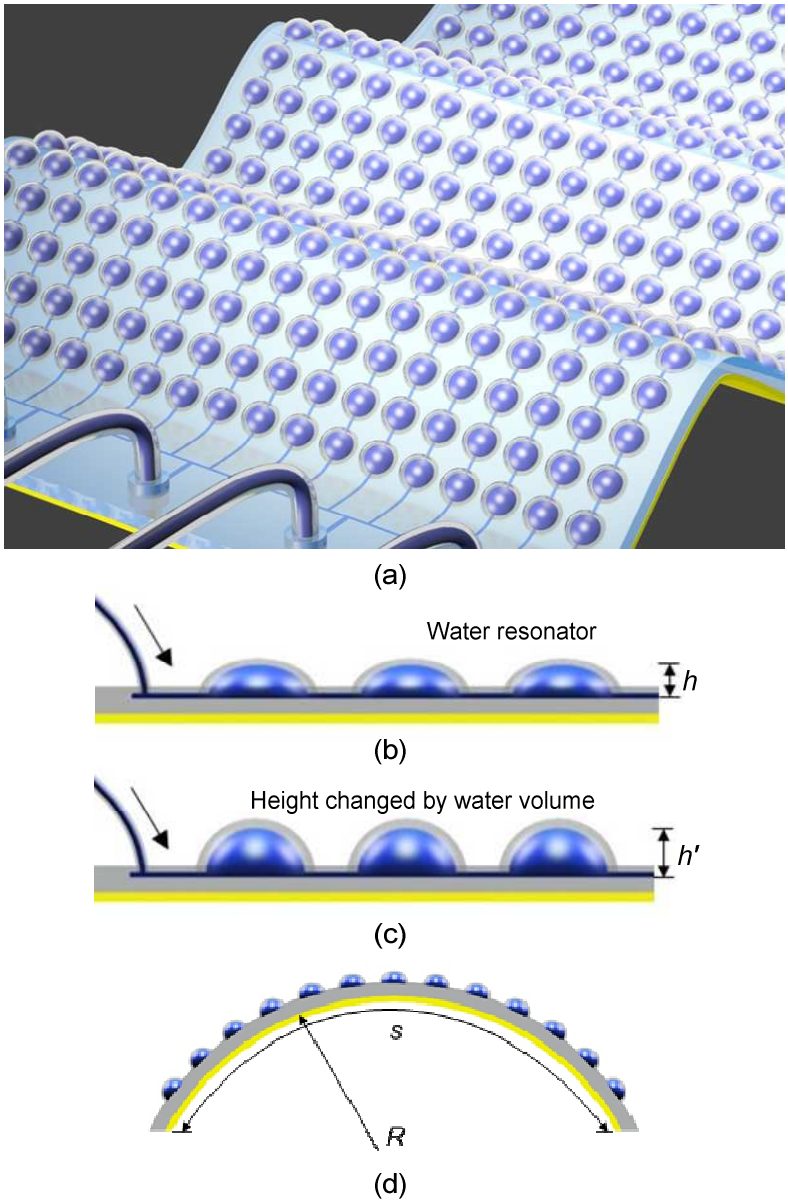

Figure 3.3 Schematic illustration of water-resonator-based metasurface. (a) Water-resonator-based metasurface consists of a top PDMS membrane layer and a bottom PDMS-metallic layer. (b) Side view of the embedded water-resonators with water injection. (c) Height of water-resonator is actively tuned by different water volumes. (d) Soft metasurface absorption functional material is bent to arbitrary curvature.

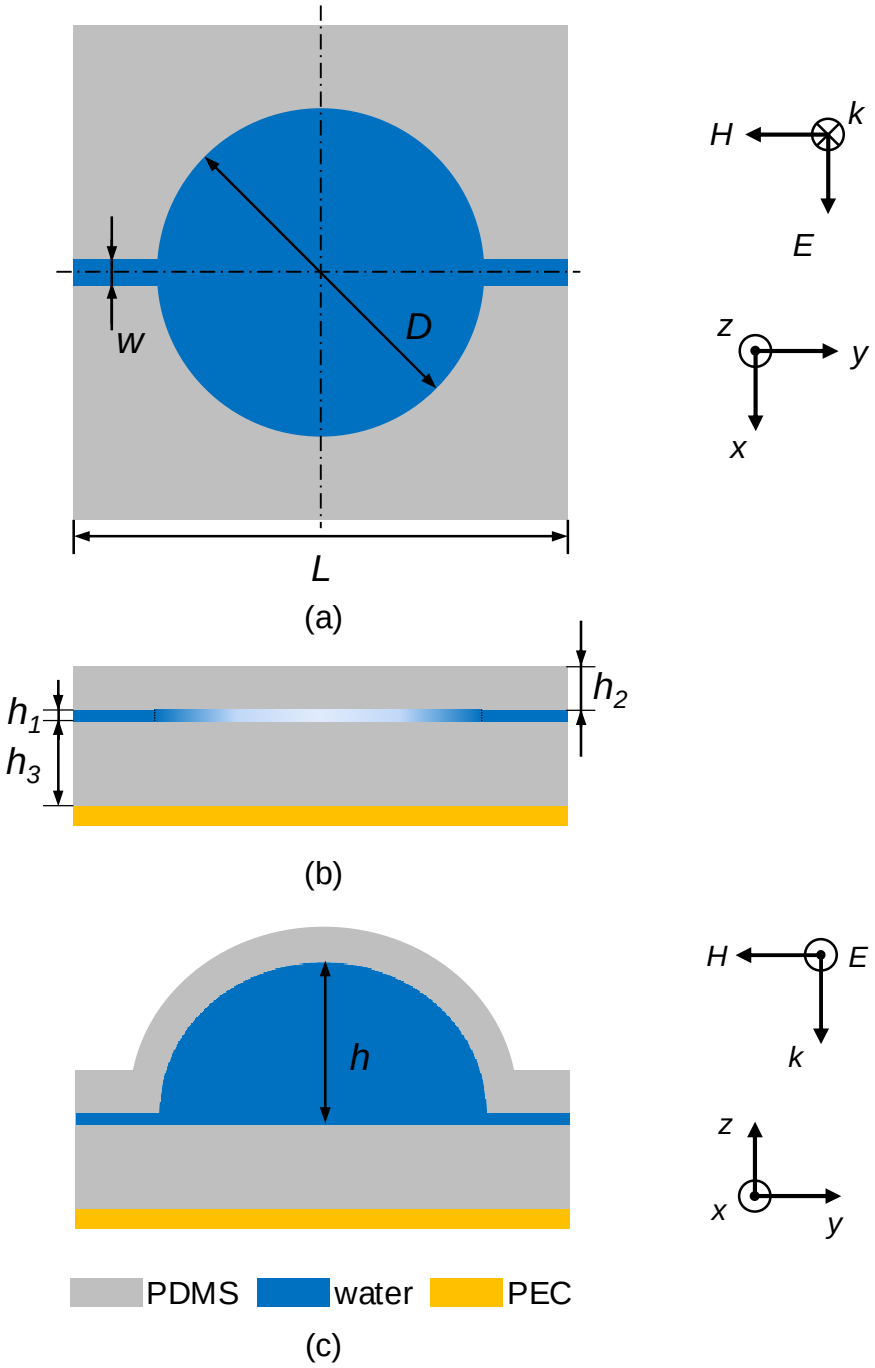

Figure 3.4 Layout of the water-resonator. (a) Top view and (b) side view of the water resonator. (c) Side view of the water resonator with the height of the water resonator h that can be changed by varying the water volume.

In order to realize the impedance-matching to free space, we create an array of water-droplets as resonant structures to control the permittivity and permeability of the metasurface. The water-resonator-based metasurface is illustrated in Fig. 3.3a. Each unit cell consists of a water sphere cap sandwiched between a top PDMS membrane and a bottom PDMS space layer with the backside being bonded to a metallic layer. A 100 μm deep circular reservoir connected with microchannel is created in the top PDMS membrane. When water is injected into the reservoir, the membrane is expanded in the vertical direction and formed a water sphere cap due to the water pressure. The water sphere cap embedded in PDMS behaves as a resonator, which can change the impedance of the metasurface by inducing a magnetic resonance. By appropriately designing the shape of the water-resonator, the impedance of the metasurface can be tailored to match with the one of free space. Together with total reflection from the metallic reflector underneath the bottom PDMS layer, the incident EM wave energy is completely absorbed by the high lossy water-resonator and thus, near-unity absorption is realized. By changing the water volume, the top PDMS membrane can be expanded or contracted, resulting in a reversible process to flexibly reconfigure the height of the water resonator as shown in Fig. 3.3b and 3.3c. This enables the dynamical control of the impedance as well as the absorption spectrum. The water-resonator-based metasurface can be bent into different radii of curvature R with a fixed sample length s due to the softness of water and PDMS as shown in Fig. 3.3d. The layout of the water-resonator is shown in Fig. 3.4. The period of the metasurface L = 5.5

mm; the diameter of the water-reservoir is D = 4.4 mm; the width and height of the channel are w = 0.3 mm and h_1 = 0.08 mm, respectively.

3.1.2 Theoretical Analysis and Numerical Simulation

Numerical Calculation Method

The optical response of the metasurface is studied by numerically calculating the *S*-parameter using the commercial simulation software of CST MICROWAVE STUDIO, which was originally based on Finite Difference Time Domain (FDTD). It simplifies the process of creating the structure by providing a powerful graphical solid modeling front end which is based on the ACIS modeling kernel. After the model has been constructed, a fully automatic meshing procedure is applied before a simulation engine is started. CST contains several different simulation technologys to suit various applications. For structures that are electrically much smaller than the shortest wavelength, the frequency domain solver is usually the better choice. Besides, the frequency domain solver also contains alternatives for the fast calculation of *S*-parameters for strongly resonating structures. Therefore, in this thesis we utilize the frequency domain solver to simulate the metasurface. Since the metasurfaces are assumed as infinite periodic structures, the boundary conditions are set as “unit cell” which virtually repeats the modeled structures to infinite 2D plane. Floquet ports (periodic waveguide ports) are used as the source of EM wave and the *S*-parameters are calculated to investigate the respond of the metasurface.

Numerical Results on Pure Water

The water-resonator is embedded in the low permittivity dielectric material, PDMS [240], forming a PDMS/water/PDMS sandwich structure. With the high ε value of water and specific geometric parameter, a magnetic resonance and a diffraction grating effect can be excited at certain frequencies in the water-resonator. Meanwhile, the high ε'' value of water in a wide frequency range enables a broadband absorption around resonance frequencies. The normalized absorption A of the water-resonator based metasurface is derived from the calculated S-parameter S_{11} and S_{21} that $A = 1 - |S_{11}|^2 - |S_{21}|^2$, where S_{11} is the reflected field amplitude and S_{21} is the transmitted amplitude, respectively. The parameter S_{21} is always zero since the metallic ground layer blocks all transmission.

The absorption spectra for different height of the top and bottom PDMS layer when the height of the water-resonator keeps at h = 1.6 mm are shown in Fig. 3.5. The absorption of the water-resonator-based metasurface is relatively insensitive to the height of the top PDMS layer as shown in Fig. 3.5a. However, when the height of the bottom PDMS layer is increasing, the absorption at the absorption peaks will first arise to near unity at h_3 = 1.0 mm and then fall to below 80% at h_3 = 2.0 mm as shown in Fig. 3.5b, because the interaction of the water-resonator and the ground metal film will be weakened when the bottom PDMS layer is too thick. In our design, the height of the top and bottom PDMS layer are set at h_2 = 0.6 mm and h_3 = 1.0 mm, respectively.

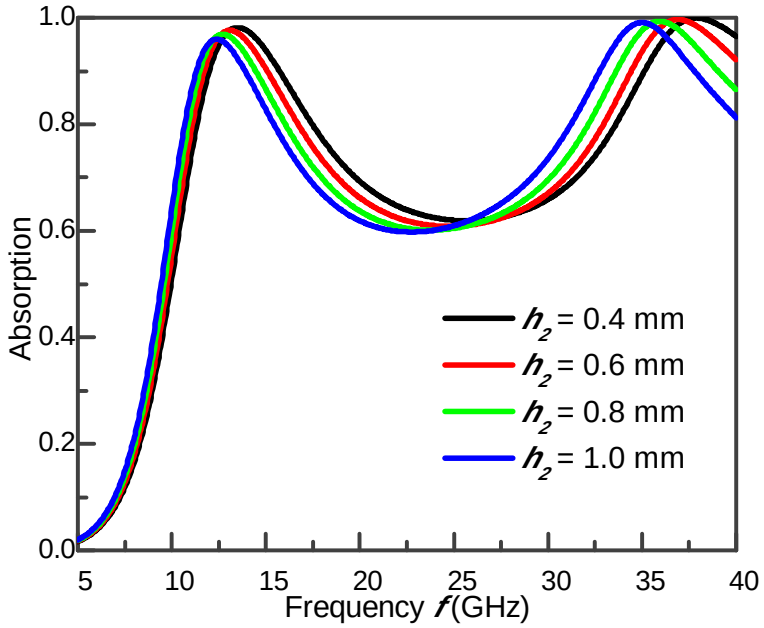

(a)

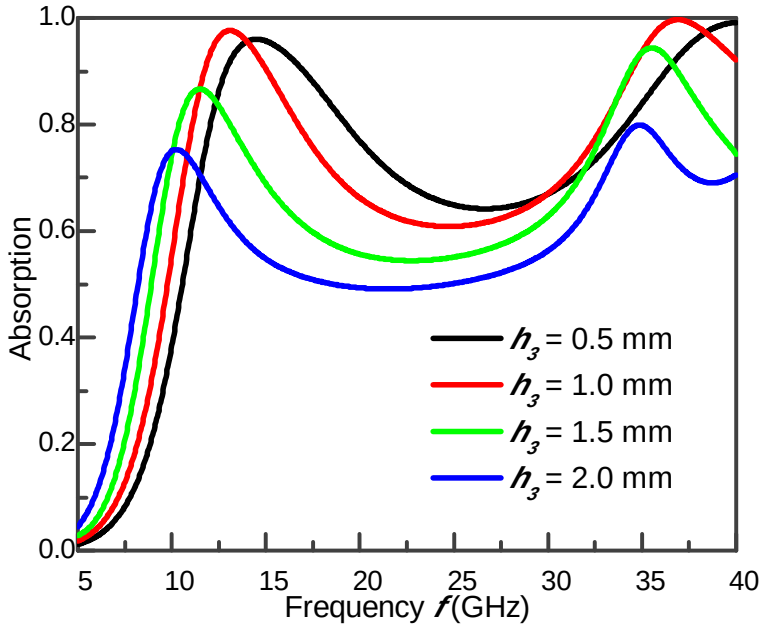

(b)

Figure 3.5 (a) Absorption spectra at h_3 = 1.0 mm when the height of the top PDMS is changed from 0.4 mm to 1.0 mm. (b) Absorption spectra at h_2 = 0.6 mm when the height of the bottom PDMS is changed from 0.5 mm to 2.0 mm.

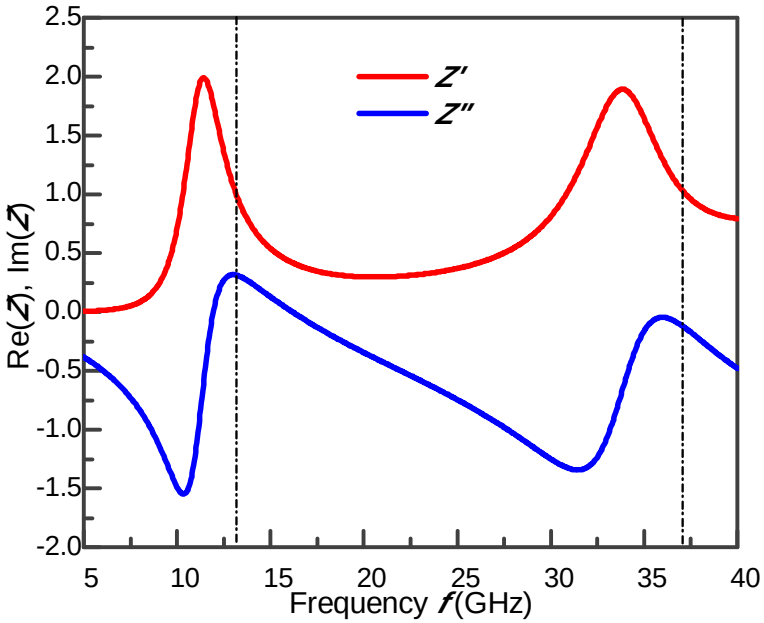

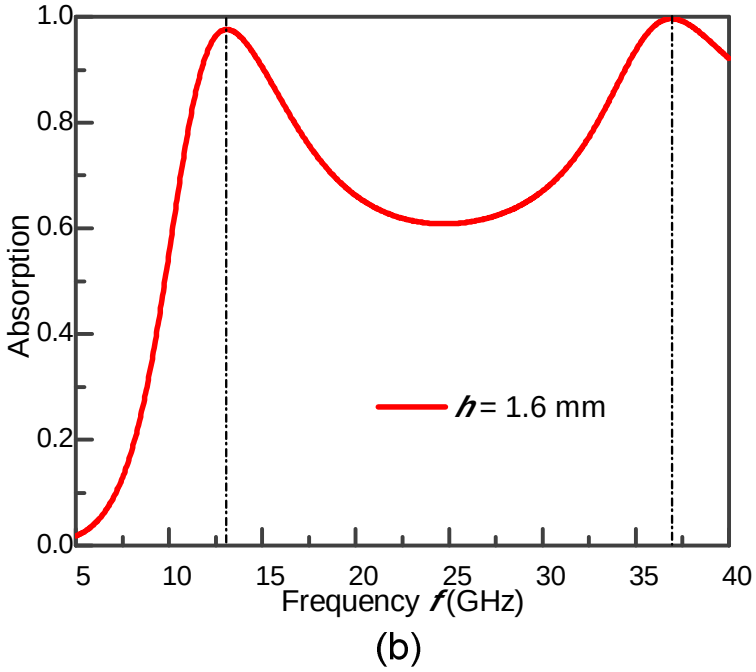

Figure 3.6 (a) The calculated impedance and (b) simulated absorption spectrum when height of water-resonator h = 1.6 mm.

The impedance $Z(\omega)$ of the water-resonator-based metasurface is retrieved from the reflection (S_{11}) and transmission (S_{21}) data of the *S*-parameters. The metasurface is characterized as an effective homogeneous slab. For a plane wave incident normally on a homogeneous slab of thickness *d* with the origin coinciding with the first face of the slab, S_{11} is equal to the reflection coefficient, and S_{21} is related to the transmission coefficient *T* by $S_{21} = Te^{ik_0 d}$, where k_0 represents the wave number of the incident wave in the free space. The refractive index *n* and normalized impedance *Z* deal with the *S*-parameters, which can be described by as [241]

$$S_{11} = \frac{R_{01}(1 - e^{i2nk_0 d})}{1 - R_{01}^2 e^{i2nk_0 d}} \tag{3.2a}$$

$$S_{21} = \frac{(1 - R_{01}^2)e^{ink_0 d}}{1 - R_{01}^2 e^{i2nk_0 d}} \tag{3.2b}$$

where

$$R_{01} = \frac{Z - 1}{Z + 1} \tag{3.3}$$

Subsequently, the impedance *Z* can be retrieved as

$$Z = \pm\sqrt{\frac{(1 + S_{11})^2 - S_{21}^2}{(1 - S_{11})^2 - S_{21}^2}} \tag{3.4}$$

where the sign in equation is determined by requirement $Z' \geq 0$ ($(\cdot)'$ and $(\cdot)''$ denote the real part and imaginary part operators, respectively). The calculated impedance $Z(\omega)$ when height of the water-resonator h = 1.6 mm is shown in Fig 3.6a. At f_1 = 13.1 GHz and f_2 = 36.9 GHz, the real impedance Z' is approaching unity ($Z' \sim 1$) and the imaginary impedance Z'' is minimized to nearly zero ($Z'' \sim 0$), such that the reflection can be suppressed to nearly zero. Simulated results of absorption spectrum is shown in Fig. 3.6b. Two absorption peaks are observed at the frequency f_1 = 13.1 GHz with near-unity absorption of 98% and f_2 = 36.9 GHz with absorption of 99%, which matches well to the prediction from impedance calculation.

The first absorption peak is attributed to the induced magnetic resonance mode, which can be examined by the current flow and field distribution in Fig. 3.7(a-c). A circular current flow is induced at f_1 and a strong magnetic field is observed in the water-resonator as shown in Fig. 3.7(a-b), respectively. Therefore, the incident microwave energy is strongly confined and absorbed in the water-resonators. The typical quadrupole profile of the electric field distribution in Fig. 3.7c also confirms the magnetic dipolar response. The second absorption peak is attributed to the grating effect [49, 242]. The periodic water-resonator structure behaves as a 2D grating, which excites spoof surface plasmon polaritons (SPPs) at the interface between the dielectric layer and metal ground as shown in Fig 3.8a. Due to the excitation of the spoof SPPs, the incident microwave is strongly confined in the water-resonator-based metasurface as shown in the magnetic and electric field

distribution in Fig. 3.8(b, c). In such a case, the incident microwave can be fully absorbed by the water-resonator-based metasurface.

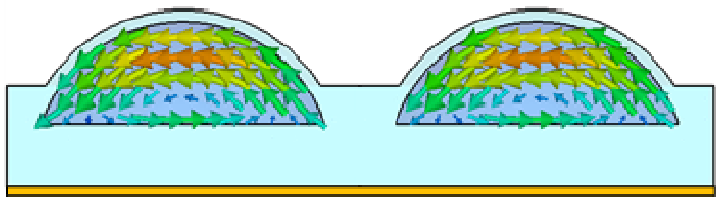

(a)

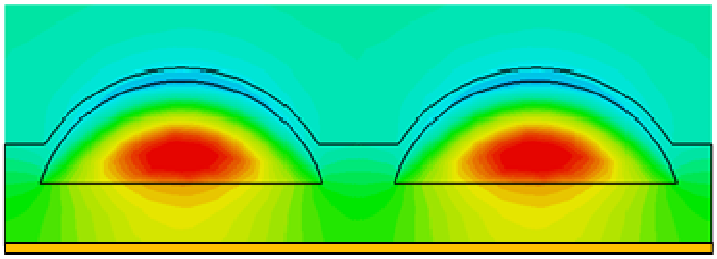

(b)

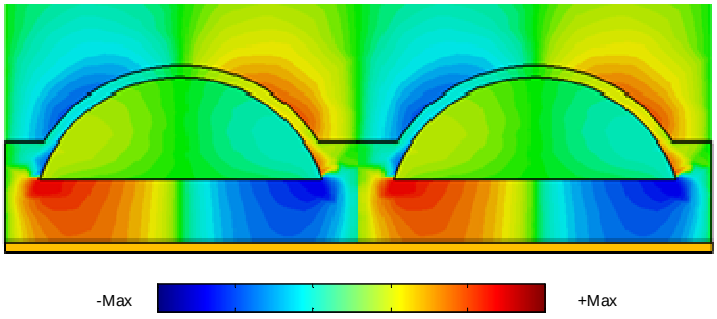

(c)

Figure 3.7 Side view of (a) current density, (b) magnetic distribution H_x and (c) electric distribution E_z at the absorption peak f_1. Scale bar presents the field amplitude for (b,c).

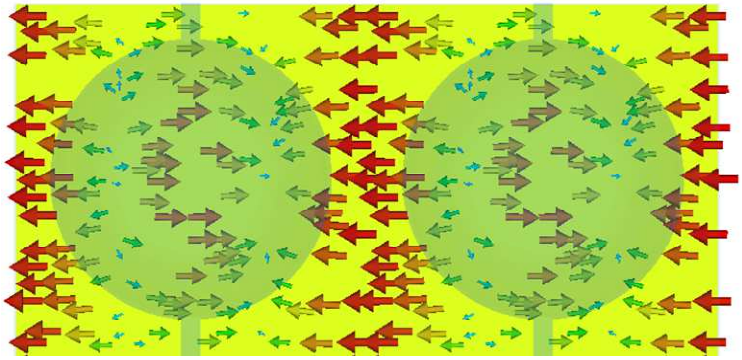

(a)

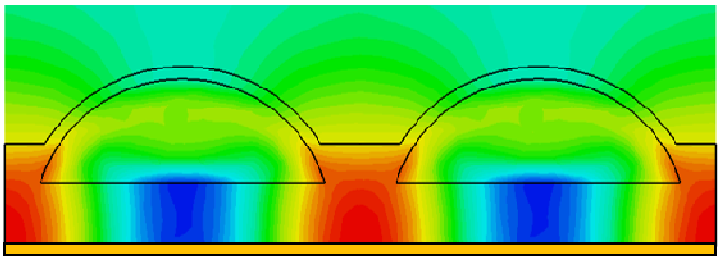

(b)

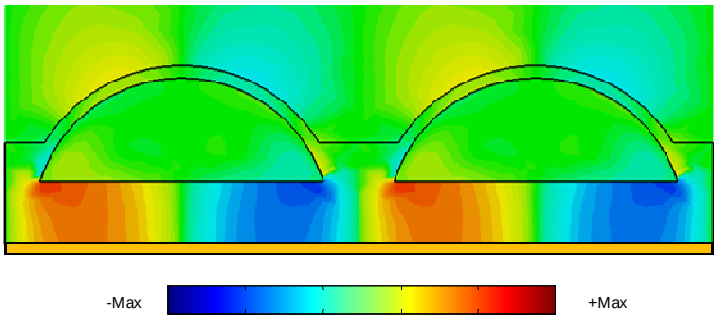

(c)

Figure 3.8 Top view of (a) surface current of the metal ground plane; side view of (b) magnetic distribution H_x and (c) electric distribution E_z at the absorption peak f_2. Scale bar presents the field amplitude for (b,c).

Numerical Results on Water-Ethanol Solution

Besides a perfect absorption, there is also strong demand for controllable absorptivity in many potential applications. The water-resonator-based metasurface provides a very convenient approach to control the absorptivity by simply replacing water with other different dielectric constant liquids. Fig. 3.9 shows that both the real part (ε') and imaginary part (ε'') of the effective permittivity of the mixture solution decrease with an increased concentration of ethanol in the solution [243]. The decreasing of ε' undermines the microwave confinement in the original water-resonator, while the decreasing of ε'' further reduces the wave absorption in the metasurface. Fig. 3.10 shows the simulation results of the absorption spectra with different concentrations of ethanol solutions when the height of the water-resonator keeps at 0.4 mm. The absorption level decreases from about 90% to below 20% in the entire measured frequency regime, when the ethanol concentration in the solution is increased from 0% (pure water) to 100% (pure ethanol).

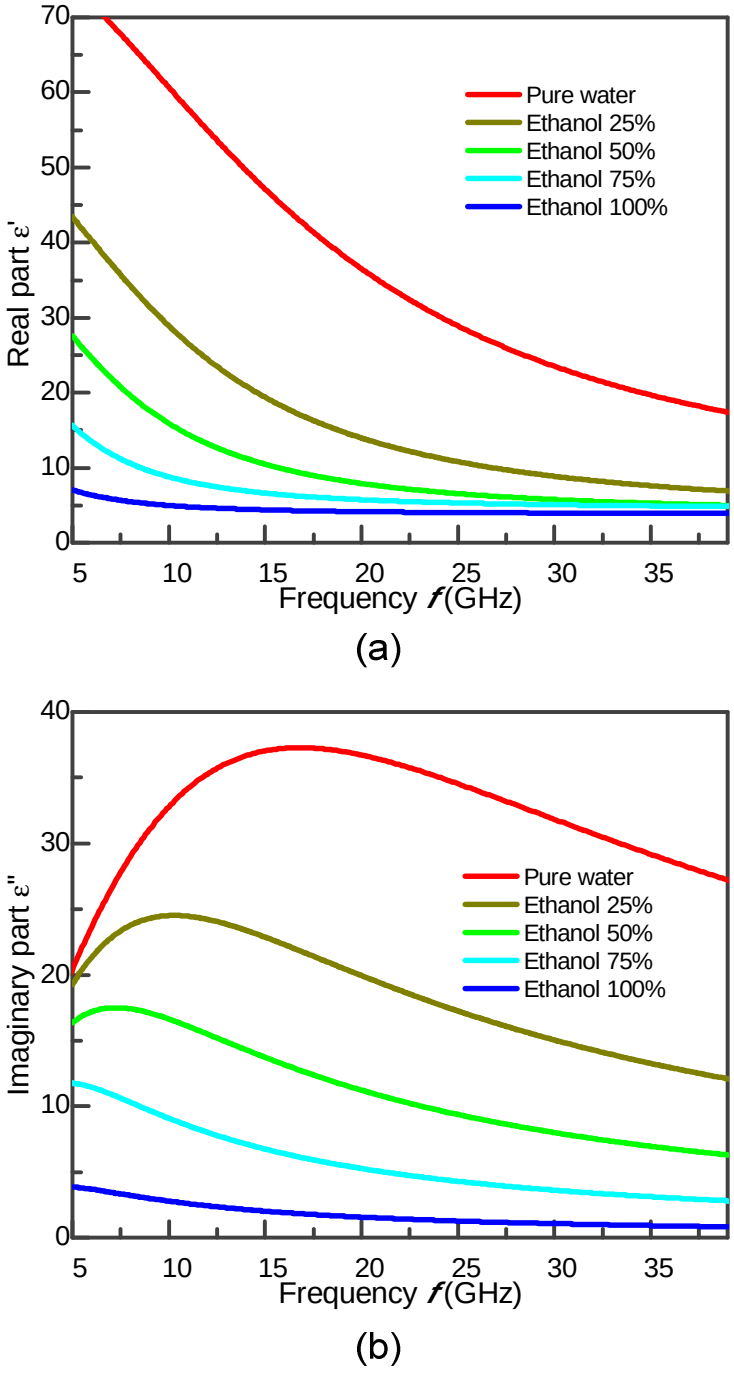

Figure 3.9 Complex permittivity of water-ethanol solution with different concentration of ethanol. (a) Real part and (b) imaginary part of permittivity of water-ethanol solution with different concentration of ethanol, respectively.

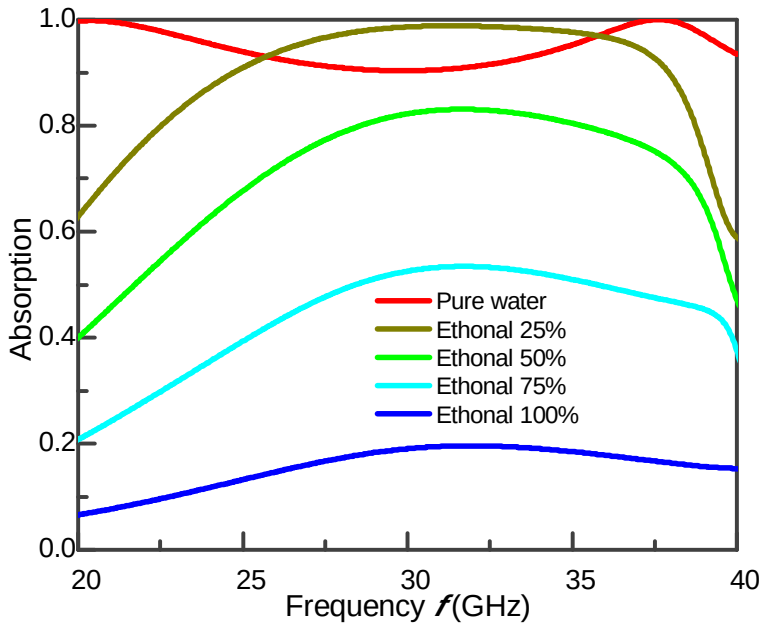

Figure 3.10 Simulation results of the absorption spectra with different concentration of ethanol solution. Height of the water-resonator is 0.4 mm.

3.2 Fabrication and Experimental Setup

3.2.1 Fabrication Processes Development

The fabrication processes of water-resonator-based metasurface are based on photolithography as shown in Fig. 3.11. A 675-μm thick silicon wafer is used as the substrate, which is baked in a 120℃ oven for 15 min after cleaning by acetone and IPA. The photoresist AZ 4620 is coated on the wafer and produces a uniformly thick layer through spin coating as shown in Fig. 3.11a. The photoresist-coated wafer is then prebaked to drive off excess photoresist solvent. After prebaking, the silicon wafer with photoresist is exposed under a patterned plastic mask as shown in Fig. 3.11b. The UV exposure procedure causes a chemical change of the photoresist and allows it to be removed by developer, thus the unexposed part remains on the silicon wafer as shown in Fig. 3.11c. The remaining photoresist functions as a mask in the following etching process. The plasma chemical agent is then applied onto the silicon wafer to remove the uppermost layer of the uncovered area of the silicon wafer. The silicon mould with desired pattern is then obtained after removing the remaining photoresist as shown in Fig. 3.11d. The next step is how to use the silicon mould to fabricate the PDMS channel. The PDMS was prepared by mixing the base and curing agent with the weight proportion of 11:1. After putting in a vacuumizer to expel the suspended air, the PDMS is poured onto the silicon mould as shown in Fig. 3.11e and followed by baking it in a 75℃ oven for 2 hours. The pattern is then transferred to the PDMS by peeling off it from silicon substrate as shown in Fig. 3.11f. A plane PDMS layer is fabricated using

the same process as the patterned PDMS through a flat silicon wafer without pattern. The patterned PDMS layer is bonded to the plane PDMS layer to form the microfluidic channel by plasma bonding as shown in Fig. 3.11g. So far the PDMS channel is fabricated for further liquid injection. The PDMS sample can be bonded to arbitrary surface for measurement as shown in Fig. 3.11h.

The fabricated metasurface in which water is injected into the water reservoirs with different volumes is shown in Fig. 3.12. The water-resonator-based metasurface consists of 24 × 24 elements with a 5.5-mm period and the total footprint of the metasurface is 132 mm × 132 mm. The top PDMS membrane is expanded to various extents by changing the injected water volume, leading to a controllable height of the water resonator from h = 0.4 mm to 1.6 mm as shown in Fig. 3.12(a-b). The water-resonator-based metasurface can also be bent into an arbitrary curved surface due to the flexibility of water and PDMS as shown in Fig. 3.12c. The water-resonators are confined in the water reservoirs formed by the two PDMS layers, which can minimize the gravitational effect on water-resonators.

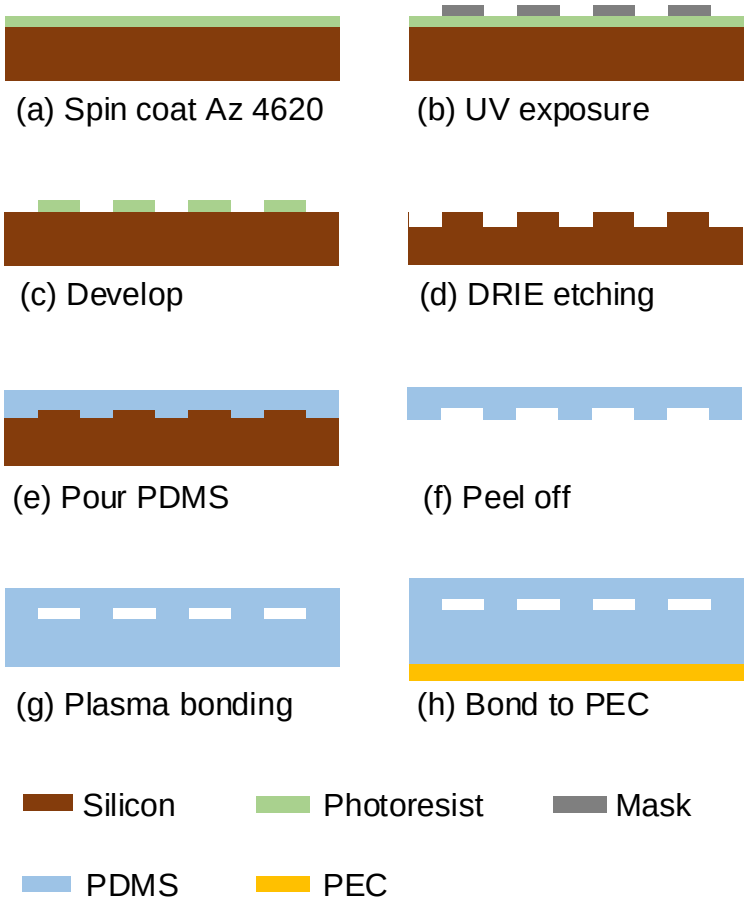

Figure 3.11 Fabrication processes of water-resonator-based metasurface. (a) Spin coating the photoresist AZ4620 on an 8-inch silicon substrate. (b) UV exposure under a patterned plastic mask. (c) Mask pattern is transferred in the photoresist after developing. (d) A silicon mould with desired pattern is obtained through DRIE etching. (e) PDMS with the weight proportion 11:1 (PDMS base: curing agent) is poured on the silicon mould. (f) Peel off the PDMS from silicon substrate. (g) Patterned PDMS layer is plasma bonded to a plane PDMS layer to form the microfluidic channel. (h) PDMS sample is bonded to the metallic layer.

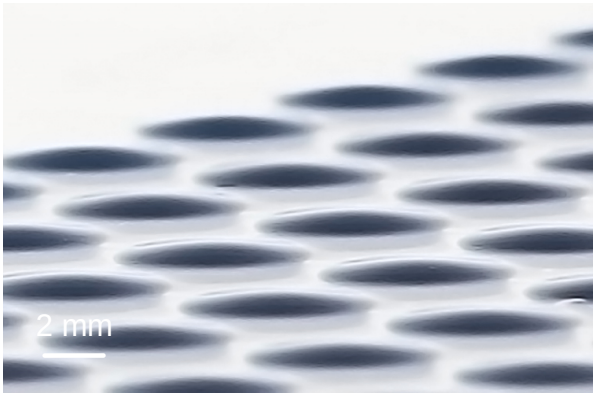

(a)

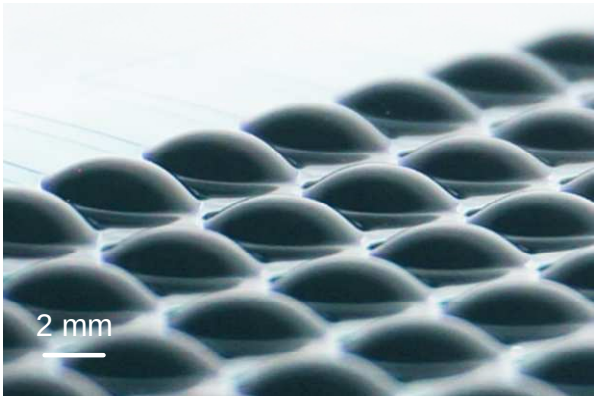

(b)

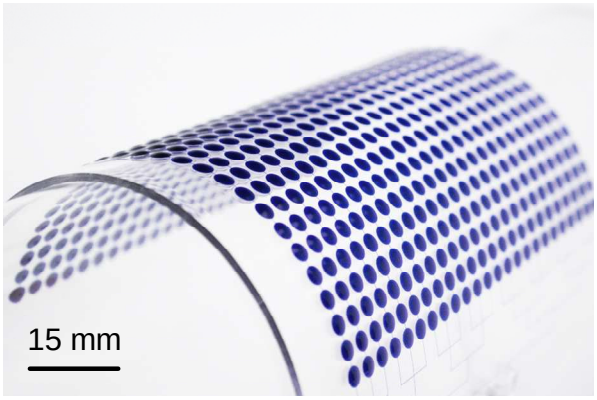

(c)

Figure 3.12 Photographs of water-resonator-based metasurface. (a) Water is injected into the PDMS with height of h = 0.4 mm. (b) Height of water-resonator is increased to h = 1.6 mm by increasing the water volume. (c) The metasurface is bent to any arbitrary curvature.

3.2.2 Experimental Setup for Microwave Measurements

The measurement of the water-resonator-based metasurface is carried out in the anechoic chamber room as shown in Fig. 3.13a. Two horn antennas are connected to a vector network analyzer (VNA, Agilent N4693A) as the microwave source and receiver, which is placed 1.2 m away from the sample in order to characterize the far-field reflection properties. Since few horn antennas can cover such wide frequency range from 5 GHz to 40 GHz, two sets of wideband double-ridged horn antennas are utilized from 5 – 18 GHz to 18 – 40 GHz as shown in Fig. 3.13(b,c).

The measurement setup of the water-resonator-based metasurface is schematically presented in Fig. 3.14. For planar metasurface measurement, the setup is shown in Fig. 3.14a. The source antenna (tinted in red) can move along the left arc with an incident angle of φ_i. On the other hand, the receiver (tinted in green) can move along the right arc with a reflective angle of $\varphi_r = \varphi_i$. For curved metasurface measurement, the setup is shown in Fig. 3.14b. The source antenna is fixed at the incident angle of 0° in a holder. The incident wave is assumed as plane wave. The receiver direction $\varphi_r' = \varphi_i'$. The contact point of the source antenna extension line and the sample is represented as A, while the contact point of the receiver extension line and the sample is represented as B_n. The arc length of AB_n is defined as S_n. In the measurement, the position of B_n is chosen as $S_n = 10n$ mm ($n = 0, 1, 2 \cdots 6$).

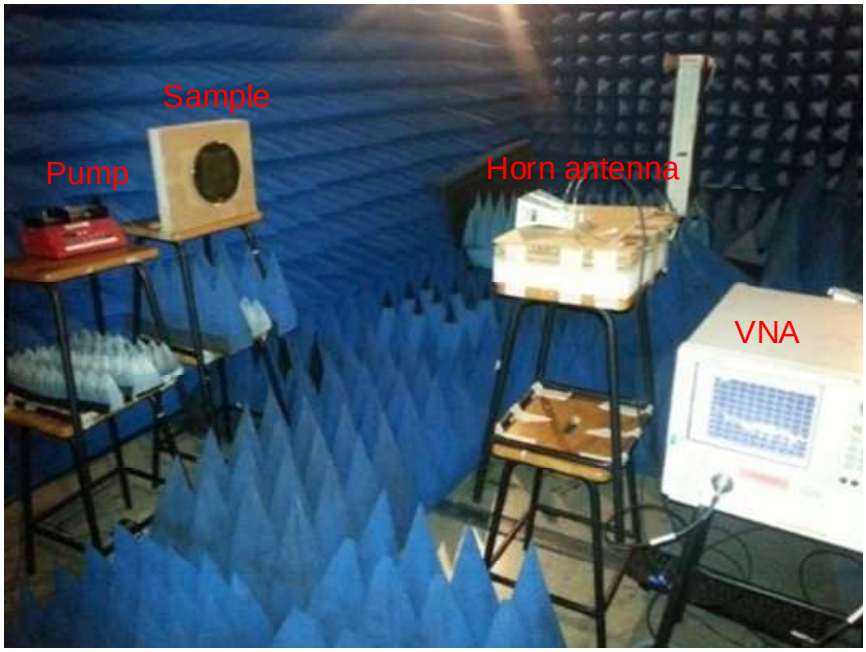

(a)

(b)

(c)

Figure 3.13 (a) Microwave measurement in the anechoic chamber room. The horn antennas are connected to the VNA and placed 1.2 m away from the sample in order to characterize the far-field reflection properties. The measurement consists of two parts, (b) one from 5 – 18 GHz and (c) the other from 18 – 40 GHz.

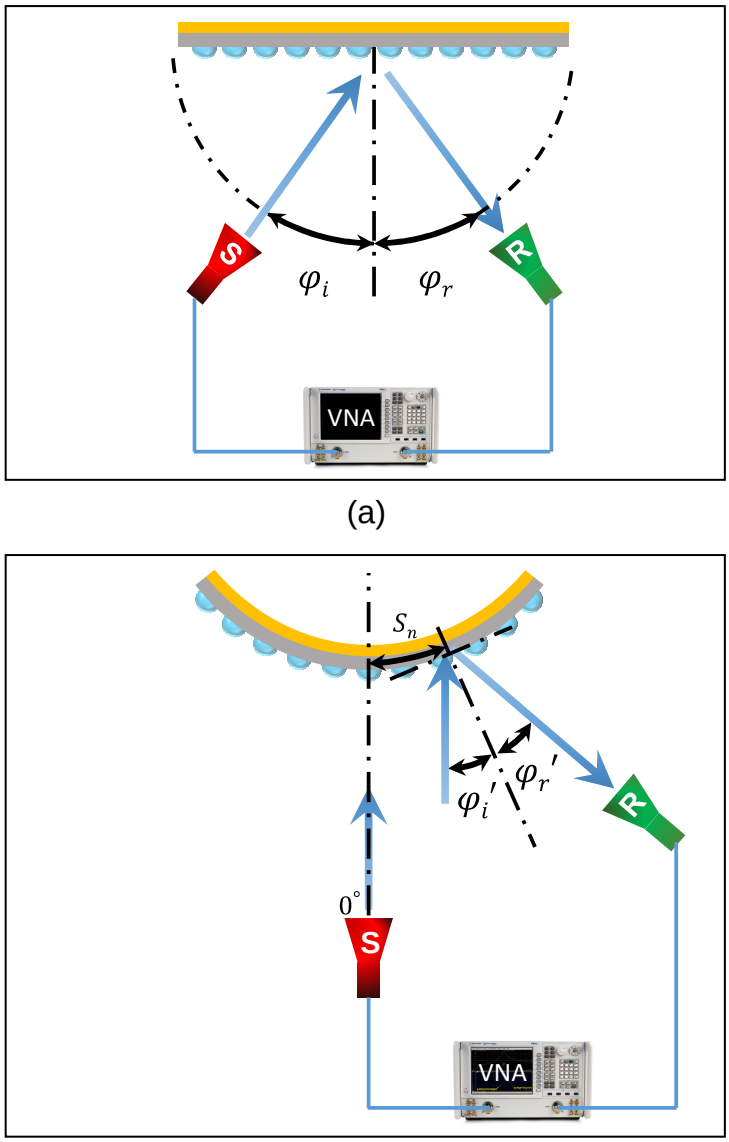

Figure 3.14 Experimental setup for the far-field measurement. (a) Measurement setup for planar metasurface. Two dual-polarized quadruple-ridged horns serves as the source (tinted in red) and receiver (tinted in green), respectively. The source and receiver can move along the arc to examine different incident and reflect angle. (b) Measurement setup for curved metasurface. The source is fixed at the incident angle of 0°in a holder, while the receiver direction $\varphi_r' = \varphi_i'$.

3.3 Experimental Results and Discussions

3.3.1 Ultra-Broadband Absorption

The absorption properties of the water-resonator-based metasurface are first investigated by changing the height of the water resonators. The absorption peak at the lower frequency shows a red shift from K band (20 GHz) to Ku band (15 GHz) when the height of the water-resonator is increased from 0.4 mm to 1.2 mm as shown in Fig. 3.15, because the effective length of the magnetic resonance is increased. On the other hand, the absorption peak at the higher frequency is not shifted because it is caused by grating effect from the periodic resonator array. As a result, the bandwidth of absorption is tuned by both magnetic resonance and grating effect when the water-resonator height is changed. The tunable broadband absorption is simulated and experimentally demonstrated as shown in Fig. 3.15a and b, respectively, which realizes a maximum absorption of 99%. When the height of the water-resonator is 0.4 mm, the absorption bandwidth of the central frequency is 78.5% and 78.9% with over 90% absorption in the simulation and experimental results, respectively. The mismatch of the bandwidth is less than 2% between the experimental and simulation results, which is mainly induced by the fabrication error. Each water-resonator are not uniform due to the inhomogeneous pressure in the water reservoir. These non-monodispersed water-resonators affect the bandwidth of the absorption.

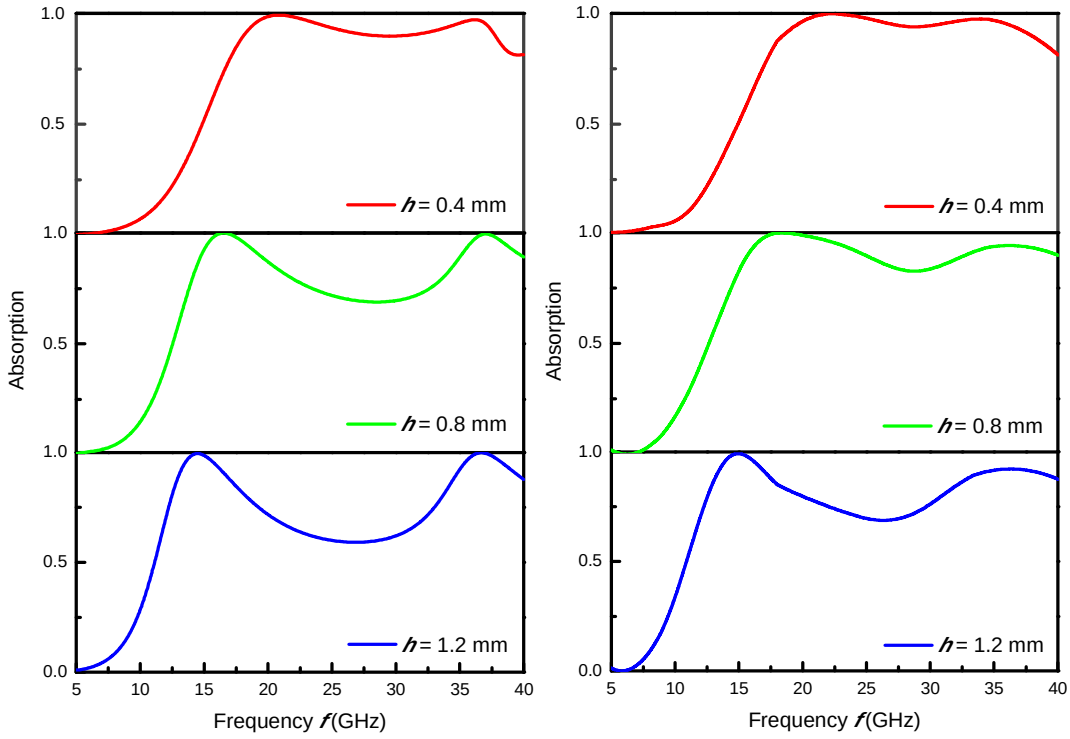

Figure 3.15 Absorption spectra with different heights of water-resonators under normal incidence. (a) Simulation and (b) experimental results of the absorption spectrum when the height of the water-resonator is changed from 0.4 mm to 0.8 mm and 1.2 mm.

To demonstrate that the microwave is indeed absorbed by the water-resonator-based metasurface but not scattered to other directions, experimental setup for different reflected angles measurement is established as shown in Fig. 3.16. The source antenna is fixed at the incident angle of 0° and the receiver can move along the arc to examine the reflection at different angles. A bare aluminum metal plate

is measured as a reference as shown in Fig. 3.17a. A significant scattering is observed from the plate at reflection angle up to 15^0. When the metallic plate is covered by the water-resonator-based metasurface, the scattering of the microwave is suppressed to near zero at all reflection angles as shown in Fig. 3.17b.

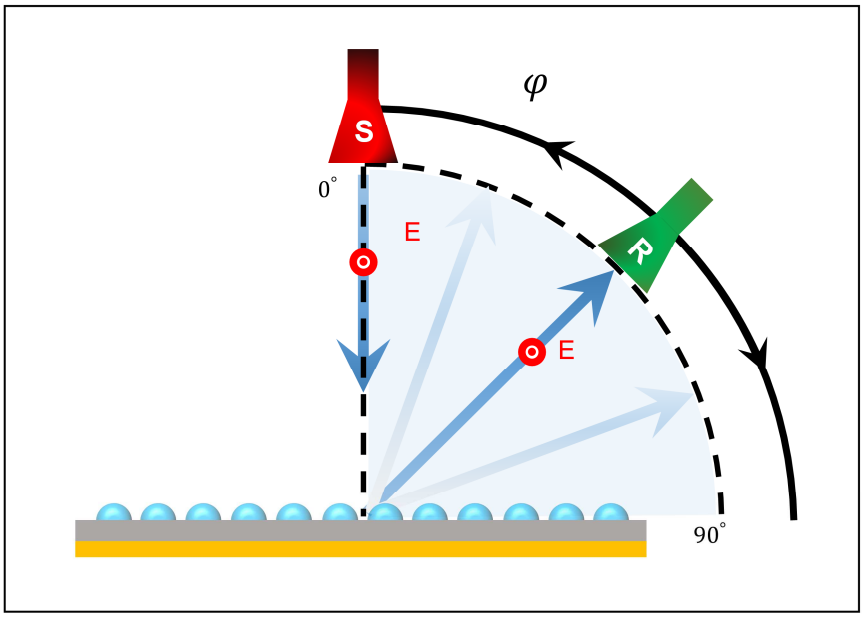

Figure 3.16 Measurement setup for angular reflection of metasurface. Microwave is normally incident on the metasurface and reflection at different angles is measured.

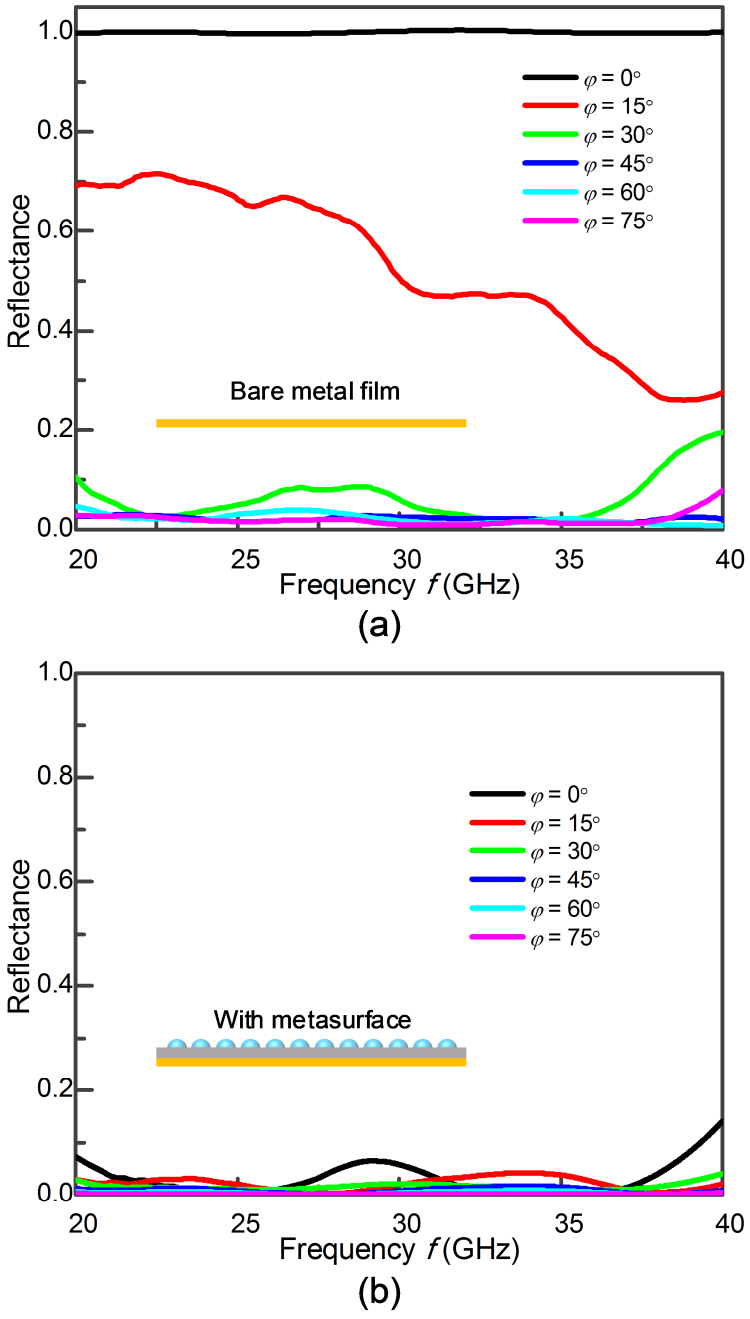

Figure 3.17 (a) Reflection from a bare Al metal plate is measured as a reference. A significant scattering is observed from the plate at reflection angle up to 15°. (b) No scattering wave is observed when the metallic is covered with the water-resonator based metasurface at all reflection angles.

3.3.2 Wide-Angle Absorption

The water-resonator-based metasurface is also demonstrated to realize a wide incident angle absorption in a broad bandwidth. Fig. 3.18 shows the measured absorption spectra of the metasurface under both TE and TM polarization incidence while the height of the water resonator keeps at 0.4 mm. The absorption bandwidth keeps at about 66.7% related to the central frequency with the absorption level higher than 80%. With the presence of the water channels, the absorption is slightly different for TE and TM mode in normal incidence at high frequency due to the polarization dependence of magnetic resonance and grating effect, which is consistent with the simulation results as shown in Fig. 3.19. The large incident angle broadband absorption of water-resonator-based metasurface could promises an omnidirectional broadband absorption on arbitrary curved surfaces.

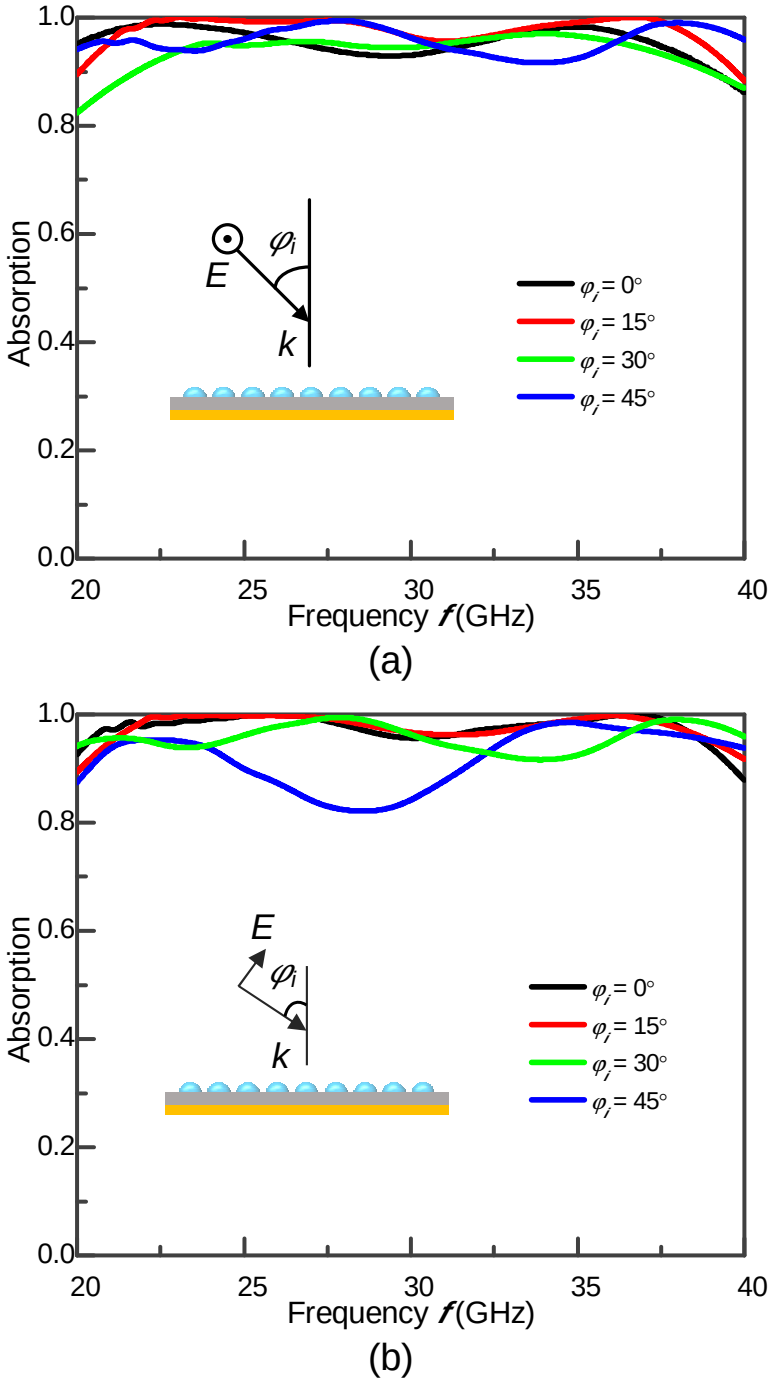

Figure 3.18 A broadband absorbing material with wide incident angle. Measured absorption spectra with (a) TE mode and (b) TM mode, respectively, by changing the incident angle from 0° to 45°. Height of the water-resonator is 0.4 mm.

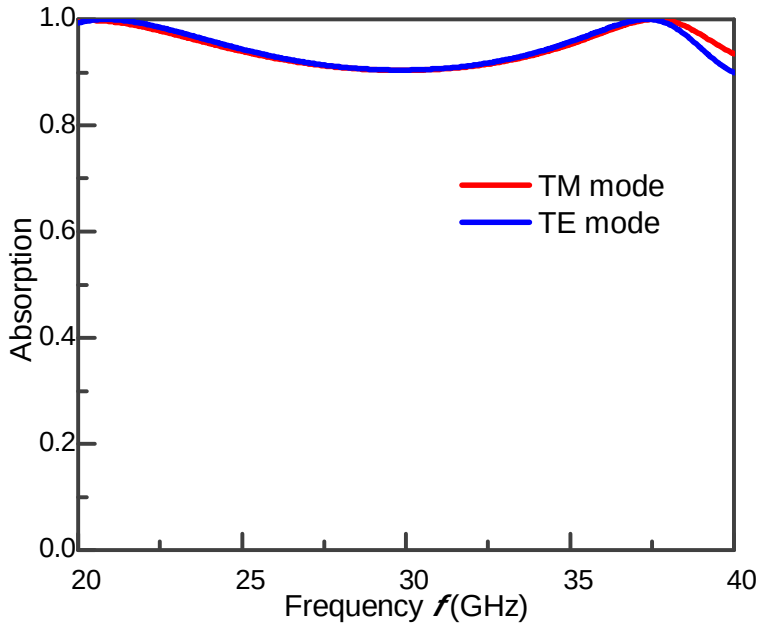

Figure 3.19 Simulation results of the absorption spectra with TE and TM mode in normal incidence when the height of water resonators is 0.4 mm. Blue line and red line represent the absorption spectra for TM and TE mode, respectively. The existence of the water micro channels slightly affects the absorption spectra due to the polarization dependence of magnetic resonance and grating effect.

3.3.3 Omnidirectional Absorption on Curved Surfaces

When a curved surface is illuminated by a plane wave, the reflective wave will scatter into different directions. Due to the large-angle absorption and high flexibility of soft water-resonator-based metasurface, an omnidirectional absorbing material is presented when the water-resonator-based metasurface is bent. Both the

specular reflective wave and the abnormal scattering wave are suppressed under normal illumination. Here, omnidirectional absorption means no reflection and scattering is observed in all directions when the microwave is normally incident on the metasurface. The omnidirectional broadband absorption of the curved metasurface absorption functional material is characterized and compared with the absorption of a bare metal curved surface with the same curvature. Fig. 3.20a shows the reflection spectra of a bare metal curved surface with a small curvature of R = 200 mm and s = 130 mm. High reflectance is detected at all directions from φ = 0º to φ = 75º (each step size of 15º), where φ is the azimuth angle of the detector position. When the metal curved surface is covered by the water-resonator-based metasurface (h = 0.4 mm), the reflection to all directions is significantly suppressed to almost zero from 20 to 40 GHz as shown in Fig. 3.20b. Similar results are observed when the metal curved surface is bent to a larger curvature of R = 100 mm. The reflectance (Fig. 3.21a) from φ = 0º to φ = 75º is suppressed to negligible level with the cover of water-resonator-based metasurface as shown in Fig. 3.21b. As a result, an omnidirectional and ultra-broadband absorption functional material on curved surfaces is achieved with a bandwidth of 66.7% from 20 GHz to 40 GHz.

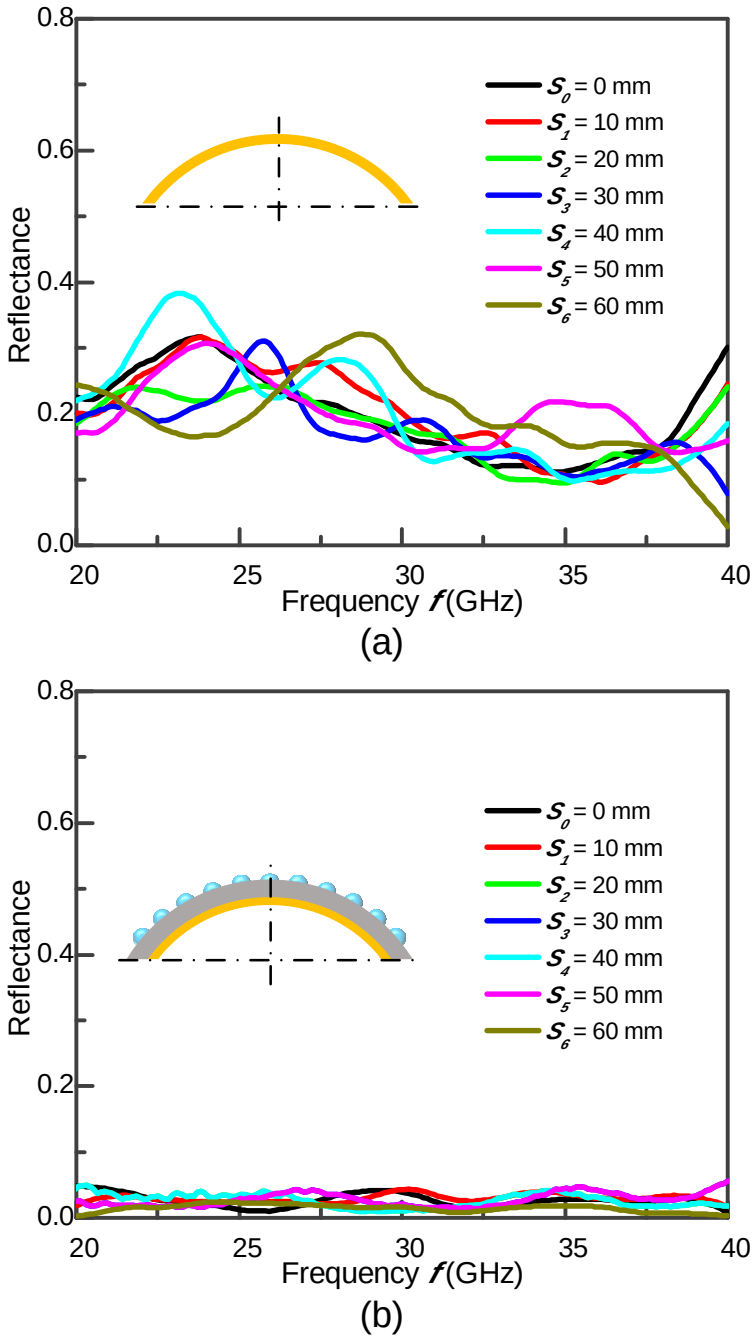

Figure 3.20 An omnidirectional broadband absorbing material on curved surface. (a) Reflectance spectrum at different reflective positions (see Figure S7) of a bare metal curved surface and (b) the curved water-resonator-based metasurface when the curvature is small (R = 200 mm), respectively.

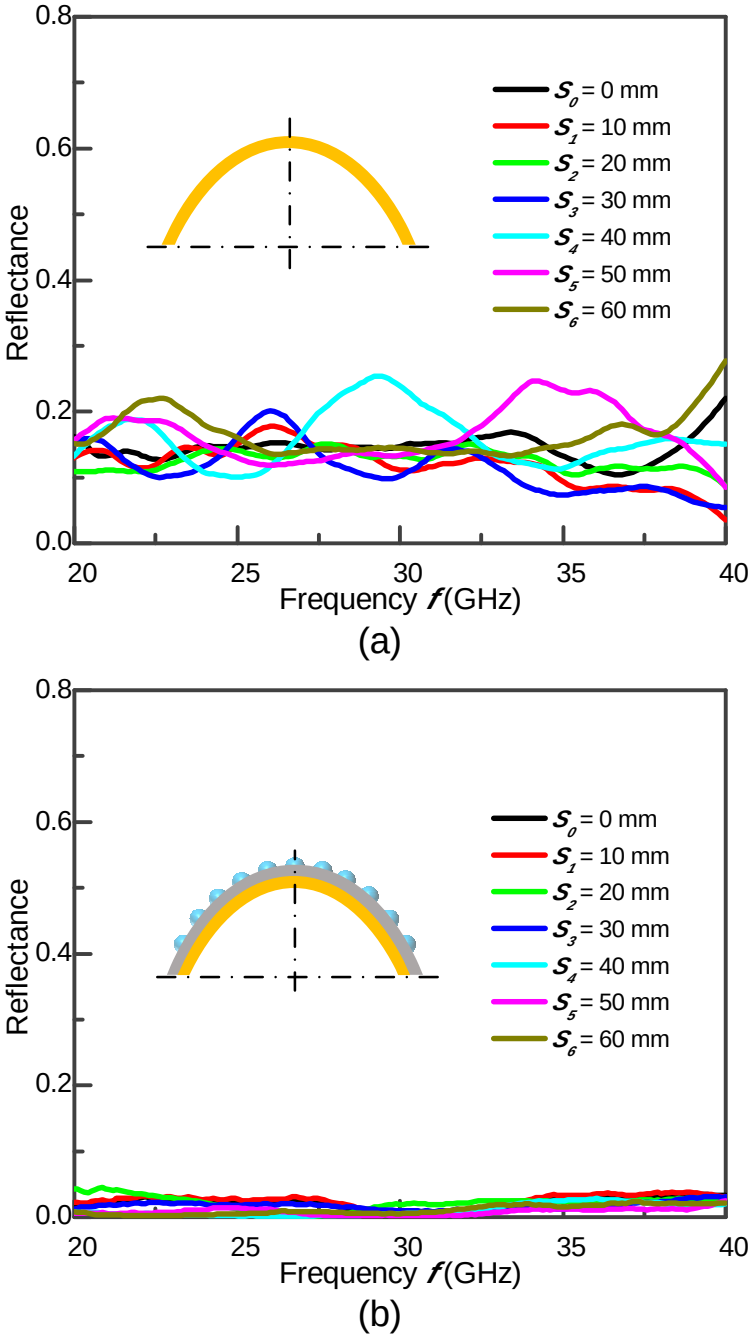

Figure 3.21 An omnidirectional broadband absorbing material on large curvature of curved surface. (a) Reflectance spectrum at different reflective angles of a bare metal curved surface and (b) the curved water-resonator-based metasurface when the curvature is increased (R = 100 mm), respectively.

3.3.4 Broadband Tunable Absorption

The water-resonator-based metasurface can be injected by the ethanol solutions with different concentrations to change the absorptivity. Fig. 3.22 shows the experimental results of the absorption spectra with different concentrations of ethanol solutions, respectively. As expected, the absorption level decreases from about 90% to below 20% in the entire measured frequency regime, when the ethanol concentration in the solution is increased from 0% (pure water) to 100% (pure ethanol). As a result, the absorptivity of the water-resonator-based metasurface can be continuously controlled by simply injecting ethanol solution with the corresponding concentration.

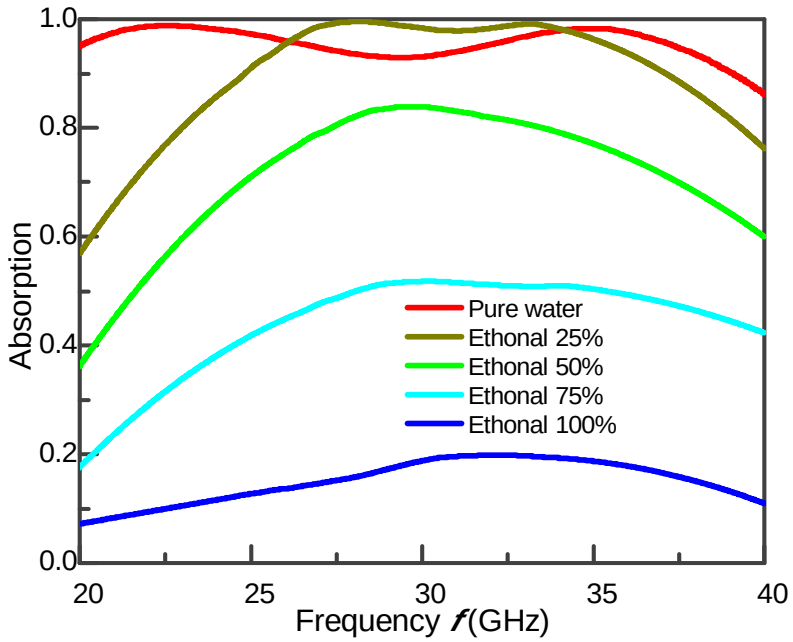

Figure 3.22 Experimental results of broadband intensity modulation with different concentrations of ethanol solution from 0% (pure water) to 100% (pure ethanol). Height of the water-resonator is 0.4 mm.

3.4 Summary

This chapter focuses on the structure design, theoretical analysis, sample fabrication and experiments of an ultra-broadband and near-unity absorption by water-resonator-based metasurface. The theoretical analysis explores the impedance matching to the free space at the water-air interface, which guides the design of the water-resonator array. The water-resonator-based metasurface induces a strong magnetic resonance, which incorporates with the grating effect, to achieve the impedance matching to free space in broad bandwidth across the entire Ku, K and Ka bands. In addition, the fabrication processes for microfluidic metasurface are developed for the liquid injection and deformation in a large tuning range using polymer PDMS material. Experiments show that the developed water-resonator-based metasurface has a bandwidth of central frequency that reaches 78.9% with higher than 90% absorption under normal incident microwave. The high absorption and large bandwidth are also preserved with oblique incidence from 0º to 45º. In addition, an omnidirectional and broadband absorbing material is realized by the curved soft metasurface. Finally, a broadband intensity modulation is demonstrated by injecting different concentrations of ethanol solution.

The innovation of the water-resonator-based metasurface is summarized as follows,

(a) This is the first demonstration of the combination of the magnetic resonance and grating effect to realize an ultra-broadband and near-unity

absorption by using dielectric material, liquid water, embedded into the soft material, PDMS, across the entire Ku, K and Ka bands. Compared to other materials, liquid water not only provides high lossy properties which is essential to the absorption, but also has high flexibility in the control of the shape of the structure.

(b) A real time control on the broadband absorption, including the absorption frequency and absorption strength, is firstly demonstrated by incorporating with the microfluidic technology. It has the capability to reshape the liquid-resonator by simply changing the volume of the liquid in the microfluidic reservoir created in the PDMS.

(c) A curved water-resonator-based metasurface is demonstrated due to the softness of water and PDMS, which functions as an omnidirectional and broadband absorbing material on arbitrary curved surfaces.

CHAPTER 4

LIQUID-METAL-BASED METASURFACE

This chapter presents the design, fabrication and experiment of the liquid-pillar-based metasurface for frequency-agile and wide-angle absorption in terahertz regime. The structure designs of the liquid-pillar-based metasurface are presented, which is using a liquid-metal-pillar array confined in the triple layer structure, PDMS/silicon/PDMS. Subsequently, theoretical analysis on the absorption induced by strong magnetic resonance is discussed. The combination of the PDMS and silicon to break the tuning limitation in 2D plane and realize a large tuning range of the metasurface is discussed. Next, the fabrication processes for the liquid-pillar-based metasurface are illustrated. Finally, the experimental results are presented and discussed, including a polarization-independent absorption due to the symmetric pattern of the liquid-metal-pillars, a frequency-agile absorption by tuning the heights of the liquid-metal-pillars and a wide-angle absorption in broad bandwidth by adjusting the liquid-metal-pillars height to compensate the frequency shift.

4.1 Design and Theoretical Analysis

Terahertz absorption material can be designed by metasurface using a dielectric layer sandwiched between a metallic structure layer and a metal ground layer, matching the impedance to the free space and blocking all of the transmissions, respectively. In general, the metasurface absorption materials usually rely on the electric and magnetic response of the top metallic structures, as well as the magnetic response induced by the inductive coupling between the metallic structures and the ground plane. The magnetic responses play an important role in the realization of impedance matching. However, the magnetic dipole moments induced by the top metallic structures are usually perpendicular to the incident magnetic field, which results in a week interaction in between. Vertical split-ring resonator is therefore developed to provide an alternative method to enhance the magnetic response by erecting the split-ring resonator up along the propagating direction [244, 245], resulting in a strong magnetic response between the incident magnetic field and the magnetic dipole induced by the split-ring resonator, which can be exploited to realize the impedance matching. In additional, it is desirable to have terahertz absorption materials with frequency-agile and wide-angle functionality. The metasurface incorporated with microfluidic technology provides a great opportunity to reconfigure the geometry of the structures, leading to a large tunability on the absorption frequency due to the high size dependence of the resonant frequency. The development of the microfluidic technology in microscale put the microfluidic metasurface in terahertz into practice as discussed in Chapter

2. Here, a liquid-metal-based metasurface is demonstrated by using microfluidic technology, which can be tuned in the vertical propagating direction for frequency-agile and wide-angle absorption.

4.1.1 Design of Liquid-Metal-Based Metasurface

The control method of the liquid-metal-based metasurface is shown in Fig. 4.1(a), which consists of three layers. A silicon layer with penetrated cavities is sandwiched by two PDMS layers. Liquid-metal is injected from the bottom PDMS layer through the microchannel and filled into each silicon cavities. The height of the liquid-metal-pillars can be controlled by the air pressure applied from the air inlet in the top PDMS layer, which breaks the tuning limitation in 2D plane and provides a broadband tuning range of the metasurface. By applying different air pressures, the liquid-metal-pillars height can be increased or decreased, resulting in a reversible process for flexibly reconfiguring the resonators. The adjacent liquid-metal-pillars form a U-shape resonator so as to induce magnetic dipoles that are parallel to the incident magnetic field, resulting in strong interaction in between.

The U-shape Resonator is a variant of previously demonstrated designs that exhibit a Lorentz-like resonant response described by an effective complex permittivity $\varepsilon(\omega) = \varepsilon' + i\varepsilon''$ and permeability $\mu(\omega) = \mu' + i\mu''$, where ε' and ε'' are the real and imaginary parts of permittivity, μ' and μ'' are the real and imaginary parts of permeability, respectively [246-248].

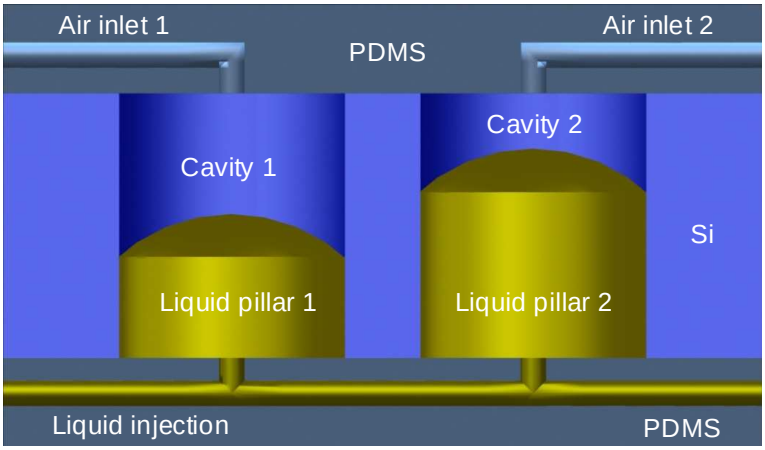

(a)

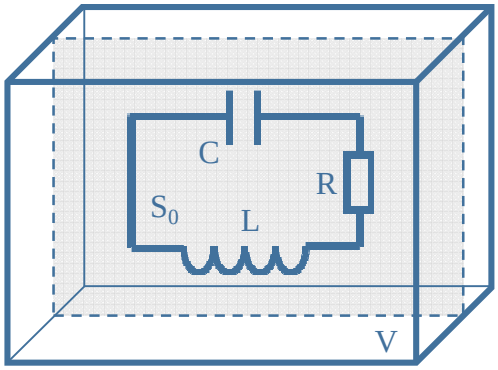

(b)

Figure 4.1 (a) Design of the liquid-metal-based metasurface consists of liquid-metal confined in the silicon cavities that can be tuned in the vertical direction by using microfluidic technology. Liquid-metal is injected from the bottom PDMS layer and filled into the silicon cavity. The height of the liquid-metal-pillar can be controlled by applying different air pressures from the air inlet in top PDMS layer. (b) Equivalent circuit model of U-shape resonator.

It can be described qualitatively in terms of its equivalent circuit as shown in Fig. 4.1(b). The gap between the adjacent two liquid-metal-pillars can be thought of as a capacitor, where the effective capacitance is denoted as *C*. Such two liquid-metal-pillars connecting with the bottom liquid reservoir form an inductive loop, where the effective inductance is denoted as *L*. The effective resistance is denoted as *R*. The resonant frequency of the U-shape resonator can be described as [249]

$$\omega = \frac{1}{2\pi\sqrt{\left(L + \mu_r S_0^2 / V\right)C}} \tag{4.1}$$

where μ_r is the permeability of the surrounding medium which is silicon in this paper. The area of U-shape resonator S_0 and the volume of a unit cell V is described as

$$S_0 = Gh, V = P^2 h \tag{4.2}$$

where G is the gap between two adjacent liquid-metal-pillars, h is the height of the liquid-metal-pillars, P is the periodic of the liquid-metal-based metasurface. Such that the resonant frequency of the U-shape resonator can be determined as

$$\omega = \frac{1}{2\pi\sqrt{\left(L + \mu_r Gh / P^2\right)C}} \tag{4.3}$$

By constructing the height of the liquid-metal-pillars, the corresponding equivalent capacitor and inductor will be changed, leading to a tunable frequency

of the U-shape resonator. For example, when the height of the liquid-metal-pillars h is increasing, the effective size of the capacitor is increasing, such that the effective capacitance C is increasing. Meanwhile, the cross section area of the inductive loop is also increasing, such that the effective inductance L is increasing. Therefore, the resonant frequency ω would shift to lower frequencies from Eq. 3 when h is increasing, and vice versa.

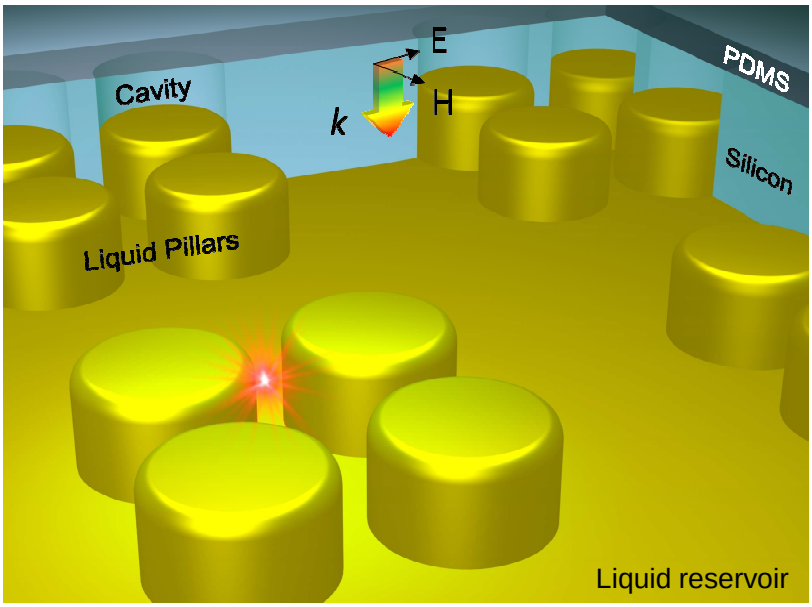

Figure 4.2 Schematic of tunable absorption material by using liquid-metal-based metasurface consisting of liquid-metal-pillar array embedded in silicon cavities.

Based on this control method and theoretical analysis, four liquid-metal-pillars are patterned into array in realization of a frequency-agile and wide-angle absorption as shown in Fig. 4.2. The U-shape resonators induce magnetic resonance, leading to strong confinement and absorption of the terahertz wave in

the metasurface. Furthermore, the absorption performance will not be deteriorated under oblique incidence, which promises the realization of a wide-angle absorption material. In order to achieve an identical tuning of the liquid-metal-pillars, the air inlet are connected with each other in the top PDMS layer, creating a uniform air pressure.

4.1.2 Absorption with Different Thickness

In the simulation, the liquid metal is mercury, which is modeled with high electrical conductivity σ = 1.04 × 10^6 S/m. Silicon is modeled as a loss free dielectric with real part of permittivity ε_{si}' = 11.9. PDMS is modeled as a lossy dielectric material [250]. The absorption of the metasurface can be derived by the scattering parameter (*S*-parameter) using microwave studio of CST (Computer Simulation Technology), i. e. $A = 1 - R - T = 1 - |S_{11}|^2 - |S_{21}|^2$.

In order to investigate the influence of the PDMS and silicon layer, we construct a four stacked layers, PDMS/silicon/mercury/PDMS, as shown in Fig. 4.3. The height of the mercury layer is h_3 = 50 μm, which will block all of the transmissions. The height of the bottom PDMS layer is h_4 = 1 mm. The simulation results of the absorption spectra with different height of silicon layer when the height of the top PDMS layer h_1 = 0 μm is shown in Fig. 4.4. When the height of the silicon layer is h_2 = 0 μm, the bare mercury film behaves as a metallic mirror, which reflects all the incident light, leading to a near zero absorption as shown in the red line. However, when the height of the silicon layer is increasing, a Fabry-

Perot cavity resonance is induced in the silicon layer, resulting in an absorption peak in the spectrum as shown in the green line and blue line. In the following design, the height of silicon layer is chosen as h_2 = 100 μm.

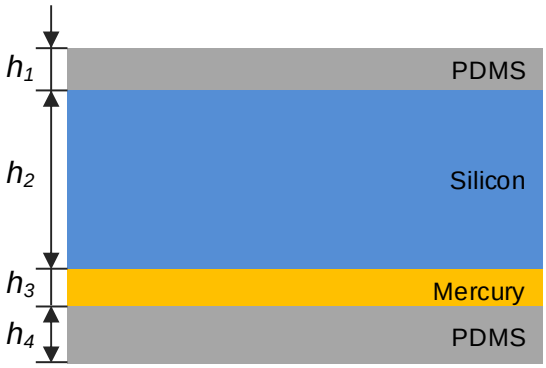

Figure 4.3 Layout of PDMS/silicon/mercury/PDMS film without pattern. The height of the mercury layer is h_3 = 50 μm; the height of the bottom PDMS layer is h_4 = 1 mm.

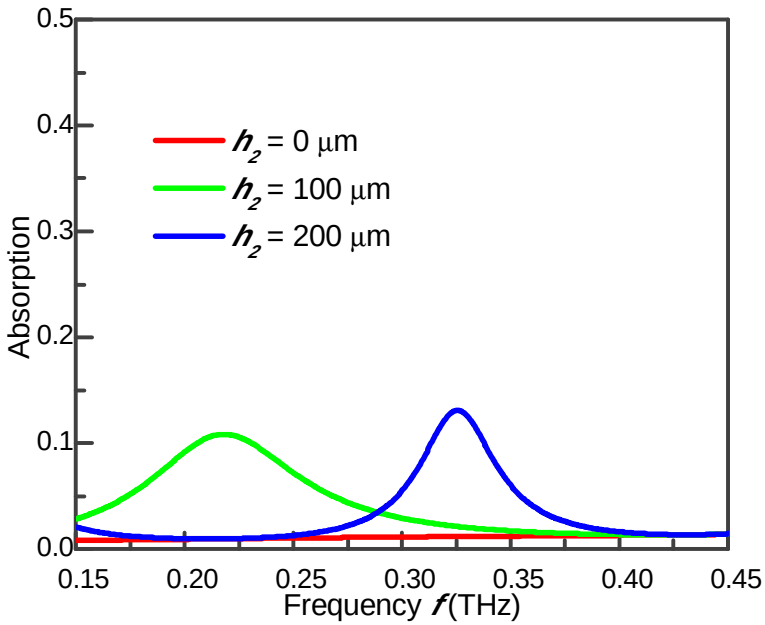

Figure 4.4 Simulation results of the absorption spectra with different height of silicon layer, when the height of the top PDMS layer is h_1 = 0 μm.

The influence of the top PDMS layer is similar to the silicon layer, which induces multi Fabry-Pérot cavity resonances as shown in Fig. 4.5. However, the absorption at the whole frequency window is increasing when the height of the PDMS is increasing due to the lossy property of the PDMS. Although absorption is the first priority in our design, the increasing height of the PDMS destroy the frequency selected absorption so as to make the absorption undistinguishable in the frequency domain. Since the ultimate goal of the liquid-metal-based metasurface is to design a frequency-agile absorption material by changing the height of the liquid-metal-pillars, it is desirable to suppress the influence of the PDMS to minimum. In contrast, the height of the top PDMS layer should be enough to support the control channels. As a trade-off, the top PDMS layer is designed as h_1 = 300 μm.

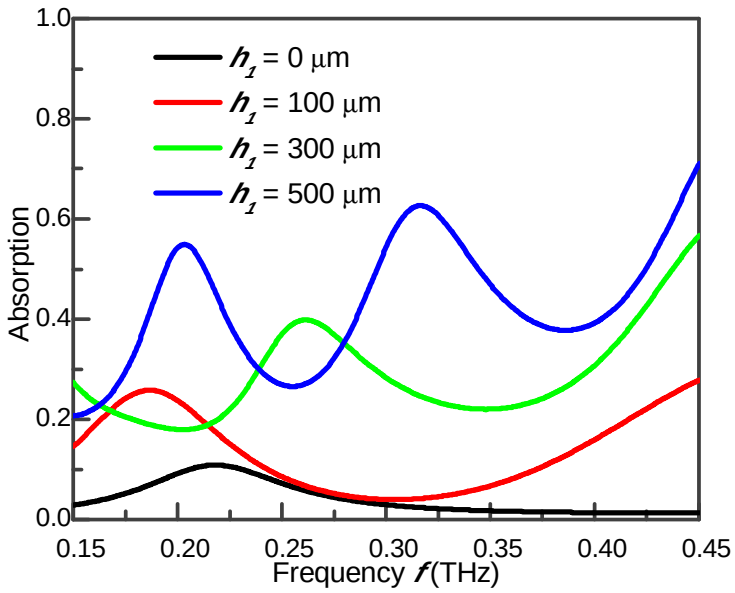

Figure 4.5 Simulation results of the absorption spectra with different height of the PDMS layer, when the height of the silicon layer is h_2 = 100 μm.

4.1.3 Theoretical Analysis and Numerical Simulation

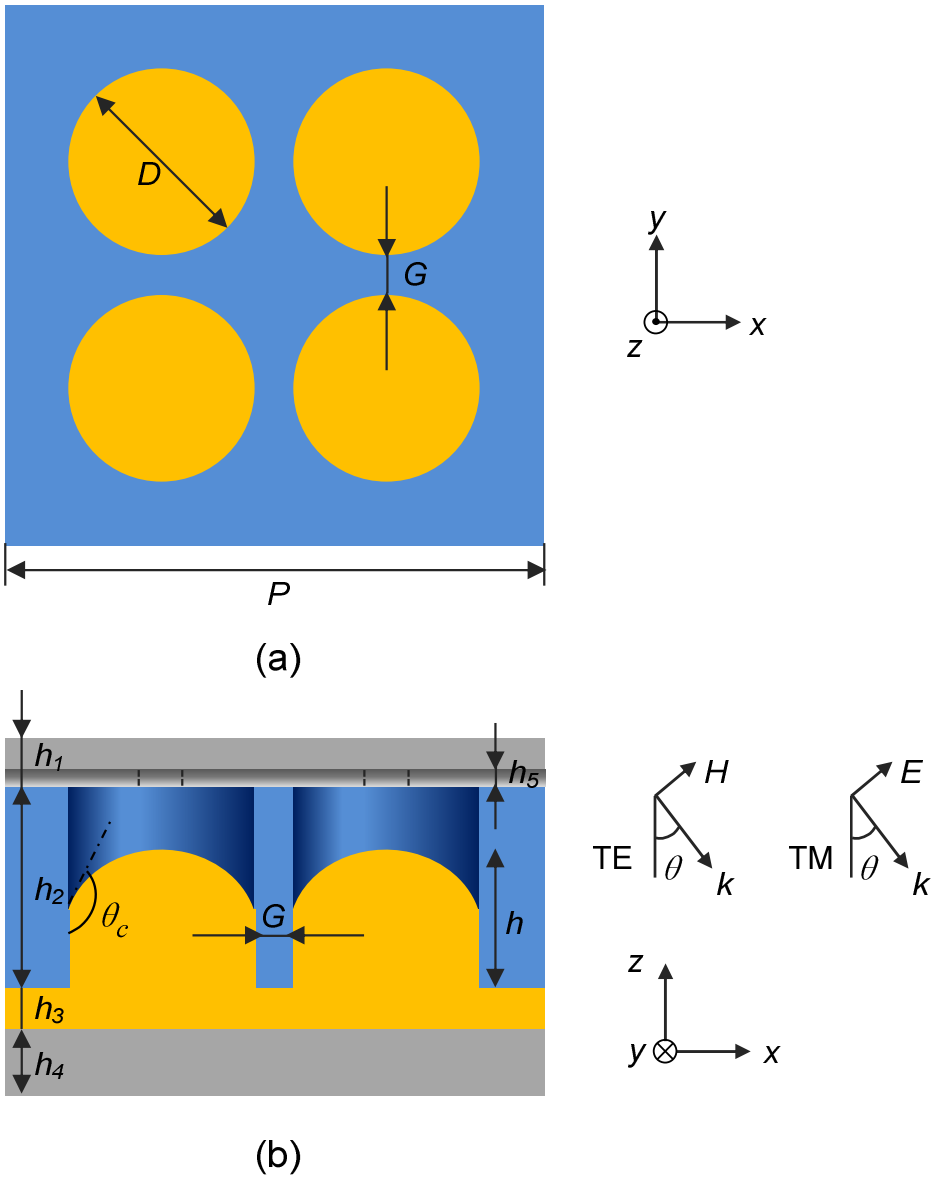

Figure 4.6 Layout for one single element with four liquid-metal-pillars. (a) The top view and (b) side view of one single element with the height of the liquid-metal-pillars h that can be controlled by applying different air pressure from the top PDMS channels.

The layout for one single element with four liquid-metal-pillars is shown in Fig. 4.6. The period of the liquid-metal-based metasurface is P = 300 μm; the diameter of the silicon cavity (and liquid-metal-pillars) is D = 100 μm; as discussed in the last section, the height of the top PDMS layer and silicon layer is designed as h_1 = 300 μm and h_2 = 100 μm, respectively; the height of the liquid reservoir is h_3 = 50 μm; the height of the bottom PDMS layer is h_4 = 1 mm; the height of the top PDMS channels is h_5 = 50 μm; the contact angle of the mercury in the silicon cavity is θ_c = 141°. The gap between the silicon cavity (and liquid-metal-pillars) is denoted as G = 30 μm.

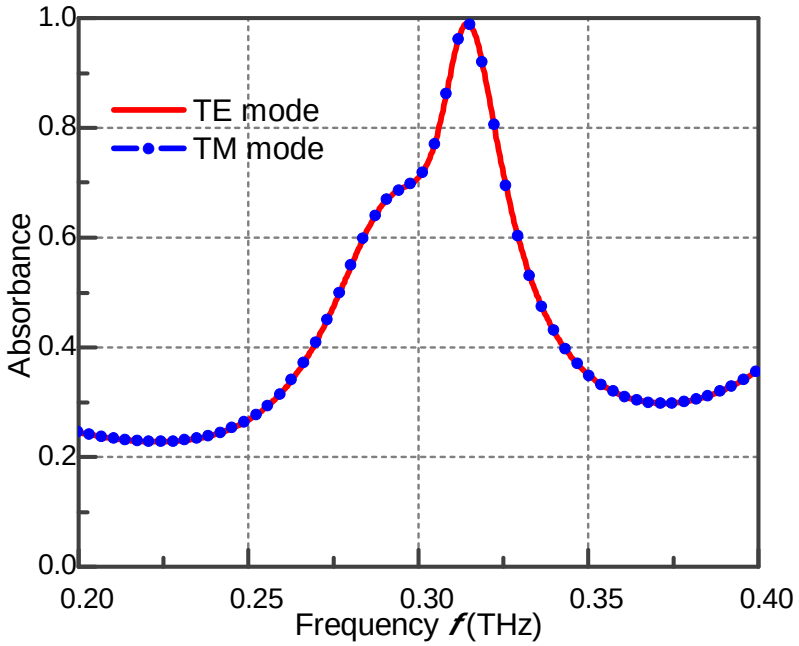

Figure 4.7 Simulation results of the absorption spectra with TE mode (red line) and TM mode (blue dot) when the heights of the liquid-metal-pillars are h = 70 μm.

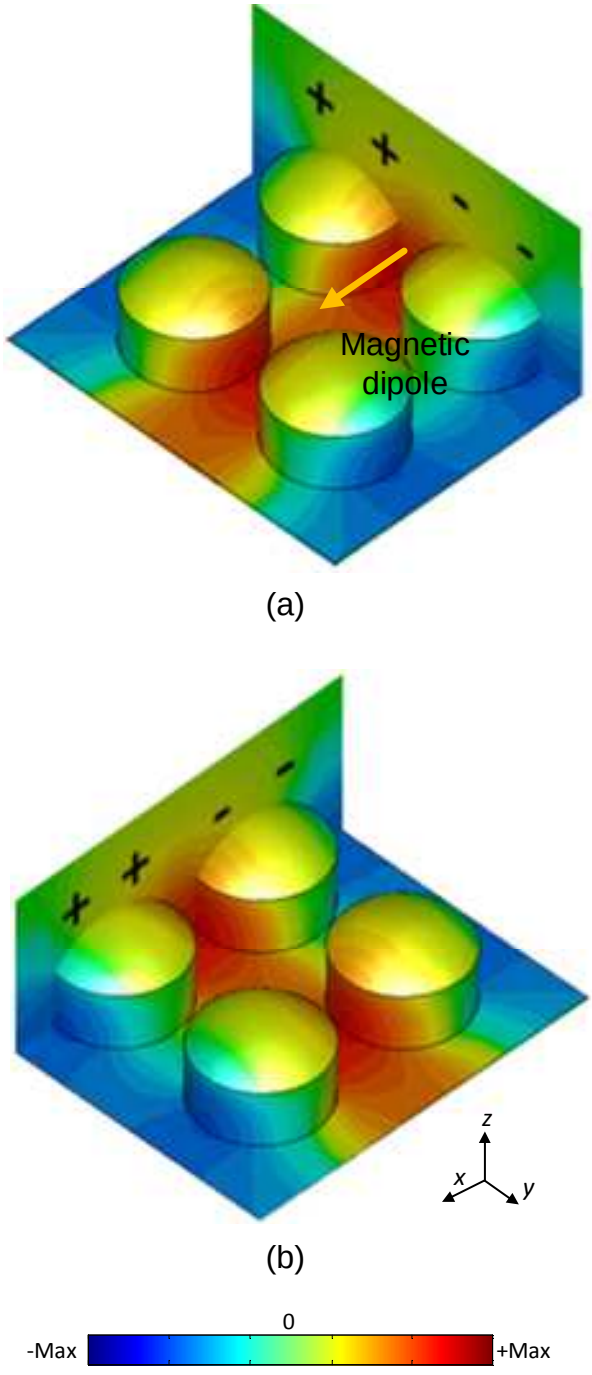

Figure 4.8 (a) Magnetic field distribution at the peak frequency (0.32 THz) with TE mode. (b) Magnetic field distribution at the peak frequency (0.32 THz) with TM mode.

The polarization-independent feature under normal incidence is numerically calculated in Fig. 4.7, when the height of the liquid-metal-pillars is 70 µm. The symmetric structural design with four identical liquid-metal-pillars in an element enables the polarization-independent characteristics of the absorption. The absorption spectra are completely overlapped with TE and TM mode incidence (See definition in Fig. 4.3). An absorption peak is induced at 0.32 THz with near-unity absorption of 99%. This absorption peak is attributed to the induced magnetic resonance mode, which can be examined by the magnetic field distribution in Figs. 4.8a and b with TE and TM mode incidence, respectively. Different charges are accumulated at the surface of the adjacent liquid-metal-pillars and an LC resonance is formed in the gap. The current loop is induced in the U-shape resonator, which is responsible for the strong enhancement of the magnetic field in the gap, and for the creation of a magnetic resonance. The direction of the induced magnetic dipole is parallel to the incident magnetic field, leading to a strong coupling in between. Since the U-shape resonators are patterned into four-pillar array periodically, the adjacent U-shape resonators couple with each other and induce another magnetic resonance at the side of the elements as shown in Fig. 4.8a. In the absorption spectrum, another absorption peak is also observed at around 0.29 THz, which is induced by the Fabry-Pérot cavity as discussed in section 4.2.1.

In order to realize the dynamic control of the absorption frequency, the effective length of the magnetic plasmon resonance can be controlled by tuning the height of the liquid-metal-pillars. The increasing height of the liquid-metal-pillars results in a red shift of the magnetic resonance as shown in Fig. 4.9. When the

height of the liquid-metal-pillars is 40 μm, the corresponding effective length of the magnetic resonance is decreased as shown in Fig. 4.10a and thus, the absorption peak frequency is increased to 0.414 THz with absorption higher than 90%. When the height of the liquid-metal-pillars is changed to 90 μm, the effective length of the magnetic resonance is increased as shown in Fig. 4.10b, resulting in a decreased absorption peak frequency to 0.246 THz with absorption higher than 90%. The tuning range of the absorption peak frequency reaches 50.9% of the central frequency with absorption higher than 90%.

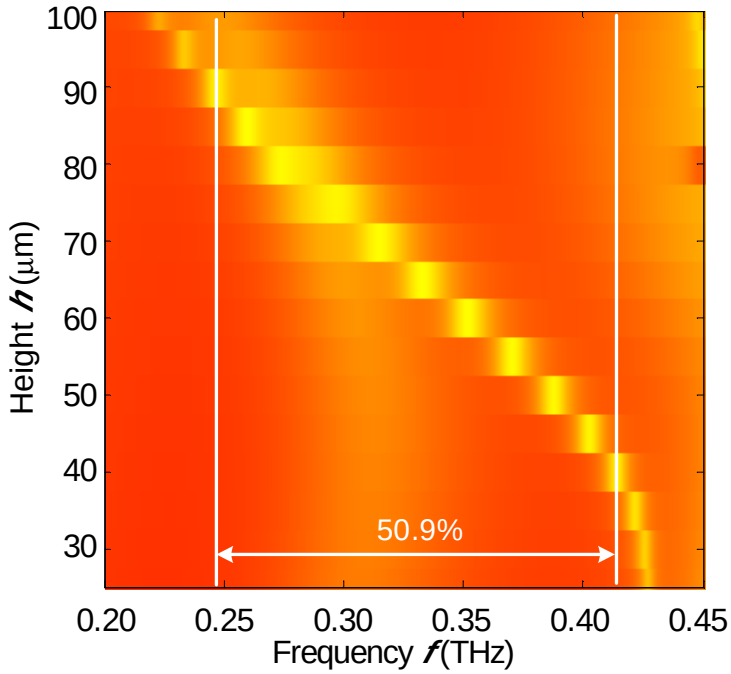

Figure 4.9. Simulation results of the absorption color map with TM mode when the height of the liquid-metal-pillars is tuned from h = 25 μm to h = 100 μm. A tunable absorption material by using the liquid-metal-based metasurface is achieved from 0.246 to 0.414 THz with a tuning range covers 50.9% of the central frequency.

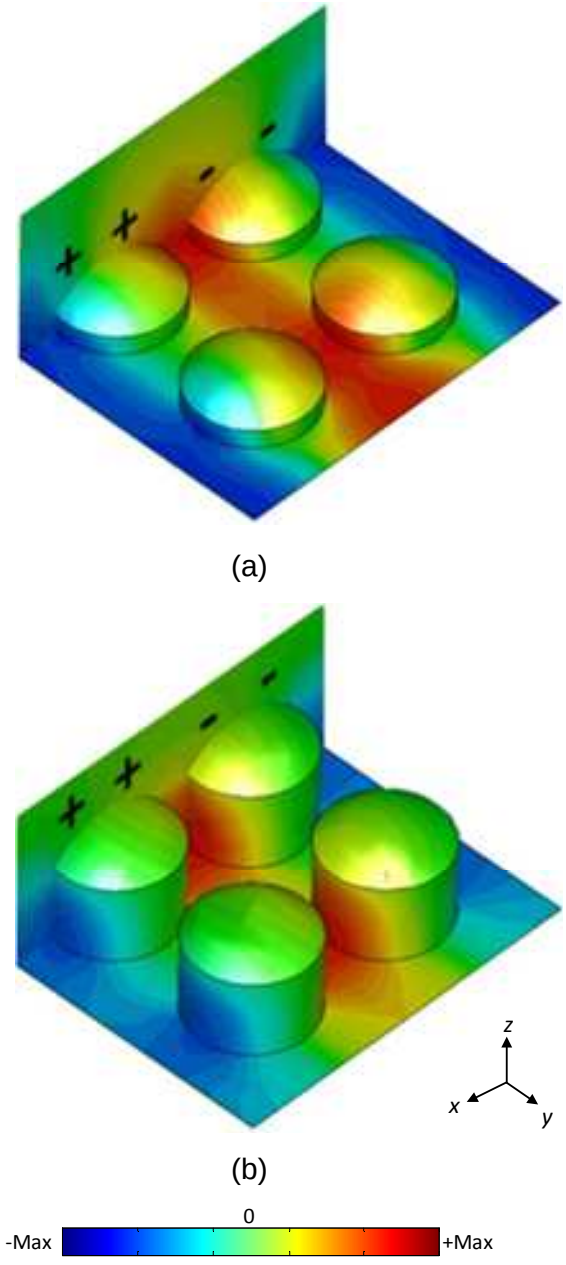

Figure 4.10 (a) Magnetic field distribution at peak frequency (0.414 THz) when the heights of the liquid-metal-pillars are 40 μm. (b) Magnetic field distribution at the peak frequency (0.246 THz) when the heights of the liquid-metal-pillars are 100 μm.

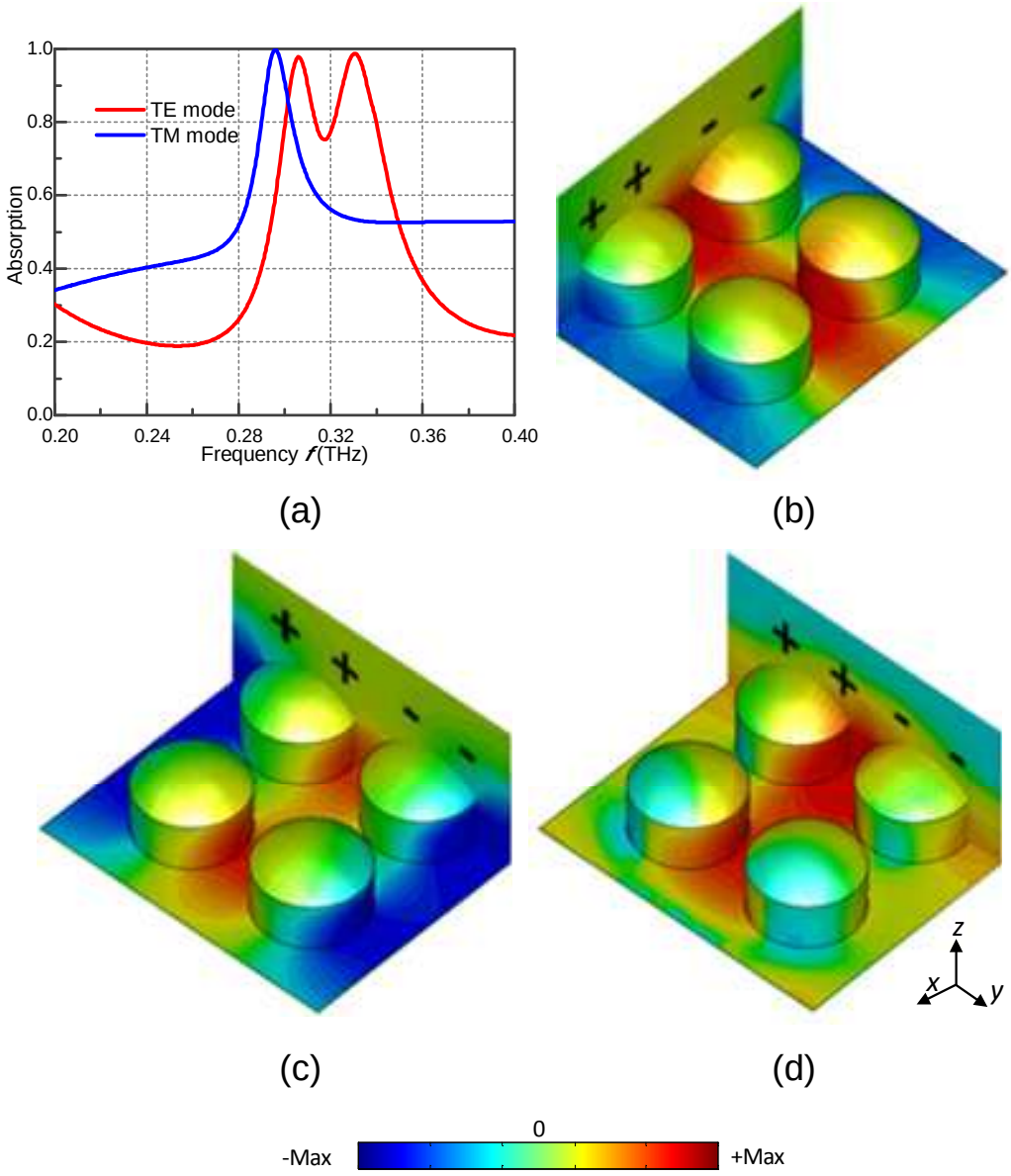

Figure 4.11 Simulation results of the absorption spectra with incident angle θ = 60° when the heights of the pillars keep at 72 μm. (a) Absorption spectra with TE and TM mode. (b) The magnetic field distribution at the absorption peak frequency with TM mode. (c) and (d) The magnetic field distribution at the first and second absorption peak frequency with TE mode, respectively.

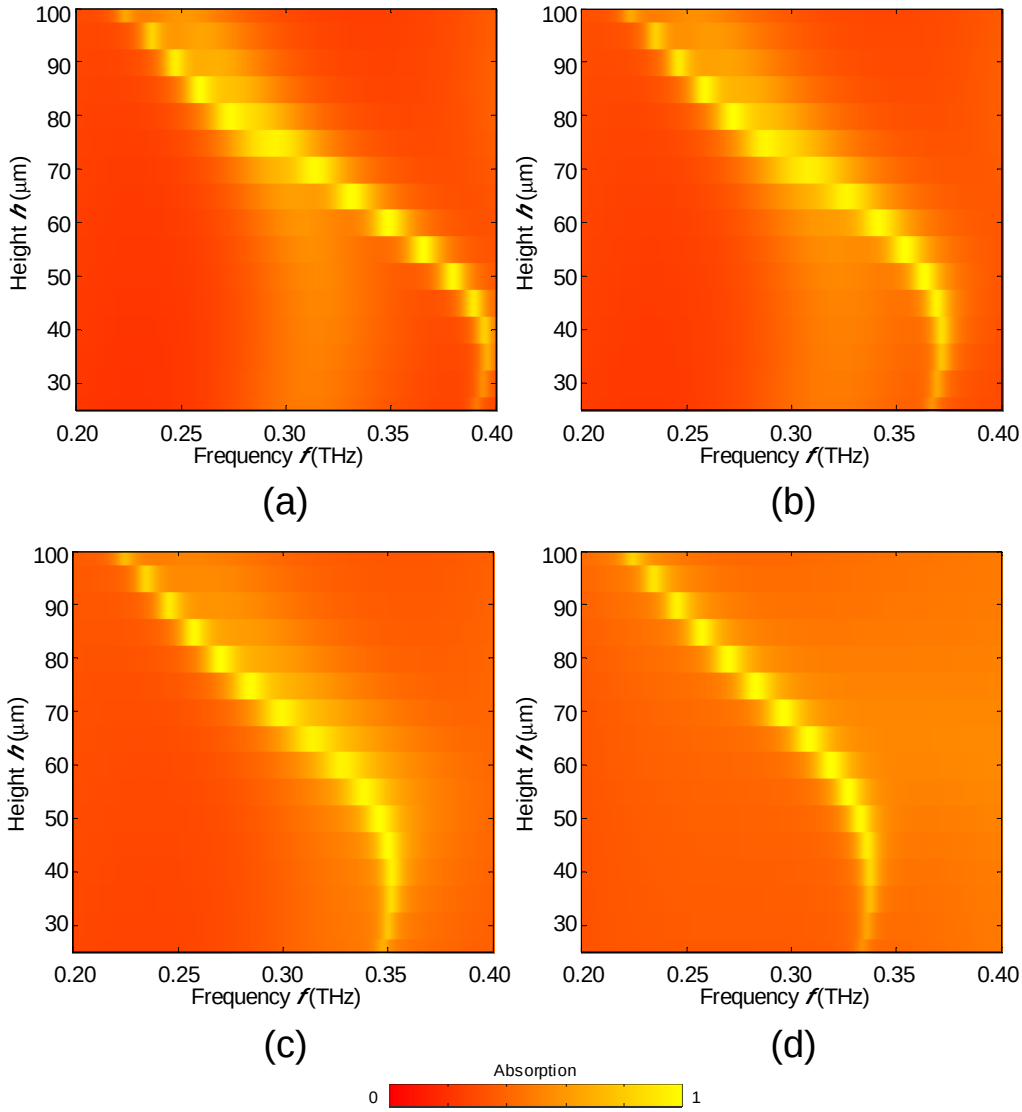

Figure 4.12 Simulation results of the absorption color map with TM mode when the heights of the liquid-metal-pillars are changed from 25 μm to 100 μm at the incident angle of (a) θ = 15°, (b) θ = 30°, (c) θ = 45° and (d) θ = 60°.

Here, we also investigate the electromagnetic response of the liquid-metal-based metasurface with oblique incidence. The simulation results of the absorption spectra with incident angle $\theta = 60°$ are shown in Fig. 4.11a. A magnetic resonance is induced with TM mode incidence as shown in Fig. 4.11b. The absorption peak maintains in a single band with 99% absorption as shown in Fig. 4.11a (blue line). However, a higher order of magnetic response occurs with TE mode incidence as shown in Fig. 4.11d, which induces another absorption peak as shown in the red line in Fig. 4.11a. In this paper, we focus on TM mode incidence with oblique incidence. When the incident angle is increasing from 0° to 60°, the tuning range of the absorption peak frequency covers 27.6% of the central frequency from 0.25 to

0.33 THz with absorption higher than 90% as shown in Fig. 4.12, which realizes a wide-angle absorption in broad bandwidth under TM mode incidence.

4.2 Fabrication and Experimental Setup

4.2.1 Fabrication Processes Development

The fabrication processes of the liquid-metal-based metasurface consist of two parts, including DRIE etching for silicon layer and soft lithography for PDMS layer as shown in Fig. 4.13. The fabrication processes for silicon layer are shown in Fig 4.13(a-f). The photoresist AZ 4620 is spin coated on the silicon wafer as shown in Fig 4.13a, following by prebaking to expel the excess photoresist solvent. The prebaked wafer is exposed under UV light with a patterned plastic mask as shown in Fig 4.13b. After developing to remove the exposed photoresist as shown in Fig 4.13c, the uncovered part of the silicon wafer is etched with a depth of 120 μm as shown in Fig 4.13d. The photoresist is removed by acetone as shown in Fig. 4.13e. A 100-μm thick silicon wafer is then fabricated by grinding process using Backgrinder machine as shown in Fig. 4.13f. The top and bottom PDMS layer is fabricated by soft photolithography as shown in Fig. 4.13(g-k). The photoresist SU-8 is a negtive photoresist, whereby the parts exposed to UV light become insoluble and can't be washed away during development. The remaining parts of the photoresist is highly cross-linked with high stability to chemicals and has good mechanical properties to avoid removing, which is suitble in the fabrication of mould for PDMS channels. After the SU-8 photoresist is applied to the silicon substrate as shown in Fig. 4.13g, it must be soft baked to evaporate the solvent and density the film on a level hot plate. SU-8 is virtually transparent and insensitive above the wavelength of 400nm but has high actinic absorption below 350nm.

Following UV light exposure with a plastic mask as shown in Fig. 4.13h, A post exposure bake is necessary to selectively cross-link the exposed portions of the photoresist, which becomes insoluble to the developer, while the unexposed portions is washed away. The SU-8 mould is then obtained by rinsing with IPA and dried with a gentle stream of air as shown in Fig. 4.13i. A hard bake is also applied to further cross link the photoresist on a hot plate. The next step is to fabricate the PDMS channel by using the SU-8 mould. The PDMS is prepared by mixing the base and curing agent with the weight proportion of 11:1. After putting in a vacuumizer to expel the suspended air, the PDMS is poured onto the SU-8 mould as shown in Fig. 4.13j and followed by baking it in a 75℃ oven for 2 hours. The pattern is then transferred to the PDMS by peeling off it from SU-8 mould as shown in Fig. 4.13k. Finally, the silicon layer is plasma bonded to the top and bottom PDMS layer as shown in Fig. 4.13l and 4.13m, respectively.

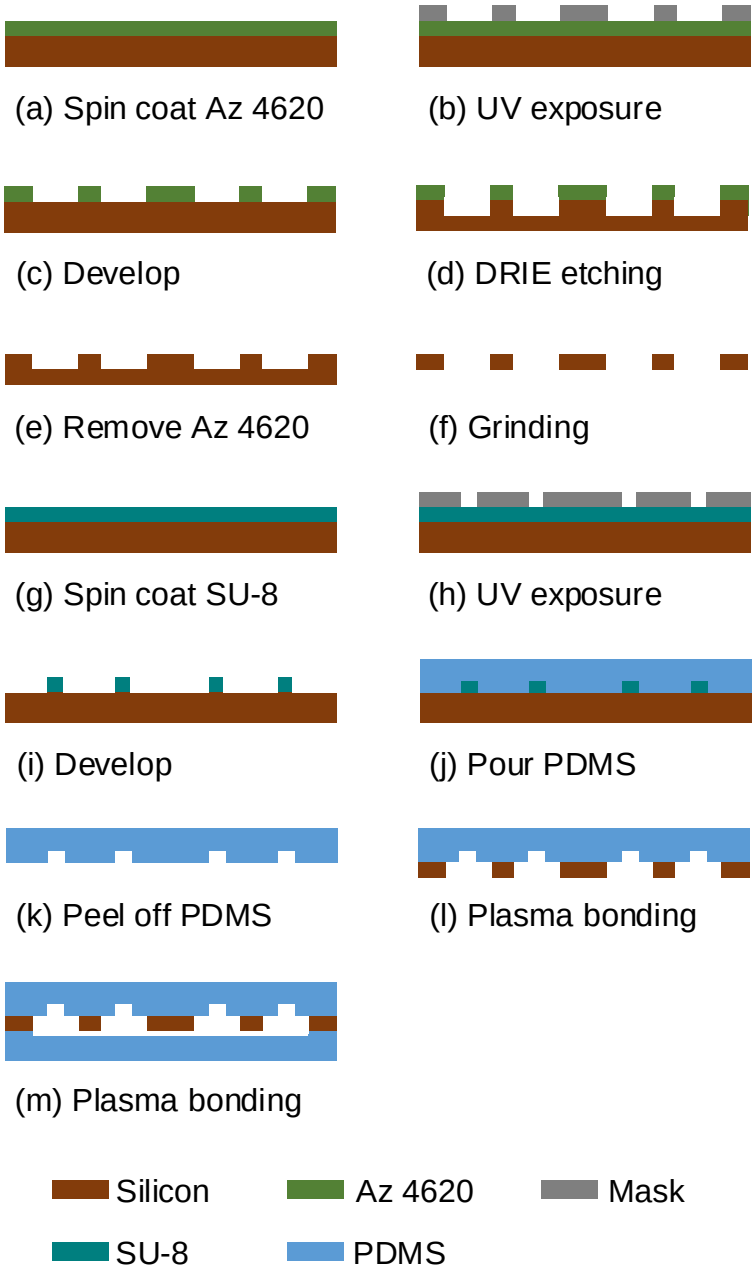

Figure 4.13. The fabrication processes of the liquid-metal-based metasurface. (a-f) Silicon layer is fabricated by DRIE etching. (g-k) Top and bottom PDMS layers are fabricated by soft lithography technology. (l,m) The liquid-metal-based metasurface is obtained by plasma bonding.

The photograph of fabricated metasurface is shown in Fig. 4.14. The liquid-metal-based metasurface consists of 70 × 70 elements with 300 μm period. The height of the liquid-metal-pillars are tuned by the volume of the air pumped out of the microfluidic channel, which is controlled by a syringe pump. The pumping speed from the syringe pump is approximately 3.6 mL/min. It takes about 10 ms to change the height of the liquid-metal-pillars from 0 to 100 μm and for them to stabilize. The capillary action of the liquid-metal-pillars in the silicon cavity is balancing the air pressure. The force due to surface tension $F_{ST} = \gamma\pi D\cos\theta_c$ = 113 μN (where γ = 0.465 N/m is the coefficient of surface tension, D and θ_c can refer to the definition in Fig. 4.6). The gravity of each liquid-metal-pillar is $G = \rho\pi D^2 hg$ = 0.1 μN (ρ = 13.6 g/cm^3 is the density of mercury, h = 100 μm is the maximum height of the liquid-metal-pillars, g = 9.8 m/s^2 is the gravitational acceleration) which is thousand times smaller than the capillary action. The gravity does not affect the absorption if the metasurface is upside down. The confocal images of the fabricated liquid-metal-pillars taken by Leica TCS SP8 Confocal are presented in Fig. 4.15. The height of the liquid-metal-pillars can be reconfigured by applying different air pressures from the top air channels as shown in Fig. 4.15(a-d).

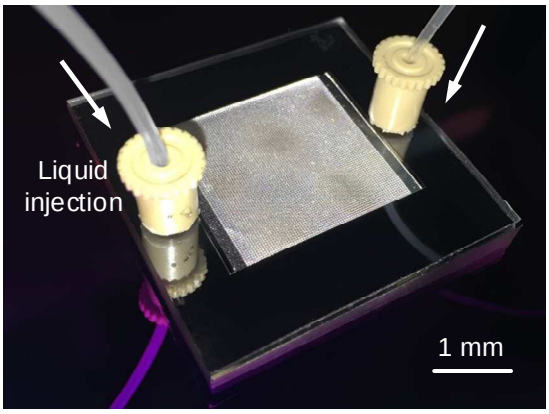

(a)

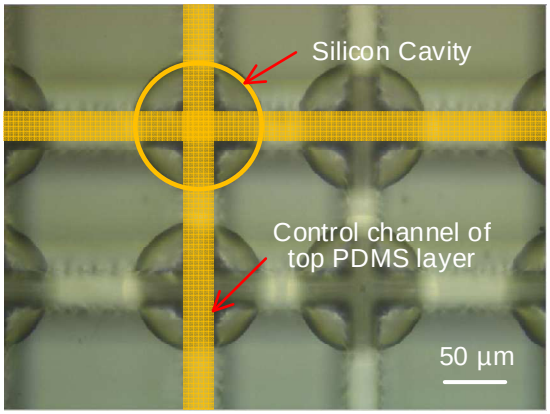

(b)

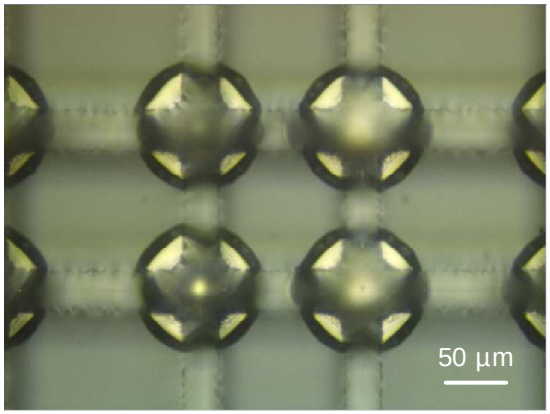

(c)

Figure 4.14 (a) Photograph of the liquid-metal-based metasurface. (b) Top view microscope image for a single element of metasurface without liquid-metal injection. (c) Top view microscope image with liquid-metal injection.

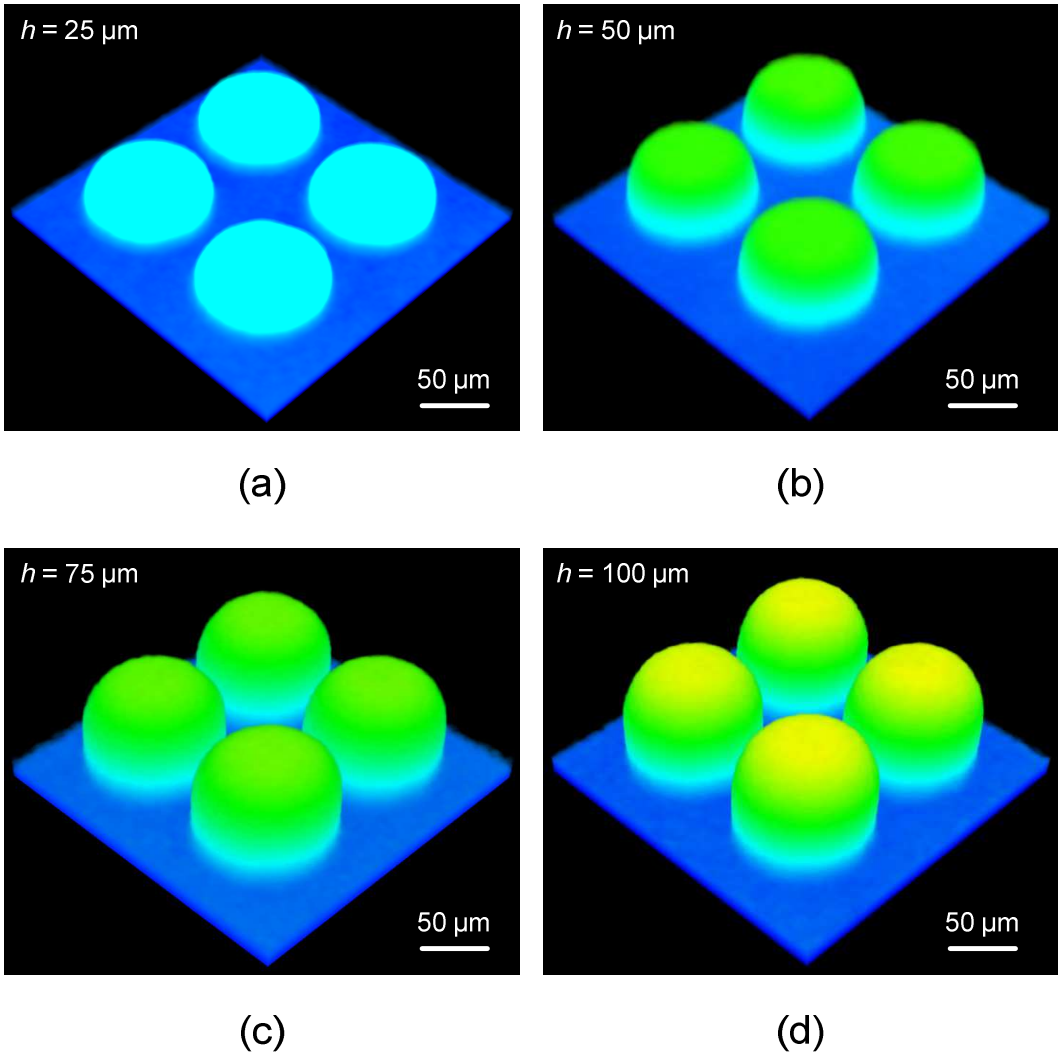

Figure 4.15 Fabrication results of the liquid-metal-based metasurface. Confocal images for a single element of four-pillars with the height of the liquid-metal-pillars at (a) h = 25 μm, (b) h = 50 μm, (c) h = 75 μm and (d) h = 100 μm.

4.2.2 Experimental setup for Terahertz Measurement

The measurement of the liquid-pillar-based metasurface is carried out by using the terahertz spectrometer (TPS Spectra 3000) as shown in Fig. 4.16. The optical path of the reflection measurement is shown in Fig. 4.17. The generated pulse of terahertz radiation is incident to the sample with an incident angle of θ1 by orienting the direction of the mirror M2. The reflection terahertz wave is reflected by mirrors M3 and M4 to the detector with a reflection angle θ2 = θ1.

Figure 4.16 Terahertz spectrometer (TPS Spectra 3000) for spectra measurement.

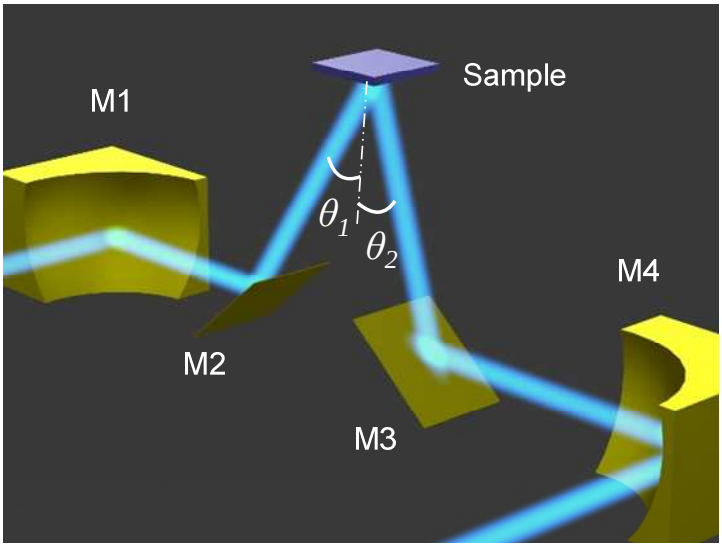

Figure 4.17 Schematic illustration of the optical path for the reflection measurement.

4.3 Experimental Results and Discussions

4.3.1 Polarization-Independent Absorption

The measured results under normal incidence when the height of the liquid-metal-pillars kept at 70 μm are shown in Fig. 4.18. An absorption peak occurs at 0.32 THz with the absorption close to near unity, and an additional absorption peak that is induced by the FP cavity is observed at around 0.29 THz, which agrees with the simulation results as shown in Fig. 4.7. There is a slight difference in the bandwidth of the absorption spectra between the simulation and experimental results due to the fabrication errors. All liquid-metal-pillars are not perfectly uniform due to the inhomogeneous pressure in the silicon cavity. These non-

monodispersed liquid-metal-pillars will affect the bandwidth of the absorption. The absorption spectra with TE mode and TM mode are almost overlapped, which verify the polarization-independent feature of the absorption material.

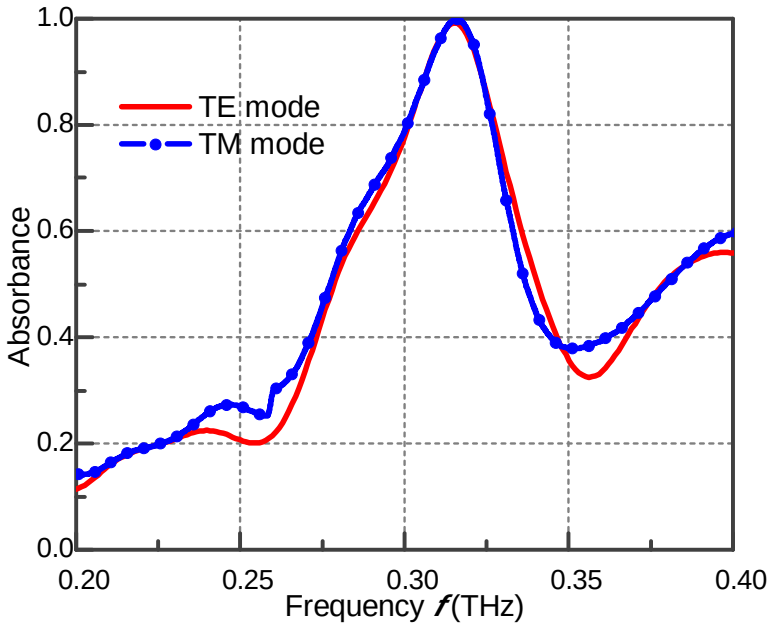

Figure 4.18 Experimental results of the absorption spectra of the liquid-metal-based metasurface with TE mode (red line) and TM mode (blue dot) incidence when the heights of the liquid-metal-pillars is h = 70 μm.

4.3.2 Frequency-agile absorption

The frequency-agile absorption can be realized by tuning the effective length of the magnetic resonance. By applying different air pressure, the height of the liquid-metal-pillars can be changed from 0 to 100 μm, so as to tune the absorption

frequency of liquid-metal-based metasurface. Fig. 4.19 shows the absorption color map when the height of the liquid-metal-pillars is increased from 30 to 90 μm. The absorption peak frequency is tuned from 0.246 to 0.415 THz. The tuning range of the absorption peak frequency reaches 51.1% of the central frequency with absorption higher than 90%, which is slightly different from the simulation results as shown in Fig 4.9 due to the fabrication error of the liquid-metal-pillars. The mismatch in the tuning range is less than 2% between the experimental and simulation results.

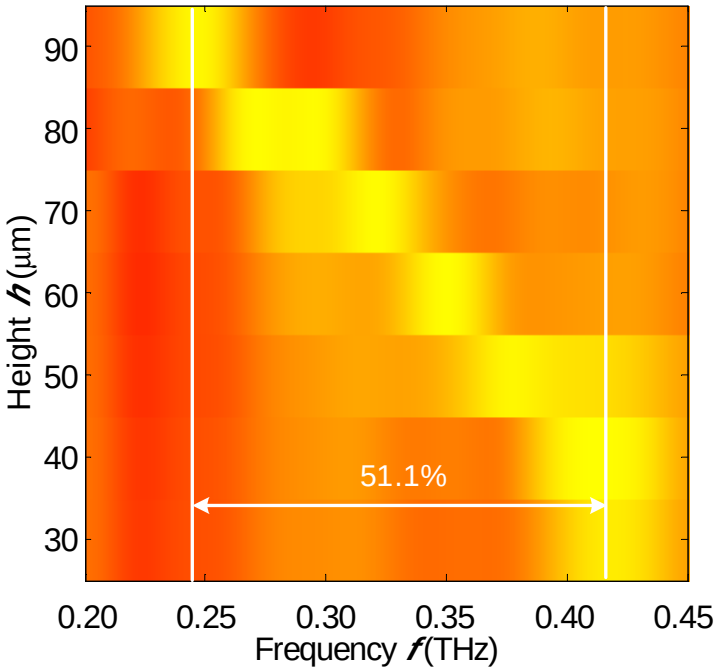

Figure 4.19 Absorption color map of the tunable absorption material in TM mode normal incidence when the height of the liquid-metal-pillars is tuned from h = 30 μm to h = 90 μm.

4.3.3 Wide-Angle Absorption

Fig. 4.20a shows the experimental results of the absorption spectra with different incident angles (TM mode) when the height of the liquid-metal-pillars is 50 μm. The absorption peak slightly shifts to lower frequency when the incident angle is increasing as shown in Fig. 4.20b and the absorption maintains at nearly 99%. Such frequency shift caused by the change of the incident angle will restrict its potential applications in EM shielding and color imaging, etc. The red shift can be compensated by decreasing the height of the liquid-metal-pillars, which realizes a wide-angle absorption with broad bandwidth. The experimental results of the wide-angle absorption material tuned by different heights of the liquid-metal-pillars is shown in Fig. 4.21. We demonstrate three absorption frequencies that is fixed at 0.25 THz (Fig. 4.21a), 0.28 THz (Fig. 4.21b) and 0.33 THz (Fig. 4.21c) when the incident angle is changed from 0° to 60°. By continuously tuning the height of the liquid-metal-pillars, the wide-angle absorption can cover all the frequencies from 0.25 THz to 0.33 THz with a tuning range of the central frequency 27.6%. The absorption outside the central frequency stays as high as 60%, which is caused by the top lossy PDMS layer. It can be suppressed by using low loss dielectric materials in terahertz regime.

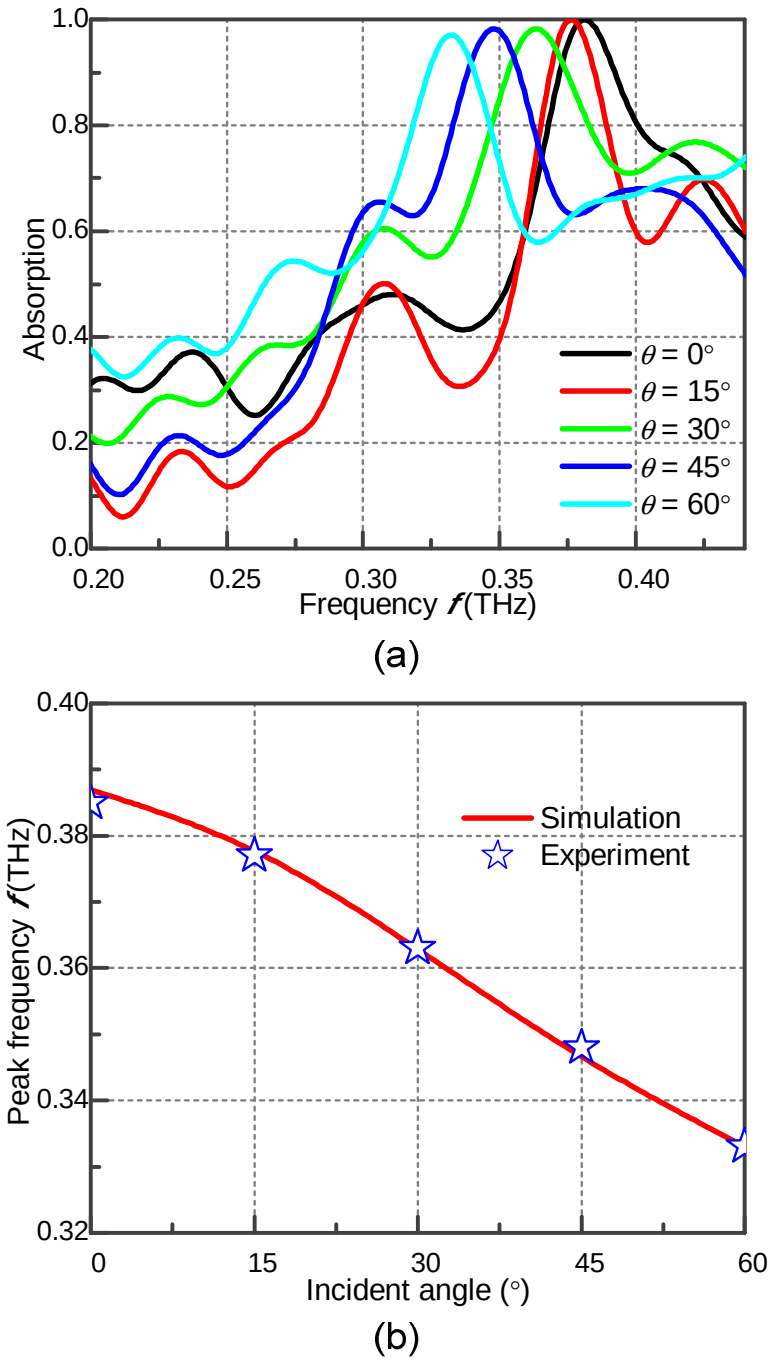

Figure 4.20 Experimental results of the metasurface absorption material with different incident angles (TM mode) when the height of the pillars keeps at 50 μm. (a) Absorption spectra when the incident angle is changed from 0º to 60º. (b) Peak frequency as the function of the incident angle.

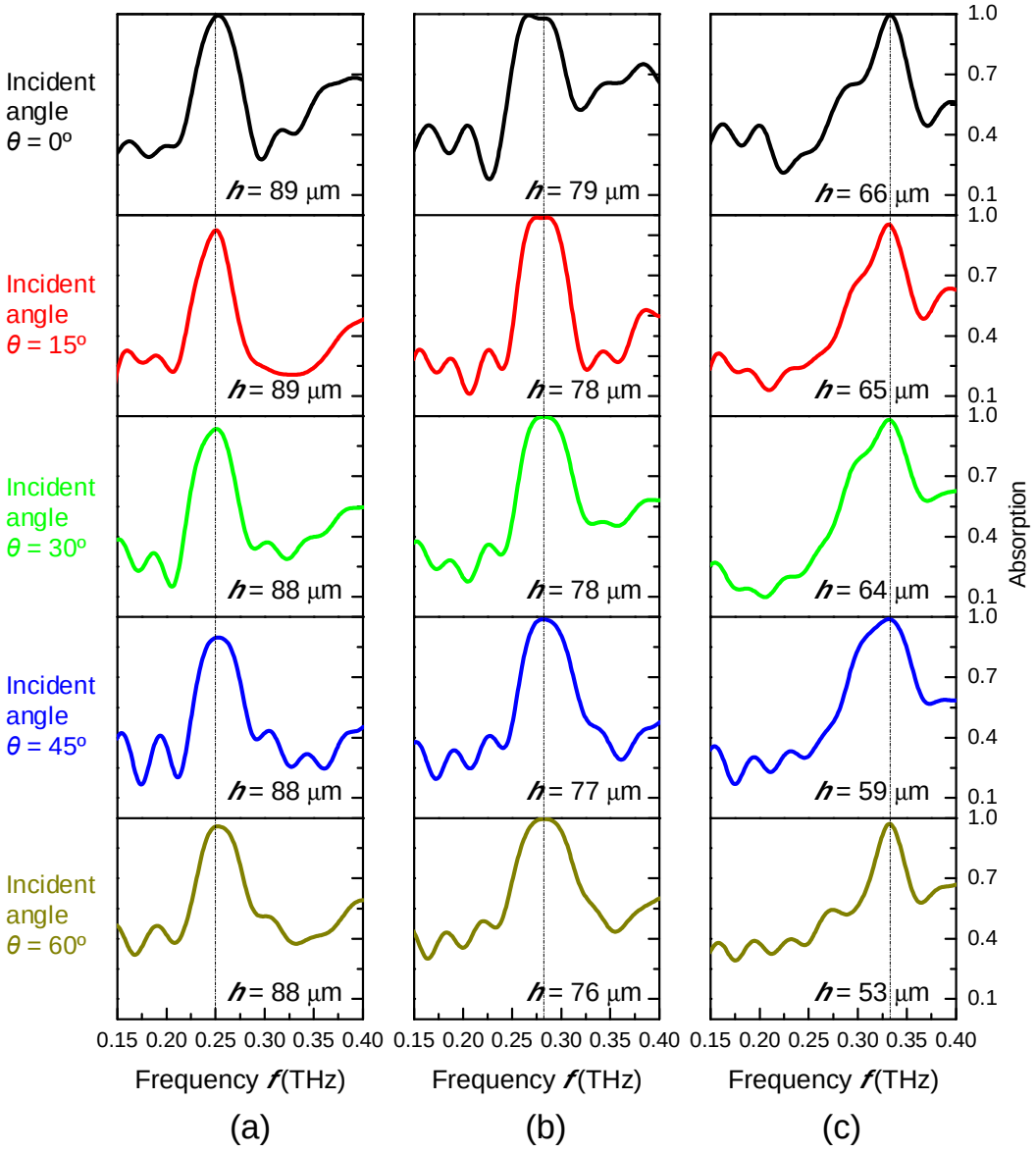

Figure 4.21 Experimental results of the broadband and wide-angle absorption material with TM incidence when the incident angle is 0° (black line), 15° (red line), 30° (green line), 45° (blue line) and 60° (dark yellow line). By tuning the height of the mercury pillars, the absorption peak frequency can be fixed at (a) 0.25 THz, (b) 0.28 THz and (c) 0.33 THz. The tuning range of the central frequency reaches 27.6%.

4.4 Summary

This chapter focuses on the structure design, numerical analysis, sample fabrication and experiments of a frequency-agile and wide-angle absorption in terahertz regime by using liquid-pillar-based metasurface. The liquid-pillar-based metasurface induces a strong magnetic resonance by erecting the U-resonator up long the propagating direction, which not only strongly couples with the incident magnetic field, but also break the tuning limitation in 2D plane. In addition, the fabrication processes for microfluidic metasurface in terahertz are developed for the liquid injection and reconfiguration in a large tuning range by combining silicon and PDMS together. Experiments show that the developed liquid-metal-based metasurface is polarization-independent and has a tuning range in central frequency of 51.1% with higher than 90% absorption under normal incident microwave. Finally, a wide-angle absorption material with a tuning range in central frequency of 27.6% is achieved when the incident angle is changed from 0° to 60°.

The innovation of the liquid-pillar-based metasurface is summarized as follows,

(a) The combination of silicon structure layer and PDMS control layer for the liquid-metal injection and reconfiguration in microscale is developed. The triple layers structure, PDMS/silicon/PDMS allows the tuning of the liquid-metal in the vertical direction to break the tuning limitation in 2D plane, which provide a significant milestone for the tunable metasurface.

(b) A real time control on the absorption frequency by tuning the height of the liquid-metal-pillars is firstly demonstrated in the terahertz regime. The coupling mechanism between the liquid-metal-pillars is investigated numerically, which provide a good understanding on the way to control the absorption.

(c) A wide-angle absorption with broad bandwidth is firstly demonstrated with large angular tolerance up to 60^0. The mechanism of the broadband wide-angle absorption is numerically investigated.

CHAPTER 5

TUNABLE CHIRAL METASURFACE

This chapter presents the structure design, numerical analysis, sample fabrication and experiments of a tunable chiral metasurface for tunable asymmetric transmission. The tunable chiral metasurface can be controlled from achiral to chiral by using microfluidic technology, whereby the transmission can be controlled from symmetric to asymmetric transmission. The structure designs of the tunable chiral metasurface are presented, which are using a bilayer of metallic spiral structures patterned on both sides of the PDMS layer and could be reconfigured by using microfluidic technology. Subsequently, theoretical analysis on the interaction of the dual-spiral structures using plasmon hybridization is discussed. Next, the fabrication processes for tunable chiral metasurface combining photolithography and E-beam evaporation are presented. Finally, the experimental results of tunable asymmetric transmission are presented and discussed, either with wide incident angle or a curved metasurface.

5.1 Design and Theoretical Analysis

Chiral materials exhibit asymmetric transmission originating from their different responses to left and right circularly polarized light. Studying of asymmetric transmission for circularly polarized light was reported in the planar chiral metasurfaces. However, such planar chiral metasurfaces are only chiral in the two-dimensional space, in which the asymmetric transmission is absent for linear polarization. Efforts on the asymmetric transmission for linear polarization have been made by introducing symmetric broken along the propagation direction in the metasurface structures. In optical communication, it is desirable to change the wave propagation from asymmetric transmission to symmetric transmission. However, previously proposed chiral metasurfaces lack the tunability to control chirality from chiral to achiral, which is essential for the propagation wave changing from asymmetric transmission to symmetric transmission. An array of metallic dual-spiral structures patterned on both sides of the PDMS layer is proposed to control the chirality from achiral to chiral by controlling the spiral structures from planar to three-dimensional (3D) through microfluidic technology.

5.1.1 Design of Tunable Chiral Metasurface

Theory of Asymmetric Transmission

The transmission of polarized light can be described using Jones matrices [231, 251]. Assuming a plane wave that is propagating in positive *z*-direction

$$\boldsymbol{E}_i(\boldsymbol{r},t)=\begin{pmatrix} I_x \\ I_y \end{pmatrix} e^{i(kz-\omega t)} \tag{5.1}$$

where ω is the frequency; k is the wave vector; I_x and I_y is the complex amplitudes of polarized wave in x and y direction, respectively. The transmitted field T_x and T_y through the medium is represented by

$$\boldsymbol{E}_t(\boldsymbol{r},t)=\begin{pmatrix} T_x \\ T_y \end{pmatrix} e^{i(kz-\omega t)} \tag{5.2}$$

The complex amplitudes of the transmitted field and incident field can be described by Jones matrix **T** as

$$\begin{pmatrix} T_x \\ T_y \end{pmatrix}=\begin{pmatrix} T_{xx} & T_{xy} \\ T_{yx} & T_{yy} \end{pmatrix}\begin{pmatrix} I_x \\ I_y \end{pmatrix}=\boldsymbol{T}_{lin}^{f}\begin{pmatrix} I_x \\ I_y \end{pmatrix} \tag{5.3}$$

where the superscript *f* and subscript *lin* indicate the forward propagation direction and a special linear base with base vectors parallel to the coordinate axes, i.e., decomposing the incident wave into x and y directions are T_{xx} and T_{yx}, respectively.

If no magneto-optical material exists in the medium, the Jones matrix for the backward propagation direction $\boldsymbol{T}^b$ can be obtained by applying the reciprocity theorem

$$\boldsymbol{T}_{lin}^{b}\begin{pmatrix} T_{xx} & -T_{yx} \\ -T_{xy} & T_{yy} \end{pmatrix} \tag{5.4}$$

The off-diagonal elements of the Jones matrices for forward and backward propagation interchange their values and the sign become negative indicating a phase difference of 180°.

The asymmetric transmission for a given linear base vector is defined as the difference between the transmittance of forward and backward propagation direction, which is characterized by the Δ parameter as

$$\begin{aligned} \Delta_{lin}^{(x)} &= (|T_{xx}|^2 + |T_{yx}|^2) - (|T_{xx}|^2 + |-T_{xy}|^2) = |T_{yx}|^2 - |T_{xy}|^2 \\ &= -\left[(|T_{yy}|^2 + |T_{xy}|^2) - (|T_{yy}|^2 + |-T_{yx}|^2) \right] = -\Delta_{lin}^{(y)} \end{aligned} \tag{5.5}$$

From Eq. 5.5, it is clear that the asymmetric transmission parameter is determined by difference of off-diagonal elements of the respective Jones matrix.

Design Method

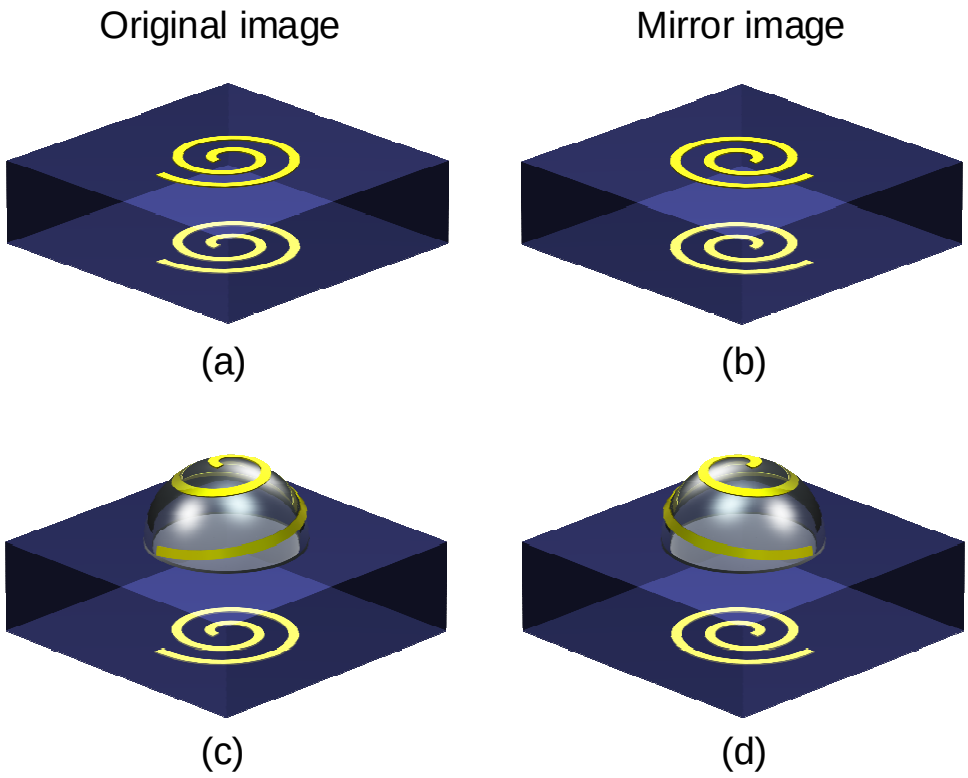

Figure 5.1 Design of one element of the tunable chiral metasurface tuned from achiral to chiral, which consists of a dielectric medium sandwiched between two metallic spiral structures. When both spiral structures are planar, the metasurface is achiral because (a) the original image is superimposable on (b) its mirror image. The metasurface becomes chiral when the top spiral structure is reconfigured in the vertical direction, since (c) the original image is not superimposable on (d) its mirror image.

The tunable chiral metasurface reported here consists of a dielectric medium sandwiched between two metallic spiral structures as shown in Fig. 5.1. When the dual-spiral structures are planar, the metasurface is achiral, since the mirror image is superimposable on its original image as shown in Fig. 5.1a and b. However, the metasurface becomes chiral when the top spiral structure is reconfigured in the vertical direction, because the mirror image of the dual-spiral structure is not superimposable on its original image as shown in Fig. 5.1c and d. Such a chiral structure is patterned into square array and can exhibit asymmetric transmission for linear polarized wave as shown in Fig. 5.2.

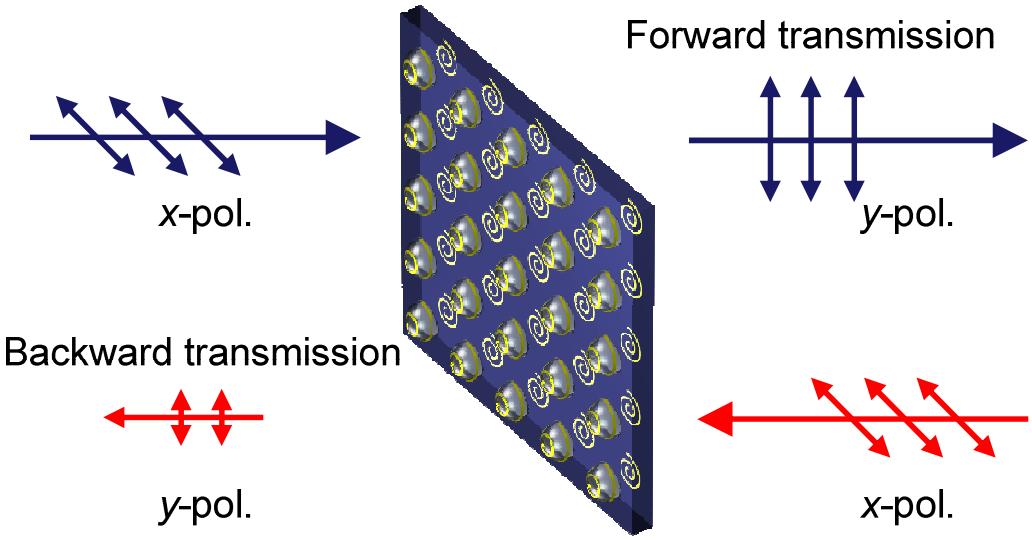

Figure 5.2 Schematic illustration of the asymmetric transmission for linear polarized wave through chiral metasurface.

The schematic of the tunable chiral metasurface incorporating with microfluidic technology is shown in Fig. 5.3a and the dimension of each single element is shown in Fig. 5.4. The period of the metasurface is P = 5 mm. The Archimedean spiral is used as the metallic structure with an inner radius of R_{in} = 0.7 mm, outer radius of R_{out} = 2.0 mm, width of w = 0.3 mm and thickness of 600 nm. The relative twist of the bottom spiral φ_1 = 0^0. The height of the top PDMS layer, bottom PDMS layer and microfluidic channel are h_1 = 0.5 mm, h_2 = 1 mm and h_3 = 80 μm, respectively. The diameter of the air reservoir is D = 4 mm. The original state of the metasurface is planar as shown in Fig. 5.3b without air injection. Such planar metasurface is achiral which exhibits symmetric transmission under forward and backward incidence. Since the bottom PDMS membrane is much thicker than the top PDMS membrane, when the air is injected into the reservoir, the top PDMS membrane is expanded and formed a PDMS sphere cap due to air pressure, while the bottom PDMS layer maintains planar. The top expanded PDMS membrane stretches the top spiral structures out of plane and become 3D spiral. By applying different air pressure, the top PDMS membrane can be expanded or contracted, resulting in a reversible process to flexibly reconfigure the height of the spiral structure h as shown in Figs 5.3c and 5.3d. The symmetric breaking of the two spiral structures introduces chirality and the transmission under forward and backward incidence become asymmetric. Thereby, the tunable chiral metasurface can be dynamically controlled from achiral to chiral, which enables the control of transmission from symmetric to asymmetric.

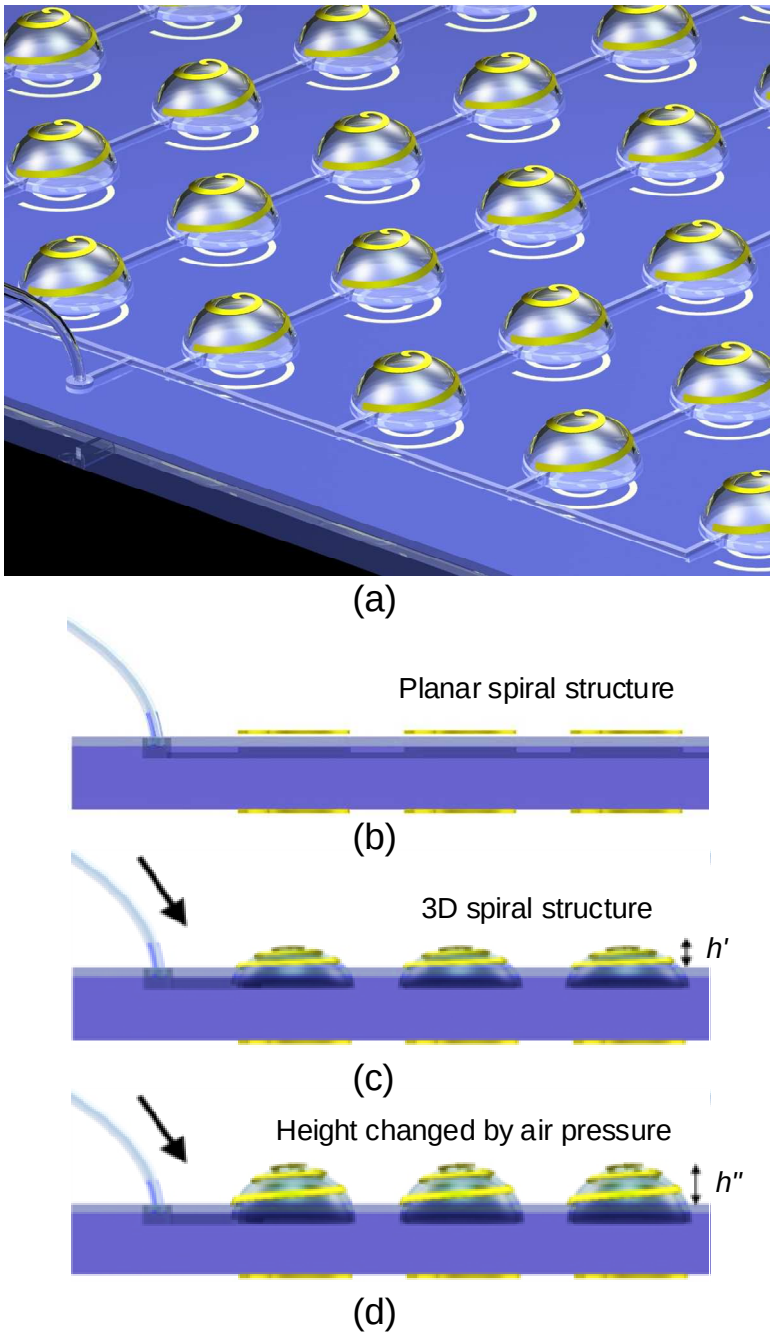

Figure 5.3 Schematic of tunable chiral metasurface. (a) Dual-spiral structure array incorporating with microfluidic technology. (b) Side view of the original state of planar dual-spiral structure. (c, d) Height of top spiral structures is tuned by different air pressure.

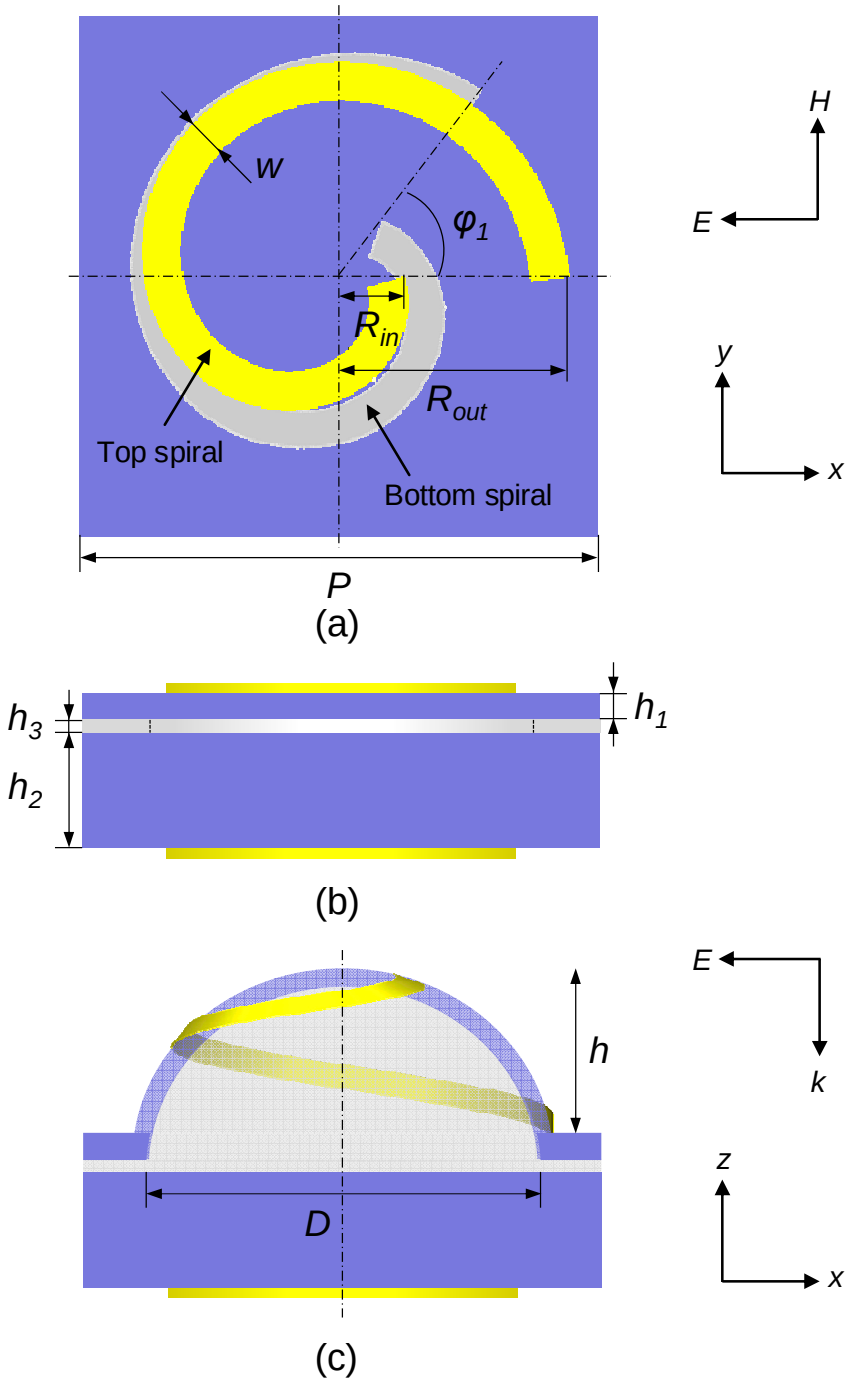

Figure 5.4 Layout of the tunable chiral metasurface. (a) Top view and (b) side view of the dual-spiral metasurface. (c) Side view of the dual-spiral metasurface with the height of the spiral structure h that can be changed by varying the air pressure.

5.1.2 Theoretical Analysis and Numerical Simulation

The optical response of metasurface is studied by CST MICROWAVE STUDIO with periodic boundary condition. The dual-spiral structure is patterned on both sides of low permittivity dielectric material, PDMS, forming a metal/PDMS/metal sandwich structure. The coupling between these two spirals contributes to the resonances at certain frequencies for the metasurface. Simulation results of the forward and backward transmission of co-polarization and cross-polarization when both spiral structures are planar are shown in Fig. 5.5a and 5.5b, respectively. Since the metasurface is achiral, the forward and backward transmission are completely overlap, i.e. $T_{yx}^{f} = T_{xy}^{f} = T_{yx}^{b} = T_{xy}^{b}$ (the superscripts f and b indicate microwave incidence under forward and backward propagation direction, respectively). Two resonance peaks occur in the cross-polarization transmission at f_1 = 25.8 GHz and f_2 = 37.1 GHz, respectively, which are induced by the coupling between these two spiral structures. The surface current distribution are similar under forward and backward incidence as shown in Fig. 5.6 and Fig. 5.7, respectively. The surface current direction of top and bottom spiral structures is asymmetric at the lower frequency f_1 as shown in Fig. 5.6a and 5.7a while it is symmetric at the higher frequency f_2 as shown in Fig. 5.6b and 5.7b. The interaction between these two spiral structures can be explained by the plasmon hybridization model as shown in Fig. 5.8. The lower energy mode ω_- corresponds to a bonding mode due to the positive interaction between top and bottom spiral

structures while the higher energy mode ω_+ corresponds to an anti-bonding mode due to the negative interaction.

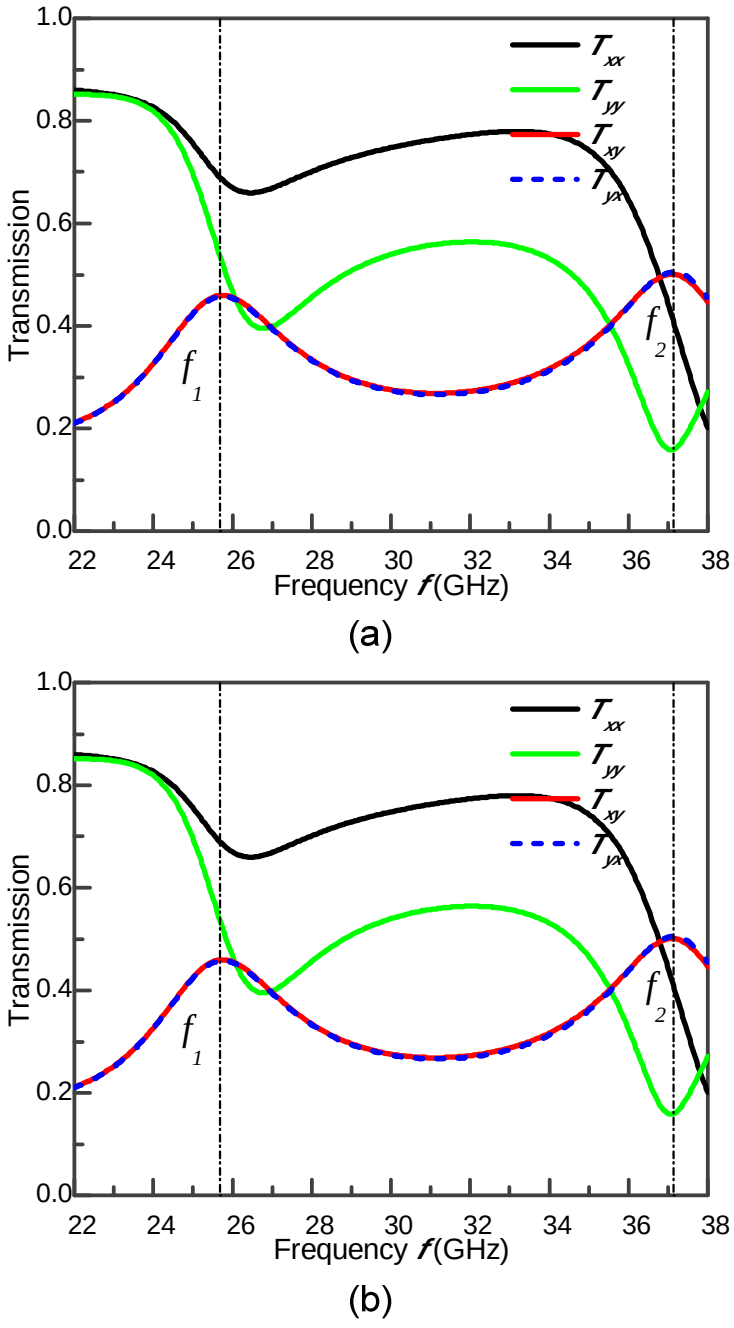

Figure 5.5 Simulation results of the transmission under (a) forward incidence and (b) backward incidence when both layer of spiral structures are planar.

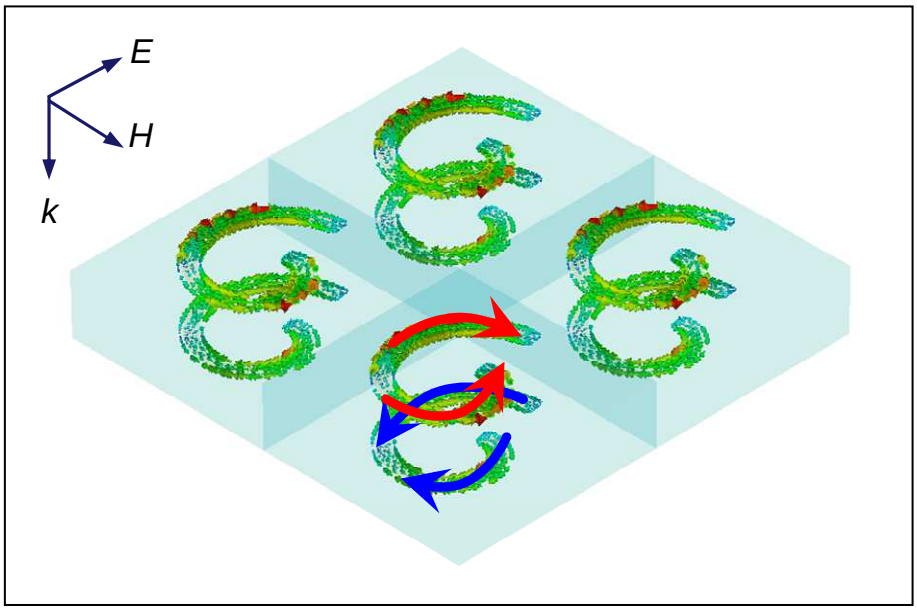

(a)

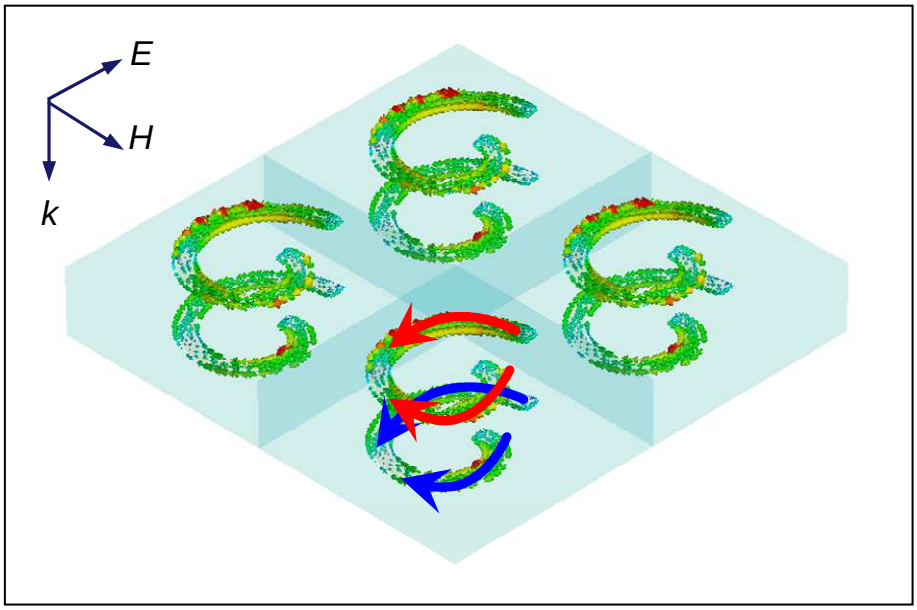

(b)

Figure 5.6 Simulation results of the surface current distribution when both layer of spiral structures are planar at (a) the first peak f_1 and (b) second peak f_2 under forward incidence.

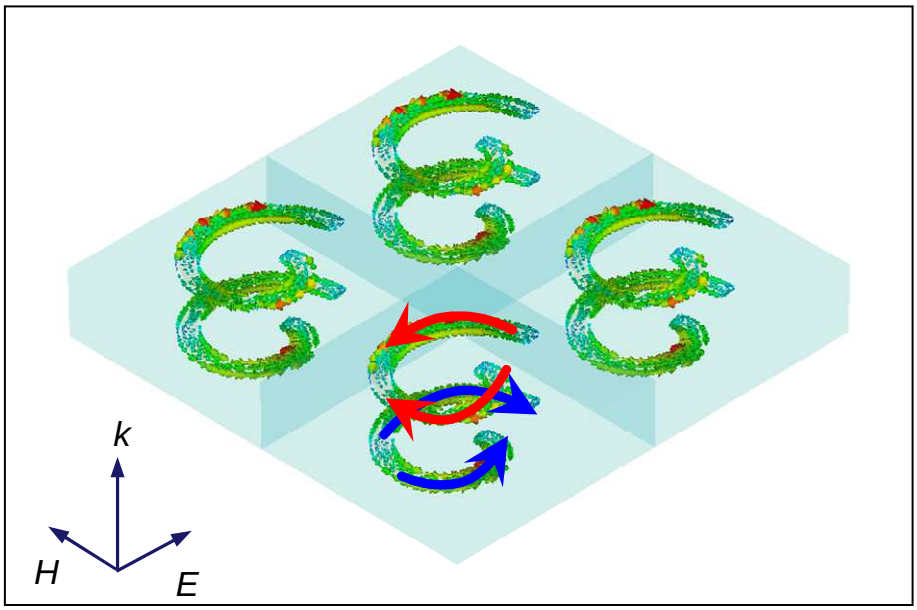

(a)

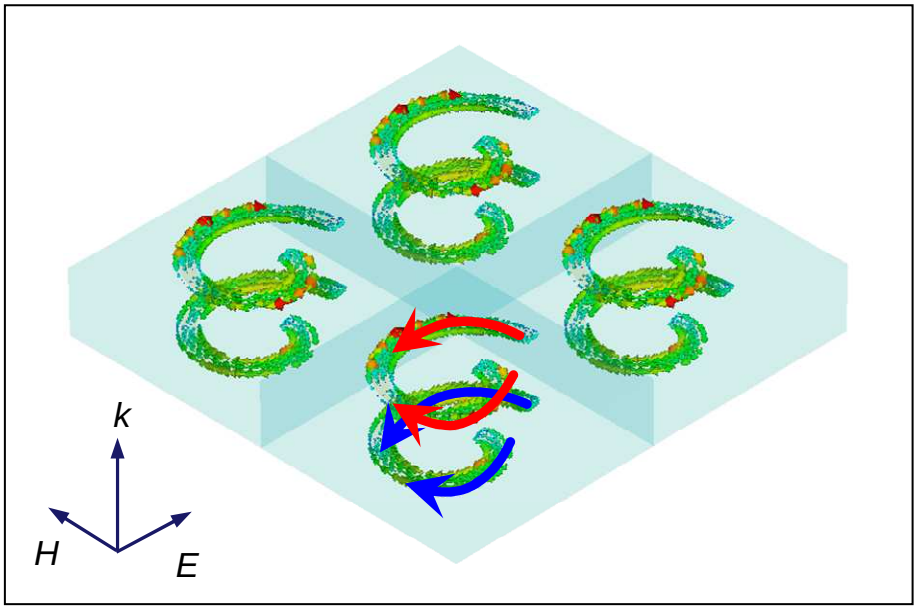

(b)

Figure 5.7 Simulation results of the surface current distribution when both layer of spiral structures are planar at (a) the first peak f_1 and (b) second peak f_2 under backward incidence.

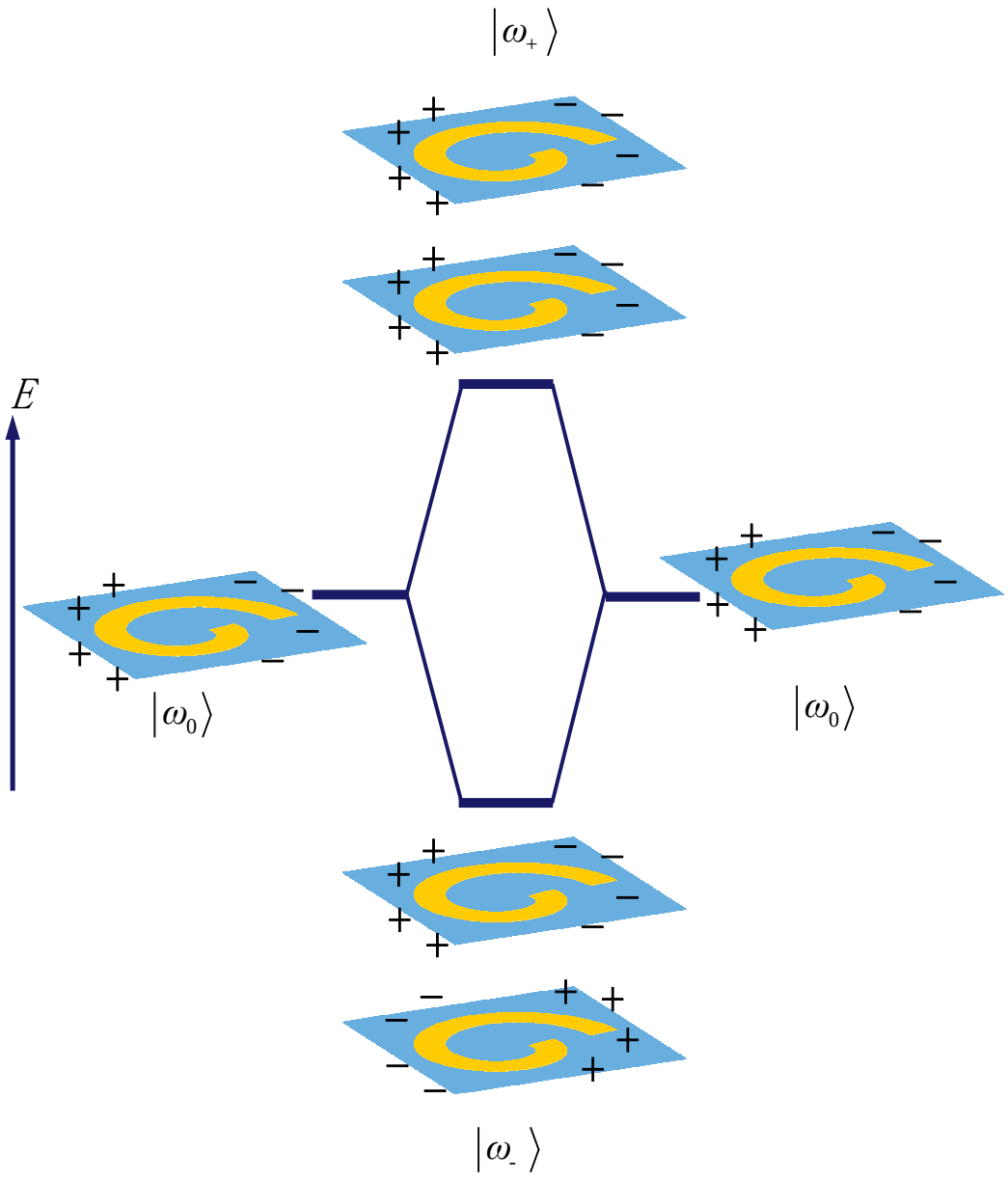

Figure 5.8 The energy-level diagram describing the plasmon hybridization in the tunable chiral metasurface resulting from the interaction between the top and bottom spiral plasmons. A positive interaction will lower the overall energy of the hybridized mode and result in a bonding mode (ω_-) while a negative interaction results in an anti-bonding mode (ω_+).

The height of the top spiral structures can be controlled by applying different air pressures in the microfluidic channels, resulting in a three-dimensional chiral structures. The simulation results of the forward and backward transmission of co-polarization and cross-polarization are shown in Fig. 5.9a and 5.9b, respectively, when the height of the top spiral structures is h = 1.0 mm. Such chiral metasurface exhibits asymmetric transmission of the forward and backward propagation wave, i.e. $T_{yx}^{f} \neq T_{yx}^{b}, T_{xy}^{f} \neq T_{xy}^{b}$. However, due to the reciprocal properties of the metasurface in Eqs. 5.4, the following relationship is satisfied, i.e. $T_{yx}^{f} = T_{xy}^{b}, T_{xy}^{f} = T_{yx}^{b}$. The surface current distribution under forward and backward incidence are shown in Fig. 5.10 and Fig. 5.11, respectively. A bonding mode in the two spiral structures is induced at the lower frequency of f_1 = 25.9 GHz while an anti-bonding mode is induced at the higher frequency of f_2 = 35.8 GHz. The strength of the surface current distribution indicates that the coupling strength is different between the forward and backward incidence at both resonance peaks, resulting in the asymmetric transmission of the forward and backward propagation wave. The asymmetric transmission parameter for linear polarized wave reaches 5% as shown in Fig. 5.12. In this way, the tunable chiral metasurface is controlled from achiral to chiral, leading to a controllable propagation wave from symmetric transmission to asymmetric transmission.

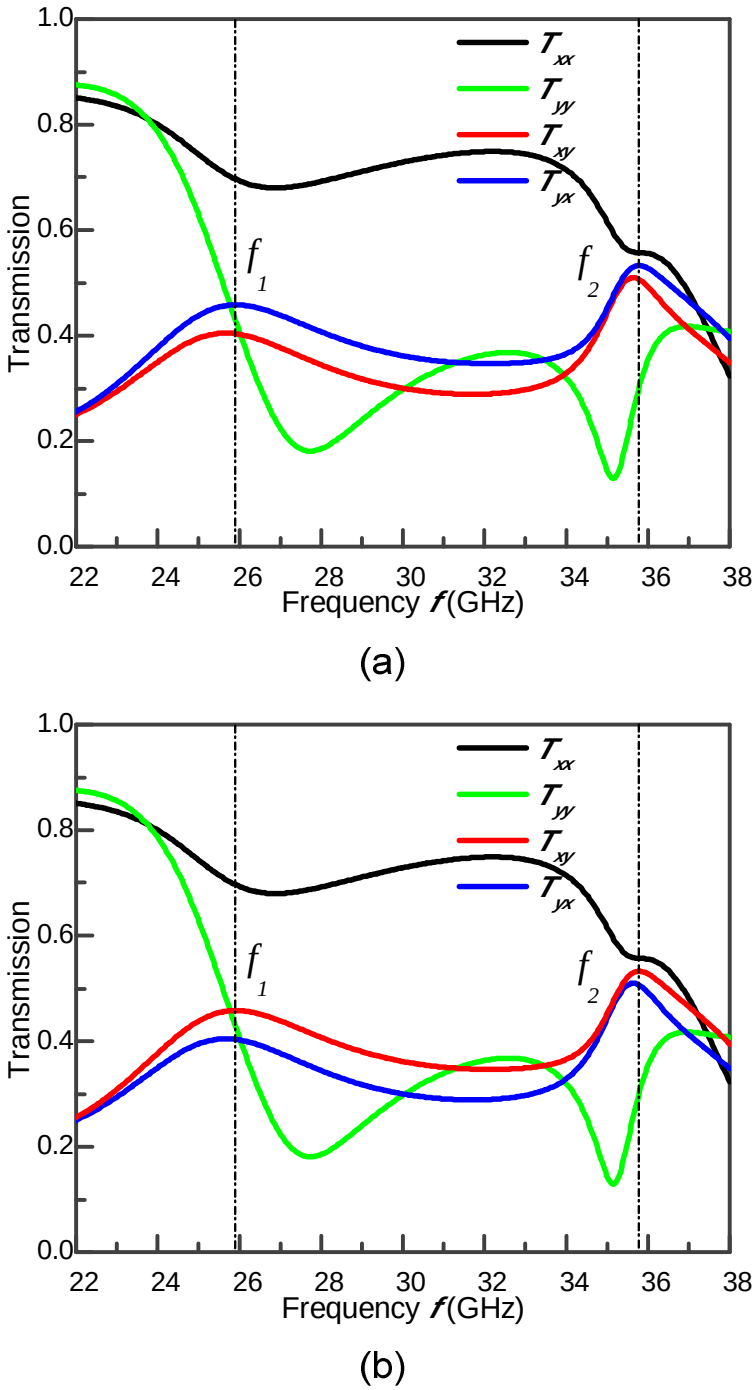

Figure 5.9 Simulation results of the transmission under (a) forward incidence and (b) backward incidence when the height of the top spiral structure is h = 1.0 mm.

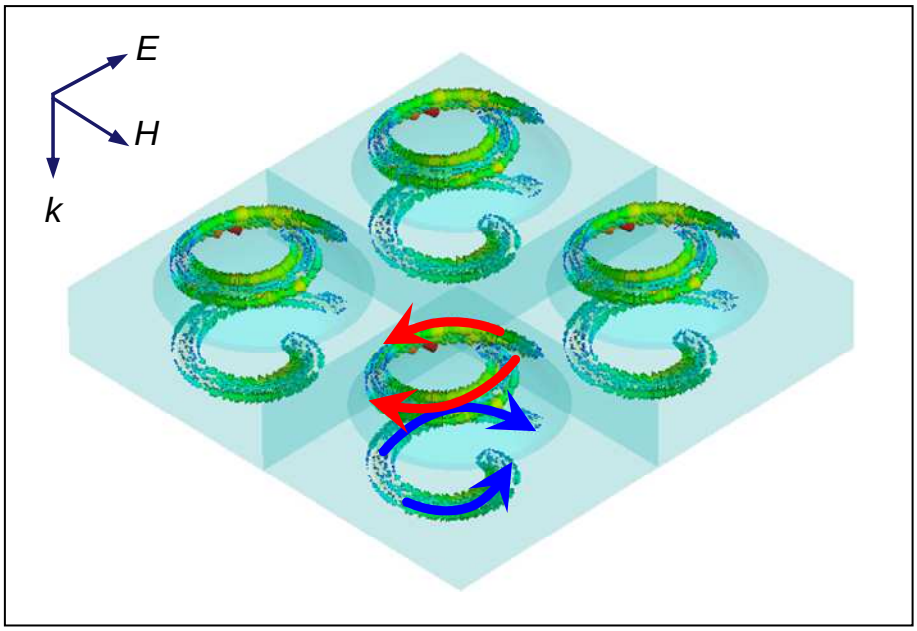

(a)

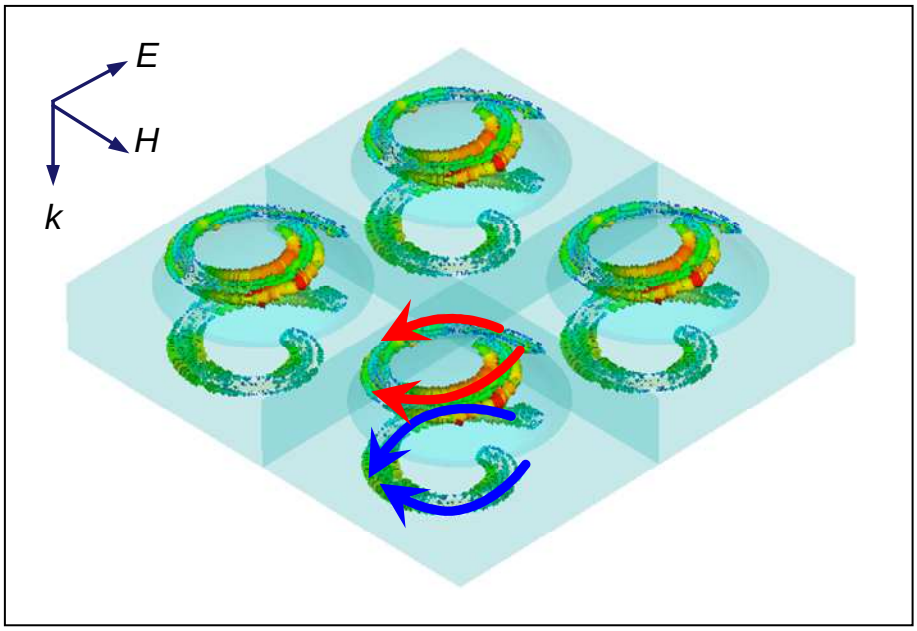

(b)

Figure 5.10 Simulation results of the surface current distribution at (a) the first peak f_1 and (b) second peak f_2 under forward incidence, when the height of top spiral structures is h = 1.0 mm.

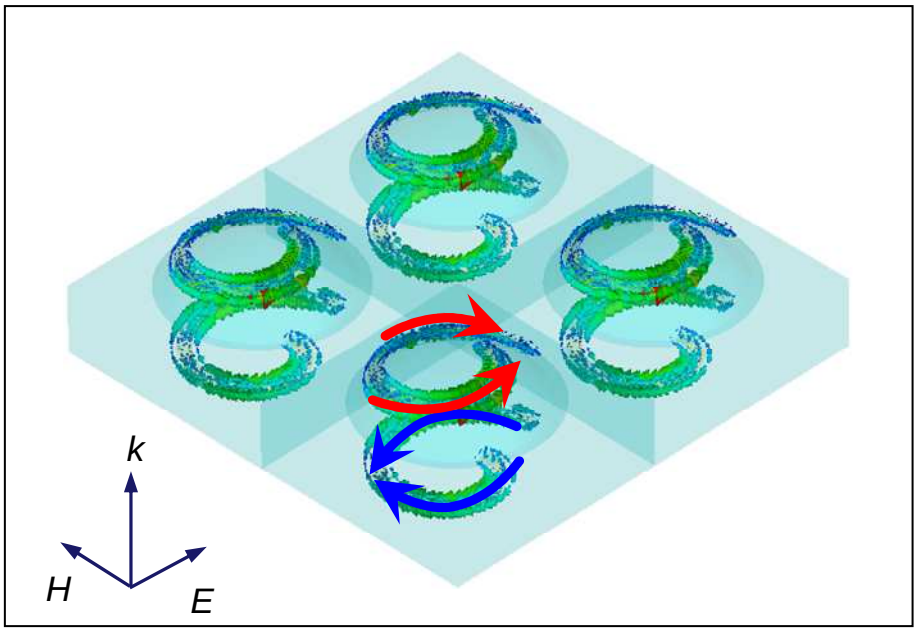

(a)

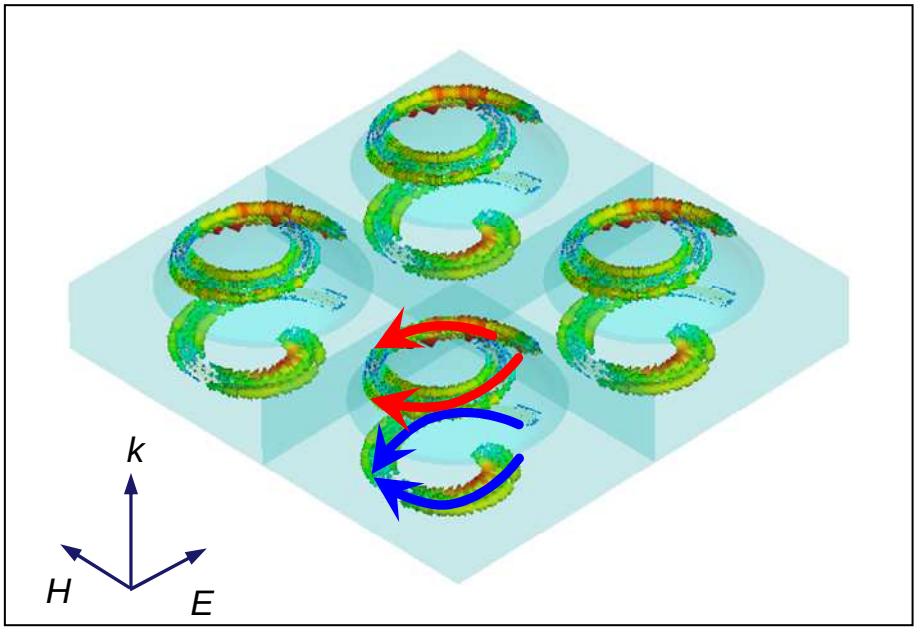

(b)

Figure 5.11 Simulation results of the surface current distribution at (a) the first peak f_1 and (b) second peak f_2 under backward incidence, when the height of top spiral structures is h = 1.0 mm.

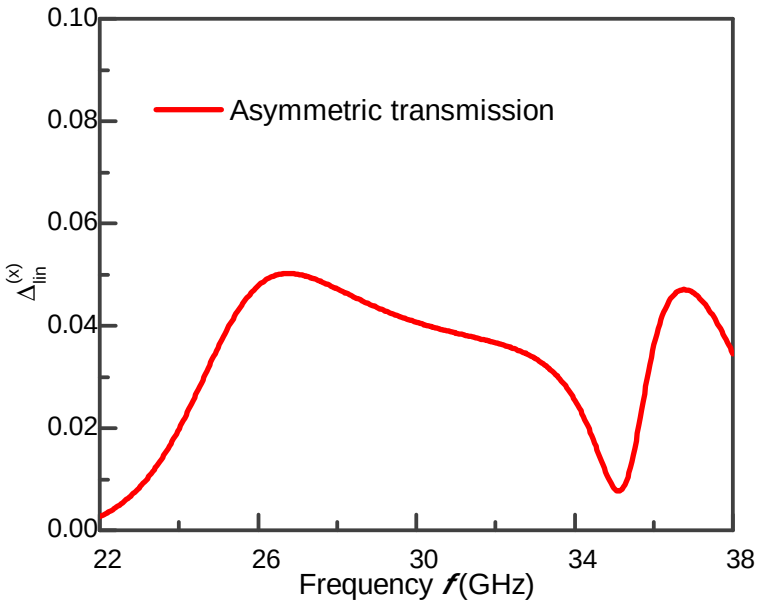

Figure 5.12 Simulation results of the asymmetric transmission at the height of top spiral structures h = 1.0 mm.

Asymmetric Transmission Enhancement

The asymmetric transmission reported in Section 5.2.4 is relative low. In order to enhance the asymmetric transmission, the dual-sprial structures are patterned asymmetrically on both sides of the PDMS as shown in Fig. 5.13. In this configuration, when both spiral structures are planar, the metasurface is chiral. The height of the top PDMS layer, bottom PDMS layer and PDMS channel is h_1 = 0.5 mm, h_2 = 0.42 mm, h_3 = 80 μm, which satisfy the relationship of $h_1 - h_3 = h_2$, i.e. the height of PDMS membrane under top and bottom spiral structures are the same. Therefore, when air is injected into the microfluidic channel, both spiral structures will be deformed with an equal height of *h*.

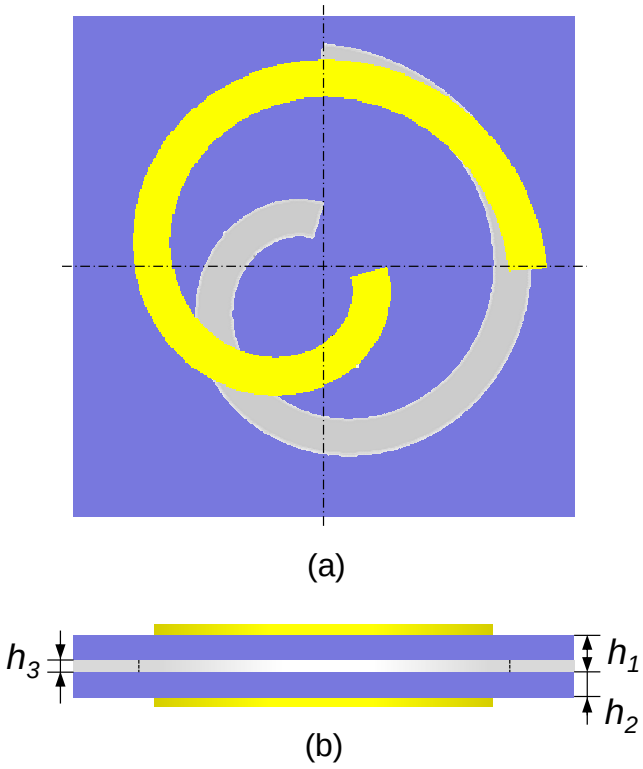

Figure 5.13 Top view of the dual-spiral structure patterned asymmetrically on both sides of the PDMS.

The simulation results of the transmission T_{yx} under forward and backward transmission are shown in Fig. 5.14. When the spiral is planar, i.e. h = 0 mm, the metasurface exhibit chirality, such that the forward and backward transmission are different as shown in the black line. Two resonance peaks occurs at around 28 and 37 GHz due to the plasmon hybridization. When the height of the spiral is increasing from 0 to 1.4 mm, the frequency distance between two resonance peaks is decreasing, because the coupling between top and bottom spiral structures is weakened. The asymmetric transmission parameter is shown in Fig. 5.15a, which shows a maximum Δ reaches over 50%. At the frequency of 37 GHz, the asymmetric transmission exhibit large tunability, which can be tuned from 50% to

0 when the height of the spiral structures is changed from 0 mm to 1.4 mm as shown in Fig. 5.15.

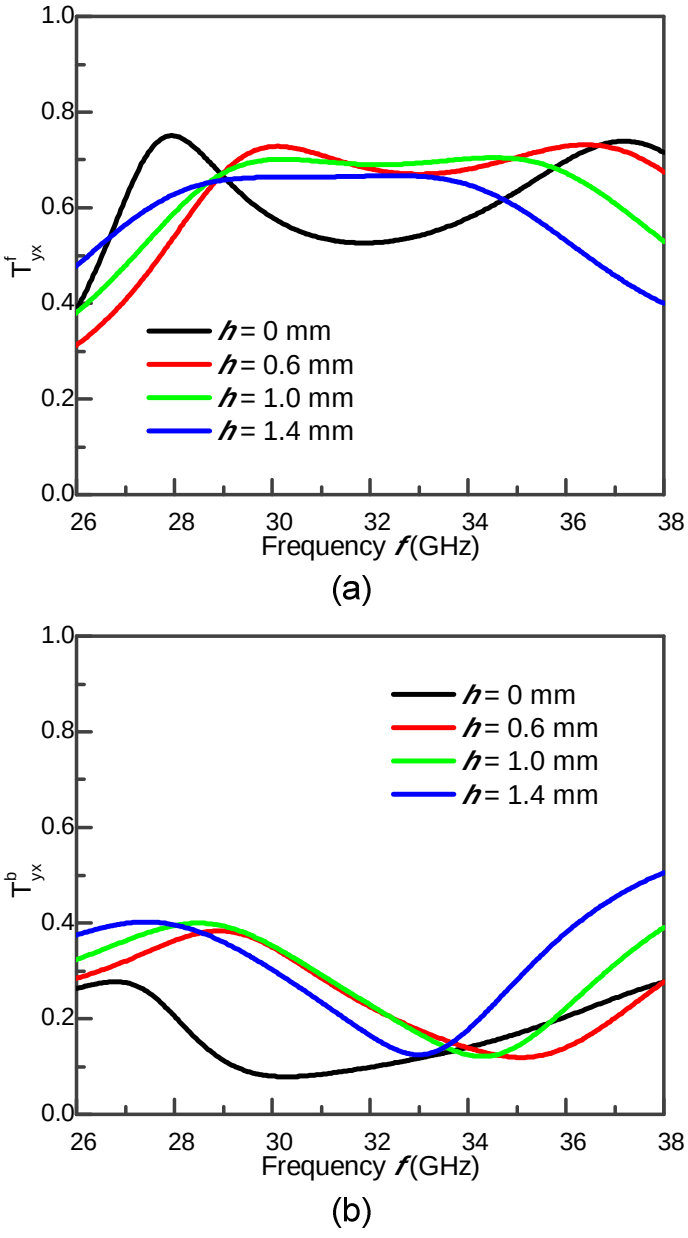

Figure 5.14 Simulation results of the transmission T_{yx} when the height of the spiral structures is changed from 0 to 1.4 mm under (a) forward incidence and (b) backward incidence.

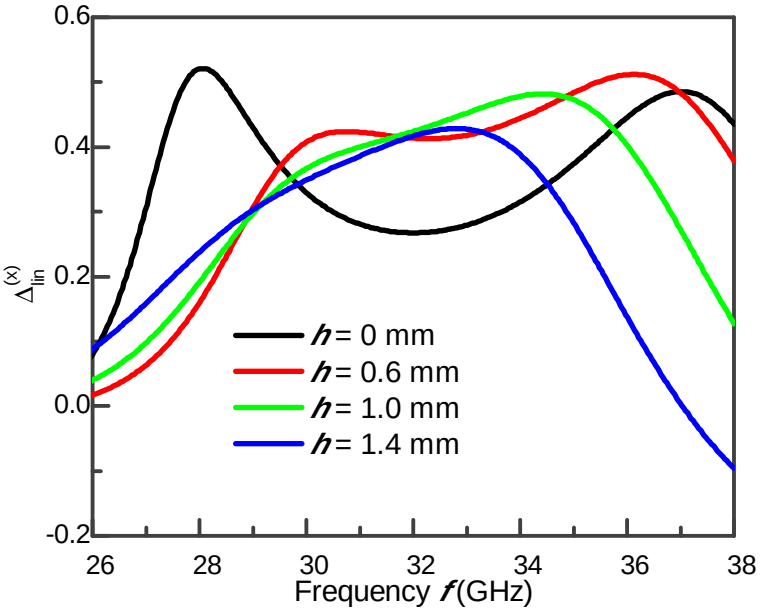

(a)

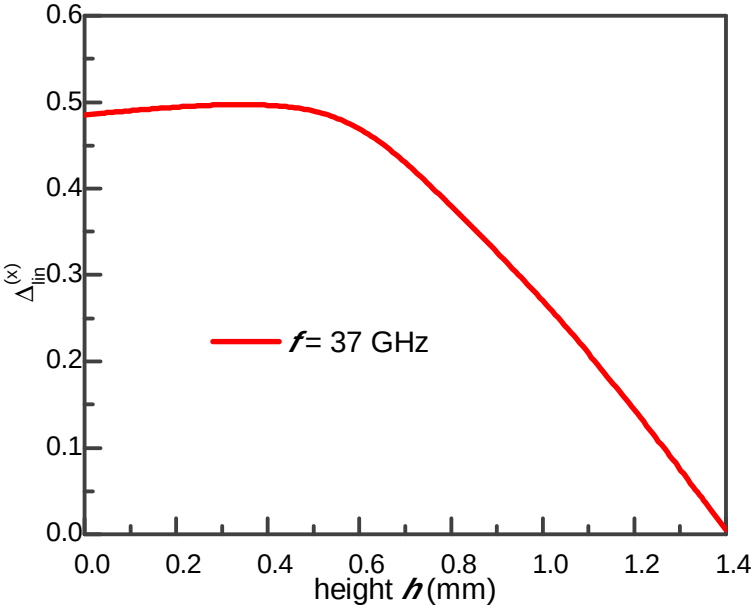

(b)

Figure 5.15 Simulation results when the height of the spiral structures is changed from 0 to 1.4 mm. (a) Asymmetric transmission parameter Δ. (b) Asymmetric transmission as a function of h at the frequency of 37 GHz.

5.2 Experimental Results and Discussions

5.2.1 Fabrication Processes Development

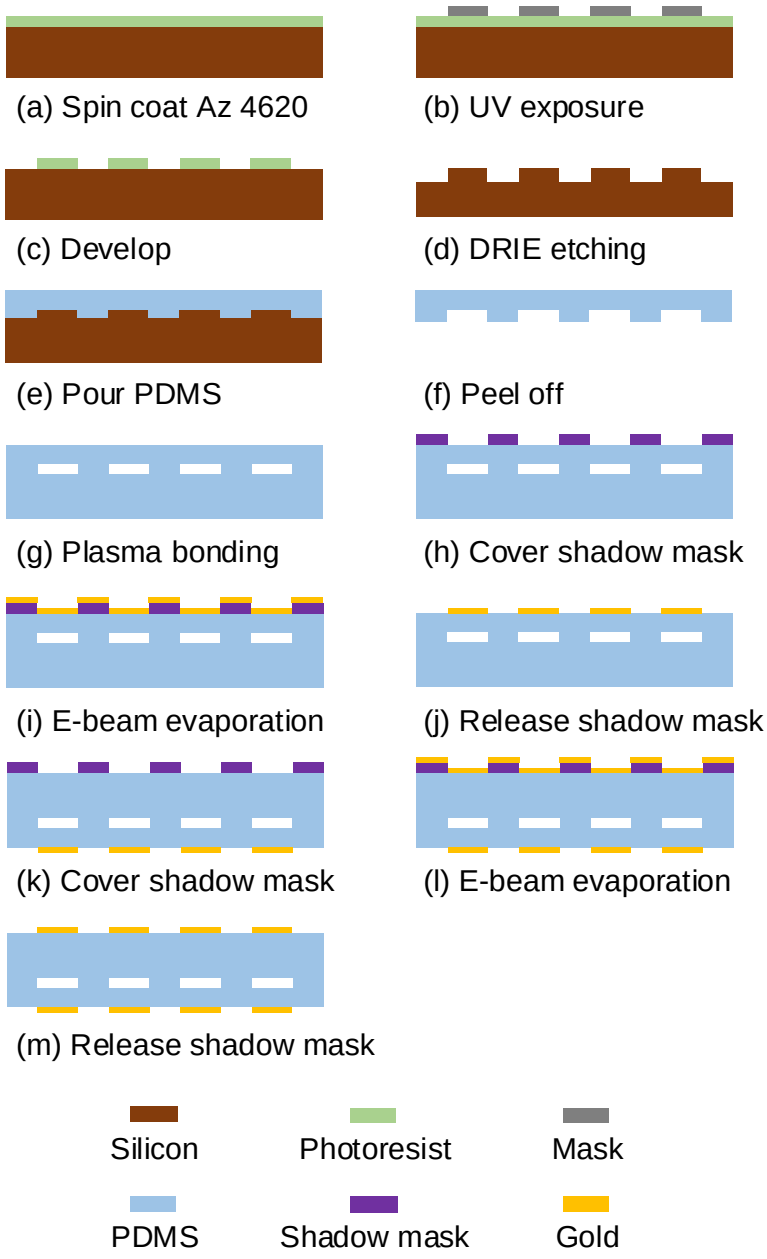

Figure 5.16 Fabrication processes of tunable chiral metasurface combining photolithography and E-beam evaporation.

The fabrication processes of the tunable chiral metasurface combining the photolithography and E-beam evaporation is shown in Fig. 5.16. The fabrication of the PDMS channel is shown in Fig. 5.16(a-g), which has been reported in Section 3.2.1. The spiral structures is deposited on both sides of the PDMS by using E-beam evaporation as shown in .Fig. 5.16(h-m). A showdown mask with desired pattern is used for metal deposition as shown in Fig. 5.16h. A 3-nm thickness of chrome film and a 650-nm thickness of gold film is deposited in sequence on PDMS by using E-beam evaporation as shown in Fig. 5.16i. The metal pattern is obtained by removing the shadow mask as shown in Fig. 5.16j. The PDMS sample is flipped over for the metal deposition on the other side of PDMS. The shadow mask should be aligned well with the metal pattern deposited previously under the microscope as shown in Fig. 5.16k. Likewise, a 3-nm thickness of chrome film and a 650-nm thickness of gold film is deposited in sequence on PDMS by using E-beam evaporation as shown in Fig. 5.16l. After removing the shadow mask, the metasurface is obtained in Fig. 5.16m.

The fabrication results of the tunable chiral metasurface is shown in Fig. 5.17a. The metasurface consists of 24 × 24 elements with a 5-mm period and the total footprint of the metasurface is 120 mm × 120 mm. The original state of the spiral structures is planar as shown in Fig. 5.17b. When the air pressure is applied in the microfluidic channels, the top PDMS membrane is expanded, leading to a controllable height of the spiral structure as shown in Fig. 5.17c. The tunable chiral metasurface can also be bent into an arbitrary curved surface due to the flexibility of the PDMS.

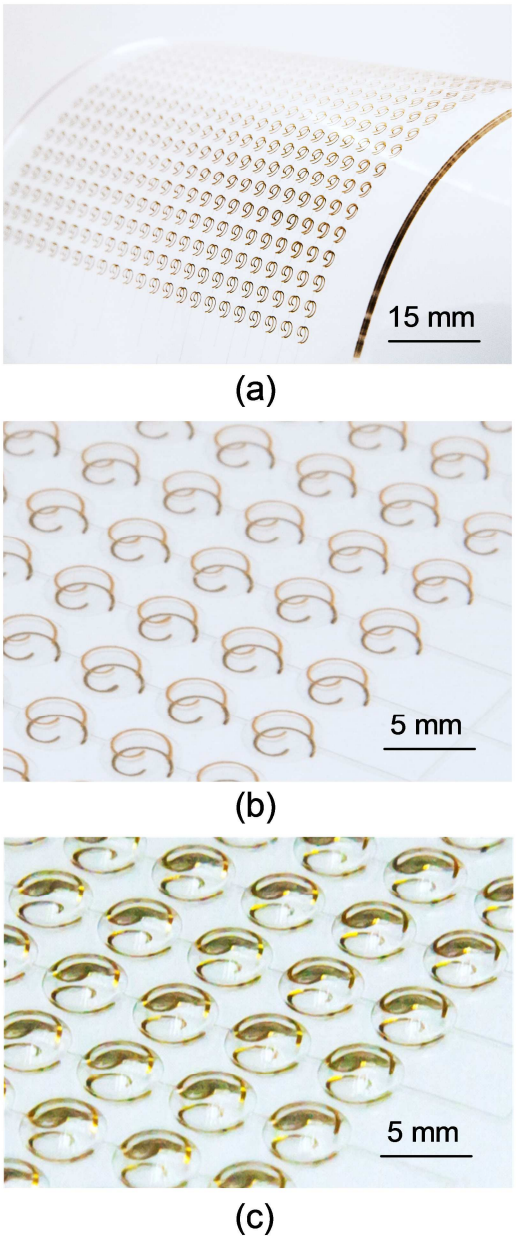

Figure 5.17 Photographs of the tunable chiral metasurface. (a) Full view of the tunabel chiral metasurface with two spiral structure layers deposited on both sides of the PDMS. (b) Planar dual-spiral metasurface without air injection into the PDMS channels. (c) Height of the spiral structures is increased to h = 1.5 mm by injecting air into the PDMS channels.

5.2.2 Tunable Asymmetric Transmission

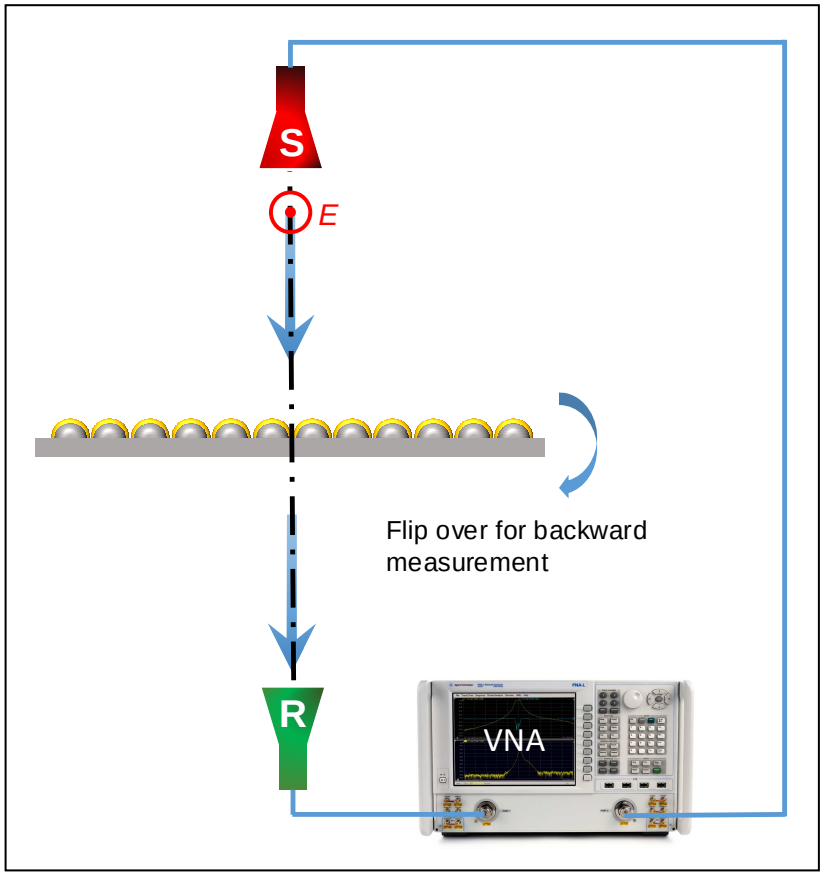

Figure 5.18 Experimental setup for the measurement of microwave transmission. Two dual-polarized quadruple-ridged horns serve as the source (tinted in red) and receiver (tinted in green), respectively, which are connected to a vector network analyzer. The backward transmission is measured by flipping over the sample.

The measurement of the tunable chiral metasurface is carried out in the anechoic chamber room, which has been reported in Section 3.2.2. The transmission measurement setup is shown in Fig. 5.18. The experimental results when two spiral

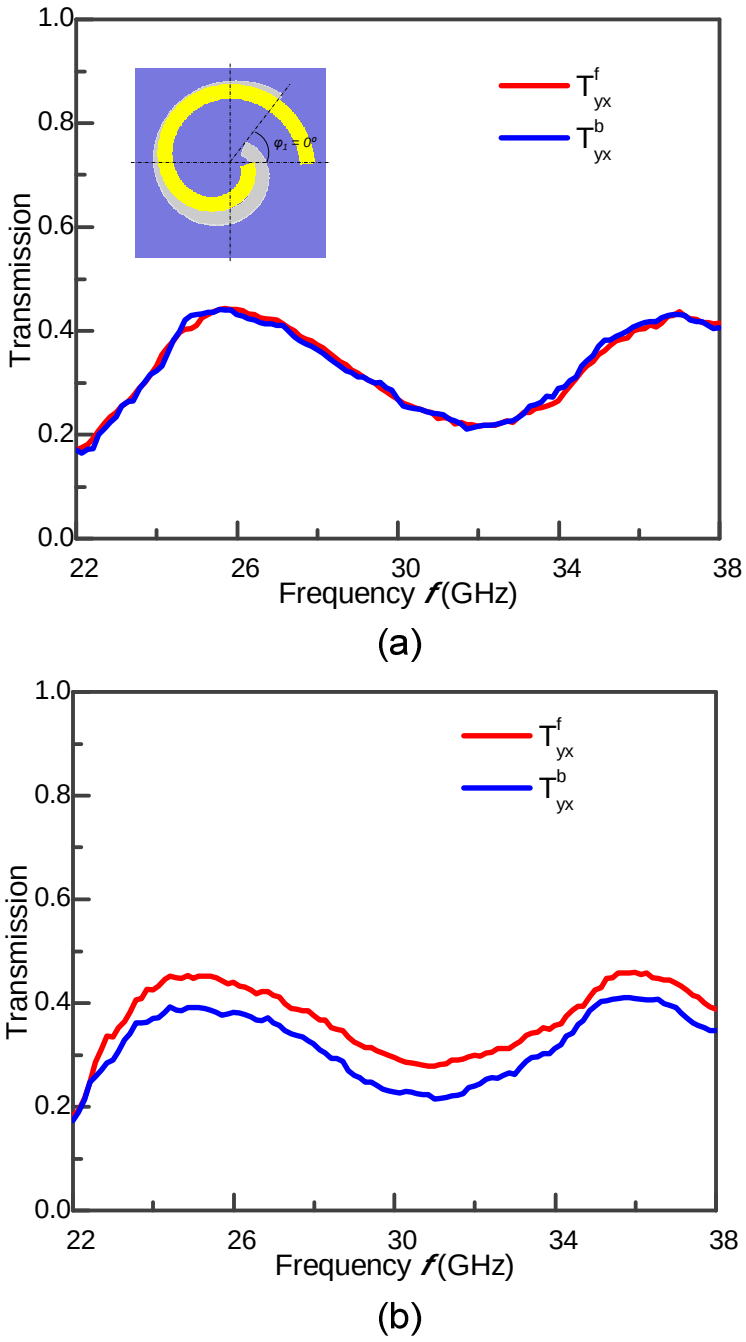

Figure 5.19 Experimental results of the transmission T_{yx} with symmetrically spiral pattern under forward and backward incidence when (a) both layers of spiral structures are planar and (b) the height of the top spiral structures is h = 1.0 mm.

structures are patterned symmetrically on both sides of the PDMS are shown in Fig. 5.19. When both layers of spiral structures are planar, the dual-spiral metasurface is achiral, resulting in symmetric transmission as shown in Fig. 5.19a. When the height of the top spiral structures is 1 mm, the forward and backward transmission become different as shown in Fig. 5.19b. The asymmetric transmission parameter is near zero as shown in Fig. 5.20 (red line) while it reaches 0.05 at h = 1.0 mm as shown in blue line. As a results, the transmission through the dual-spiral metasurface is controlled from symmetric transmission to asymmetric transmission.

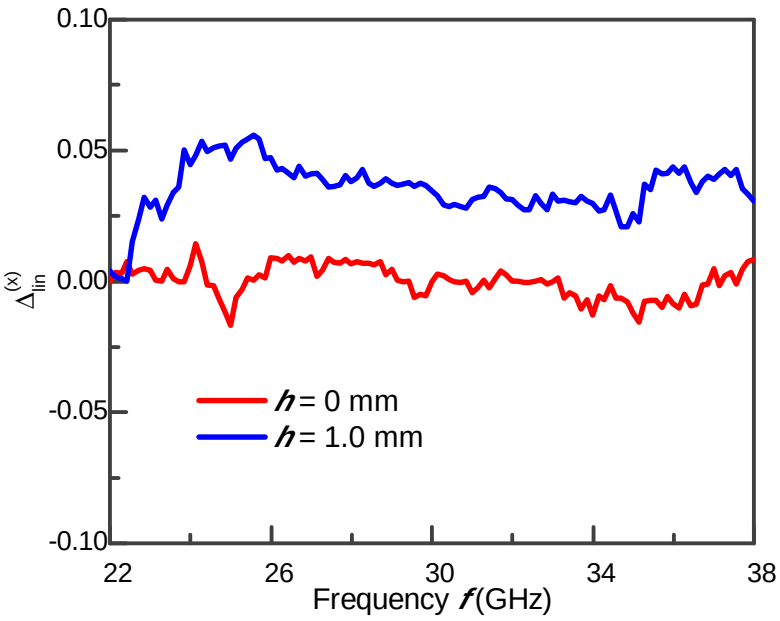

Figure 5.20 Experimental results of the transmission through the dual-spiral metasurface with symmetrically spiral pattern, which can be controlled from symmetric transmission at h = 0 mm to asymmetric transmission at h = 1.0 mm.

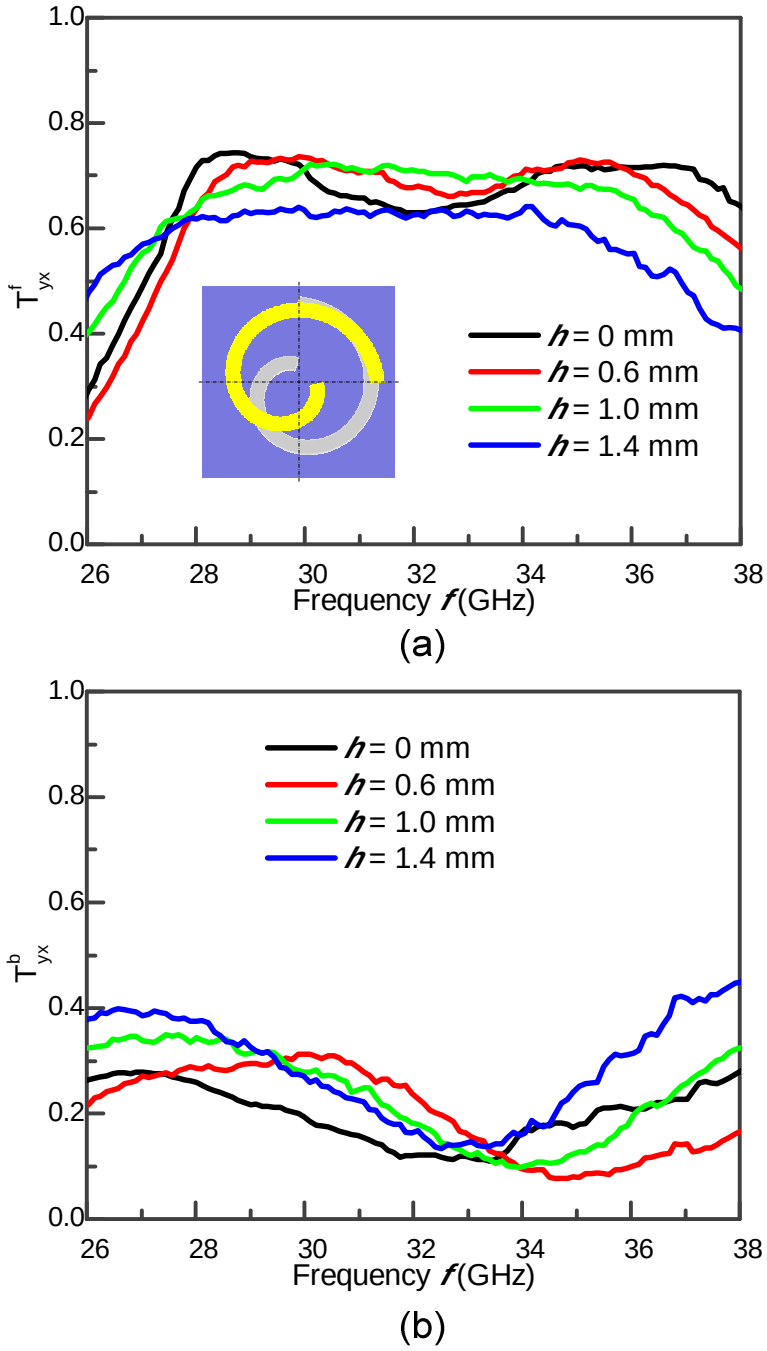

Figure 5.21 Experimental results of the transmission T_{yx} with asymmetrically spiral pattern when the height of the spiral structures is changed from 0 to 1.4 mm under (a) forward incidence and (b) backward incidence.

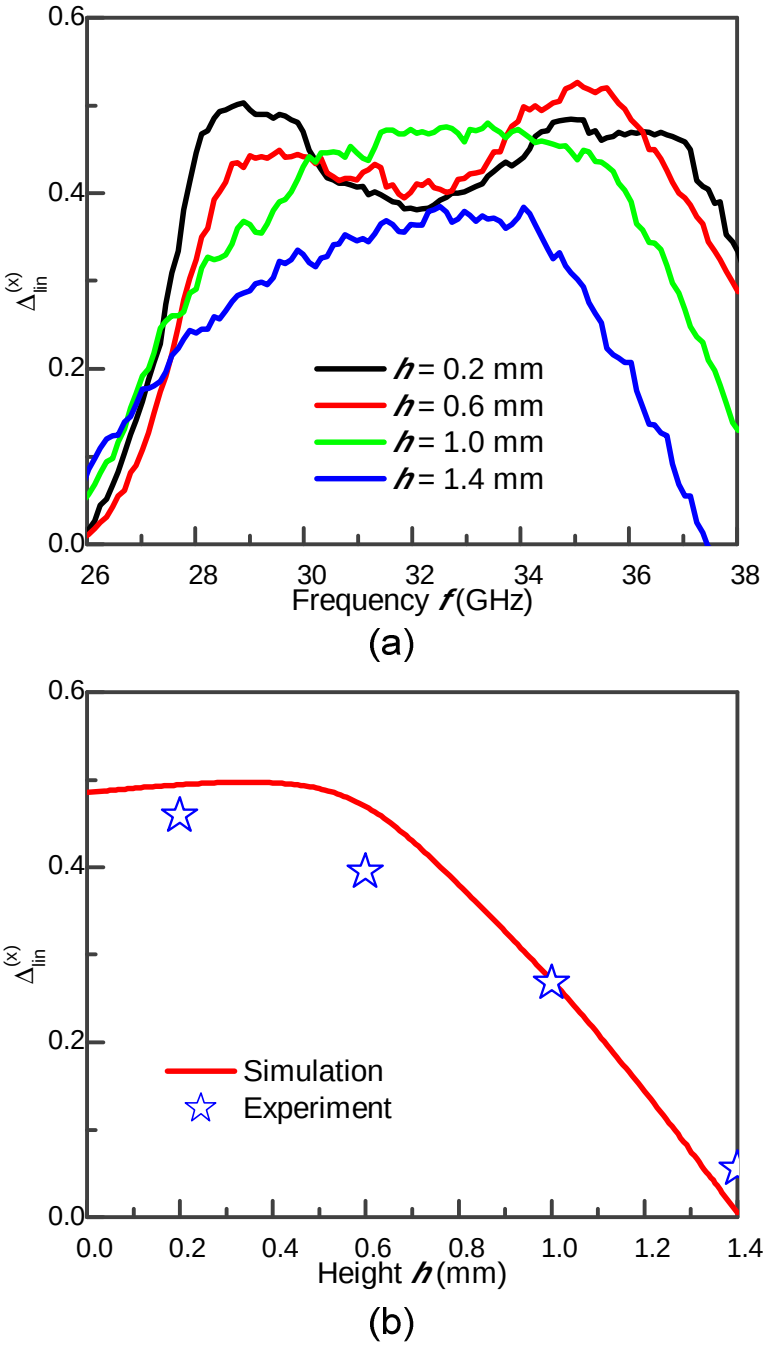

Figure 5.22 Experimental results with asymmetrically spiral pattern when the height of the spiral structures h is changed from 0 to 1.4 mm. (a) Asymmetric transmission parameter Δ. (b) Asymmetric transmission as a function of h at the frequency of 37 GHz.

The experimental results when two spiral structures are patterned asymmetrically on both sides of the PDMS are shown in Fig. 5.21. The asymmetric pattern of the spiral structures makes the metasurface chiral when both spiral structures are planar, resulting in asymmetric transmission under forward and backward incidence as shown in black line. The difference between the forward transmission and backward transmission is significantly enhanced. The asymmetric transmission reaches 50% as shown in Fig. 2.22a. At the frequency of 37 GHz, the metasurface exhibits large tunability on asymmetric transmission as shown in Fig. 2.22b. The asymmetric transmission can be tuned from 50% to 0 when the height of spiral structures is changed from 0 to 1.4 mm. The slight mismatch between simulation and experimental results is induced by fabrication error. The spiral structures are not uniform due to inhomogeneous pressure in the air reservoirs.

5.2.3 Wide-Angle Asymmetric Transmission

Here we also investigate the asymmetric transmission of dual-spiral metasurface under oblique incidence. The experimental setup for oblique incident measurement is shown in Fig. 5. 23. The transmission with different incident angles can be measured by tilting the sample with an angle of θ. The incident microwave is TE mode. The backward transmission can be measured by flipping over the sample. The experimental results of the transmission T_{yx} when the incident angle is changed from 0^0 to 45^0 with the height of the spiral structures h = 1.0 mm are shown in Fig. 5.24. The forward transmission is much higher than the backward transmission.

When the incident angle is increasing, the bandwidth of the forward transmission becomes narrow. The backward transmission keep at low level when the incident angle is increasing. As a results, the bandwidth of the asymmetric transmission (>40%) becomes narrow as shown in Fig. 5.25.

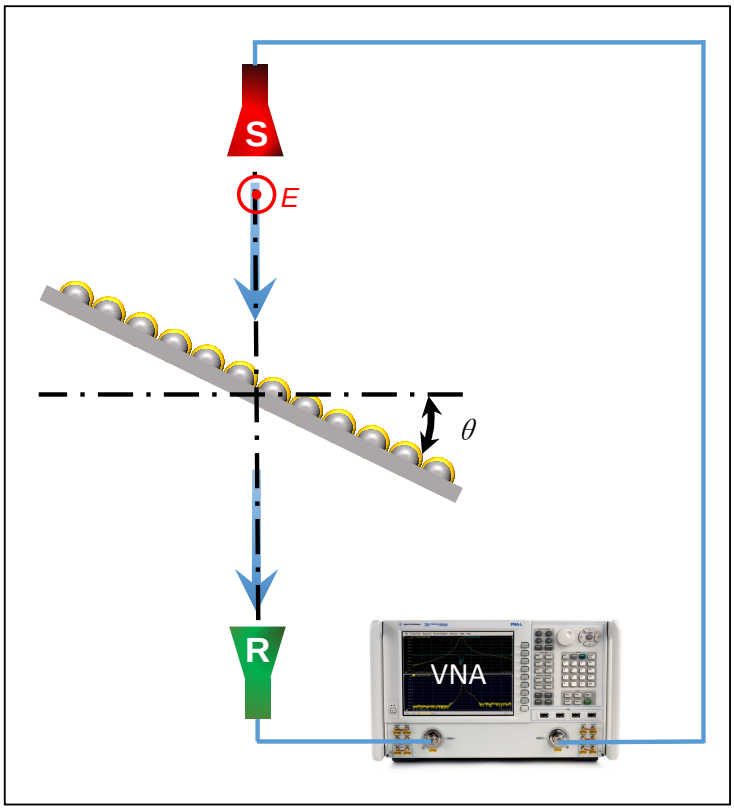

Figure 5.23 Experimental setup for transmission measurement under oblique incidence. The transmission with different incident angles can be measured by tilting the sample with an angle of θ varying from 0^{o} to 45^{o} with a step of 15^{o}. The incident mode is TE mode. The backward transmission is measured by flipping over the sample.

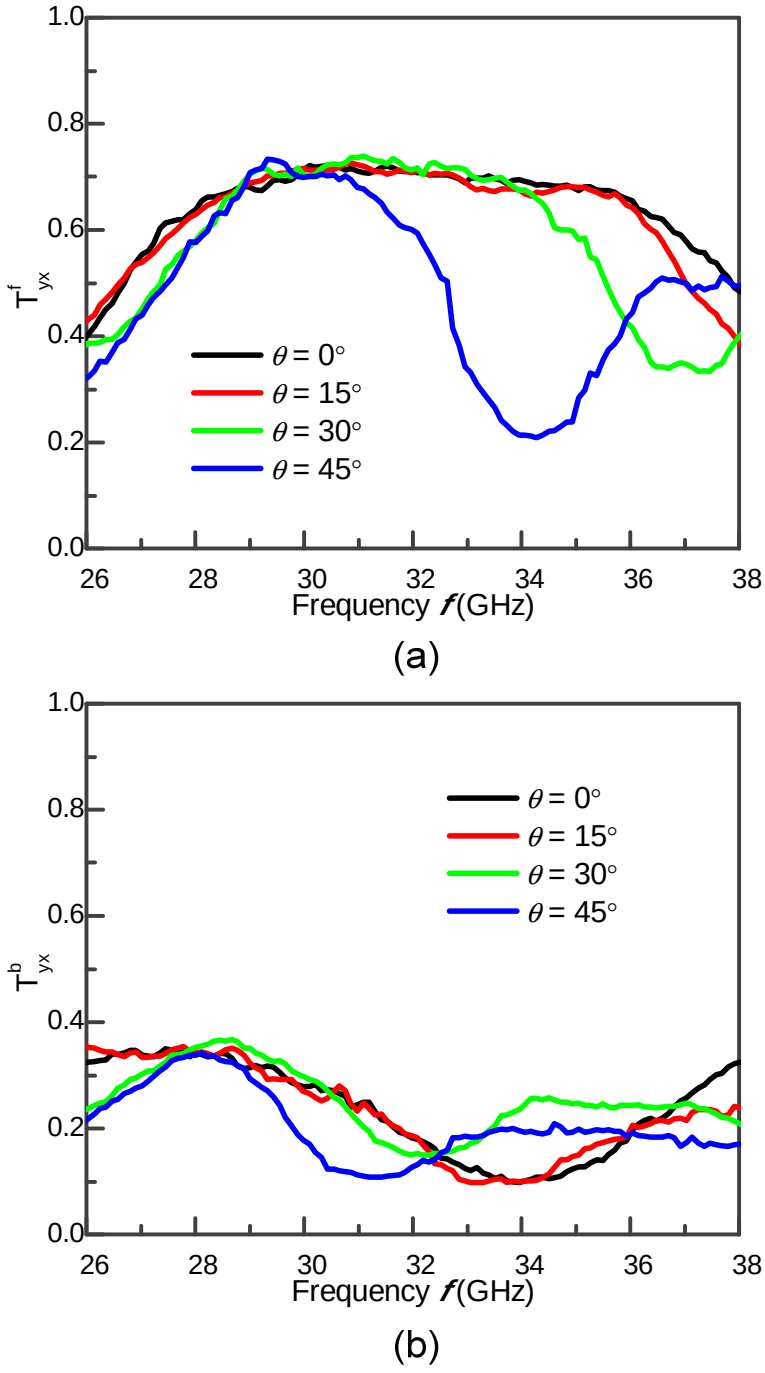

Figure 5.24 Experimental results of the transmission T_{yx} for TE mode oblique incidence with the height of the spiral structures of h = 1.0 mm under (a) forward incidence and (b) backward incidence.

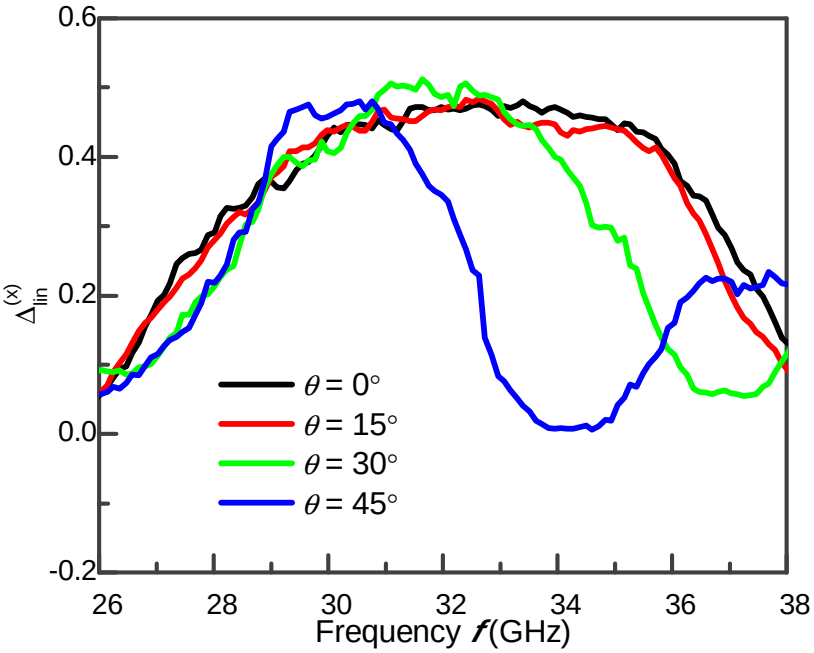

Figure 5.25 Experimental results of the asymmetric transmission with oblique TE incidence when the incident angle is changed from 0° to 45° with the height of the spiral structures h = 1.0 mm.

5.2.4 Asymmetric Transmission on Curved Surfaces

The asymmetric transmission is also demonstrated with different curvature of the dual-spiral metasurface. Since the PDMS is soft, the dual-spiral metasurface can be bent into different curvature. The experimental setup for the curved metasurface is shown in Fig. 5.26. The extent of bending is defined as the overall height of sample *d*. Similarly, the backward transmission is measured by flipping over the sample. The height of the spiral structures is *h* = 1.0 mm. The experimental results of the forward and backward transmission when overall height of the sample is

changed from 10 mm to 40 mm are shown in Fig. 5.27a and b, respectively. The asymmetric transmission is shown in Fig. 5.28. When *d* is increasing, the asymmetric transmission maintains at high level with a broad bandwidth.

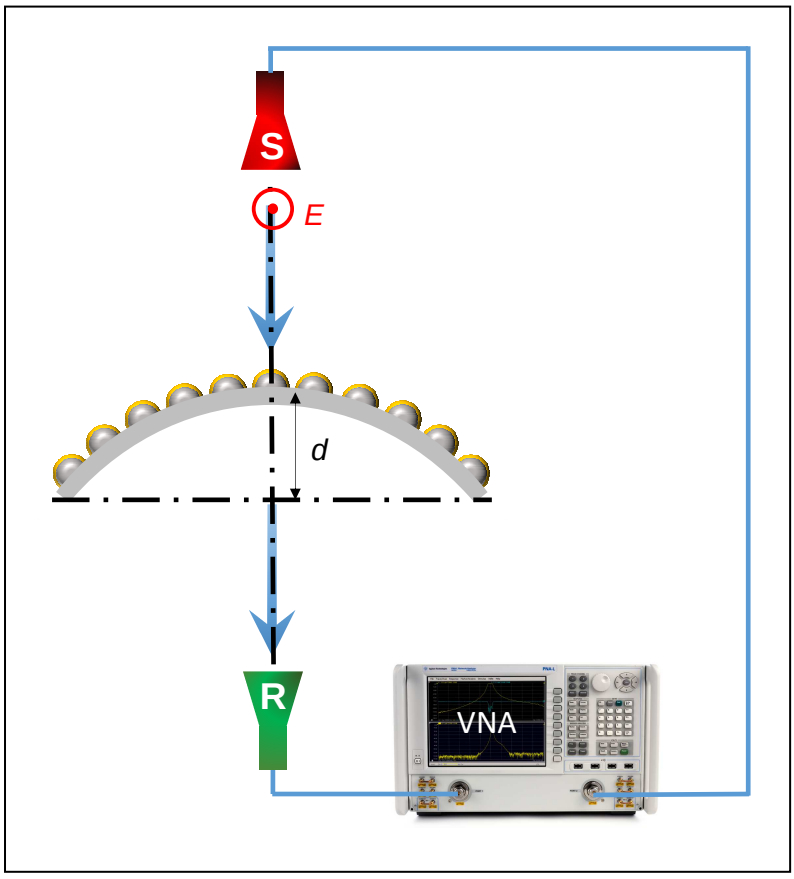

Figure 5.26 Experimental setup for transmission measurement when the tunable chiral metasurface is bent into different curvature. The extent of the bending is defined as the overall height of the sample d. The backward transmission is measured by flipping over the sample.

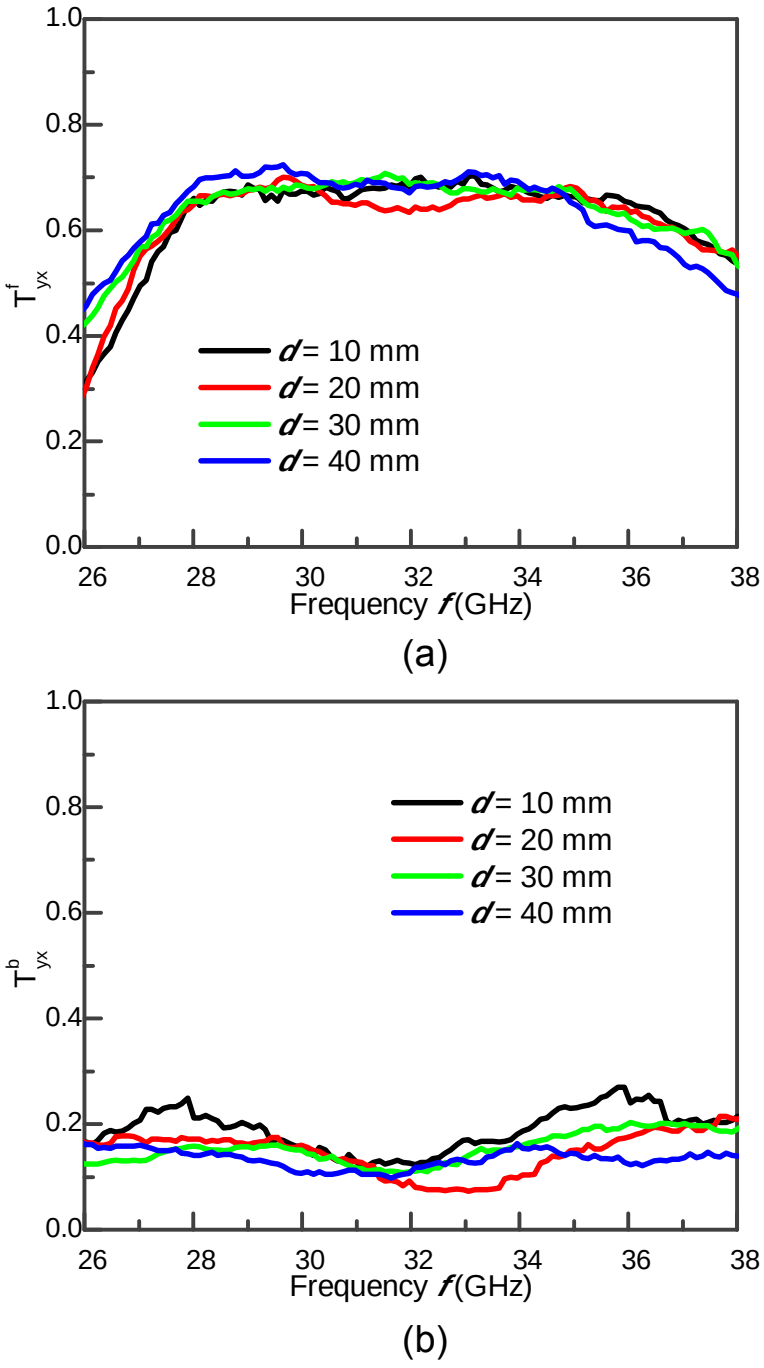

Figure 5.27 Experimental results of the transmission T_{yx} when the tunable chiral metasurface is bent into different curvature with the height of the spiral structures of h = 1.0 mm under (a) forward incidence and (b) backward incidence.

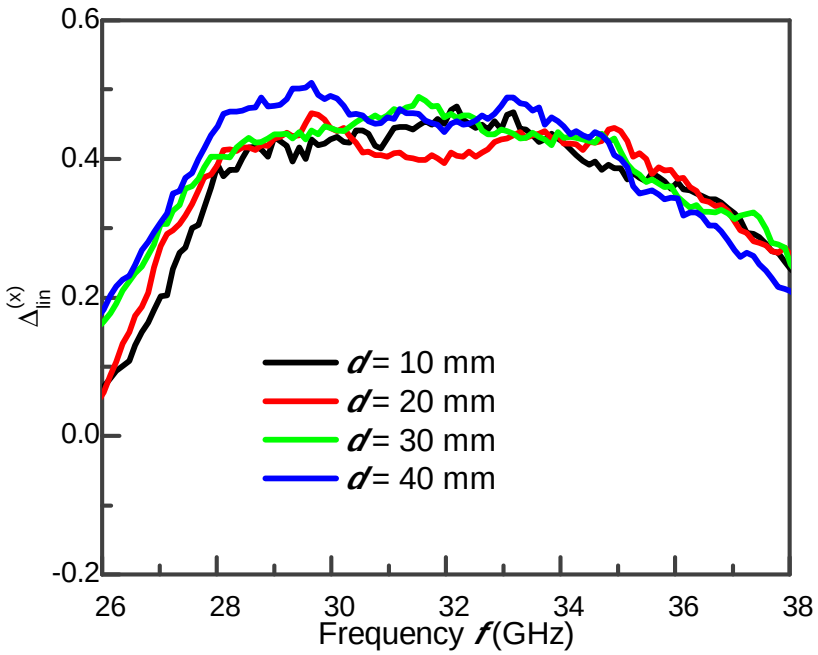

Figure 5.28 Experimental results of the asymmetric transmission when the tunable chiral metasurface is bent into different curvature with the height of the spiral structures of h = 1.0 mm.

5.3 Summary

This chapter focuses on the structure design, numerical analysis, sample fabrication and experiments of a tunable chiral metasurface for tunable asymmetric transmission. The theoretical analysis explores the generation of asymmetric transmission, which guides the design of the spiral structures. The dual-spiral structures interact strongly with each other and induce two resonance peaks due to the plasmon hybridization. In addition, the fabrication processes for solid metal incorporating with microfluidic technology are developed with a large tuning range

using polymer PDMS material. Experiments show that the developed dual-spiral metasurface controls the microwave from symmetric transmission to asymmetric transmission. A large tunability of the asymmetric transmission is realized from 50% to 0. The high asymmetric transmission is preserved with oblique incidence from 0º to 45º. In addition, the asymmetric transmission maintains at high level with a broad bandwidth is realized under different curvature of the curved dual-spiral metasurface.

The innovation of the tunable chiral metasurface is summarized as follows,

(a) This is the first demonstration of the solid metal reconfigured by the microfluidic technology to realize a tunable chiral metasurface from achiral to chiral, whereby the transmission through the metasurface can be controlled from symmetric transmission to asymmetric transmission.

(b) The fabrication processes for the reconfiguration of the solid metal using microfluidic technology is developed by combining photolithography and E-beam evaporation. A large tunability on the asymmetric transmission is realized by changing the air pressure in the microfluidic reservoir created in the PDMS.

(c) A curved dual-spiral metasurface is demonstrated due to the softness of water and PDMS, which has high asymmetric transmission in a broad bandwidth.

CHAPTER 6

CONCLUSIONS

6.1 Conclusions

Three different meta-liquid-based metasurfaces to actively control different electromagnetic response such as the absorption and transmission in microwave and terahertz regime have been innovated, i.e. water-resonator-based metasurface, liquid-metal-based metasurface, and tunable chiral metasurface. Various aspects, including theoretical studies, structure designs, fabrication technologies and experimental characterizations have been presented. The contents cover mainly the theoretical analysis and structure designs based on the microfluidic technology, and experiments of the three successfully designed meta-liquid-based metasurfaces. The major conclusions are listed here.

The water-resonator-based metasurface is studied theoretically, fabricated and experimented. The working principle in employing the magnetic resonance and diffraction grating effect for near-unity and ultra-broadband absorption are discussed thoroughly. The far-field measurement for omnidirectional absorption is developed. In addition, different concentrations of water-ethanol solutions are investigated to tune the absorption of the metasurface.

(a) This is the first demonstration of the combination of magnetic resonance and grating effect to realize an ultra-broadband and near-unity absorption

by using dielectric material, liquid water, embedded into the soft material, PDMS, across the entire Ku, K and Ka bands. Compared to other materials, liquid water not only provides high lossy properties which is essential to absorption, but also has much flexibility in the control of the shape of the structure.

(b) A real time control on the broadband absorption, including the absorption frequency and absorption strength, is firstly demonstrated by incorporating with the microfluidic technology. It has the capability to reshape the liquid-resonator by simply changing the volume of liquid in the microfluidic reservoir created in the PDMS.

(c) A curved water-resonator-based metasurface is demonstrated due to the softness of water and PDMS, which functions as an omnidirectional and broadband absorbing material on arbitrary curved surfaces.

A liquid-metal-based metasurface is theoretically studied, fabricated and experimented. A triple layer structure, PDMS/silicon/PDMS, is filled with liquid-metal for the formation and reconfiguration of the liquid-metal-pillars. The tuning method of the liquid-metal-pillars that are confined in the penetrated silicon cavities is provided. A frequency-agile and wide-angle absorption is studied and discussed.

(a) The combination of silicon structure layer and PDMS control layer for the liquid-metal injection and reconfiguration in microscale is developed. The triple layers structure, PDMS/silicon/PDMS allows the tuning of the liquid-

metal in the vertical direction to break the tuning limitation in 2D plane, which is a significant milestone for the tunable metasurface.

(b) A real time control on the absorption frequency is achieved by tuning the height of the liquid-metal-pillars in the terahertz regime. The coupling mechanism between the liquid-metal-pillars is investigated numerically, which provide a good understanding of how to control the absorption.

(c) A wide-angle absorption with broad bandwidth is firstly demonstrated with large angular tolerance up to 60^0. The mechanism of the broadband wide-angle absorption is numerically investigated.

A tunable chiral metasurface, which consists of a dielectric layer sandwiched between two metallic spiral layers, is theoretically studied, fabricated and experimented. The tunable chiral metasurface provide a real time control of the propagating wave from symmetric transmission to asymmetric transmission. The fabrication processes incorporating with e-beam evaporation are developed. In addition, the enhancement of the asymmetric transmission by structure modification is studied and discussed.

(a) This is the first demonstration of solid metal reconfigured by the microfluidic technology to realize a tunable chiral metasurface from achiral to chiral, whereby the propagating microwave through the metasurface can be controlled from symmetric transmission to asymmetric transmission.

(b) The fabrication processes for the reconfiguration of solid metal using microfluidic technology is developed by combining the photolithography

and E-beam evaporation. A large tunability on the asymmetric transmission is realized by changing air pressure in the microfluidic reservoir created in the PDMS.

(c) A curved dual-spiral metasurface is demonstrated due to the softness of water and PDMS, which has high asymmetric transmission in a broad bandwidth.

6.2 Recommendations

Recommendations for future research are summarized as follows

(a) The reconfiguration of the metasurface is realized by microfluidic technology, which utilizes a pump to apply different pressure. Despite the successful demonstrations of the electromagnetic response using the microfluidic technology, the tuning speed is limited. Hence this impedes the potential applications of the meta-liquid-based metasurfaces, where fast tuning speed is required. One possible solution is to scale down the reconfigured structures. Smaller size of metasurface can significantly facilitate the tuning speed.

(b) Although the absorption bandwidth demonstrated in Chapter 3 is ultra-broad, it can still be broadened by using inhomogeneous water-resonator array. The non-uniform pattern of water-resonators will induce multiple magnetic resonance so as to facilitate the bandwidth. To realize non-uniform distribution of water-resonators, a random access tuning method is required as discussed in Chapter 2.

(c) The tuning range of the absorption and asymmetric transmission demonstrated in Chapter 3 and Chapter 5, respectively, can be further increased by expanding the top PDMS membrane to a greater degree. However, the increasing pressure will break the bonding of top and bottom PDMS. One possible approach is to make the top PDMS membrane thinner, such that smaller pressure is required to expand the top PDMS

membrane. This thinner PDMS membrane can be achieved by using a spin coater with high spinning speed.

(d) The tuning range of the absorption frequency demonstrated in Chapter 4 can be further facilitated by using a thicker silicon substrate so as to increase the maximum height of the liquid-metal-pillars. However, the increasing height of the silicon results in more FP resonance peaks in the spectrum. One approach is to replace the silicon with lower refractive index material, such as crystal quartz.

(e) The liquid material we are using in Chapter 4 is mercury which is toxic. Although the mercury is totally sealed in the PDMS reservoir, it still impedes its practical applications. One approach to solve the limitation is to replace the mercury with non-toxic material, such as galinstan.

(f) In the tunable chiral metasurface design, strong asymmetric transmission is successfully demonstrated. However, it can be improved by enhancing the chirality of the metasurface. One approach is to using multi-layer spiral structures.

AUTHOR'S PUBLICATIONS

Journal Paper

1. W. M. Zhu, Q. H. Song, L. B. Yan, W. Zhang, P. C. Wu, L. K. Chin, H. Cai, D. P. Tsai, Z. X. Shen, T. W. Deng, S. K. Ting, Y. D. Gu, G. Q. Lo, D. L. Kwong, Z. C. Yang, R. Huang, A. Q. Liu and N. Zheludev, "A Flat Lens with Tunable Phase Gradient by Using Random Access Reconfigurable Metamaterial", *Advanced Materials*, **27** (32), 4739-4743, 2015.

2. Q. H. Song, W. Zhang, P. C. Wu, W. M. Zhu, Z. X. Shen, P. H. J. Chong, Q. X. Liang, Z. C. Yang, Y. L. Hao, H. Cai, H. F. Zhou, Y. D. Gu, G. Q. Lo, D. P. Tsai, T. Bourouina, Y. Leprince-Wang and A. Q. Liu, "Water-Resonator-Based Metasurface: An Ultra-Broadband and Near-Unity Absorption", *Advanced Optical Materials*, **5**, 1601103, 2017.

3. Q. H. Song, P. C. Wu, W. Zhang, W. M. Zhu, J. H. Teng, Q. X. Liang, Z. X. Shen, P. H. J. Chong, D. P. Tsai, T. Bourouina, Y. Leprince-Wang and A. Q. Liu, "Liquid-Metal-Based Metasurface for Terahertz Absorption Material: Frequency-Agile and Wide-Angle", *APL Materials*, **5**, 066103, 2017.

4. Q. H. Song, W. Zhang, W. M. Zhu, P. C. Wu, C. W. Qiu, Z. X. Shen, D. P. Tsai, T. Bourouina, Y. Leprince-Wang and A. Q. Liu, "Active Bianisotropic Chiral Metasurface For Asymmetric Transmission". *Advanced Materials* (Submitted).

Conference Paper

1. Q. H. Song, W. M. Zhu, W. Zhang and A. Q. Liu, "Tunable Meta-Liquid-material based on mercury microdroplets," 5th International Conference on Metamaterials, Photonic Crystals and Plasmonics (META2014), Singapore, 2014, (Oral).
2. Q. H. Song, P. C. Wu, W. M. Zhu, W. Zhang, Z. X. Shen, Q. X. Liang, Z. C. Yang, Y. F. Jin, Y. L. Hao, T. Bourouina, Y. Leprince-Wang, and A. Q. Liu, "Transition from plasmon coupling to plasmon-microcavity hybridization," 35th International Conference on Lasers and Electro-Optics (CLEO2015), San Jose, USA, 2015 (Oral).
3. Q. H. Song, W. Zhang, H. Cai, Y. D. Gu, P. C. Wu, W. M. Zhu, Q. X. Liang, Z. C. Yang, Y. F. Jin, Y. L. Hao, D. L. Kwong, T. Bourouina, Y. Leprince-Wang and A. Q. Liu, "A Tunable Metamaterial for Wide-Angle and Broadband Absorption Through Meta-Water-Capsule Coatings", 36th International Conference on Lasers and Electro-Optics (CLEO 2016), San Jose, CA, USA, 2016 (Oral).

BIBLIOGRAPHY

[1] D. Barber and I. C. Freestone, "An investigation of the origin of the colour of the Lycurgus Cup by analytical transmission electron microscopy", *Archaeometry*, **32**, pp. 33-45 (1990).

[2] J. B. Pendry, D. Schurig and D. R. Smith, "Controlling electromagnetic fields", *Science*, **312**, pp. 1780-1782 (2006).

[3] D. R. Smith, J. B. Pendry and M. C. Wiltshire, "Metamaterials and negative refractive index", *Science*, **305**, pp. 788-792 (2004).

[4] N. Yu and F. Capasso, "Flat optics with designer metasurfaces", *Nature Mater.*, **13**, pp. 139-150 (2014).

[5] R. A. Shelby, D. R. Smith and S. Schultz, "Experimental verification of a negative index of refraction", *Science*, **292**, pp. 77-79 (2001).

[6] Y. Liu and X. Zhang, "Metamaterials: a new frontier of science and technology", *Chem. Soc. Rev.*, **40**, pp. 2494-2507 (2011).

[7] H.-T. Chen, W. J. Padilla, J. M. Zide, A. C. Gossard, A. J. Taylor and R. D. Averitt, "Active terahertz metamaterial devices", *Nature*, **444**, pp. 597-600 (2006).

[8] I. C. Khoo, "Nonlinear optics, active plasmonics and metamaterials with liquid crystals", *Prog. Quant. Electron.*, **38**, pp. 77-117 (2014).

[9] M. A. Unger, H.-P. Chou, T. Thorsen, A. Scherer and S. R. Quake, "Monolithic microfabricated valves and pumps by multilayer soft lithography", *Science*, **288**, pp. 113-116 (2000).

[10] T. S. Kasirga, Y. N. Ertas and M. Bayindir, "Microfluidics for reconfigurable electromagnetic metamaterials", *Appl. Phys. Lett.*, **95**, pp. 214102 (2009).

[11] W. Zhu, B. Dong, Q. Song, W. Zhang, R. Huang, S. Ting and A. Liu, "Tunable meta-fluidic-materials base on multilayered microfluidic system",

presented at *Micro Electro Mechanical Systems (MEMS), 2014 IEEE 27th International Conference on*, 2014.

[12] Q. Wu, C. P. Scarborough, B. G. Martin, R. K. Shaw, D. H. Werner, E. Lier and X. Wang, "A Ku-Band Dual Polarization Hybrid-Mode Horn Antenna Enabled by Printed-Circuit-Board Metasurfaces", *IEEE. T. Antenn. Propag*, **61**, pp. 1089-1098 (2013).

[13] G.-T. Chiu and J. M. Shaw, "Optical lithography: introduction", *Ibm. J. Res. Dev.*, **41**, pp. 3-6 (1997).

[14] R. Pease, "Electron beam lithography", *Contemp. Phys.*, **22**, pp. 265-290 (1981).

[15] S. Y. Chou, P. R. Krauss and P. J. Renstrom, "Nanoimprint lithography", *Journal of Vacuum Science & Technology B: Microelectronics and Nanometer Structures Processing, Measurement, and Phenomena*, **14**, pp. 4129-4133 (1996).

[16] V. G. Veselago, "The electrodynamics of substances with simultaneously negative values of and μ", *Soviet physics uspekhi*, **10**, pp. 509 (1968).

[17] J. B. Pendry, A. J. Holden, D. Robbins and W. Stewart, "Magnetism from conductors and enhanced nonlinear phenomena", *Ieee. T. Microw. Theory*, **47**, pp. 2075-2084 (1999).

[18] D. R. Smith, W. J. Padilla, D. Vier, S. C. Nemat-Nasser and S. Schultz, "Composite medium with simultaneously negative permeability and permittivity", *Phys. Rev. Lett.*, **84**, pp. 4184 (2000).

[19] Q. Zhao, L. Kang, B. Du, H. Zhao, Q. Xie, X. Huang, B. Li, J. Zhou and L. Li, "Experimental demonstration of isotropic negative permeability in a three-dimensional dielectric composite", *Phys. Rev. Lett.*, **101**, pp. 027402 (2008).

[20] O. Paul, C. Imhof, B. Reinhard, R. Zengerle and R. Beigang, "Negative index bulk metamaterial at terahertz frequencies", *Opt. Express*, **16**, pp. 6736-6744 (2008).

[21] N. Wongkasem, A. Akyurtlu, J. Li, A. Tibolt, Z. Kang and W. D. Goodhue, "Novel broadband terahertz negative refractive index metamaterials: Analysis and experiment", *Prog. Electromagn. Res.*, **64**, pp. 205-218 (2006).

[22] V. M. Shalaev, W. Cai, U. K. Chettiar, H.-K. Yuan, A. K. Sarychev, V. P. Drachev and A. V. Kildishev, "Negative index of refraction in optical metamaterials", *Opt. Lett.*, **30**, pp. 3356-3358 (2005).

[23] J. Valentine, S. Zhang, T. Zentgraf, E. Ulin-Avila, D. A. Genov, G. Bartal and X. Zhang, "Three-dimensional optical metamaterial with a negative refractive index", *Nature*, **455**, pp. 376-379 (2008).

[24] S. Zhang, W. Fan, N. Panoiu, K. Malloy, R. Osgood and S. Brueck, "Experimental demonstration of near-infrared negative-index metamaterials", *Phys. Rev. Lett.*, **95**, pp. 137404 (2005).

[25] H.-K. Yuan, U. K. Chettiar, W. Cai, A. V. Kildishev, A. Boltasseva, V. P. Drachev and V. M. Shalaev, "A negative permeability material at red light", *Opt. Express*, **15**, pp. 1076-1083 (2007).

[26] S. P. Burgos, R. De Waele, A. Polman and H. A. Atwater, "A single-layer wide-angle negative-index metamaterial at visible frequencies", *Nature Mater.*, **9**, pp. 407-412 (2010).

[27] H. J. Lezec, J. A. Dionne and H. A. Atwater, "Negative refraction at visible frequencies", *Science*, **316**, pp. 430-432 (2007).

[28] N. Landy, S. Sajuyigbe, J. Mock, D. Smith and W. Padilla, "Perfect metamaterial absorber", *Phys. Rev. Lett.*, **100**, pp. 207402 (2008).

[29] J. E. Raynolds, B. A. Munk, J. B. Pryor and R. J. Marhefka, "Ohmic loss in frequency-selective surfaces", *J. Appl. Phys.*, **93**, pp. 5346-5358 (2003).

[30] F. Bilotti, L. Nucci and L. Vegni, "An SRR based microwave absorber", *Microw. Opt. Technol. Let*, **48**, pp. 2171-2175 (2006).

[31] B. Bian, S. Liu, S. Wang, X. Kong, H. Zhang, B. Ma and H. Yang, "Novel triple-band polarization-insensitive wide-angle ultra-thin microwave metamaterial absorber", *J. Appl. Phys.*, **114**, pp. 194511 (2013).

[32] H. Tao, C. Bingham, D. Pilon, K. Fan, A. Strikwerda, D. Shrekenhamer, W. Padilla, X. Zhang and R. Averitt, "A dual band terahertz metamaterial absorber", *Journal of physics D: Applied physics*, **43**, pp. 225102 (2010).

[33] Y. Ma, Q. Chen, J. Grant, S. C. Saha, A. Khalid and D. R. Cumming, "A terahertz polarization insensitive dual band metamaterial absorber", *Opt. Lett.*, **36**, pp. 945-947 (2011).

[34] X. Liu, T. Tyler, T. Starr, A. F. Starr, N. M. Jokerst and W. J. Padilla, "Taming the blackbody with infrared metamaterials as selective thermal emitters", *Phys. Rev. Lett.*, **107**, pp. 045901 (2011).

[35] X. Liu, T. Starr, A. F. Starr and W. J. Padilla, "Infrared spatial and frequency selective metamaterial with near-unity absorbance", *Phys. Rev. Lett.*, **104**, pp. 207403 (2010).

[36] M. K. Hedayati, M. Javaherirahim, B. Mozooni, R. Abdelaziz, A. Tavassolizadeh, V. S. K. Chakravadhanula, V. Zaporojtchenko, T. Strunkus, F. Faupel and M. Elbahri, "Design of a perfect black absorber at visible frequencies using plasmonic metamaterials", *Adv. Mater.*, **23**, pp. 5410-5414 (2011).

[37] T. Cao, C.-w. Wei, R. E. Simpson, L. Zhang and M. J. Cryan, "Broadband polarization-independent perfect absorber using a phase-change metamaterial at visible frequencies", *Sci. Rep.*, **4**, pp. 3955 (2014).

[38] Y. Avitzour, Y. A. Urzhumov and G. Shvets, "Wide-angle infrared absorber based on a negative-index plasmonic metamaterial", *Phys. Rev. B*, **79**, pp. 045131 (2009).

[39] J. Hao, J. Wang, X. Liu, W. J. Padilla, L. Zhou and M. Qiu, "High performance optical absorber based on a plasmonic metamaterial", *Appl. Phys. Lett.*, **96**, pp. 251104 (2010).

[40] F. Ding, Y. Cui, X. Ge, Y. Jin and S. He, "Ultra-broadband microwave metamaterial absorber", *Appl. Phys. Lett.*, **100**, pp. 103506 (2012).

[41] Y. Cui, K. H. Fung, J. Xu, H. Ma, Y. Jin, S. He and N. X. Fang, "Ultrabroadband light absorption by a sawtooth anisotropic metamaterial slab", *Nano Lett.*, **12**, pp. 1443-1447 (2012).

[42] A. K. Azad, W. J. Kort-Kamp, M. Sykora, N. R. Weisse-Bernstein, T. S. Luk, A. J. Taylor, D. A. Dalvit and H.-T. Chen, "Metasurface broadband solar absorber", *Sci. Rep.*, **6**, pp. (2016).

[43] N. Landy, C. Bingham, T. Tyler, N. Jokerst, D. Smith and W. Padilla, "Design, theory, and measurement of a polarization-insensitive absorber for terahertz imaging", *Phys. Rev. B*, **79**, pp. 125104 (2009).

[44] X. Shen, T. J. Cui, J. Zhao, H. F. Ma, W. X. Jiang and H. Li, "Polarization-independent wide-angle triple-band metamaterial absorber", *Opt. Express*, **19**, pp. 9401-9407 (2011).

[45] D. R. Smith, J. Gollub, J. J. Mock, W. J. Padilla and D. Schurig, "Calculation and measurement of bianisotropy in a split ring resonator metamaterial", *J. Appl. Phys.*, **100**, pp. 024507 (2006).

[46] D. Smith, D. Schurig and J. Mock, "Characterization of a planar artificial magnetic metamaterial surface", *Phys. Rev. E*, **74**, pp. 036604 (2006).

[47] H. Tao, C. Bingham, A. Strikwerda, D. Pilon, D. Shrekenhamer, N. Landy, K. Fan, X. Zhang, W. Padilla and R. Averitt, "Highly flexible wide angle of incidence terahertz metamaterial absorber: Design, fabrication, and characterization", *Phys. Rev. B*, **78**, pp. 241103 (2008).

[48] B. Wang, T. Koschny and C. M. Soukoulis, "Wide-angle and polarization-independent chiral metamaterial absorber", *Phys. Rev. B*, **80**, pp. 033108 (2009).

[49] M. Pu, C. Hu, M. Wang, C. Huang, Z. Zhao, C. Wang, Q. Feng and X. Luo, "Design principles for infrared wide-angle perfect absorber based on plasmonic structure", *Opt. Express*, **19**, pp. 17413-17420 (2011).

[50] O. Luukkonen, F. Costa, C. R. Simovski, A. Monorchio and S. A. Tretyakov, "A thin electromagnetic absorber for wide incidence angles and both polarizations", *IEEE. T. Antenn. Propag*, **57**, pp. 3119-3125 (2009).

[51] N. Yu, P. Genevet, M. A. Kats, F. Aieta, J.-P. Tetienne, F. Capasso and Z. Gaburro, "Light propagation with phase discontinuities: generalized laws of reflection and refraction", *Science*, **334**, pp. 333-337 (2011).

[52] N. Yu, F. Aieta, P. Genevet, M. A. Kats, Z. Gaburro and F. Capasso, "A broadband, background-free quarter-wave plate based on plasmonic metasurfaces", *Nano Lett.*, **12**, pp. 6328-6333 (2012).

[53] R. Blanchard, G. Aoust, P. Genevet, N. Yu, M. A. Kats, Z. Gaburro and F. Capasso, "Modeling nanoscale V-shaped antennas for the design of optical phased arrays", *Phys. Rev. B*, **85**, pp. 155457 (2012).

[54] F. Aieta, P. Genevet, M. A. Kats, N. Yu, R. Blanchard, Z. Gaburro and F. Capasso, "Aberration-free ultrathin flat lenses and axicons at telecom wavelengths based on plasmonic metasurfaces", *Nano Lett.*, **12**, pp. 4932-4936 (2012).

[55] F. Aieta, P. Genevet, N. Yu, M. A. Kats, Z. Gaburro and F. Capasso, "Out-of-Plane Reflection and Refraction of Light by Anisotropic Optical Antenna Metasurfaces with Phase Discontinuities", *Nano Lett.*, **12**, pp. 1702-1706 (2012).

[56] X. Zhang, Z. Tian, W. Yue, J. Gu, S. Zhang, J. Han and W. Zhang, "Broadband terahertz wave deflection based on C-shape complex metamaterials with phase discontinuities", *Adv. Mater.*, **25**, pp. 4567-4572 (2013).

[57] L. Liu, X. Zhang, M. Kenney, X. Su, N. Xu, C. Ouyang, Y. Shi, J. Han, W. Zhang and S. Zhang, "Broadband metasurfaces with simultaneous control of phase and amplitude", *Adv. Mater.*, **26**, pp. 5031-5036 (2014).

[58] Q. Yang, J. Gu, D. Wang, X. Zhang, Z. Tian, C. Ouyang, R. Singh, J. Han and W. Zhang, "Efficient flat metasurface lens for terahertz imaging", *Opt. Express*, **22**, pp. 25931-25939 (2014).

[59] X. Li, S. Xiao, B. Cai, Q. He, T. J. Cui and L. Zhou, "Flat metasurfaces to focus electromagnetic waves in reflection geometry", *Opt. Lett.*, **37**, pp. 4940-4942 (2012).

[60] Y.-W. Huang, W. T. Chen, W.-Y. Tsai, P. C. Wu, C.-M. Wang, G. Sun and D. P. Tsai, "Aluminum plasmonic multicolor meta-hologram", *Nano Lett.*, **15**, pp. 3122-3127 (2015).

[61] W. T. Chen, K.-Y. Yang, C.-M. Wang, Y.-W. Huang, G. Sun, I.-D. Chiang, C. Y. Liao, W.-L. Hsu, H. T. Lin and S. Sun, "High-efficiency broadband meta-hologram with polarization-controlled dual images", *Nano Lett.*, **14**, pp. 225-230 (2013).

[62] X. Ding, F. Monticone, K. Zhang, L. Zhang, D. Gao, S. N. Burokur, A. de Lustrac, Q. Wu, C. W. Qiu and A. Alù, "Ultrathin Pancharatnam–Berry Metasurface with Maximal Cross-Polarization Efficiency", *Adv. Mater.*, **27**, pp. 1195-1200 (2015).

[63] L. Huang, X. Chen, H. Mühlenbernd, G. Li, B. Bai, Q. Tan, G. Jin, T. Zentgraf and S. Zhang, "Dispersionless phase discontinuities for controlling light propagation", *Nano Lett.*, **12**, pp. 5750-5755 (2012).

[64] M. Tymchenko, J. S. Gomez-Diaz, J. Lee, N. Nookala, M. A. Belkin and A. Alù, "Gradient nonlinear Pancharatnam-Berry metasurfaces", *Phys. Rev. Lett.*, **115**, pp. 207403 (2015).

[65] G. Zheng, H. Mühlenbernd, M. Kenney, G. Li, T. Zentgraf and S. Zhang, "Metasurface holograms reaching 80% efficiency", *Nat. Nanotechnol.*, **10**, pp. 308-312 (2015).

[66] S. Zhang, D. A. Genov, Y. Wang, M. Liu and X. Zhang, "Plasmon-induced transparency in metamaterials", *Phys. Rev. Lett.*, **101**, pp. 047401 (2008).

[67] R. D. Kekatpure, E. S. Barnard, W. Cai and M. L. Brongersma, "Phase-coupled plasmon-induced transparency", *Phys. Rev. Lett.*, **104**, pp. 243902 (2010).

[68] R. Singh, W. Cao, I. Al-Naib, L. Cong, W. Withayachumnankul and W. Zhang, "Ultrasensitive terahertz sensing with high-Q Fano resonances in metasurfaces", *Appl. Phys. Lett.*, **105**, pp. 171101 (2014).

[69] S. H. Mousavi, I. Kholmanov, K. B. Alici, D. Purtseladze, N. Arju, K. Tatar, D. Y. Fozdar, J. W. Suk, Y. Hao and A. B. Khanikaev, "Inductive

tuning of Fano-resonant metasurfaces using plasmonic response of graphene in the mid-infrared", *Nano Lett.*, **13**, pp. 1111-1117 (2013).

[70] D. A. Powell, I. V. Shadrivov and Y. S. Kivshar, "Nonlinear electric metamaterials", *Appl. Phys. Lett.*, **95**, pp. 084102 (2009).

[71] E. Poutrina, D. Huang and D. R. Smith, "Analysis of nonlinear electromagnetic metamaterials", *New J. Phys.*, **12**, pp. 093010 (2010).

[72] A. A. Zharov, I. V. Shadrivov and Y. S. Kivshar, "Nonlinear properties of left-handed metamaterials", *Phys. Rev. Lett.*, **91**, pp. 037401 (2003).

[73] F. Niesler, N. Feth, S. Linden, J. Niegemann, J. Gieseler, K. Busch and M. Wegener, "Second-harmonic generation from split-ring resonators on a GaAs substrate", *Opt. Lett.*, **34**, pp. 1997-1999 (2009).

[74] B. K. Canfield, H. Husu, J. Laukkanen, B. Bai, M. Kuittinen, J. Turunen and M. Kauranen, "Local field asymmetry drives second-harmonic generation in noncentrosymmetric nanodimers", *Nano Lett.*, **7**, pp. 1251-1255 (2007).

[75] G. A. Wurtz, R. Pollard, W. Hendren, G. Wiederrecht, D. Gosztola, V. Podolskiy and A. V. Zayats, "Designed ultrafast optical nonlinearity in a plasmonic nanorod metamaterial enhanced by nonlocality", *Nat. Nanotechnol.*, **6**, pp. 107-111 (2011).

[76] W. R. Somerville, D. A. Powell and I. V. Shadrivov, "Second harmonic generation with zero phase velocity waves", *Appl. Phys. Lett.*, **98**, pp. 161111 (2011).

[77] H. Kim, A. B. Kozyrev, A. Karbassi and D. W. van Der Weide, "Compact left-handed transmission line as a linear phase–voltage modulator and efficient harmonic generator", *IEEE. T. Microw. Theory*, **55**, pp. 571-578 (2007).

[78] D. Schurig, J. Mock, B. Justice, S. A. Cummer, J. B. Pendry, A. Starr and D. Smith, "Metamaterial electromagnetic cloak at microwave frequencies", *Science*, **314**, pp. 977-980 (2006).

[79] B. Edwards, A. Alù, M. G. Silveirinha and N. Engheta, "Experimental verification of plasmonic cloaking at microwave frequencies with metamaterials", *Phys. Rev. Lett.*, **103**, pp. 153901 (2009).

[80] A. Alù and N. Engheta, "Achieving transparency with plasmonic and metamaterial coatings", *Phys. Rev. E*, **72**, pp. 016623 (2005).

[81] A. Alù, "Mantle cloak: Invisibility induced by a surface", *Phys. Rev. B*, **80**, pp. 245115 (2009).

[82] J. Li and J. Pendry, "Hiding under the carpet: a new strategy for cloaking", *Phys. Rev. Lett.*, **101**, pp. 203901 (2008).

[83] R. Liu, C. Ji, J. Mock, J. Chin, T. Cui and D. Smith, "Broadband ground-plane cloak", *Science*, **323**, pp. 366-369 (2009).

[84] J. Lee, J. Blair, V. Tamma, Q. Wu, S. Rhee, C. Summers and W. Park, "Direct visualization of optical frequency invisibility cloak based on silicon nanorod array", *Opt. Express*, **17**, pp. 12922-12928 (2009).

[85] X. Ni, Z. J. Wong, M. Mrejen, Y. Wang and X. Zhang, "An ultrathin invisibility skin cloak for visible light", *Science*, **349**, pp. 1310-1314 (2015).

[86] H.-J. Lee and J.-G. Yook, "Biosensing using split-ring resonators at microwave regime", *Appl. Phys. Lett.*, **92**, pp. 254103 (2008).

[87] H.-J. Lee, H.-S. Lee, K.-H. Yoo and J.-G. Yook, "DNA sensing using split-ring resonator alone at microwave regime", *J. Appl. Phys.*, **108**, pp. 014908 (2010).

[88] F. Miyamaru, S. Hayashi, C. Otani, K. Kawase, Y. Ogawa, H. Yoshida and E. Kato, "Terahertz surface-wave resonant sensor with a metal hole array", *Opt. Lett.*, **31**, pp. 1118-1120 (2006).

[89] C. Debus and P. H. Bolivar, "Frequency selective surfaces for high sensitivity terahertz sensing", *Appl. Phys. Lett.*, **91**, pp. 184102 (2007).

[90] J. B. Jackson and N. J. Halas, "Surface-enhanced Raman scattering on tunable plasmonic nanoparticle substrates", *Proc. Natl. Acad. Sci.*, **101**, pp. 17930-17935 (2004).

[91] J. N. Anker, W. P. Hall, O. Lyandres, N. C. Shah, J. Zhao and R. P. Van Duyne, "Biosensing with plasmonic nanosensors", *Nature Mater.*, **7**, pp. 442-453 (2008).

[92] P. Markowicz, W. Law, A. Baev, P. Prasad, S. Patskovsky and A. Kabashin, "Phase-sensitive time-modulated surface plasmon resonance polarimetry for wide dynamic range biosensing", *Opt. Express*, **15**, pp. 1745-1754 (2007).

[93] A. Kabashin, P. Evans, S. Pastkovsky, W. Hendren, G. Wurtz, R. Atkinson, R. Pollard, V. Podolskiy and A. Zayats, "Plasmonic nanorod metamaterials for biosensing", *Nature Mater.*, **8**, pp. 867-871 (2009).

[94] H. Yoshida, Y. Ogawa, Y. Kawai, S. Hayashi, A. Hayashi, C. Otani, E. Kato, F. Miyamaru and K. Kawase, "Terahertz sensing method for protein detection using a thin metallic mesh", *Appl. Phys. Lett.*, **91**, pp. 253901 (2007).

[95] T. Driscoll, G. Andreev, D. Basov, S. Palit, S. Cho, N. Jokerst and D. Smith, "Tuned permeability in terahertz split-ring resonators for devices and sensors", *Appl. Phys. Lett.*, **91**, pp. 062511 (2007).

[96] R. Melik, N. K. Perkgoz, E. Unal, Z. Dilli and H. V. Demir, "Design and Realization of a Fully On-Chip High-$ Q $ Resonator at 15 GHz on Silicon", *Ieee. T. Electron Dev.*, **55**, pp. 3459-3466 (2008).

[97] R. Melik, N. K. Perkgoz, E. Unal, C. Puttlitz and H. V. Demir, "Bio-implantable passive on-chip RF-MEMS strain sensing resonators for orthopaedic applications", *J. Micromech. Microeng.*, **18**, pp. 115017 (2008).

[98] R. Melik and H. V. Demir, "Implementation of high quality-factor on-chip tuned microwave resonators at 7 GHz", *Microw. Opt. Technol. Let*, **51**, pp. 497-501 (2009).

[99] A. Arbabi, A. Rohani, D. Saeedkia and S. Safavi-Naeini, "A terahertz plasmonic metamaterial structure for near-field sensing applications", presented at *Infrared, Millimeter and Terahertz Waves, 2008. IRMMW-THz 2008. 33rd International Conference on*, 2008.

[100] M. Puentes, B. Stelling, M. Schüßler, A. Penirschke, C. Damm and R. Jakoby, "Dual mode sensor for belt conveyor systems based on planar metamaterials", presented at *Sensors, 2009 IEEE*, 2009.

[101] X. Xu, B. Peng, D. Li, J. Zhang, L. M. Wong, Q. Zhang, S. Wang and Q. Xiong, "Flexible visible–infrared metamaterials and their applications in highly sensitive chemical and biological sensing", *Nano Lett.*, **11**, pp. 3232-3238 (2011).

[102] Q. Wang, X. Zhang, Y. Xu, Z. Tian, J. Gu, W. Yue, S. Zhang, J. Han and W. Zhang, "A Broadband Metasurface-Based Terahertz Flat-Lens Array", *Adv. Opt. Mater.*, **3**, pp. 779-785 (2015).

[103] N. Yu, P. Genevet, F. Aieta, M. A. Kats, R. Blanchard, G. Aoust, J.-P. Tetienne, Z. Gaburro and F. Capasso, "Flat optics: controlling wavefronts with optical antenna metasurfaces", *IEEE. J. Sel. Top. Quant*, **19**, pp. 4700423-4700423 (2013).

[104] X. Chen, L. Huang, H. Mühlenbernd, G. Li, B. Bai, Q. Tan, G. Jin, C.-W. Qiu, S. Zhang and T. Zentgraf, "Dual-polarity plasmonic metalens for visible light", *Nature Commun.*, **3**, pp. 1198 (2012).

[105] X. Chen, L. Huang, H. Mühlenbernd, G. Li, B. Bai, Q. Tan, G. Jin, C. W. Qiu, T. Zentgraf and S. Zhang, "Reversible Three-Dimensional Focusing of Visible Light with Ultrathin Plasmonic Flat Lens", *Adv. Opt. Mater.*, **1**, pp. 517-521 (2013).

[106] M. Khorasaninejad, F. Aieta, P. Kanhaiya, M. A. Kats, P. Genevet, D. Rousso and F. Capasso, "Achromatic metasurface lens at telecommunication wavelengths", *Nano Lett.*, **15**, pp. 5358-5362 (2015).

[107] W. Zhu, Q. Song, L. Yan, W. Zhang, P. C. Wu, L. K. Chin, H. Cai, D. P. Tsai, Z. X. Shen and T. W. Deng, "A flat lens with tunable phase gradient by using random access reconfigurable metamaterial", *Adv. Mater.*, **27**, pp. 4739-4743 (2015).

[108] Z. Wei, Y. Cao, X. Su, Z. Gong, Y. Long and H. Li, "Highly efficient beam steering with a transparent metasurface", *Opt. Express*, **21**, pp. 10739-10745 (2013).

[109] D. F. Sievenpiper, J. H. Schaffner, H. J. Song, R. Y. Loo and G. Tangonan, "Two-dimensional beam steering using an electrically tunable impedance surface", *IEEE. T. Antenn. Propag*, **51**, pp. 2713-2722 (2003).

[110] A. Ourir, S. N. Burokur, R. Yahiaoui and A. de Lustrac, "Directive metamaterial-based subwavelength resonant cavity antennas–Applications for beam steering", *C. R. Phys.*, **10**, pp. 414-422 (2009).

[111] J. Cheng and H. Mosallaei, "Optical metasurfaces for beam scanning in space", *Opt. Lett.*, **39**, pp. 2719-2722 (2014).

[112] X. Ni, A. V. Kildishev and V. M. Shalaev, "Metasurface holograms for visible light", *Nature Commun.*, **4**, pp. (2013).

[113] S. A. Kuznetsov, M. A. Astafev, M. Beruete and M. Navarro-Cía, "Planar holographic metasurfaces for terahertz focusing", *Sci. Rep.*, **5**, pp. 7738 (2015).

[114] D. Wen, F. Yue, G. Li, G. Zheng, K. Chan, S. Chen, M. Chen, K. F. Li, P. W. H. Wong and K. W. Cheah, "Helicity multiplexed broadband metasurface holograms", *Nature Commun.*, **6**, pp. (2015).

[115] C. Sönnichsen, B. M. Reinhard, J. Liphardt and A. P. Alivisatos, "A molecular ruler based on plasmon coupling of single gold and silver nanoparticles", *Nat. Biotechnol.*, **23**, pp. 741-745 (2005).

[116] G. L. Liu, Y. Yin, S. Kunchakarra, B. Mukherjee, D. Gerion, S. D. Jett, D. G. Bear, J. W. Gray, A. P. Alivisatos and L. P. Lee, "A nanoplasmonic molecular ruler for measuring nuclease activity and DNA footprinting", *Nat. Nanotechnol.*, **1**, pp. 47-52 (2006).

[117] N. Liu, M. Hentschel, T. Weiss, A. P. Alivisatos and H. Giessen, "Three-dimensional plasmon rulers", *Science*, **332**, pp. 1407-1410 (2011).

[118] H. Zhu, S. Cheung, K. L. Chung and T. Yuk, "Linear-to-circular polarization conversion using metasurface", *IEEE. T. Antenn. Propag*, **61**, pp. 4615-4623 (2013).

[119] N. K. Grady, J. E. Heyes, D. R. Chowdhury, Y. Zeng, M. T. Reiten, A. K. Azad, A. J. Taylor, D. A. Dalvit and H.-T. Chen, "Terahertz metamaterials for linear polarization conversion and anomalous refraction", *Science*, **340**, pp. 1304-1307 (2013).

[120] L.-J. Black, Y. Wang, C. De Groot, A. Arbouet and O. L. Muskens, "Optimal polarization conversion in coupled dimer plasmonic nanoantennas for metasurfaces", *ACS Nano*, **8**, pp. 6390-6399 (2014).

[121] K. Song, Y. Liu, C. Luo and X. Zhao, "High-efficiency broadband and multiband cross-polarization conversion using chiral metamaterial", *J. Phys. D: Appl. Phys.*, **47**, pp. 505104 (2014).

[122] Y. Guo, Y. Wang, M. Pu, Z. Zhao, X. Wu, X. Ma, C. Wang, L. Yan and X. Luo, "Dispersion management of anisotropic metamirror for super-octave bandwidth polarization conversion", *Sci. Rep.*, **5**, pp. 8434 (2015).

[123] R. Brown, "Absorption and scattering of light by small particles", *J. Mod. Optic.*, **31**, pp. 3-3 (1984).

[124] L. Lewin, "The electrical constants of a material loaded with spherical particles", *Journal of the Institution of Electrical Engineers-Part III: Radio and Communication Engineering*, **94**, pp. 65-68 (1947).

[125] C. L. Holloway, E. F. Kuester, J. Baker-Jarvis and P. Kabos, "A double negative (DNG) composite medium composed of magnetodielectric spherical particles embedded in a matrix", *IEEE. T. Antenn. Propag*, **51**, pp. 2596-2603 (2003).

[126] A. Ahmadi and H. Mosallaei, "Physical configuration and performance modeling of all-dielectric metamaterials", *Phys. Rev. B*, **77**, pp. 045104 (2008).

[127] O. G. Vendik and M. Gashinova, "Artificial double negative (DNG) media composed by two different dielectric sphere lattices embedded in a

dielectric matrix", presented at *Microwave Conference, 2004. 34th European*, 2004.

[128] I. Vendik, O. Vendik and M. Gashinova, "Artificial dielectric medium possessing simultaneously negative permittivity and magnetic permeability", *Tech. Phys. Lett.*, **32**, pp. 429-433 (2006).

[129] L. Peng, L. Ran, H. Chen, H. Zhang, J. A. Kong and T. M. Grzegorczyk, "Experimental observation of left-handed behavior in an array of standard dielectric resonators", *Phys. Rev. Lett.*, **98**, pp. 157403 (2007).

[130] M. Khorasaninejad and F. Capasso, "Broadband multifunctional efficient meta-gratings based on dielectric waveguide phase shifters", *Nano Lett.*, **15**, pp. 6709-6715 (2015).

[131] I. Fernandez-Corbaton and G. Molina-Terriza, "Role of duality symmetry in transformation optics", *Phys. Rev. B*, **88**, pp. 085111 (2013).

[132] I. Fernandez-Corbaton, M. Fruhnert and C. Rockstuhl, "Dual and chiral objects for optical activity in general scattering directions", *ACS Photonics*, **2**, pp. 376-384 (2015).

[133] I. Staude, A. E. Miroshnichenko, M. Decker, N. T. Fofang, S. Liu, E. Gonzales, J. Dominguez, T. S. Luk, D. N. Neshev and I. Brener, "Tailoring directional scattering through magnetic and electric resonances in subwavelength silicon nanodisks", *ACS Nano*, **7**, pp. 7824-7832 (2013).

[134] A. B. Evlyukhin, C. Reinhardt and B. N. Chichkov, "Multipole light scattering by nonspherical nanoparticles in the discrete dipole approximation", *Phys. Rev. B*, **84**, pp. 235429 (2011).

[135] M. Decker, I. Staude, M. Falkner, J. Dominguez, D. N. Neshev, I. Brener, T. Pertsch and Y. S. Kivshar, "High-Efficiency Dielectric Huygens' Surfaces", *Adv. Opt. Mater.*, **3**, pp. 813-820 (2015).

[136] K. E. Chong, I. Staude, A. James, J. Dominguez, S. Liu, S. Campione, G. S. Subramania, T. S. Luk, M. Decker and D. N. Neshev, "Polarization-independent silicon metadevices for efficient optical wavefront control", *Nano Lett.*, **15**, pp. 5369-5374 (2015).

[137] M. Khorasaninejad, W. T. Chen, R. C. Devlin, J. Oh, A. Y. Zhu and F. Capasso, "Metalenses at visible wavelengths: Diffraction-limited focusing and subwavelength resolution imaging", *Science*, **352**, pp. 1190-1194 (2016).

[138] Y. Yang, I. I. Kravchenko, D. P. Briggs and J. Valentine, "All-dielectric metasurface analogue of electromagnetically induced transparency", *Nature Commun.*, **5**, pp. (2014).

[139] M. A. Kats, R. Blanchard, P. Genevet and F. Capasso, "Nanometre optical coatings based on strong interference effects in highly absorbing media", *Nature Mater.*, **12**, pp. 20-24 (2013).

[140] R. Yahiaoui, K. Hanai, K. Takano, T. Nishida, F. Miyamaru, M. Nakajima and M. Hangyo, "Trapping waves with terahertz metamaterial absorber based on isotropic Mie resonators", *Opt. Lett.*, **40**, pp. 3197-3200 (2015).

[141] R. Kakimi, M. Fujita, M. Nagai, M. Ashida and T. Nagatsuma, "Capture of a terahertz wave in a photonic-crystal slab", *Nature Photon.*, **8**, pp. 657-663 (2014).

[142] R. Alaee, M. Albooyeh, A. Rahimzadegan, M. S. Mirmoosa, Y. S. Kivshar and C. Rockstuhl, "All-dielectric reciprocal bianisotropic nanoparticles", *Phys. Rev. B*, **92**, pp. 245130 (2015).

[143] M. Albooyeh, R. Alaee, C. Rockstuhl and C. Simovski, "Revisiting substrate-induced bianisotropy in metasurfaces", *Phys. Rev. B*, **91**, pp. 195304 (2015).

[144] D. Markovich, K. Baryshnikova, A. Shalin, A. Samusev, A. Krasnok, P. Belov and P. Ginzburg, "Enhancement of artificial magnetism via resonant bianisotropy", *Sci. Rep.*, **6**, pp. (2016).

[145] Y. Yang, W. Wang, A. Boulesbaa, I. I. Kravchenko, D. P. Briggs, A. Puretzky, D. Geohegan and J. Valentine, "Nonlinear Fano-resonant dielectric metasurfaces", *Nano Lett.*, **15**, pp. 7388-7393 (2015).

[146] C. Wu, N. Arju, G. Kelp, J. A. Fan, J. Dominguez, E. Gonzales, E. Tutuc, I. Brener and G. Shvets, "Spectrally selective chiral silicon metasurfaces based on infrared Fano resonances", *Nature Commun.*, **5**, pp. (2014).

[147] K. E. Chong, B. Hopkins, I. Staude, A. E. Miroshnichenko, J. Dominguez, M. Decker, D. N. Neshev, I. Brener and Y. S. Kivshar, "Observation of Fano resonances in all-dielectric nanoparticle oligomers", *Small*, **10**, pp. 1985-1990 (2014).

[148] Y. Yang, W. Wang, P. Moitra, I. I. Kravchenko, D. P. Briggs and J. Valentine, "Dielectric meta-reflectarray for broadband linear polarization conversion and optical vortex generation", *Nano Lett.*, **14**, pp. 1394-1399 (2014).

[149] A. Arbabi, Y. Horie, M. Bagheri and A. Faraon, "Dielectric metasurfaces for complete control of phase and polarization with subwavelength spatial resolution and high transmission", *Nat. nanotechnol.*, pp. (2015).

[150] Y. Liu, X. Ling, X. Yi, X. Zhou, S. Chen, Y. Ke, H. Luo and S. Wen, "Photonic spin Hall effect in dielectric metasurfaces with rotational symmetry breaking", *Opt. Lett.*, **40**, pp. 756-759 (2015).

[151] Y. Li, Y. Liu, X. Ling, X. Yi, X. Zhou, Y. Ke, H. Luo, S. Wen and D. Fan, "Observation of photonic spin Hall effect with phase singularity at dielectric metasurfaces", *Opt. Express*, **23**, pp. 1767-1774 (2015).

[152] Y. He, P. He, V. G. Harris and C. Vittoria, "Role of ferrites in negative index metamaterials", *IEEE. T. Magn.*, **42**, pp. 2852-2854 (2006).

[153] G. He, R.-x. Wu, Y. Poo and P. Chen, "Magnetically tunable double-negative material composed of ferrite-dielectric and metallic mesh", *J. Appl. Phys.*, **107**, pp. 093522 (2010).

[154] V. A. Fedotov, A. Tsiatmas, J. Shi, R. Buckingham, P. De Groot, Y. Chen, S. Wang and N. Zheludev, "Temperature control of Fano resonances and transmission in superconducting metamaterials", *Opt. Express*, **18**, pp. 9015-9019 (2010).

[155] H.-T. Chen, H. Yang, R. Singh, J. F. O'Hara, A. K. Azad, S. A. Trugman, Q. Jia and A. J. Taylor, "Tuning the resonance in high-temperature superconducting terahertz metamaterials", *Phys. Rev. Lett.*, **105**, pp. 247402 (2010).

[156] A. Tsiatmas, A. Buckingham, V. Fedotov, S. Wang, Y. Chen, P. De Groot and N. Zheludev, "Superconducting plasmonics and extraordinary transmission", *Appl. Phys. Lett.*, **97**, pp. 111106 (2010).

[157] M. W. Coffey and J. R. Clem, "Unified theory of effects of vortex pinning and flux creep upon the rf surface impedance of type-II superconductors", *Phys. Rev. Lett.*, **67**, pp. 386 (1991).

[158] C. Kurter, A. Zhuravel, J. Abrahams, C. Bennett, A. Ustinov and S. M. Anlage, "Superconducting RF metamaterials made with magnetically active planar spirals", *Ieee. T. Appl. Supercon.*, **21**, pp. 709-712 (2011).

[159] C. Kurter, P. Tassin, A. P. Zhuravel, L. Zhang, T. Koschny, A. V. Ustinov, C. M. Soukoulis and S. M. Anlage, "Switching nonlinearity in a superconductor-enhanced metamaterial", *Appl. Phys. Lett.*, **100**, pp. 121906 (2012).

[160] S. Liu, H.-X. Xu, H. C. Zhang and T. J. Cui, "Tunable ultrathin mantle cloak via varactor-diode-loaded metasurface", *Opt. Express*, **22**, pp. 13403-13417 (2014).

[161] M. Yoo and S. Lim, "Active metasurface for controlling reflection and absorption properties", *Appl. Phys. Express*, **7**, pp. 112204 (2014).

[162] H. Wakatsuchi, J. Rushton, J. Lee, F. Gao, M. Jacob, S. Kim and D. Sievenpiper, "Experimental demonstration of nonlinear waveform-dependent metasurface absorber with pulsed signals", *Electron. Lett.*, **49**, pp. 1530-1531 (2013).

[163] W. Zhang, W. M. Zhu, H. Cai, M.-L. J. Tsai, G.-Q. Lo, D. P. Tsai, H. Tanoto, J.-H. Teng, X.-H. Zhang and D.-L. Kwong, "Resonance switchable metamaterials using MEMS fabrications", *IEEE. J. Sel. Top. Quant*, **19**, pp. 4700306-4700306 (2013).

[164] W. Zhu, A. Liu, T. Bourouina, D. Tsai, J. Teng, X. Zhang, G. Lo, D. Kwong and N. Zheludev, "Microelectromechanical Maltese-cross metamaterial with tunable terahertz anisotropy", *Nature Commun.*, **3**, pp. 1274 (2012).

[165] A. Liu, W. Zhu, D. Tsai and N. I. Zheludev, "Micromachined tunable metamaterials: a review", *J. Optics*, **14**, pp. 114009 (2012).

[166] W. Zhang, A. Liu, W. Zhu, E. Li, H. Tanoto, Q. Wu, J. H. Teng, X. Zhang, M. Tsai and G.-Q. Lo, "Micromachined switchable metamaterial with dual resonance", *Appl. Phys. Lett.*, **101**, pp. 151902 (2012).

[167] W. Zhu, A. Liu, W. Zhang, J. Tao, T. Bourouina, J. Teng, X. Zhang, Q. Wu, H. Tanoto and H. Guo, "Polarization dependent state to polarization independent state change in THz metamaterials", *Appl. Phys. Lett.*, **99**, pp. 221102 (2011).

[168] Y. H. Fu, A. Q. Liu, W. M. Zhu, X. M. Zhang, D. P. Tsai, J. B. Zhang, T. Mei, J. F. Tao, H. C. Guo and X. H. Zhang, "A Micromachined Reconfigurable Metamaterial via Reconfiguration of Asymmetric Split-Ring Resonators", *Adv. Funct. Mater.*, **21**, pp. 3589-3594 (2011).

[169] C. C. Chen, A. Ishikawa, Y. H. Tang, M. H. Shiao, D. P. Tsai and T. Tanaka, "Uniaxial-isotropic Metamaterials by Three-Dimensional Split-Ring Resonators", *Adv. Opt. Mater.*, **3**, pp. 44-48 (2015).

[170] H. Tao, A. Strikwerda, K. Fan, W. Padilla, X. Zhang and R. Averitt, "Reconfigurable terahertz metamaterials", *Phys. Rev. Lett.*, **103**, pp. 147401 (2009).

[171] H. Tao, A. C. Strikwerda, K. Fan, W. J. Padilla, X. Zhang and R. D. Averitt, "MEMS based structurally tunable metamaterials at terahertz frequencies", *J. Infrared Millim. Terahertz Waves*, **32**, pp. 580-595 (2011).

[172] A. H. Yang, S. D. Moore, B. S. Schmidt, M. Klug, M. Lipson and D. Erickson, "Optical manipulation of nanoparticles and biomolecules in sub-wavelength slot waveguides", *Nature*, **457**, pp. 71-75 (2009).

[173] H. Cai, K. Xu, A. Liu, Q. Fang, M. Yu, G.-Q. Lo and D. L. Kwong, "Nano-opto-mechanical actuator driven by gradient optical force", *Appl. Phys. Lett.*, **100**, pp. 013108 (2012).

[174] R. Zhao, J. Zhou, T. Koschny, E. Economou and C. Soukoulis, "Repulsive Casimir force in chiral metamaterials", *Phys. Rev. Lett.*, **103**, pp. 103602 (2009).

[175] M. Liu, T. Zentgraf, Y. Liu, G. Bartal and X. Zhang, "Light-driven nanoscale plasmonic motors", *Nat. Nanotechnol.*, **5**, pp. 570-573 (2010).

[176] I. M. Pryce, K. Aydin, Y. A. Kelaita, R. M. Briggs and H. A. Atwater, "Highly strained compliant optical metamaterials with large frequency tunability", *Nano Lett.*, **10**, pp. 4222-4227 (2010).

[177] H. Tao, A. Strikwerda, K. Fan, C. Bingham, W. Padilla, X. Zhang and R. Averitt, "Terahertz metamaterials on free-standing highly-flexible polyimide substrates", *J. Phys. D: Appl. Phys.*, **41**, pp. 232004 (2008).

[178] H. Tao, J. J. Amsden, A. C. Strikwerda, K. Fan, D. L. Kaplan, X. Zhang, R. D. Averitt and F. G. Omenetto, "Metamaterial silk composites at terahertz frequencies", *Adv. Mater.*, **22**, pp. 3527-3531 (2010).

[179] H. Tao, L. R. Chieffo, M. A. Brenckle, S. M. Siebert, M. Liu, A. C. Strikwerda, K. Fan, D. L. Kaplan, X. Zhang and R. D. Averitt, "Metamaterials on paper as a sensing platform", *Adv. Mater.*, **23**, pp. 3197-3201 (2011).

[180] R. Melik, E. Unal, N. Kosku Perkgoz, C. Puttlitz and H. V. Demir, "Flexible metamaterials for wireless strain sensing", *Appl. Phys. Lett.*, **95**, pp. 181105 (2009).

[181] K. Iwaszczuk, A. C. Strikwerda, K. Fan, X. Zhang, R. D. Averitt and P. U. Jepsen, "Flexible metamaterial absorbers for stealth applications at terahertz frequencies", *Opt. Express*, **20**, pp. 635-643 (2012).

[182] J. G. Ok, H. Seok Youn, M. Kyu Kwak, K.-T. Lee, Y. Jae Shin, L. Jay Guo, A. Greenwald and Y. Liu, "Continuous and scalable fabrication of flexible

metamaterial films via roll-to-roll nanoimprint process for broadband plasmonic infrared filters", *Appl. Phys. Lett.*, **101**, pp. 223102 (2012).

[183] A. Di Falco, M. Ploschner and T. F. Krauss, "Flexible metamaterials at visible wavelengths", *New J. Phys.*, **12**, pp. 113006 (2010).

[184] D. Chanda, K. Shigeta, S. Gupta, T. Cain, A. Carlson, A. Mihi, A. J. Baca, G. R. Bogart, P. Braun and J. A. Rogers, "Large-area flexible 3D optical negative index metamaterial formed by nanotransfer printing", *Nat. Nanotechnol.*, **6**, pp. 402-407 (2011).

[185] Y. Yoo, H. Zheng, Y. Kim, J. Rhee, J.-H. Kang, K. Kim, H. Cheong, Y. Kim and Y. Lee, "Flexible and elastic metamaterial absorber for low frequency, based on small-size unit cell", *Appl. Phys. Lett.*, **105**, pp. 041902 (2014).

[186] I. Khoo, D. Werner, X. Liang, A. Diaz and B. Weiner, "Nanosphere dispersed liquid crystals for tunable negative-zero-positive index of refraction in the optical and terahertz regimes", *Opt. Lett.*, **31**, pp. 2592-2594 (2006).

[187] X. Wang, D.-H. Kwon, D. H. Werner, I.-C. Khoo, A. V. Kildishev and V. M. Shalaev, "Tunable optical negative-index metamaterials employing anisotropic liquid crystals", *Appl. Phys. Lett.*, **91**, pp. 143122 (2007).

[188] A. Minovich, D. N. Neshev, D. A. Powell, I. V. Shadrivov and Y. S. Kivshar, "Tunable fishnet metamaterials infiltrated by liquid crystals", *Appl. Phys. Lett.*, **96**, pp. 193103 (2010).

[189] F. Zhang, Q. Zhao, W. Zhang, J. Sun, J. Zhou and D. Lippens, "Voltage tunable short wire-pair type of metamaterial infiltrated by nematic liquid crystal", *Appl. Phys. Lett.*, **97**, pp. 134103 (2010).

[190] F. Zhang, W. Zhang, Q. Zhao, J. Sun, K. Qiu, J. Zhou and D. Lippens, "Electrically controllable fishnet metamaterial based on nematic liquid crystal", *Opt. Express*, **19**, pp. 1563-1568 (2011).

[191] O. Buchnev, J. Ou, M. Kaczmarek, N. Zheludev and V. Fedotov, "Electro-optical control in a plasmonic metamaterial hybridised with a liquid-crystal cell", *Opt. Express*, **21**, pp. 1633-1638 (2013).

[192] O. Buchnev, J. Wallauer, M. Walther, M. Kaczmarek, N. I. Zheludev and V. A. Fedotov, "Controlling intensity and phase of terahertz radiation with an optically thin liquid crystal-loaded metamaterial", *Appl. Phys. Lett.*, **103**, pp. 141904 (2013).

[193] J. Dintinger, B. J. Tang, X. Zeng, F. Liu, T. Kienzler, G. H. Mehl, G. Ungar, C. Rockstuhl and T. Scharf, "A Self-Organized Anisotropic Liquid-Crystal Plasmonic Metamaterial", *Adv. Mater.*, **25**, pp. 1999-2004 (2013).

[194] S. Savo, D. Shrekenhamer and W. J. Padilla, "Liquid crystal metamaterial absorber spatial light modulator for THz applications", *Adv. Opt. Mater.*, **2**, pp. 275-279 (2014).

[195] D. C. Zografopoulos and R. Beccherelli, "Tunable terahertz fishnet metamaterials based on thin nematic liquid crystal layers for fast switching", *Sci. Rep.*, **5**, pp. (2015).

[196] J. Wang, S. Liu, S. Guruswamy and A. Nahata, "Reconfigurable liquid metal based terahertz metamaterials via selective erasure and refilling to the unit cell level", *Appl. Phys. Lett.*, **103**, pp. 221116 (2013).

[197] A. Andryieuski, S. M. Kuznetsova, S. V. Zhukovsky, Y. S. Kivshar and A. V. Lavrinenko, "Water: Promising Opportunities for Tunable All-dielectric Electromagnetic Metamaterials", *Sci. Rep.*, **5**, pp. (2015).

[198] M. V. Rybin, D. S. Filonov, K. B. Samusev, P. A. Belov, Y. S. Kivshar and M. F. Limonov, "Phase diagram for the transition from photonic crystals to dielectric metamaterials", *Nature Commun.*, **6**, pp. (2015).

[199] Y. J. Yoo, S. Ju, S. Y. Park, Y. Ju Kim, J. Bong, T. Lim, K. W. Kim, J. Y. Rhee and Y. P. Lee, "Metamaterial absorber for electromagnetic waves in periodic water droplets", *Sci. Rep.*, **5**, pp. (2015).

[200] D. Shrekenhamer, W.-C. Chen and W. J. Padilla, "Liquid crystal tunable metamaterial absorber", *Phys. Rev. Lett.*, **110**, pp. 177403 (2013).

[201] D. H. Werner, D.-H. Kwon, I.-C. Khoo, A. V. Kildishev and V. M. Shalaev, "Liquid crystal clad near-infrared metamaterials with tunable negative-zero-positive refractive indices", *Opt. Express*, **15**, pp. 3342-3347 (2007).

[202] Q. Zhao, L. Kang, B. Du, B. Li, J. Zhou, H. Tang, X. Liang and B. Zhang, "Electrically tunable negative permeability metamaterials based on nematic liquid crystals", *Appl. Phys. Lett.*, **90**, pp. 011112 (2007).

[203] J. A. Bossard, X. Liang, L. Li, S. Yun, D. H. Werner, B. Weiner, T. S. Mayer, P. F. Cristman, A. Diaz and I. Khoo, "Tunable frequency selective surfaces and negative-zero-positive index metamaterials based on liquid crystals", *IEEE. T. Antenn. Propag*, **56**, pp. 1308-1320 (2008).

[204] F. Zhang, Q. Zhao, L. Kang, D. P. Gaillot, X. Zhao, J. Zhou and D. Lippens, "Magnetic control of negative permeability metamaterials based on liquid crystals", *Appl. Phys. Lett.*, **92**, pp. 193104 (2008).

[205] G. Pawlik, K. Tarnowski, W. Walasik, A. C. Mitus and I. Khoo, "Liquid crystal hyperbolic metamaterial for wide-angle negative–positive refraction and reflection", *Opt. Lett.*, **39**, pp. 1744-1747 (2014).

[206] M. Decker, C. Kremers, A. Minovich, I. Staude, A. E. Miroshnichenko, D. Chigrin, D. N. Neshev, C. Jagadish and Y. S. Kivshar, "Electro-optical switching by liquid-crystal controlled metasurfaces", *Opt. Express*, **21**, pp. 8879-8885 (2013).

[207] P. C. Wu, W. Zhu, Z. X. Shen, P. H. J. Chong, W. Ser, D. P. Tsai and A. Q. Liu, "Broadband Wide-Angle Multifunctional Polarization Converter via Liquid-Metal-Based Metasurface", *Adv. Opt. Mater.*, pp. (2017).

[208] J. Wang, S. Liu, S. Guruswamy and A. Nahata, "Reconfigurable terahertz metamaterial device with pressure memory", *Opt. Express*, **22**, pp. 4065-4074 (2014).

[209] J. Melin and S. R. Quake, "Microfluidic large-scale integration: the evolution of design rules for biological automation", *Annu. Rev. Biophys. Biomol. Struct.*, **36**, pp. 213-231 (2007).

[210] T. Thorsen, S. J. Maerkl and S. R. Quake, "Microfluidic large-scale integration", *Science*, **298**, pp. 580-584 (2002).

[211] J. Wang, S. Liu and A. Nahata, "Reconfigurable plasmonic devices using liquid metals", *Opt. Express*, **20**, pp. 12119-12126 (2012).

[212] K. Ling, K. Kim and S. Lim, "Flexible liquid metal-filled metamaterial absorber on polydimethylsiloxane (PDMS)", *Opt. Express*, **23**, pp. 21375-21383 (2015).

[213] M. Kubo, X. Li, C. Kim, M. Hashimoto, B. J. Wiley, D. Ham and G. M. Whitesides, "Stretchable microfluidic radiofrequency antennas", *Adv. Mater.*, **22**, pp. 2749-2752 (2010).

[214] L. D. Barron, "Molecular light scattering and optical activity", Cambridge University Press, (2004).

[215] S. Tretyakov, I. Nefedov, A. Sihvola, S. Maslovski and C. Simovski, "Waves and energy in chiral nihility", *J. Electromagnet. Wave*, **17**, pp. 695-706 (2003).

[216] J. Pendry, "A chiral route to negative refraction", *Science*, **306**, pp. 1353-1355 (2004).

[217] S. Zhang, Y.-S. Park, J. Li, X. Lu, W. Zhang and X. Zhang, "Negative refractive index in chiral metamaterials", *Phys. Rev. Lett.*, **102**, pp. 023901 (2009).

[218] E. Plum, J. Zhou, J. Dong, V. Fedotov, T. Koschny, C. Soukoulis and N. Zheludev, "Metamaterial with negative index due to chirality", *Phys. Rev. B*, **79**, pp. 035407 (2009).

[219] Z. Li, K. B. Alici, E. Colak and E. Ozbay, "Complementary chiral metamaterials with giant optical activity and negative refractive index", *Appl. Phys. Lett.*, **98**, pp. 161907 (2011).

[220] R. Zhao, L. Zhang, J. Zhou, T. Koschny and C. Soukoulis, "Conjugated gammadion chiral metamaterial with uniaxial optical activity and negative refractive index", *Phys. Rev. B*, **83**, pp. 035105 (2011).

[221] Z. Li, R. Zhao, T. Koschny, M. Kafesaki, K. B. Alici, E. Colak, H. Caglayan, E. Ozbay and C. Soukoulis, "Chiral metamaterials with negative refractive index based on four “U” split ring resonators", *Appl. Phys. Lett.*, **97**, pp. 081901 (2010).

[222] A. Papakostas, A. Potts, D. Bagnall, S. Prosvirnin, H. Coles and N. Zheludev, "Optical manifestations of planar chirality", *Phys. Rev. Lett.*, **90**, pp. 107404 (2003).

[223] Y. Zhao, M. Belkin and A. Alù, "Twisted optical metamaterials for planarized ultrathin broadband circular polarizers", *Nature Commun.*, **3**, pp. 870 (2012).

[224] E. Plum, V. Fedotov and N. Zheludev, "Optical activity in extrinsically chiral metamaterial", *Appl. Phys. Lett.*, **93**, pp. 191911 (2008).

[225] Z. Wei, Y. Cao, Y. Fan, X. Yu and H. Li, "Broadband polarization transformation via enhanced asymmetric transmission through arrays of twisted complementary split-ring resonators", *Appl. Phys. Lett.*, **99**, pp. 221907 (2011).

[226] C. Pan, M. Ren, Q. Li, S. Fan and J. Xu, "Broadband asymmetric transmission of optical waves from spiral plasmonic metamaterials", *Appl. Phys. Lett.*, **104**, pp. 121112 (2014).

[227] J. Shi, H. Ma, C. Guan, Z. Wang and T. Cui, "Broadband chirality and asymmetric transmission in ultrathin 90-twisted Babinet-inverted metasurfaces", *Phys. Rev. B*, **89**, pp. 165128 (2014).

[228] T. Xu and H. J. Lezec, "Visible-frequency asymmetric transmission devices incorporating a hyperbolic metamaterial", *Nature Commun.*, **5**, pp. (2014).

[229] V. Fedotov, P. Mladyonov, S. Prosvirnin, A. Rogacheva, Y. Chen and N. Zheludev, "Asymmetric propagation of electromagnetic waves through a planar chiral structure", *Phys. Rev. Lett.*, **97**, pp. 167401 (2006).

[230] L. Wu, Z. Yang, Y. Cheng, M. Zhao, R. Gong, Y. Zheng, J. a. Duan and X. Yuan, "Giant asymmetric transmission of circular polarization in layer-by-layer chiral metamaterials", *Appl. Phys. Lett.*, **103**, pp. 021903 (2013).

[231] C. Menzel, C. Helgert, C. Rockstuhl, E.-B. Kley, A. Tünnermann, T. Pertsch and F. Lederer, "Asymmetric transmission of linearly polarized light at optical metamaterials", *Phys. Rev. Lett.*, **104**, pp. 253902 (2010).

[232] M. Kang, J. Chen, H.-X. Cui, Y. Li and H.-T. Wang, "Asymmetric transmission for linearly polarized electromagnetic radiation", *Opt. Express*, **19**, pp. 8347-8356 (2011).

[233] M. Mutlu, A. E. Akosman, A. E. Serebryannikov and E. Ozbay, "Asymmetric transmission of linearly polarized waves and polarization angle dependent wave rotation using a chiral metamaterial", *Opt. Express*, **19**, pp. 14290-14299 (2011).

[234] C. Huang, J. Zhao, T. Jiang and Y. Feng, "Asymmetric transmission of linearly polarized electromagnetic wave through chiral metamaterial structure", *J. Electromagnet. Wave*, **26**, pp. 1192-1202 (2012).

[235] M. Mutlu, A. E. Akosman, A. E. Serebryannikov and E. Ozbay, "Diodelike asymmetric transmission of linearly polarized waves using magnetoelectric coupling and electromagnetic wave tunneling", *Phys. Rev. Lett.*, **108**, pp. 213905 (2012).

[236] F. Dincer, C. Sabah, M. Karaaslan, E. Unal, M. Bakir and U. Erdiven, "Asymmetric transmission of linearly polarized waves and dynamically wave rotation using chiral metamaterial", *Prog. Electromagn. Res.*, **140**, pp. 227-239 (2013).

[237] J. Shi, X. Liu, S. Yu, T. Lv, Z. Zhu, H. F. Ma and T. J. Cui, "Dual-band asymmetric transmission of linear polarization in bilayered chiral metamaterial", *Appl. Phys. Lett.*, **102**, pp. 191905 (2013).

[238] C. Huang, Y. Feng, J. Zhao, Z. Wang and T. Jiang, "Asymmetric electromagnetic wave transmission of linear polarization via polarization conversion through chiral metamaterial structures", *Phys. Rev. B*, **85**, pp. 195131 (2012).

[239] R. Buchner, J. Barthel and J. Stauber, "The dielectric relaxation of water between 0°C and 35°C", *Chem. Phys. Lett.*, **306**, pp. 57-63 (1999).

[240] J. C. Booth, N. D. Orloff, J. Mateu, M. Janezic, M. Rinehart and J. A. Beall, "Quantitative permittivity measurements of nanoliter liquid volumes in microfluidic channels to 40 GHz", *IEEE. T. Instrum. Meas.*, **59**, pp. 3279-3288 (2010).

[241] X. Chen, T. M. Grzegorczyk, B.-I. Wu, J. Pacheco Jr and J. A. Kong, "Robust method to retrieve the constitutive effective parameters of metamaterials", *Phys. Rev. E*, **70**, pp. 016608 (2004).

[242] Y. Qu, Q. Li, H. Gong, K. Du, S. Bai, D. Zhao, H. Ye and M. Qiu, "Spatially and Spectrally Resolved Narrowband Optical Absorber Based on 2D Grating Nanostructures on Metallic Films", *Adv. Opt. Mater.*, pp. (2016).

[243] Y. W. Afsar, "Measurement of complex permittivity of liquids using waveguide techniques", *Prog. Electromagn. Res.*, **42**, pp. 131-142 (2003).

[244] P. C. Wu, G. Sun, W. T. Chen, K.-Y. Yang, Y.-W. Huang, Y.-H. Chen, H. L. Huang, W.-L. Hsu, H. P. Chiang and D. P. Tsai, "Vertical split-ring resonator based nanoplasmonic sensor", *Appl. Phys. Lett.*, **105**, pp. 033105 (2014).

[245] P. C. Wu, W.-L. Hsu, W. T. Chen, Y.-W. Huang, C. Y. Liao, A. Q. Liu, N. I. Zheludev, G. Sun and D. P. Tsai, "Plasmon coupling in vertical split-ring resonator metamolecules", *Sci. Rep.*, **5**, pp. (2015).

[246] D. Schurig, J. Mock and D. Smith, "Electric-field-coupled resonators for negative permittivity metamaterials", *Appl. Phys. Lett.*, **88**, pp. 041109 (2006).

[247] W. Padilla, M. Aronsson, C. Highstrete, M. Lee, A. Taylor and R. Averitt, "Electrically resonant terahertz metamaterials: Theoretical and experimental investigations", *Phys. Rev. B*, **75**, pp. 041102 (2007).

[248] H.-T. Chen, J. F. O'Hara, A. J. Taylor, R. D. Averitt, C. Highstrete, M. Lee and W. J. Padilla, "Complementary planar terahertz metamaterials", *Opt. Express*, **15**, pp. 1084-1095 (2007).

[249] T. J. Cui, D. R. Smith and R. Liu, "Metamaterials", Springer, Vol. 3, (2014).

[250] D.-S. Kim, D.-H. Kim, S. Hwang and J.-H. Jang, "Broadband terahertz absorber realized by self-assembled multilayer glass spheres", *Opt. Express*, **20**, pp. 13566-13572 (2012).

[251] A. Drezet, C. Genet, J.-Y. Laluet and T. W. Ebbesen, "Optical chirality without optical activity: How surface plasmons give a twist to light", *Opt. Express*, **16**, pp. 12559-12570 (2008).

Résumé Long de la Thèse

Description synthétique

Les dispositifs optiques affectent les ondes électromagnétiques (EMs) en modifiant la phase, l'amplitude et la polarisation, idéalement de la manière souhaitée en fonction de l'application. Les composants optiques conventionnels souffrent toutefois de limitations inhérentes à l'encombrement car dans ce cas, les variations de phase, d'amplitude et de polarisation dépendent de la propagation de la lumière sur des distances beaucoup plus grandes que la longueur d'onde. C'est ainsi qu'il y a un intérêt croissant suscité par des composants optiques plats et ultra-minces réalisés à partir d'une méta-surface, laquelle est obtenue à partir de structures artificielles conçues et réalisées à une échelle sub-longueur d'onde. La permittivité et la perméabilité d'une méta-surface peuvent être conçues de manière flexible de sorte à présenter des réponses optiques qui peuvent être très différentes de celles de leurs homologues naturels, ce qui conduit à de meilleures propriétés et parfois à un comportement extraordinaire. De plus, la réponse optique d'une méta-surface peut être efficacement contrôlée et accordée sur une large gamme, à travers diverses approches, qui permettent d'envisager des applications de ces méta-surfaces dans de nombreux domaines.

Cette thèse porte sur la conception, la fabrication et l'expérimentation de méta-surfaces à base de méta-liquides pour le contrôle et la modulation d'ondes EMs. Ces méta-surfaces sont basées sur l'utilisation des techniques de micro-fabrication photo-lithographiques combinées à la technologie micro-fluidique. En incorporant divers matériaux comprenant un matériau diélectrique liquide, un métal liquide et un métal solide dans un réseau de canaux micro-fluidique, il est possible de manipuler davantage les réponses optiques de la méta-surface, telles que

l'absorption, la transmission et la chiralité. Dans un premier temps, une méta-surface à base d'un résonateur à eau a été théoriquement conçue et démontrée expérimentalement en utilisant l'un des matériaux les plus abondants, les moins coûteux et les plus biocompatibles : l'eau, pour une absorption quasi-totale et ultra-large bande sur l'ensemble des bandes Ku, K et Ka. Dans un deuxième temps, une méta-surface à base de métal liquide est présentée pour une absorption accordable en fréquence dans le régime Térahertz et indépendante de l'angle. L'approche proposée peut conduire à une large plage d'accordabilité en fréquence de l'absorption en contrôlant la forme du métal liquide selon la direction de propagation. Dans un troisième temps, nous proposons une méta-surface chirale accordable, constituée de deux structures métalliques disposées sur les deux faces d'une couche diélectrique en PDMS. Cette méta-surface peut être accordée de l'état achirale vers l'état chirale lorsque la structure supérieure en spirale est étirée depuis sa forme initiale planaire jusqu'à une forme 3D. Ainsi, l'onde de propagation peut être réglée depuis une transmission symétrique jusqu'à une transmission antisymétrique.

Chapitre 1. Introduction

L'introduction porte sur la motivation, les objectifs et les principales contributions de cette thèse de doctorat. Nos travaux de recherche sont motivés par le potentiel applicatif d'un contrôle et d'une manipulation efficaces des ondes EMs, y compris dans les domaines micro-ondes et Térahertz, à travers des méta-surfaces originales à base de méta-liquide et utilisant des procédés de micro-fabrication. Le développement de la méta-surface à base de méta-liquide offre une grande liberté de contrôle dynamique de l'onde EM pour des applications réelles, ce qui permet d'atteindre des propriétés optiques qui vont au-delà de ce qui est possible avec des matériaux classiques. Plus précisément, les méta-surfaces, en particulier celles

basées sur des méta-liquides, offrent d'innombrables possibilités pour la manipulation de l'onde EM par la focalisation, l'absorption, la rotation, la déformation, la redirection des ondes, etc.

L'objectif principal de cette recherche est de développer des méta-surfaces à base de méta-liquide pour les applications d'ondes hyperfréquences et Térahertz. Ces méta-surfaces à base de méta-liquide sont basées sur un support mince constitué d'un matériau souple, le polydiméthylsiloxane (PDMS), et utilisent la technologie micro-fluidique pour contrôler la forme des structures afin de réaliser différentes fonctions. Trois types de méta-surfaces à base de méta-liquide et utilisant différentes combinaisons de matériaux sont étudiés. Il s'agit (1) d'une méta-surface basée sur un résonateur micro-onde à base d'eau, en utilisant de l'eau liquide et une solution d'eau et d'éthanol; (2) d'une méta-surface dans le régime Térahertz à base de métal liquide en utilisant du mercure; (3) une méta-surface chirale accordable dans le domaine micro-ondes en structurant le métal solide sur le support souple en PDMS. Un des objectifs technologiques est dans ce cas de développer des systèmes micro-fluidiques qui puissent fournir, par conception micro-fluidique, de nouvelles fonctionnalités de manipulation d'ondes EM. Les recherches comprennent l'analyse théorique, la conception de la structure, le développement du processus de fabrication et les études expérimentales. L'analyse théorique des trois méta-surfaces oriente la conception du système micro-fluidique correspondant, y compris la conception des structures et du système de contrôle. Différents procédés de fabrication sont développés dans cette thèse, recourant notamment à la micro-photolithographie et l'évaporation par faisceau d'électrons. Les études expérimentales sont effectuées sur les méta-surfaces développées pour la caractérisation et la mesure des ondes EMs.

Les principales contributions de cette thèse reposent sur divers aspects de l'analyse théorique, la conception et la réalisation de microstructures ainsi que sur des résultats expérimentaux obtenus sur les trois méta-surfaces méta-liquides

considérées et visant la manipulation des ondes EMs. Les principaux aspects originaux de ce travail sont énumérés ci-dessous:

(1) Une nouvelle approche pour la manipulation des ondes EMs est proposée en utilisant des méta-surfaces à base de métaux disposés sur un substrat souple en PDMS. Les réponses optiques des méta-surfaces sont contrôlées de façon efficace et accordées sur une large gamme grâce à la technologie micro-fluidique. Les méta-surfaces proposées, à base de méta-liquide, fournissent un nouveau paradigme pour le contrôle dynamique sur les ondes micro-ondes et Térahertz

(2) Des procédés de fabrication de canaux PDMS, des structures en silicium et des motifs métalliques sont développés pour la structure résonante élémentaire de la méta-surface et de son système de contrôle. L'accordabilité est essentiellement démontrée par différentes réponses optiques mesurées.

(3) Une absorption quasi-total et ultra-large bande est obtenue sur l'ensemble des bandes Ku, K et Ka en utilisant une méta-surface à base de résonateurs à eau. Le modèle théorique de l'adaptation d'impédance est développé et il est le fondement dans la conception de la structure à base d'eau. L'eau confinée dans le PDMS agit comme un résonateur qui induit non seulement la résonance magnétique pour l'adaptation d'impédance mais aussi l'absorption des micro-ondes. (Voir chapitre 3)

(4) Une absorption omnidirectionnelle sur une surface incurvée est démontrée. En outre, le dispositif expérimental pour la caractérisation en champ lointain de l'absorption omnidirectionnelle a été développé à cet effet. (Voir chapitre 3)

(5) Une absorption accordable en fréquence dans le domaine Térahertz et indépendante des angles a été conçue, fabriquée et caractérisée expérimentalement, en utilisant une méta-surface à base de métal liquide. La gamme d'accordabilité de la fréquence centrale a atteint 51,1% avec une absorption supérieure à 90%. La plage de réglage est maintenue à un niveau élevé avec une tolérance angulaire jusqu'à 60°. (Voir chapitre 4)

(6) Une méta-surface chirale accordable est développée ainsi que le modèle théorique de sa conception. Les structures bicouches combinées à un contrôle micro-fluidique ont permis une nouvelle fonctionnalité, celle d'accorder la méta-surface de l'état achiral à l'état chiral. L'onde électromagnétique a ainsi pu être accordée de la transmission symétrique à la transmission asymétrique. (Voir chapitre 5)

(7) La transmission asymétrique est améliorée à plus de 50% dans les structures bicouches convenablement conçues. Elle peut être réduite graduellement et de façon continue jusqu'à 0, en appliquant une pression d'air différente pour reconfigurer la forme géométrique des structures. (Voir chapitre 5)

Chapitre 2. Etat de l'Art Bibliographique

Dans ce chapitre, nous examinons les notions générales de base relatives à ce projet de doctorat. Le chapitre se compose de quatre parties. La section 2.1 présente un aperçu des concepts fondamentaux de la méta-surface. La permittivité électrique et la perméabilité magnétique de la méta-surface peuvent être contrôlées pour réaliser diverses propriétés en concevant rationnellement la géométrie et la composition des structures. Ces propriétés incluent l'indice de réfraction négatif, l'absorption parfaite, la discontinuité de phase, la transparence induite par voie électromagnétique, la conversion de polarisation, etc. De nouvelles propriétés permettent des applications considérables dans de nombreux domaines, tels que le revêtement invisible, la bio-détection, l'imagerie en super résolution, la règle plasmonique, le polariseur, etc.

La section 2.2 présente un diagramme alternatif pour concevoir la méta-surface en utilisant des matériaux diélectriques. Comparée à la méta-surface à base de métal, la méta-surface diélectrique induit une résonance de Mie au lieu de la résonance

plasmonique. La résonance de Mie induite dans les particules diélectriques est basée sur des courants de déplacement, qui peuvent adapter la permittivité et la perméabilité effectives de la méta-surface. Cependant, la méta-surface diélectrique est capable de fournir des efficacités de transmission élevés pour la création de fronts d'onde optiques arbitraires et un facteur Q élevé de transparence induite par voie électromagnétique, et ceci en utilisant des matériaux diélectriques à faible perte. L'absorption élevée recourant aux méta-surfaces diélectriques basées sur des matériaux à forte perte est également discutée.

La section 2.3 présente brièvement des méta-surfaces à base de méta-liquide qui sont réalisées en partie à base de matériaux liquides, soit le milieu environnant, soit la structure résonante, soit les deux. Ils appartiennent à la classe des méta-surfaces accordables, capables de donner lieu à un contrôle en temps réel de leurs propriétés par des sollicitations externes. Trois types de méta-surfaces à base de méta-liquide sont décrits, y compris les méta-surfaces à base de cristaux liquides, les méta-surfaces à base de métaux liquides et les méta-surfaces à base de diélectrique liquide. Ces méta-surfaces à base de méta-liquides offrent d'excellentes possibilités soit pour changer l'indice de réfraction des structures liquides, soit pour remodeler en continu les structures liquides de l'état de non-remplissage à l'état de remplissage complet. Ils offrent la possibilité d'un accord uniforme pour toutes les structures ou alors celle d’un accord d'accès aléatoire pour chaque cellule unitaire individuelle.

La section 2.4 décrit les concepts fondamentaux de la méta-surface chirale dans laquelle un couplage croisé entre le champ électrique et le champ magnétique est induit lorsque l'onde EM la traverse. La méta-surface chirale fournit également une nouvelle voie vers l'indice de réfraction négatif. En outre, d'autres propriétés optiques utilisant la méta-surface chirale sont également passées en revue, telles que la réactivité optique, le dichroïsme circulaire et la transmission asymétrique.

Chapitre 3. Méta-surface à base de résonateur d'eau

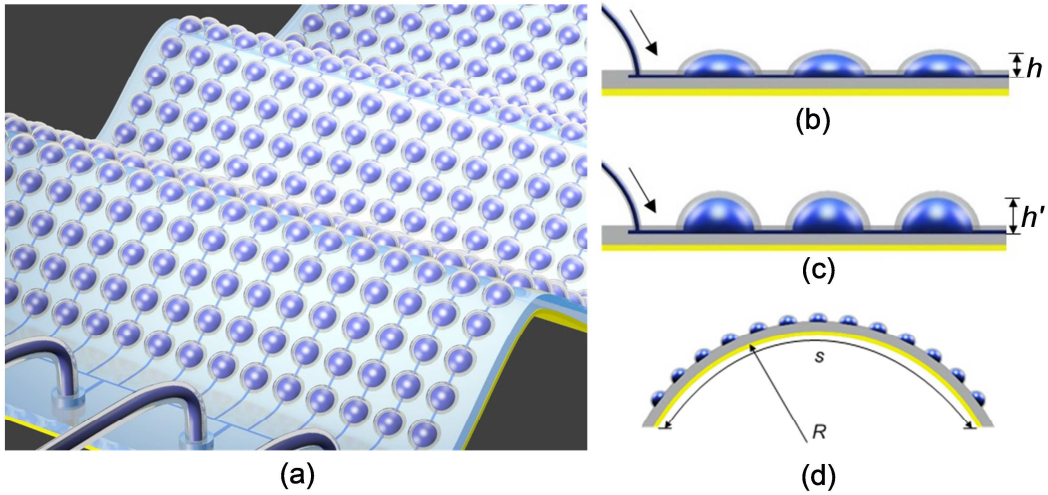

Fig. 1 *Méthode schématique (a) et d'accordabilité (b), (c), (d), de la méta-surface à base de résonateurs à eau.*

Ce chapitre présente la conception théorique, la fabrication et les expériences de la méta-surface à base de résonateurs à eau pour une absorption ultra-large bande et quasi-unitaire dans l'ensemble des bandes Ku, K et Ka.

La section 3.1 présente la conception et l'analyse théorique de la méta-surface à base de résonateurs à eau. Le résonateur à eau est incorporé dans le matériau PDMS à faible permittivité, formant une structure en sandwich PDMS / eau / PDMS comme montré sur la Fig. 1a. La membrane PDMS supérieure est dilatée à différents degrés en modifiant le volume d'eau injecté, conduisant à une hauteur contrôlable du résonateur à eau de h = 0,4 mm à 1,6 mm, comme le montre la Fig. 1 (b-c). Avec la valeur élevée de la partie réelle ε de la permittivité de l'eau et des paramètres géométriques spécifiques, une résonance magnétique et un effet de réseau de diffraction peuvent être excités à certaines fréquences du résonateur à eau. Dans le même temps, la valeur élevée de la partie imaginaire ε" de la permittivité de l'eau dans une large gamme de fréquences permet une absorption de large bande autour des fréquences de résonance. Grâce à l'analyse théorique de

l'adaptation d'impédance de l'interface eau-air et à la combinaison de l'effet de résonance magnétique et de diffraction, l'absorption ultra-large bande est obtenue.

La section 3.2 comprend les procédés de fabrication et le dispositif expérimental pour la mesure dans le domaine micro-ondes. Les procédés de fabrication de la méta-surface basée sur les résonateurs à eau sont basés sur la photolithographie. La section 3.3 présente les résultats expérimentaux de la méta-surface à base de résonateurs à eau. L'absorption double bande induite par l'effet combiné de résonance magnétique et de diffraction peut être contrôlé en ajustant la hauteur des résonateurs à eau. Le pic d'absorption à la fréquence inférieure montre un décalage spectral négatif (*red-shift*) de la bande K (20 GHz) à la bande Ku (15 GHz) lorsque la hauteur du résonateur d'eau est augmentée de 0,4 mm à 1,2 mm, car la longueur effective de la résonance magnétique est alors augmentée. D'autre part, le pic d'absorption à la fréquence supérieure n'est pas décalé car il est provoqué par l'effet de réseau à partir du réseau de résonateurs périodiques dont la période n’est pas affectée. En conséquence, l'absorption ultra-large bande est obtenue lorsque ces deux pics d'absorption se confondent. Une telle absorption large bande a une tolérance angulaire jusqu'à 45°. La méta-surface à base de résonateurs à eau peut également être mise en flexion vers une surface incurvée arbitraire comme illustré sur la Fig. 1d et ce, grâce à la flexibilité du PDMS et de l'eau. Ce degré de liberté supplémentaire permet une absorption omnidirectionnelle sur différentes surfaces courbes. De plus, la méta-surface à base de résonateurs à eau peut être remplie par des solutions d'éthanol dans l’eau à différentes concentrations pour modifier l'absorption, ce qui est également démontré expérimentalement sous forme d’un modulateur d'intensité à large bande.

Chapitre 4. Méta-surface à base de métaux liquides

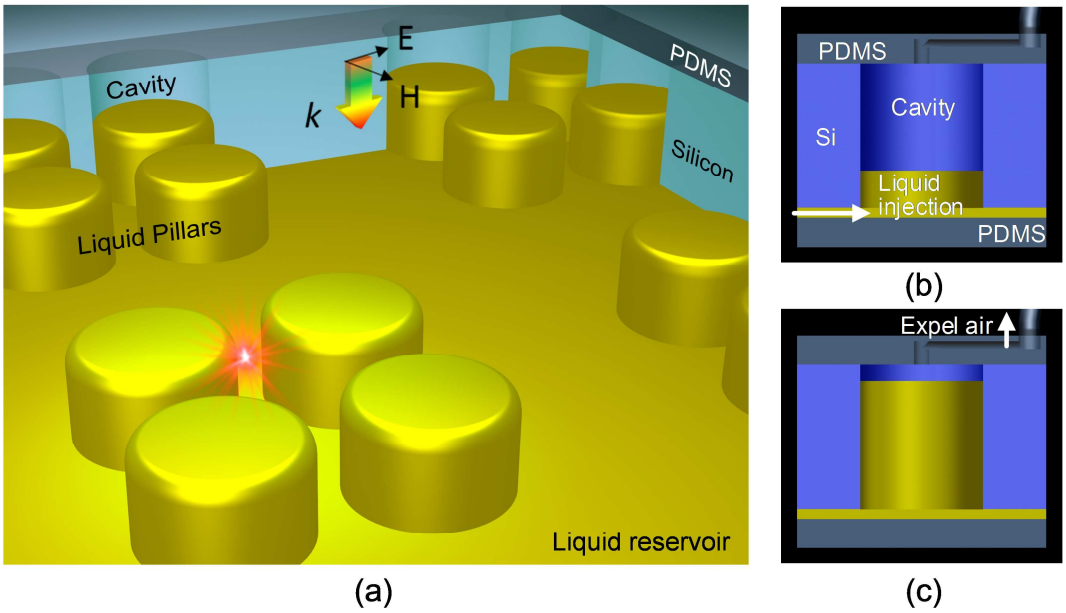

Fig. 2 *Méthode schématique (a) et de réglage (b), (c), de la méta-surface à base de métaux liquides.*

Ce chapitre présente la conception, la fabrication et les expériences réalisées sur des méta-surfaces à base de structures en piliers liquides, pour l'absorption accordable en fréquence et indépendante de l'angle dans la gamme des Térahertz.

La section 4.1 présente la conception et l'analyse théorique de la méta-surface basée sur les piliers liquides. La méta-surface à base de piliers liquides se compose d'une couche de silicium avec des cavités micro-usinées et prises en sandwich par deux couches PDMS, comme illustré dans la Fig. 2a. Le liquide métallique est injecté à partir de la couche PDMS inférieure à travers un micro-canal et introduit dans chaque cavité de silicium comme représenté sur la Fig. 2b. La hauteur des piliers métal liquide peut être contrôlée par la pression d'air appliquée depuis l'entrée d'air dans la couche PDMS supérieure, comme le montre la Fig. 2c, qui rompt ainsi la limitation d'accord dans le plan 2D et fournit, par le degré de liberté supplémentaire de la hauteur, une plage d'accord large bande de la méta-surface.

En appliquant des pressions d'air différentes, on peut ainsi augmenter ou diminuer la hauteur des colonnes métal liquide, ce qui aboutit à un processus réversible de reconfiguration flexible des résonateurs. La structure symétrique avec quatre piliers métal liquide identiques dans chaque élément de base permet des caractéristiques d'absorption qui sont indépendantes de la polarisation. L'analyse numérique montre que l'absorption élevée est attribuée au mode de résonance magnétique. Afin de réaliser le contrôle dynamique de la fréquence d'absorption, la longueur effective de la résonance magnétique plasmonique peut être contrôlée en ajustant la hauteur des piliers en métal liquide. La hauteur croissante des piliers métal liquide entraîne un décalage spectral négatif (*red-shift*) de la résonance magnétique.

La section 4.2 présente brièvement les procédés de fabrication et le dispositif expérimental pour les mesures dans la gamme Térahertz. La section 4.3 présente les résultats expérimentaux obtenus sur la méta-surface à base de métaux liquides. Tout d'abord, le caractère indépendant de la polarisation est démontré expérimentalement. Ensuite, l'absorption agile en fréquence est discutée en ajustant la hauteur des piliers métal liquide de 0 à 100 μm. La plage de réglage de la fréquence du pic d'absorption atteint 51,1% de la fréquence centrale avec une absorption supérieure à 90%. De plus, les spectres d'absorption avec différents angles d'incidence (mode TM) montrent un décalage négatif de la fréquence de pics d'absorption lorsque l'angle d'incidence augmente. Une telle diminution de la fréquence peut toutefois être compensée si besoin en diminuant la hauteur des piliers métal liquide. En réglant en continu la hauteur des piliers métal liquide, l'absorption indépendante de l'angle peut couvrir toutes les fréquences de 0,25 THz à 0,33 THz avec une plage de réglage de la fréquence centrale de 27,6%.

Chapitre 5. Méta-surface chirale accordable

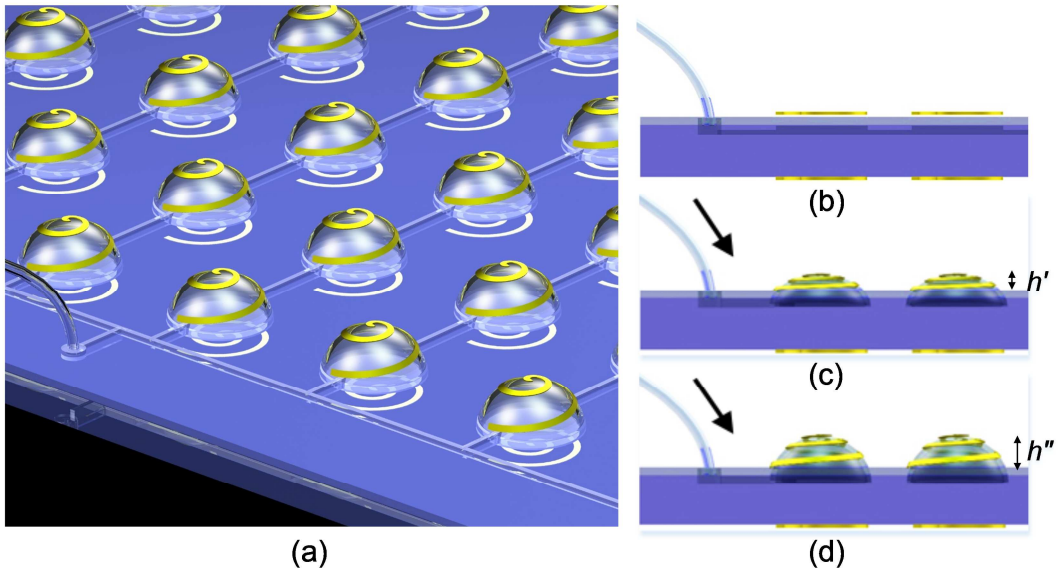

Fig. 3 *Schéma et méthode de contrôle de la méta-surface chirale accordable.*

Ce chapitre présente la conception, la fabrication de la structure et les expériences réalisées sur la méta-surface chirale accordable pour une transmission asymétrique accordable. La méta-surface chirale accordable peut être contrôlée d'achiral à chirale en utilisant une technique de contrôle micro-fluidique, grâce à quoi la transmission peut être commandée de la transmission symétrique à la transmission asymétrique.

La section 5.1 présente la conception de la structure et l'analyse numérique de la méta-surface chirale accordable. La théorie de la transmission asymétrique de l'onde polarisée linéairement est présentée. La méta-surface chirale accordable est constituée d'une couche de PDMS prise en sandwich entre deux structures métalliques en forme de spirales, comme illustré sur la Fig. 3a. L'état initial de la méta-surface est plan, comme le montre la Fig. 3b, avant injection d'air. Une telle méta-surface planaire est achirale et présente une transmission symétrique sous incidence avant et arrière. Comme la membrane PDMS inférieure est beaucoup plus épaisse que la membrane PDMS supérieure, lorsque l'air est injecté dans les

canaux micro-fluidiques, la membrane PDMS supérieure est dilatée et forme un capuchon de PDMS de forme quasi-hémi-sphérique du fait de la pression d'air appliquée, tandis que la couche PDMS inférieure reste plane. La membrane supérieure de PDMS étire ainsi les structures spirales supérieures hors du plan qui deviennent des spirales 3D. En appliquant une pression d'air différente, la membrane PDMS supérieure peut être dilatée ou contractée, ce qui a pour résultat un processus réversible de reconfiguration flexible de la hauteur de la structure en spirale, comme le montre la Fig. 3 (c-d). La rupture symétrique des deux structures en spirale introduit la chiralité et la transmission sous incidence avant et arrière donnant lieu à une réponse asymétrique. Le modèle théorique d'hybridation plasmonique est introduit pour expliquer les deux pics de résonance dans les spectres de transmission. La simulation numérique montre que l'onde de propagation peut être commandée de la transmission symétrique à la transmission asymétrique quand les structures en spirale supérieures sont accordées de l'éat planaire 2D à l'état 3D.

La section 5.2 présente d'abord les procédés de fabrication combinant la photolithographie et l'évaporation par faisceau d'électrons. Ensuite, on démontre expérimentalement la transmission asymétrique accordable en imprimant les structures en spirale symétriquement sur les deux faces de la couche de PDMS. La transmission asymétrique peut être encore améliorée à 50% en imprimant les structures en spirale de façon asymétrique sur les deux faces en PDMS. A la fréquence de 37 GHz, la transmission asymétrique peut être accordée de 50% à 0 lorsque la hauteur des structures en spirale passe de 0 à 1,4 mm.

Chapitre 6. Conclusion et recommandations

Ce chapitre résume les travaux de recherche et fournit diverses recommandations pour les perspectives de travaux futurs. La section 6.1 décrit les principales conclusions des trois méta-surfaces méta-liquides considérées.

La méta-surface basée sur le résonateur à eau est la première démonstration de la combinaison de l'effet de résonance magnétique et de réseau de diffraction pour réaliser une absorption ultra-large bande et proche de l'unité sur l'ensemble des bandes Ku, K et Ka. Cette démonstration a été réalisée en utilisant un matériau diélectrique, incorporé dans le matériau PDMS souple. Par rapport à d'autres matériaux, l'eau liquide fournit non seulement des propriétés de pertes fortes, ce qui est essentiel à l'absorption, mais offre également beaucoup de souplesse dans le contrôle de la forme de la structure. De plus, un contrôle en temps réel de l'absorption large bande, y compris la fréquence d'absorption et la résistance à l'absorption, est démontré par l'intégration de la technologie micro-fluidique. De plus, une méta-surface incurvée à base de résonateurs à eau est présentée de manière innovante comme un absorbeur omnidirectionnel sur des surfaces incurvées.

La méta-surface à base de métal liquide combine la couche structurée en silicium à échelle microscopique et la couche de contrôle PDMS pour l'injection du métal liquide en vue de la reconfiguration. Les structures à triple couche permettent l'accord du métal liquide dans la direction verticale pour briser la limitation d'accord dans le plan 2D. Ceci constitue un jalon important pour ces méta-surfaces accordables. Un contrôle en temps réel est également démontré sur la fréquence d'absorption en ajustant la hauteur des piliers de métal liquide dans le régime Térahertz. De plus, une absorption indépendante de l'angle est également démontrée avec une grande tolérance angulaire jusqu'à 60°. Le mécanisme de l'absorption à grand angle est étudié numériquement.

La méta-surface chirale accordable est la première démonstration de reconfiguration de structures métalliques solides grâce à l'apport de la technologie micro-fluidique. Ceci a été mis en œuvre pour réaliser une méta-surface chirale accordable de l'état achiral à l'état chiral. Par conséquent les micro-ondes transmises par ces méta-surfaces ont pu être commandés d'une transmission symétrique à une transmission asymétrique. Les procédés de fabrication pour la reconfiguration géométrique du métal solide s'appuient sur les techniques de micro-fluidique et sont mis en œuvre en combinant la photolithographie et l'évaporation par faisceau d'électrons. Une grande accordabilité sur la transmission asymétrique est réalisée en modifiant la pression d'air dans le réservoir micro-fluidique créé dans le PDMS.

Dans la section 6.2, les recommandations pour les perspectives de travaux futurs sont résumées comme suit :

La reconfiguration des méta-surfaces est réalisée par la mise en œuvre de la technologie micro-fluidique, laquelle utilise une pompe pour contrôler la pression. Malgré les démonstrations réussies de réponses électromagnétiques accordables par voie micro-fluidique, la vitesse d'accord reste toutefois limitée. Une solution possible consiste à réduire la taille des structures reconfigurées. Une méta-surface de plus petite taille pourrait considérablement améliorer la vitesse d'accord.

Bien que la largeur de bande d'absorption démontrée dans le chapitre 3 soit déjà en ultra-large bande, elle peut encore être élargie en utilisant un réseau non homogène de résonateurs à eau. La configuration proposée de réseau non uniforme de résonateurs à eau devrait induire une résonance magnétique multiple de manière à améliorer davantage la bande passante. Pour réaliser une distribution non uniforme des résonateurs à eau, une méthode d'accord par accès aléatoire est requise, comme indiqué au chapitre 2.

La gamme d'accord de l'absorption et de la transmission asymétrique démontrée dans les chapitres 3 et 5, peut être encore augmentée en étendant la membrane PDMS supérieure à un degré plus important. Cependant, la pression croissante peut conduire à la rupture de la liaison des couches PDMS supérieure et inférieure. Une approche alternative possible consiste à rendre la membrane PDMS supérieure plus fine, de telle sorte qu'une pression plus faible suffise à dilater la membrane PDMS supérieure, ce qui peut être obtenu en utilisant un dispositif d'enduction par centrifugation à vitesse plus élevée pour la réalisation de cette membrane.

La gamme d'accord de la fréquence d'absorption démontrée au chapitre 4 peut en principe être encore augmentée en utilisant un substrat de silicium plus épais de sorte à augmenter la hauteur maximale des piliers de métal liquide. Cependant, la hauteur croissante du silicium donne lieu à plus de pics de résonance Fabry-Pérot (FP) dans le spectre. Une approche envisageable consisterait alors à remplacer le silicium par un matériau d'indice de réfraction inférieur, tel que le quartz cristallin.

Dans la conception de la méta-surface chirale accordable, une transmission asymétrique forte a été démontrée avec succès. Cependant, une amélioration peut être apportée en augmentant la chiralité de la méta-surface. Une approche consiste à utiliser des structures en spirale multicouches au lieu du système bicouche considéré dans nos travaux.

En conclusion, il y a encore un important potentiel pour de nombreux travaux de recherche complémentaires dans le domaine des méta-surfaces à base de méta-liquide, et qui pourrait donner lieu à des études complémentaires en vue de l’amélioration des leurs performances et l’approfondissement de leur modélisation théorique pour en faciliter la conception.

Summary

Novel and tailored electromagnetic properties can be realized using a metasurface through artificially designed structures. The effective permittivity and permeability of a metasurface can be flexibly designed and even tuned so as to exhibit electromagnetic responses that can be very different from those of their natural counterparts, leading to enhanced properties and sometimes to extra-ordinary behaviour.

This thesis focuses on the design, fabrication and experimentation of meta-liquid-based metasurfaces for electromagnetic wave control and modulation. These metasurfaces are based on the use of both photolithography-based microfabrication and microfluidic technologies implemented onto thin and flexible substrates of sub-wavelength thickness. More specifically, the incorporation within a microfluidic channel network of various materials, including liquid dielectric material, liquid metal and solid metal have been exploited to further manipulate the electromagnetic responses of the related metasurfaces, such as the absorption, transmission and chirality.

The first part of the thesis reports an ultra-broadband and wide-angle absorbing material by water-resonator-based metasurface. It consists of an array of water droplets embedded in the soft dielectric material, PDMS; it exhibited an almost perfect absorptivity over the Ku, K and Ka bands. The second part of the thesis focuses on a frequency-agile and wide-angle absorber in terahertz by liquid-metal-based metasurface, where a liquid-metal-pillar array can be continuously controlled in the vertical direction hence breaking the tuning limitation in the 2D plane. The third part of the thesis focuses on an active chiral metasurface. The metasurface can be switched from achiral to chiral by changing the spiral structure from planar pattern to 3D pattern. This functionality can manipulate the microwave transmission from symmetric to asymmetric under forward and backward incidence.

In conclusion, tunability on the absorption, transmission and chirality have been realized through microfluidic metasurfaces, which appear having high potential applications in various areas such as stealth technology, imaging system, and optical communication, to name a few.

Résumé

Des propriétés électromagnétiques nouvelles peuvent être réalisées à l'aide d'une méta-surface à travers des structures artificielles. La permittivité et la perméabilité effectives d'une méta-surface peuvent être conçues de façon flexible et même accordées de sorte à présenter des réponses électromagnétiques pouvant être très différentes de celles de leurs homologues naturels, ce qui conduit à des propriétés améliorées voire parfois à un comportement extraordinaire.

Cette thèse porte sur la conception, la fabrication et l'expérimentation de méta-surfaces micro-fluidiques pour le contrôle de propriétés des ondes électromagnétiques. Leur réalisation est basée sur des technologies relevant de la photolithographie et de la micro-fluidique, mises en œuvre sur des substrats souples d'épaisseur sub-longueur d'onde. Plus spécifiquement, nous avons exploité l'incorporation de divers matériaux dans un réseau de canaux micro-fluidiques, y compris des diélectriques liquides, un métal liquide et un métal solide pour manipuler davantage les réponses électromagnétiques des méta-surfaces correspondantes, telles que l'absorption, la transmission et la chiralité.

La première partie de la thèse présente une méta-surface très absorbante sur une ultra-large bande spectrale et. Elle est constituée d'un réseau de résonateurs formés de gouttelettes d'eau noyées dans le matériau diélectrique souple, le PDMS; l'absorption mesurée est presque parfaite sur les bandes Ku, K et Ka. La seconde partie de la thèse porte sur un absorbeur agile et indépendant de l'angle dans la gamme Térahertz ; il s'agit d'une méta-surface à base de métal liquide, où un réseau de puits métalliques liquides dont la hauteur est commandée en continu, ce qui brise la limitation d'accordabilité dans le plan 2D. La troisième partie de la thèse porte sur une méta-surface chirale active. La méta-surface peut être commutée de achiral à chiral en déformant la structure en spirale initialement plane vers une géométrie 3D. Cette fonctionnalité peut manipuler la transmission hyperfréquence de symétrique à asymétrique sous incidence avant et arrière.

En conclusion, l'optimisation de l'absorption, de la transmission et de la chiralité d'ondes électromagnétiques a été réalisée grâce à des méta-surfaces micro-fluidiques, qui semblent ainsi présenter un important potentiel applicatif dans divers domaines tels que la technologie furtive, l'imagerie et la communication optique.